CAROLINE MURAWSKI

Geboren am 22.02.1987 in Dresden,
Geburtsname: Caroline Weichsel

Efficiency Roll-Off in Organic Light-Emitting Diodes

Dissertation zur Erlangung des akademischen Grades
DOCTOR RERUM NATURALIUM

TECHNISCHE UNIVERSITÄT DRESDEN

Technische Universität Dresden
Fakultät Mathematik und Naturwissenschaften
Fachrichtung Physik
Institut für Angewandte Photophysik

Eingereicht am 21.04.2015
Verteidigt am 28.08.2015

1. Gutachter: Prof. Dr. Karl Leo
2. Gutachter: Prof. Dr. Malte C. Gather

In Erinnerung an meinen Großvater Prof. Dr. Ludwig Walther

Abstract

The efficiency of organic light-emitting diodes (OLEDs) typically decreases with increasing current density. This so-called *roll-off* impedes the market entry of OLEDs in high-brightness applications such as general lighting. One of the most important processes causing roll-off is exciton annihilation, which evolves upon high exciton densities. This mechanism is especially pronounced in phosphorescent molecules due to their long triplet lifetime. In order to reduce the roll-off in phosphorescent OLEDs, this thesis focusses on decreasing the local exciton density by modifying the exciton lifetime, the spatial exciton distribution, and the tendency of emitters to form aggregates. The obtained results lead to a deeper understanding of efficiency roll-off and help sustaining the OLED efficiency at high brightness.

The emitter lifetime can be influenced by the optical environment around the emitting dipoles through the Purcell effect. In order to study this effect, the distance between emitter and metal cathode is varied for two different OLED stacks. A strong influence of emitter position and orientation on roll-off is observed and explained by modelling the data with triplet-triplet annihilation theory. Furthermore, design principles for optimal high-brightness performance are established by simulating the roll-off as a function of emitter-cathode distance, emissive dipole orientation, and radiative efficiency.

Next, a method is developed that allows extracting the spatial exciton distribution. Therefore, a thin sensing layer that locally quenches excitons is introduced into the emission layer at varying positions. The resulting quenching profile is then fitted using a comprehensive theory based on the diffusion equation, which renders the exciton distribution and diffusion length with nanometer resolution. This method is applied to an emission layer comprising an ambipolar host material. Contrary to expectations which suggest that ambipolar materials exhibit broad exciton formation, a narrow emission zone close to the electron transport layer is found. Additional explorations of structures that might broaden the emission zone point to a narrow emission zone in double emission layers and broader exciton formation in mixed emission layers.

Previous investigations revealed a strong correlation between emitter aggregation and molecular dipole moment of the emitter. Within this thesis, the range of studied emitters is significantly extended. It is shown that homoleptic emitters show a stronger tendency to form aggregates than heteroleptic compounds. This is probably not

only related to their higher dipole-dipole potential, but also to the molecular structure. Systematic analysis of the deposition parameters shows that aggregate formation depends on the underlying material and increases with increasing substrate temperature and decreasing evaporation rate.

The two green emitters $Ir(ppy)_3$ and $Ir(ppy)_2(acac)$ are additionally studied by means of X-ray diffraction. Both emitters form crystallite grains and exhibit a preferred orientation. Doping the emitters into an amorphous host, both orientation and crystallite formation retain at the investigated doping concentrations above 20 wt %. This result is a first step toward further understanding of the mechanism of transition dipole orientation.

Kurzfassung

Die Effizienz organischer Leuchtdioden (OLEDs) nimmt üblicherweise mit ansteigender Stromdichte ab. Dieser so genannte *Roll-Off* erschwert den Markteintritt von OLEDs in Bereichen, die hohe Helligkeiten erfordern, wie beispielsweise in der Beleuchtung. Einer der wichtigsten Prozesse, die zu Roll-Off führen, ist die Annihilation von Exzitonen. Diese nimmt mit steigender Exzitonendichte zu und ist vor allem in phosphoreszenten OLEDs aufgrund der dort vorhandenen langen Triplettlebensdauer ein großer Verlustfaktor. Im Rahmen dieser Dissertation werden Methoden vorgestellt, die mittels Reduzierung der Exzitonendichte den Roll-Off in phosphoreszenten OLEDs verringern können. Dazu gehören die Veränderung der Exzitonenlebensdauer, die Untersuchung der räumlichen Verteilung der Exzitonen und die Erforschung der Bildung von Emitteraggregaten. Die gewonnenen Ergebnisse führen zu einem besseren Verständnis des Effizienz Roll-Offs und helfen, die Effizienz von OLEDs bei hohen Helligkeiten zu verbessern.

Die Emitterlebensdauer kann über den Purcell-Effekt durch Veränderung des die emittierenden Dipole umgebenden elektromagnetischen Felds beeinflusst werden. Dieser Effekt wird genutzt, indem der Abstand zwischen Emitter und Metallelektrode für zwei verschiedene OLED-Aufbauten variiert wird. Der Roll-Off ist stark abhängig von der Position und Orientierung des Emitters und kann durch Modellierung der Daten auf Basis von Triplett-Triplett-Annihilation erklärt werden. Durch Simulation des Roll-Offs in Abhängigkeit des Emitter-Kathode-Abstands, der Orientierung und der strahlenden Effizienz der emittierenden Dipole werden Prinzipien zur optimalen Leistung von OLEDs bei hohen Helligkeiten entwickelt.

Als nächstes wird eine Methode eingeführt mittels derer die räumliche Exzitonenverteilung extrahiert werden kann. Dafür wird eine dünne Sensorschicht in die Emissionsschicht eingebracht, die lokal Exzitonen auslöscht. Unter Variation der Position des Sensors wird ein Profil der Auslöschungsintensität bestimmt. Die gemessene Intensität wird mittels einer umfassenden Theorie auf Grundlage der Diffusionsgleichung angepasst, wodurch sich die räumliche Verteilung der Exzitonen und die Diffusionslänge mit einer Auflösung von 1 nm ergibt. Die Methode wird auf eine Emissionsschicht angewandt, die das ambipolare Matrixmaterial CBP enthält. Entgegen der Erwartung, dass die Exzitonenbildung in ambipolaren Materialien weiter ausgedehnt ist, ist die gemessene Emissionszone sehr schmal und

befindet sich an der Grenze zur Elektronentransportschicht. Um eine Verbreiterung des Emissionsprofils zu ermöglichen, werden weitere Strukturen untersucht. Dabei wird eine schmale Emissionszone in Doppelemissionsschichten beobachtet, wohingegen gemischte Emissionsschichten zu einer Verbreiterung der Exzitonenbildung führen können.

Vorangegangene Untersuchungen deckten einen Zusammenhang zwischen der Aggregation von Emittermolekülen und dem Dipolmoment des Emitters auf. In dieser Arbeit werden weitere Emittermoleküle untersucht, wobei eine stärkere Aggregation von homoleptischen Emittern im Vergleich zu heteroleptischen festgestellt wird. Dies ist einerseits im höheren Dipol-Dipol-Potential der homoleptischen Verbindungen und andererseits in der Molekülstruktur begründet. Eine systematische Analyse der Herstellungsparameter zeigt, dass die Aggregatbildung von dem darunter liegenden Material abhängt und mit steigender Substrattemperatur und sinkender Verdampfungsrate zunimmt.

Die zwei Grünemitter $Ir(ppy)_3$ und $Ir(ppy)_2(acac)$ werden zusätzlich mittels Röntgenspektroskopie untersucht. Beide Emitter bilden kristalline Körner und weisen eine bevorzugte Orientierung auf. Sowohl die Kristallbildung als auch die Orientierung bleiben erhalten, wenn die Emitter mit mehr als 20 Gewichtsprozent in das Matrixmaterial CBP dotiert werden. Dieses Ergebnis ist ein erster Schritt zum besseren Verständnis der in vielen Iridium-Emittern beobachteten Orientierung des Übergangsdipolmoments.

List of Publications

Journal Articles

1. *Caroline Weichsel*, Sebastian Reineke, Björn Lüssem, and Karl Leo: „Organic light-emitting diodes for lighting: High color quality by controlling energy transfer processes in host-guest-systems“, *J. Appl. Phys.* **111**, 033102 (2012).

2. *Caroline Weichsel*, Sebastian Reineke, Björn Lüssem, and Karl Leo: "Influence of the electron blocking layer on the performance of multilayer white organic light-emitting diodes", *MRS Proceedings* **1402**, U08-40 (2012).

3. *Caroline Weichsel*, Lorenzo Burtone, Sebastian Reineke, Susanne Hintschich, Malte C. Gather, Karl Leo, and Björn Lüssem: "Storage of charge carriers on emitter molecules in organic light-emitting diodes", *Phys. Rev. B* **86**, 075204 (2012).

4. *Caroline Weichsel*, Sebastian Reineke, Malte C. Gather, Karl Leo, and Björn Lüssem: "Quantification of charge carrier density in organic light-emitting diodes by time-resolved electroluminescence", *Proc. of SPIE* 84761I (2012).

5. Philipp Liehm, *Caroline Murawski*, Mauro Furno, Björn Lüssem, Karl Leo, and Malte C. Gather: "Comparing the emissive dipole orientation of two similar phosphorescent green emitter molecules in highly efficient organic light-emitting diodes", *Appl. Phys. Lett.* **101**, 253304 (2012).

6. Changhun Yun, Guohua Xie, *Caroline Murawski*, Jonghee Lee, Fabian Ventsch, Karl Leo, and Malte C. Gather: "Understanding the influence of doping in efficient phosphorescent organic light-emitting diodes with an organic p-i-n homojunction", *Org. Electr.* **14**, 1695 (2013).

7. *Caroline Murawski*, Karl Leo, and Malte C. Gather: "Efficiency roll-off in organic light-emitting diodes", *Adv. Mater.* **25**, 6801 (2013).

8. Simone Hofmann, Markus Hummert, Reinhard Scholz, Regina Luschtinetz, *Caroline Murawski*, Paul-Anton Will, Susanne Hintschich, Jörg Alex, Vygintas Jankus, Andrew P. Monkman, Björn Lüssem, Karl Leo, and Malte C. Gather: "Engineering blue fluorescent bulk emitters for OLEDs: Triplet harvesting by green phosphors", *Chem. Mater.* **26**, 2414 (2014).

9. *Caroline Murawski*, Philipp Liehm, Karl Leo, and Malte C. Gather: "Influence of cavity thickness and emitter orientation on the efficiency roll-off of phosphorescent organic light-emitting diodes", *Adv. Funct. Mater.* **24**, 1117 (2014).

10. *Caroline Murawski*, Cornelius Fuchs, Simone Hofmann, Karl Leo, and Malte C. Gather: "Alternative p-doped hole transport material for low operating voltage and high efficiency organic light-emitting diodes", *Appl. Phys. Lett.* **105**, 113303 (2014).

11. Arko Graf, Philipp Liehm, *Caroline Murawski*, Simone Hofmann, Karl Leo, and Malte C. Gather: "Correlating the transition dipole moment orientation of phosphorescent emitter molecules in OLEDs with basic material properties", *J. Mater. Chem. C* **2**, 10298 (2014).

Conference Contributions (First Author Only)

1. *Caroline Weichsel*, Sebastian Reineke, Björn Lüssem, and Karl Leo: "Investigation of a full phosphorescent OLED for lighting application", *VIIth International Krutyn Summer School: Optoelectronics on the Move*, Krutyn, poster (2010).

2. *Caroline Weichsel*, Sebastian Reineke, Björn Lüssem, and Karl Leo: "Emission layer design for warm white light emission in organic LEDs", *European Conference on Molecular Electronics (ECME)*, Barcelona, poster P-070 (2011).

3. *Caroline Weichsel*, Sebastian Reineke, Björn Lüssem, and Karl Leo: "Energy transfer processes in host-guest-systems for white light emission in organic LEDs", *Plastic Electronics Conference*, Dresden, poster (2011).

4. *Caroline Weichsel*, Sebastian Reineke, Susanne Hintschich, Björn Lüssem, and Karl Leo: "Charge carrier storage and delayed recombination in white organic light-emitting diodes", *MRS Fall*, Boston, poster U8.40 (2011).

5. *Caroline Weichsel*, Sebastian Reineke, Björn Lüssem, and Karl Leo: "Charge carrier storage on emitter molecules in organic light-emitting diodes", *DPG Frühjahrstagung*, Berlin, talk DS 16.2 (2012).

6. *Caroline Weichsel*, Sebastian Reineke, Malte C. Gather, Karl Leo, and Björn Lüssem: "Quantification of charge carrier density in organic light-emitting diodes by time-resolved electroluminescence", *SPIE Optics and Photonics*, San Diego, talk 8476-53 (2012).

7. *Caroline Murawski*, Philipp Liehm, Simone Hofmann, Karl Leo, and Malte C. Gather: "Efficiency roll-off in organic light-emitting diodes: Influence of emitter position and orientation", *DPG Frühjahrstagung*, Dresden, talk DS 8.6 (2014).

8. *Caroline Murawski*, Philipp Liehm, Simone Hofmann, Karl Leo, and Malte C. Gather: "Efficiency roll-off in organic light-emitting diodes: Influence of emitter position and orientation", *International Conference on Electroluminescence and Organic Optoelectronics (ICEL)*, Cologne, talk O-1.19 (2014).

9. *Caroline Murawski*, Philipp Liehm, Simone Hofmann, Karl Leo, and Malte C. Gather: "Efficiency roll-off in organic light-emitting diodes", *Deutsche Physikerinnentagung*, Dresden, talk M.4 (2014).

Contents

List of Publications **ix**

1 Introduction **1**

2 Principles of Organic Semiconductors **5**
2.1 Molecular Orbitals . . . 5
2.2 Optical Properties . . . 7
2.3 Intermolecular Energy Transfer . . . 10
2.4 Charge Transport . . . 11
2.5 Organic Light-Emitting Diodes . . . 13
2.5.1 Structure and Working Principle . . . 13
2.5.2 Characterization . . . 15

3 Theory of Efficiency Roll-Off **19**
3.1 Current Status . . . 19
3.2 Processes Leading to Roll-Off . . . 21
3.2.1 Triplet-Triplet Annihilation . . . 22
3.2.2 Triplet-Polaron Interaction . . . 26
3.2.3 Further Processes Influencing Roll-Off . . . 27
3.3 Interplay of the Various Processes . . . 29
3.4 Scope of this Work . . . 30

4 Experimental Methods **33**
4.1 Sample Preparation . . . 33
4.2 Measurement . . . 34
4.2.1 Thin-Film Characterization . . . 34
4.2.2 OLED Characterization . . . 35
4.3 Materials . . . 36
4.3.1 Electrodes, Transport Materials, and Blockers . . . 36
4.3.2 Materials of the Emission Layer . . . 37

5 Influence of the Optical Environment **39**
5.1 Introduction . . . 39
5.2 Influence of Emitter-Cathode Distance . . . 39
5.3 Emitter Lifetime and Orientation . . . 41
5.4 Correlation of Roll-Off and Orientation . . . 43
5.5 Simulation of Roll-Off . . . 44
5.5.1 Influence of the Electroluminescence Spectrum . . . 45
5.5.2 Influence of Orientation and Radiative Efficiency . . . 47
5.6 Conclusion . . . 48

6 Influence of the Emission Profile **51**
6.1 Preliminary Considerations . . . 51
6.1.1 Exciton Generation and Diffusion . . . 51
6.1.2 Width of the Emission Zone . . . 54
6.1.3 Dependence on the Structure of the Emission Layer . . . 56
6.2 Measurement of the Emission Profile . . . 57
6.2.1 Method . . . 57
6.2.2 Mathematical Description . . . 57
6.2.3 Experimental Realization and Evaluation . . . 60
6.3 Ambipolar Matrix Materials . . . 62
6.3.1 Device Performance . . . 62
6.3.2 Influence of the Sensing Layer . . . 63
6.3.3 Emission Profile . . . 65
6.4 Double- and Mixed Emission Layers . . . 69
6.4.1 Emission Profile . . . 70
6.4.2 Influence of the Matrix Ratio . . . 73
6.5 Summary and Outlook . . . 76

7 Influence of Molecular Aggregation **79**
7.1 Introduction . . . 79
7.2 Aggregation of Homoleptic and Heteroleptic Emitters . . . 80
7.2.1 Photoluminescence Measurements . . . 81
7.2.2 Time-Resolved Spectroscopy . . . 86
7.2.3 X-Ray Diffraction . . . 90
7.2.4 Conclusions on Emitter Orientation . . . 97
7.2.5 Comparison of the Different Methods—Emitter Aggregation . . . 98
7.3 Influence of the Matrix Material . . . 100
7.3.1 Photoluminescence Measurements . . . 102
7.3.2 Time-Resolved Spectroscopy . . . 103
7.4 Influence of Processing Parameters . . . 105
7.4.1 Substrate Heating . . . 105
7.4.2 Underlying Layer . . . 107
7.4.3 Evaporation Rate . . . 108
7.5 Summary and Implications of Aggregation on Efficiency Roll-Off . . . 108

8 Summary and Outlook **113**
8.1 Summary of Roll-Off Investigations . . . 113
8.2 Improving the High-Brightness Performance Further . . . 114
8.3 Concluding Words on Emitter Orientation . . . 116

A Appendix to Theory of Efficiency Roll-Off **117**

B Appendix to Emission and Sensing Profiles **121**
B.1 Emission Profiles . . . 121
B.2 Emission Profiles Including a Sensing Layer . . . 122
B.3 Sensing Profiles . . . 123

C Appendix to Double- and Mixed Emission Layers **125**
C.1 Sample Uniformity . . . 125

C.2 Influence of the Sensor on Current Density 126
C.3 Further D-EML and M-EML structures 126

D Appendix to Molecular Aggregation **129**

List of Chemical Compounds **131**

List of Abbreviations **133**

List of Important Symbols **135**

Bibliography **137**

Acknowledgement **155**

1 Introduction

In 1879, Thomas Alva Edison revolutionized domestic lighting by inventing the incandescent light bulb.[1] For more than 100 years, this inefficient but low-cost light source could not have been imagined to vanish from our daily life. Efficiency, however, is one of the main drawbacks of the light bulb: the power conversion efficiency reaches only around 15 lm/W, while 95 % of the applied energy is emitted as heat.[2] Furthermore, its lifetime is limited to approximately 1000 hours. Only in the 1980s, the competing fluorescent lamp became interesting for domestic lighting after a compact design had been developed. Although fluorescent lamps showed a strong improvement in both efficiency and operation lifetime, the produced light is of lower color quality and the containing mercury harms the environment. A good alternative is the environment-friendly light-emitting diode (LED), which nowadays reaches power conversion efficiencies well above 100 lm/W.[2–4] Just last year, this achievement was honored by awarding the Nobel prize in physics to the inventors of the efficient blue LED, which later enabled the production of white light from semiconductors.[5,6]

Another light source, which increasingly attracts attention in the lighting market, is the organic light-emitting diode (OLED). First invented in 1987 by Tang and van Slyke,[7] OLEDs nowadays are the basis for many small-sized displays, found for instance in mobile phones, cameras, and tablets. Compared to other light sources, they offer certain unique features, namely, emission as area instead of point source and the possibility to be produced as flexible and transparent devices. This is very interesting for displays, where area emission lies in its nature, but can also be highly attractive for lighting. Here, windows become imaginable that are transparent during day and shine during night; or it can be thought of lamps that emit their light homogeneously from across the whole ceiling.

OLEDs are furthermore attractive for lighting due to their potential to achieve good color rendering. In addition, as exemplified in Fig. 1.1, the color can easily be adjusted and tuned to special purposes. Yet, OLEDs have reached efficiencies that are on par with fluorescent tubes.[8] Furthermore, also the device lifetime becomes compatible with other light sources and OLEDs reaching more than 100 000 hours have already been demonstrated.[9] Still, suitable material combinations that yield high efficiency together with long lifetime and good color rendering are hard to find.

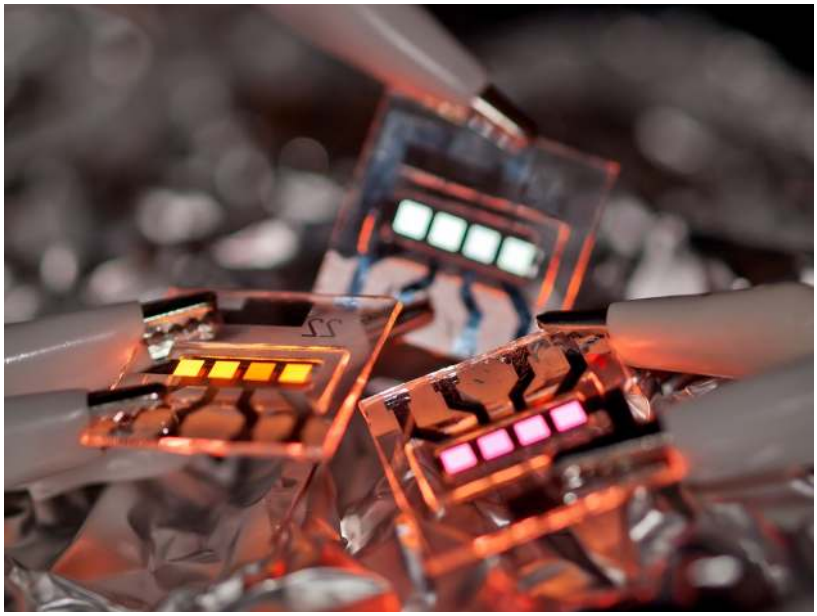

Figure 1.1: Photograph of three different OLEDs employing multiple emitters. While each OLED consists of the same materials, the different color is produced by varying the microcavity of the thin-film layer stack.

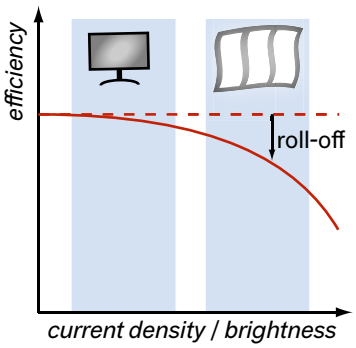

Figure 1.2: Schematic illustration of efficiency roll-off. Blue bars mark the application of OLEDs for displays and lighting.

One of the main reasons, why OLEDs so far have gained broad market entry only into displays and not into lightings is the so-called efficiency roll-off, which describes the decrease of efficiency with increasing brightness or current density. Figure 1.2 illustrates this effect and indicates two different OLED applications, which are differentiated according to their brightness regime: Displays ($100-500\,\mathrm{cd/m^2}$) and general illumination ($1000-10\,000\,\mathrm{cd/m^2}$).[10] Hence, the high brightness necessary for OLED lighting is one of the key issues that should be addressed in future in order to enable the use of OLEDs also in high-brightness applications.

The origin of efficiency roll-off is still under discussion.[11] One of the most important mechanisms is the annihilation of two excited states, which arises particularly upon high exciton densities.[12;13] Reducing the local exciton density can, thus, increase the efficiency at high brightness and shall be the main purpose of this work. Therefore, three different physical parameters are studied and methods are developed to improve each of them. The investigations include decreasing the exciton lifetime, enhancing the spatial exciton distribution, and reducing emitter aggregation.

After this short introduction, the basic principles of organic semiconductors and OLEDs are presented in Chapter 2. Chapter 3 gives a broad overview about the processes leading to roll-off and the state-of-the-art on this topic. Next, experimental techniques including sample preparation, measurement, and materials are described in Chapter 4. The results obtained in this thesis are structured according to the parameters as introduced above. In Chapter 5, the exciton lifetime is modified by changing the optical environment of the emitter. Then, in the course of Chapter 6, a method is developed to accurately measure the spatial exciton distribution. This is concurrently applied to three different emission layer designs. Chapter 7 studies molecular aggre-

gation of iridium-cored emitters using three different methods. The investigations are extended to research the influence of the host material and of the processing parameters. Finally, the thesis is closing in Chapter 8 by giving a summary and outlining work that should be done to further improve the roll-off in OLEDs.

2 Principles of Organic Semiconductors

Organic semiconductors offer interesting properties that can be used in state-of-the-art electronic devices. This chapter introduces their basic principles including the formation of molecular orbitals, optical and electrical properties, and intermolecular transfer processes. Focus is put on optical transitions and electrical doping. The final section presents the structure and working principle of organic light-emitting diodes and explains the factors which limit the device efficiency.

2.1 Molecular Orbitals

One of the interesting properties of organic semiconductors is that the optical, electrical, and structural properties can be tailored to special purposes by chemical engineering.[14] The following sections, therefore, aim at giving an overview about the relation between these properties and the molecular structure.

The basis for charge transport in organic molecules lies in the sp^2-hybridization: If several carbon atoms are close to each other, the conjugated double bonds between the atoms form an sp^2-orbital in the plane of the molecule and two p_z-orbitals per carbon atom perpendicular to the plane. The p_z-orbitals of neighboring atoms overlap and form a degenerate π-system, where electrons are delocalized. Electrons in the sp^2-orbitals instead constitute to the σ-bond. Due to the larger overlap of the sp^2-orbitals compared to the p_z-orbitals, electrons are more strongly bound in the σ-bond than in the π-bond. This is exemplified in Fig. 2.1 for the molecule ethene (C_2H_4). The σ-bonds are lying in the plane of the molecule, while the π-bond forms in a plane that lies parallel but outside the carbon atoms.

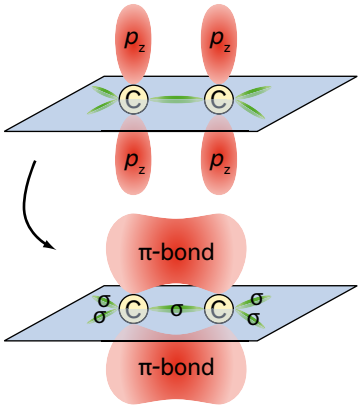

Figure 2.1: Molecular orbitals of ethene. Overlapping p_z orbitals form the π-bond. H-atoms (omitted for clarity) lie in the plane and are connected to the C-atoms with σ-bonds.

The electronic states of such a molecule are described by wave functions Ψ, which can be calculated by solving the time-independent Schrödinger equation:

$$\mathcal{H}\Psi_i = E_i\Psi_i. \tag{2.1}$$

Here, $\mathcal{H}$ denotes the Hamilton operator, which consists of the kinetic and potential energies of the nuclei and electrons as well as their interaction. Furthermore, the wave functions Ψ_i depend on the electron and nuclei positions $\vec{r}_i$ and $\vec{R}_j$, respectively.

In order to solve the Schrödinger equation, several approximations have to be introduced. First, the different mass between electrons and nuclei is assumed to cause an instantaneous respond of the electrons on a nuclear motion. This is the so-called Born-Oppenheimer

approximation.[15] The wave functions Ψ_i may therefore be separated into an electronic part $\phi_i^{\vec{R}}(\vec{r})$ and a nuclear (vibrational) part $\chi_i(\vec{R})$:

$$\Psi_i = \phi_i^{\vec{R}}(\vec{r}) \cdot \chi_i(\vec{R}). \tag{2.2}$$

This product ansatz allows solving the Schrödinger equation separately for electrons and nuclei. The solution then forms the sum of electronic (el) and vibrational (vib) contributions and reads[1]

$$E_i = E_i^{\text{el}} + E_i^{\text{vib}}. \tag{2.3}$$

The electronic transitions are typically in the visible range, whereas vibrational transitions possess energies of around 0.1 eV and, thus, lie in the near infrared. The energetic distribution of the states is illustrated in Fig. 2.2.

In order to calculate the molecular orbitals of many-electron molecules (each described by its wave function $\phi_i^{\vec{R}}(\vec{r})$) and the spatial probability distribution of an electron (given by the square modulus of its wave function $|\phi_i^{\vec{R}}(\vec{r})|^2$),[17] further approximations have to be made. In molecular orbital theory, $\phi_i^{\vec{R}}(\vec{r})$ is expressed by the product of the individual wave functions $\xi_j(\vec{r}_j)$ of each electron,

$$\phi_i^{\vec{R}}(\vec{r}) = \left[\prod_j \xi_j(\vec{r}_j)\right]_i^{\vec{R}}, \tag{2.4}$$

which assumes that the electrons move in an average potential arising from the nuclei and the charge distribution of all other electrons. In addition, the calculation may be simplified by expressing the molecular orbitals as a linear combination of atomic orbitals ζ_k (so-called LCAO method):

$$\xi_j = \sum_k c_{j,k}\zeta_k. \tag{2.5}$$

The coefficients $c_{j,k}$ can be calculated by minimizing the total energy of the system.[16]

For conjugated hydrocarbons, the electrons can be separated into two different sets: the strongly bound σ-electrons and the mobile π-electrons. Via the Hückel method,[17] the Schrödinger equation can now be solved. As a result, the orbitals split into bonding (π) and anti-bonding ($\pi^\star$) orbitals, where the π-orbital is fully occupied and the $\pi^\star$-orbital is unfilled. The same also holds for the σ-orbitals.

In the example of the molecule ethene, the molecular sp^2- and p_z-orbitals of the carbon atoms split into bonding and anti-bonding σ- and π-states (see Fig. 2.3). Due to the weaker overlap of the p_z-orbitals, the π-bonds split less compared to the σ-bonds. As a consequence, the highest occupied molecular orbital (HOMO) is the π-orbital and the lowest unoccupied molecular orbital (LUMO) is the $\pi^\star$-orbital.

According to Koopmans' theorem, the HOMO and LUMO energies of a molecular system equal the ionization potential and the electron affinity, respectively.[18] Between both states an energy gap is present, which is responsible for the optical properties of the molecule, e.g.

[1] Note that, in general, a term accounting for the rotation contribution should be added. This term is very small compared to electronic and vibrational energy and mainly contributes to the fine structure of a transition.[16]

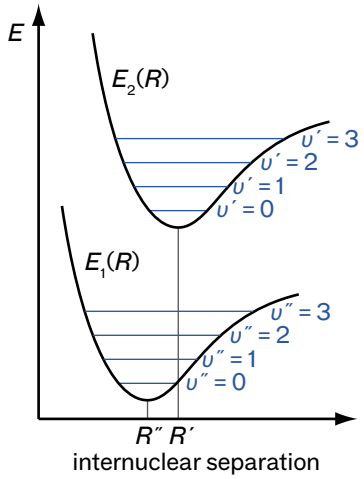

Figure 2.2: Schematic illustration of two electronic transitions $E(R)$ and their vibrational structure ν.

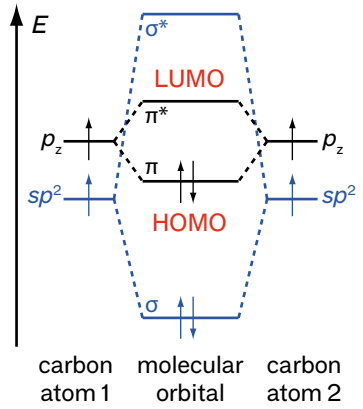

Figure 2.3: Energetic distribution of the molecular orbitals of ethene.

emission and absorption. The energy gap depends on the size of the molecule, where large molecular sizes lead to extended π-systems, which in turn decrease the energy gap.[14]

Regarding an organic solid that is composed of many single molecules at absolute zero, the π-orbitals are still fully occupied and the $\pi^\star$-orbitals are fully unoccupied. Therefore, the π-system is saturated, which prevents the formation of covalent bonds. Instead, the molecules are weakly bound by van der Waals forces. Therefore, the properties of the single molecule are mainly retained when forming a solid. Furthermore, the overlap of neigboring π-electron systems is small, which leads to an energy splitting of the vibrational states of only around 100 meV. The comparison of HOMO and LUMO to the bands observed in inorganic semiconductors only holds for single crystals. Nevertheless, as will be discussed later, charge transport is still possible in amorphous organic solids via overlapping frontier orbitals.

2.2 *Optical Properties*

Excitons Under optical excitation, an electron from the HOMO is lifted into the LUMO. The resulting electron-hole pair is described as a quasi-particle, a so-called exciton. In organic semiconductors, the excitons are strongly bound to a molecule by Coulomb attraction with binding energies in the range of 0.5 eV to 1.0 eV.[19] The optical gap is, thus, reduced by the exciton binding energy compared to the electronic gap.

In contrast to inorganic semiconductors, where excitons are delocalized and reach distances of several lattice spacings,[20] the Frenkel excitons present in organic solids are highly localized on a molecule and often even reside on the same ligand.[14;21]

Excitons may also be formed by electrical excitation, where electrons and holes are approaching each other on the LUMO and HOMO, respectively. Typically, this electrically formed exciton first resides on neighboring molecules (so-called charge transfer exciton) before moving to the same molecule.[22]

Singlet and Triplet States Excitons are divided into two classes: singlet and triplet excitons. In order to understand their difference, the molecular orbital theory is extended and the electron spin s is introduced. The molecular orbitals $\xi(\vec{r}, s)$ can be written as a product of the spatial wave function $\varphi(\vec{r})$ and the spin wave function $\psi(s)$:

$$\xi(\vec{r}s) = \varphi(\vec{r})\psi(s). \tag{2.6}$$

This wave function is an eigenfunction to the spin operators $\mathcal{S}^2$ and $\mathcal{S}_z$ with the eigenvalues s and m_s:

$$\mathcal{S}^2\xi = s(s+1)\hbar\xi, \tag{2.7a}$$

$$\mathcal{S}_z\xi = m_s\hbar\xi. \tag{2.7b}$$

Two electrons with spin quantum number $s = ½$ and secondary spin quantum number $m_s = \pm ½$ may couple to a total spin of $S = 0$ (antiparallel spins) or $S = 1$ (parallel spins). According to the multiplicity $M = (2S + 1)$, electrons with antiparallel spin occupy a singlet state ($M = 1$) and electrons with parallel spin a triplet state ($M = 3$).

In the following, the optical transitions between the electronic states are described using the Jablonski diagram illustrated in Fig. 2.4. In the ground state, electrons typically reside in a singlet state S_0, where the antiparallel spins are saturated in pairs.[16] The singlet energy gap is typically higher than the respective triplet gap, which results from the different spin configurations (antiparallel for singlets and parallel for triplets). The Pauli exclusion principle forbids that two electrons with the same spin are located on the same place. Therefore, electrons in a triplet state have to reside in different orbitals. This leads to reduced electron-electron repulsion in the triplet compared to the singlet state and, thus, to a smaller triplet energy gap.

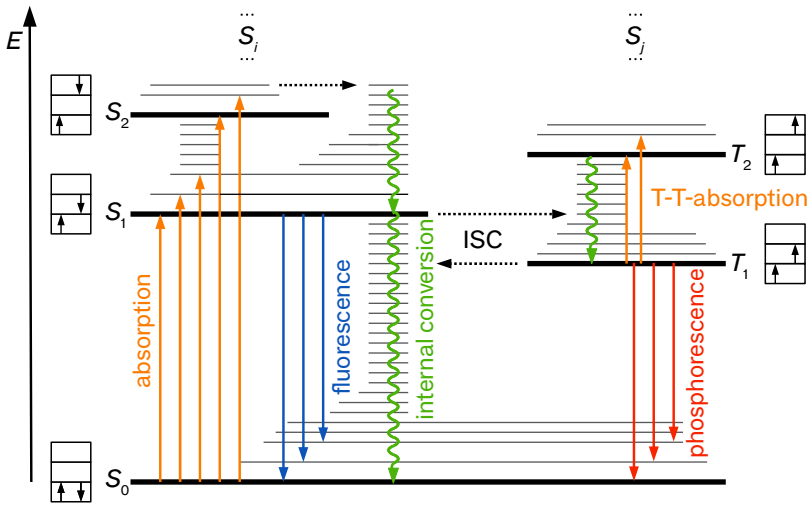

Figure 2.4: Intramolecular energy transfer (Jablonski diagram) illustrating all optical transitions between electronic and vibronic energy levels that are relevant to this work.[16]

Optical Transitions As transitions from singlet into triplet states require a spin flip, they are forbidden according to quantum mechanics. Thus, absorption of a photon rises an electron from the singlet ground state mainly into a vibrational mode of an excited singlet state.[2] From the vibrational modes, the electrons relax within picoseconds to the first excited state via internal conversion. This non-radiative deexcitation is mediated via phonons.

According to Kasha's rule, radiative emission mainly occurs from the lowest excited state of a given multiplicity (S_1 or T_1) into the ground state.[24] Emission from singlet excitons is called fluorescence while emission from the triplet state is denoted as phosphorescence. Excitons can furthermore transfer from singlet to triplet states via intersystem crossing (ISC).

While fluorescence occurs within nanoseconds, phosphorescence persists much longer. This is again related to the forbidden spin flip

[2] Absorption into the triplet state is around $10^{-9} - 10^{-10}$ times reduced compared to absorption into the singlet state.[23]

necessary for relaxation from the triplet to the ground state. The same also holds for ISC, which is typically very weak. However, the introduction of heavy metal atoms can strongly increase the spin-orbit coupling and therefore make singlet-triplet transitions highly probable.[25–27] This reduces the triplet lifetime from the millisecond time scale that is found in fluorescent compounds to lifetimes of around 1 s in phosphorescent materials.[28] Furthermore, fluorescence is not found in these compounds because all singlet excitons are transferred via ISC to the triplet state within picoseconds.[14]

As an example, two archetypal OLED-emitters shall be briefly compared: the fluorescent 4-dicyanmethylene-2-methyl-6-(p-dimethylaminostyryl)-4H-pyran (DCM) and the phosphorescent tris(2-phenylpyridine)iridium(III) ($Ir(ppy)_3$). DCM shows a singlet lifetime of $\tau_S = 1.2\,\text{ns}$ and a triplet lifetime of $\tau_T = 1.6\,\text{ms}$. Intersystem crossing takes place at a rate of $k_{ISC} = 1.5 \times 10^8\,\text{s}^{-1}$.[29–32] The heavy metal iridium that is located in the center of $Ir(ppy)_3$ strongly increases the ISC rate to $k_{ISC} = 1 \times 10^{13}\,\text{s}^{-1}$ while the triplet lifetime is reduced to $\tau_T = 1.58\,\text{s}$.[13;33]

The relaxation energy between two states and, thus, the wavelength λ of the absorbed or emitted photon, is simply given by

$$E = h\nu = h\frac{c}{\lambda} = |E_i - E_f|, \tag{2.8}$$

where i and f denote the initial and final state, respectively. Due to the Franck-Condon principle, transitions are most probable if the overlap between their vibronic modes is maximized (see Fig. 7.4).[34] As a result of the Franck-Condon principle and the Kasha rule, spectral lines of emission and absorption possess a mirror symmetry. Hereby, absorption and emission between the vibrationless ground state and the vibrationless excited state are shifted by the so-called Stokes shift. This is illustrated in Fig. 2.5.

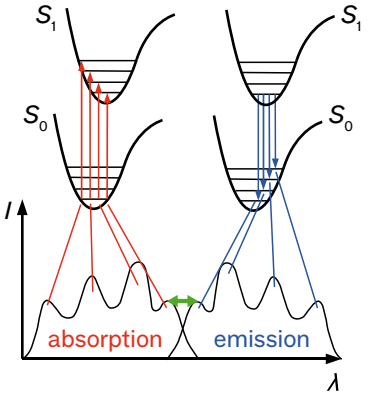

Figure 2.5: Illustration of the Kasha rule. Absorption (red) and emission (blue) possess a mirror symmetry, shifted by the Stokes shift (green arrow).

The individual spectroscopic lines that are formed by the transitions are inhomogeneously broadened due to the disorder that is present in the typically amorphous organic semiconductors. Here, polarization by the surrounding environment further contributes to the broadening. This finally leads to a Gaussian distribution of the density of states (DOS).[35;36]

Radiative Efficiency The temporal behavior of a certain excited state density n is expressed by the natural decay rate k_0, or its inverse, the natural lifetime $\tau_0 = 1/k_0$:

$$\frac{dn}{dt} = -k_0 n. \tag{2.9}$$

Solving this equation leads to the simple exponential relation

$$n = n_0 e^{-k_0 t}, \tag{2.10}$$

with the initial excited state density n_0. The intrinsic lifetime τ that can be observed in experiment depends on both radiative and non-radiative processes, k_r and k_{nr}, respectively:

$$\tau = \frac{1}{k_r + k_{nr}}. \tag{2.11}$$

Non-radiative processes include, e.g., ISC and internal conversion. In order to calculate the probability of a radiative transition, the efficiency η_{rad} can be expressed as

$$\eta_{rad} = \frac{k_r}{k_r + k_{nr}}. \tag{2.12}$$

High radiative efficiency is, thus, achieved by minimizing all non-radiative processes.[37]

2.3 *Intermolecular Energy Transfer*

Now that the intramolecular energy transfer processes have been briefly introduced in the previous section, focus is drawn to the processes observed between different molecules.[3] This energy transfer can occur both radiatively and non-radiatively. The radiative transfer takes place in two steps:

$$D^\star \rightarrow D + h\nu, \quad h\nu + A \rightarrow A^\star. \tag{2.13}$$

Here, D and A denote the donor and acceptor molecules, while an asterisk marks an excited state. The energy $h\nu$ is mediated via a photon and can reach macroscopic distances. Compared to optical excitation with energy E_0, the Lambert-Beer law relates the fraction of energy that is absorbed E_{abs} to the film's absorption coefficient α and thickness d:

$$E_{abs} = E_0 \left(1 - e^{-\alpha d}\right). \tag{2.14}$$

However, due to the Stokes shift between absorption and emission, re-absorption is neglected throughout all following investigations.[16]

Diffusion Non-radiative energy transfer is a diffusive process, where the excitons migrate via several steps driven by high local exciton densities. Concerning diffusion, energy is transferred from donor to acceptor without exchange particles, either via Förster or Dexter transfer:

$$D^\star + A \rightarrow D + A^\star. \tag{2.15}$$

The time dependent distribution of an exciton density $n(\vec{r}, t)$ can then be expressed by Fick's second law:

$$\frac{\partial n(\vec{r}, t)}{\partial t} = D\Delta n(\vec{r}, t) - \frac{n(\vec{r}, t)}{\tau} + G(\vec{r}, t). \tag{2.16}$$

The first term describes the diffusive motion with the diffusion coefficient D, the second term expresses exciton decay, and the third term includes exciton generation. Solving the diffusion equation leads to extraction of the diffusion length $l = \sqrt{D\tau}$. Although diffusion is

[3] A minor part of this section is published in Ref. 11. Reprinted with permission. Copyright 2013, Wiley VCH.

in general a process taking place in all three dimensions in space, it can be reduced to one dimension if isotropic materials are used and if excitons are generated homogeneously in the substrate plane. Then, Eq. 2.16 can be reduced to the dimension perpendicular to the substrate.

Förster Transfer As illustrated in Fig. 2.6, Förster transfer is based on a dipole-dipole coupling between two molecules and, thus, requires spin conservation.[38] Nevertheless, Förster transfer can also occur in phosphorescent materials if heavy metal atoms are introduced. It scales with R^{-6}, where R is the intermolecular distance. For the Förster radius R_F, denoting the length at which the efficiency of a Förster transfer is reduced to 50 %, experimental values between 0.8 nm and 5 nm are found in organic molecules.[39–44]

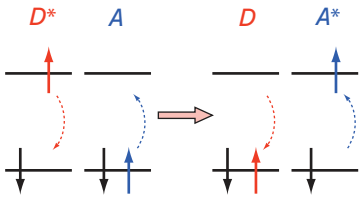

Figure 2.6: Schematic illustration of Förster transfer. Energy is exchanged via dipole coupling, while electrons remain on the same molecule.

Dexter Transfer Dexter energy transfer between two molecules occurs upon overlap of their wave functions via the exchange of electrons (see Fig. 2.7). It is very sensitive to the overlap of the molecular orbitals and its rate scales with e^{-R}.[45] Therefore, substantial Dexter energy transfer occurs only over very small distances of up to around 2 nm.[40;46;47] In contrast to Förster transfer, only the total spin of the involved molecules has to be preserved here so that an exchange of triplet excitons is possible.

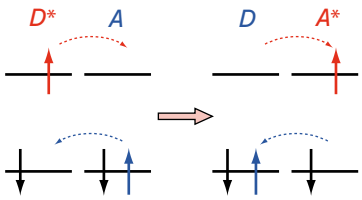

Figure 2.7: Schematic illustration of Dexter transfer. Electrons are exchanged from one molecule to the other.

Note that only in the Dexter process electrons are indeed migrating, while under the Förster framework the electrons exchange their energy but remain on the molecules. According to the different spin requirements and length scales that underlie the two mechanisms, singlet excitons typically transfer via Förster and triplets via Dexter transfer.

2.4 Charge Transport

The high disorder that is present in amorphous organic semiconductors allows charge transport only to take place via thermally assisted hopping steps between neighboring molecules. The hopping process can be described within the Gaussian disorder model to take place between Gaussian distributed density of states.[48] Then, the jump rate between two sites depends, among others, on the overlap of the electronic wave functions.[49]

Applying an electric field $\vec{F}$, charge carriers move in first approximation with a drift velocity

$$\vec{v} = \mu \vec{F}, \tag{2.17}$$

which depends on the charge carrier mobility μ.[4] Although μ is a material parameter, it may be influenced by temperature, electric field, and charge carrier density.[50–53]

Compared to inorganic semiconductors, where electronic bands are formed leading to charge carrier mobilities of approximately $10^3\,\mathrm{cm^2/(V\,s)}$, the disorder present in organic semiconductors strongly

[4] Note that, in general, μ is a tensor. However, μ is isotropic in the amorphous materials used, and, thus, can be treated as scalar here.

hinders charge transport. Instead, the mobility decreases to around $1\,\mathrm{cm}^2/(\mathrm{V\,s})$ in organic crystals and by further 4 to 6 orders of magnitude in amorphous organic solids.[14;54] Upon Ohmic injection, the low mobility limits charge transport trough the organic layers and leads to built-up of space charge at the contacts. This effect is expressed in space charge limited current (SCLC) theory,[55] where the current density J is related to the voltage V by the Mott-Gurney equation:

$$J = \frac{9}{8}\epsilon_r\epsilon_0\mu\frac{V^2}{d^3}, \tag{2.18}$$

with the relative permittivity ϵ_r, the permittivity of free space ϵ_0, and the layer thickness d. Hence, despite the low mobilities present in organic semiconductors, their very small layer thickness can still lead to significant charge transport.[14]

Although SCLC theory neglects charge diffusion and is based on the assumption of unipolar transport, it may well describe charge transport in organic semiconductors.[56] However, this only holds in the absence of traps, which can often not be avoided due to impurities or doping. As a conclusion, trapped electrons additionally contribute to the total space charge. In order to calculate the current-voltage behavior of discrete trap states, SCLC theory can be extended using an effective mobility $\mu_{\mathrm{eff}} = \mu Y$ with $Y^{-1} = 1 + N_t/N_e \exp(E_t/k_B T)$.[14;52] Now, traps are included by their density N_t and energy E_t. Furthermore, N_e refers to the density of transport states and $k_B T$ to the Boltzmann constant and temperature.

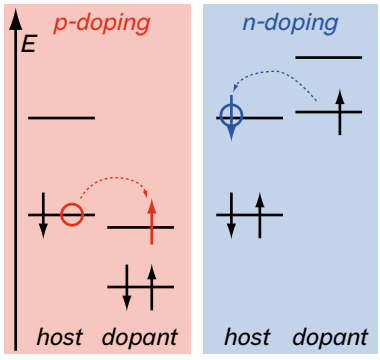

Figure 2.8: Schematic illustration of doping. Charge transfer from host to dopant (p-doping) or from dopant to host (n-doping) creates free holes (red circle) or electrons (blue circle), respectively.

Electrical Doping In order to obtain Ohmic charge injection and increase the conductivity, electrical doping is used. Here, free charge carriers are generated by doping the host with a certain dopant. For n-doping, the dopant has to possess a very high HOMO level so that electrons from the HOMO of the dopant can transfer to the LUMO of the host. For p-doping, the dopant instead has to possess a very low LUMO so that an electron can transfer from the HOMO of the host to the LUMO of the guest, which generates a free hole on the host.[57–59] The principle is shown in Fig. 2.8.

Typically, organic materials are used for p-doping.[60–62] However, for n-doping only few chemically stable molecular dopants are found[63] and still inorganic alkali metals such as Cs or Li are often used.[64;65]

The strongly increased charge carrier density upon electrical doping enhances the conductivity by several orders of magnitude, both through providing charge carriers and by enhancing the mobility.[59;66] The voltage drop over electrically doped transport layers is negligible compared to the drop over intrinsic layers. Therefore, the thickness of these doped layers can be varied up to a few hundred nanometers without influencing the electric behavior.[59;67;68]

Furthermore, electrical doping is used to ensure proper charge carrier injection from the electrodes into the organic material. As illustrated in Fig. 2.9, adjustment of the Fermi energy level to the

electrode's potential leads to band bending at the interface. A Schottky contact with an only few nanometer thick depletion zone is formed, which can be tunnelled by the charge carriers. This allows Ohmic charge injection and reduces the voltage.[19]

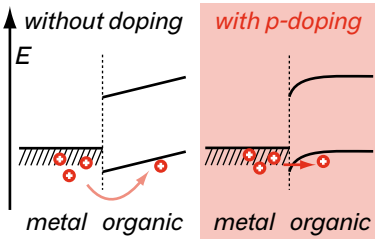

Figure 2.9: Schematic illustration of band bending at the interface between metal and organic when introducing a p-dopant.

2.5 Organic Light-Emitting Diodes

OLEDs consist of several organic semiconducting layers that are embedded between two electrodes. In brief, the working principle is as follows: Charge carriers are injected from the electrodes into the organic layers and are transported to the emitter, where they combine and form an exciton. By decaying radiatively, this exciton then creates a photon. Finally, the photon escapes the device through one of the electrodes.

While the first part of this section will explain the device structure and working principle in more detail, the second part addresses the efficiency of the mentioned processes and gives details about loss mechanisms.

2.5.1 Structure and Working Principle

The OLEDs fabricated throughout this thesis are built in bottom-emitting configuration. This means that the transparent electrode is located directly on top of a transparent substrate, through which the generated light is outcoupled.

Figure 2.10 shows the energy levels of a typical OLED structure under forward bias. In order to efficiently inject holes into the organic layers, the anode has to possess a high work function Φ_A. Analogously, the cathode should possess a low work function Φ_C to provide efficient electron injection. The different work functions create a built-in field, which can be overcome by applying a voltage. Most OLED structures in this thesis are based on the so-called *pin*-concept. Here, *p*- and *n*-doped transport layers surround an *intrinsic* emission layer.[69;70] This allows efficient charge injection and transport through the hole and electron transporting layers (HTL and

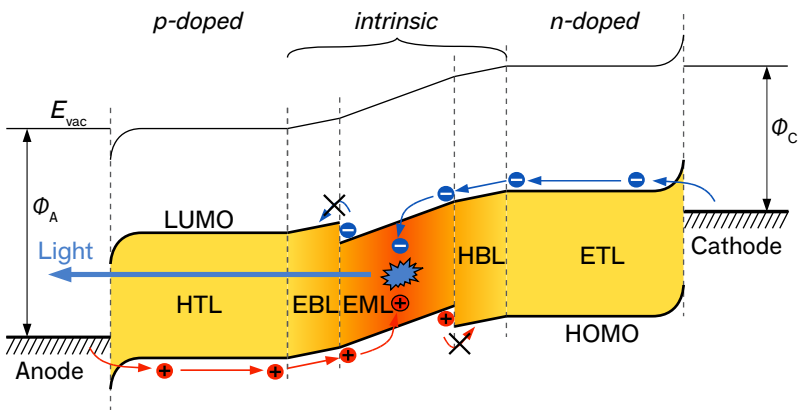

Figure 2.10: Energy levels of a typical OLED structure applying forward bias between anode and cathode.

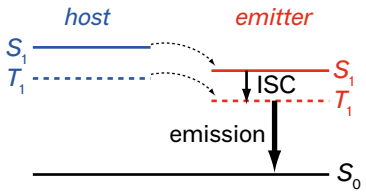

Figure 2.11: Energy levels and transitions in a phosphorescent host-guest system upon electrical excitation.

ETL, respectively) to the emission layer (EML), where electrons and holes form an exciton. In order to keep the charge carriers and excitons inside the EML, and to avoid exciton quenching at the electrical dopants, it is surrounded by thin intrinsic blocking layers (HBL and EBL, respectively).

The emission layer is typically composed of a host-guest system, where the light-emitting dye is doped with a low concentration into a host. This is especially important for phosphorescent emitter molecules in order to avoid exciton quenching due to high guest concentration.[39] Figure 2.11 schematically illustrates the energy levels and transitions in such a phosphorescent host-guest system. Usually, guest concentrations up to 20 mol % are chosen, depending on the actual material. Due to the much higher host concentration, charge transport and exciton formation typically takes place via the host while the emitter is often observed to trap charges.[71;72]

As explained in Sec. 2.2, electrical excitation creates singlet and triplet excitons with a ratio of 1 : 3. In order to efficiently transfer the excitons from host to guest, the host material has to possess a higher singlet and triplet energy gap than the emitter. Hence, quick Förster and Dexter energy transfer to the guest takes place, which avoids additional emission from the host. On the phosphor sites, singlets are transferred to triplets via intersystem crossing. Therefore, in the ideal case, all excitons are converted to the guest triplet state, from where they radiatively decay to the ground state.[53]

To ensure efficient charge to photon conversion, the layers have to provide certain properties. First, the transport layers should be highly conductive in order to circumvent a potential drop. This can be achieved by electrical doping. The doping concentration, however, should be kept as low as possible as the dopants typically absorb photons in the visible wavelength regime.[60;73;74] Next, energy barriers between the different organic layers should be avoided because these cause additional space charge at the interface, which hinders further transport. The blocking layers HBL and EBL, however, have to possess a lower HOMO and a higher LUMO than the EML, respectively, in order to restrain charge leakage to the electrodes. In addition, exciton quenching in the blocking layers has to be prevented by using blockers which possess higher singlet and triplet energy levels than the emitter.

Instead of using the *pin*-concept also intrinsic layers may be used. Efficient charge injection can then be reached by introducing 1 nm thin injection layers. Compared to *pin*-OLEDs, the intrinsic devices simplify fabrication because charge blocking layers are not needed. Furthermore, the fabrication of doped transport layers is challenging due to the low dopant concentrations used. However, high potentials have to be applied to the intrinsic transport layers in order to overcome their low conductivity. Although high external quantum efficiencies may still be achieved,[75–78] the power efficacy, thus, suffers dramatically. Furthermore, the intrinsic device concept is not useful for optical optimization.

Organic materials and also many metals that are used as electrodes are not stable at ambient conditions. Especially the contact with water and oxygen quenches the emission and leads to material decomposition. Therefore, organic thin-films have to be encapsulated under nitrogen atmosphere.[79–81]

2.5.2 *Characterization*

The external quantum efficiency (EQE) of an OLED is the ratio of photons that escape the device per injected charges, and is given as the product of several factors:[5]

$$\mathrm{EQE} = \gamma\chi\eta^{\star}_{\mathrm{rad}}\eta_{\mathrm{out}} = \mathrm{IQE}\cdot\eta_{\mathrm{out}}. \tag{2.19}$$

Here, γ is the electrical efficiency describing the ratio of decaying excitons over injected charge carriers, χ the spin factor (meaning the ratio of singlet to triplet excitons), $\eta^{\star}_{\mathrm{rad}}$ the effective radiative efficiency of the emitter, and η_{out} the outcoupling efficiency.[68] If one considers only the ratio of radiatively decaying excitons over the number of injected charge carriers, one obtains the internal quantum efficiency, IQE.

[5] A minor part of this section is published in Ref. 11. Reprinted with permission. Copyright 2013, Wiley VCH.

Electrical Efficiency The electrical efficiency is typically assumed to be very high and values above $\gamma = 0.9$ have already been measured.[68] However, if the ratio of electrons and holes in the EML is not balanced, for instance by charge carrier built-up at interfaces or bad injection for either electrons or holes, the electrical efficiency will decrease. This may be avoided by using doped transport layers.[82] Further reduction of γ may be caused by charge carrier leakage.

Spin Factor The exciton spin factor is one of the limiting factors in fluorescent materials. It describes the proportion of excitons that decay radiatively upon spin statistics. As excitons are formed by an electron and a hole both possessing a random spin of $\pm\frac{1}{2}$, 25 % of the excitons are in the singlet state and 75 % are in the triplet state.[6] In the meanwhile, new concepts for fluorescent materials which utilize also triplet excitons have achieved promising results by pushing the exciton spin factor up to $\chi = 1$.[87–89] Nevertheless, the conventional approach for the last 15 years uses phosphorescent emitters, for which efficient ISC leads to $\chi = 1$.

[6] The singlet-triplet ratio is still undergoing current research and several publications have shown deviations from the 1:3 ratio.[22,83–86]

Radiative Efficiency The third factor, the *effective* radiative efficiency $\eta^{\star}_{\mathrm{rad}}$, is based on the *intrinsic* radiative efficiency η_{rad} that has already been introduced in Eq. 2.12. In contrast to η_{rad}, $\eta^{\star}_{\mathrm{rad}}$ takes the modification of the emitter lifetime by the optical environment into account.[90–93] Compared to the intrinsic triplet lifetime τ, which is a material parameter and denotes the lifetime the exciton would have in free space, the effective lifetime $\tau^{\star}$ is defined as

$$\frac{1}{\tau^{\star}} = k^{\star} = Fk_{\mathrm{r}} + k_{\mathrm{nr}}. \tag{2.20}$$

Here, the radiative decay rate is influenced by the so-called Purcell effect, which is expressed in the factor F,

$$F(\lambda, u) = 2 \int_0^\infty u K(\lambda, u) du, \tag{2.21}$$

where $K(\lambda, u)$ denotes the spectral power density per wavelength λ and normalized in-plane wave vector u. The Purcell effect takes the different refractive indices and extinction coefficients of the layers into account. $F = 1$ if the emitter is positioned in free space. In strong optical microcavities, e.g. for light sources close to reflecting electrodes, F can strongly differ from 1. For more details on the theoretical treatment of the Purcell effect, the reader is referred to Refs. 68 and 90.

The effective radiative efficiency is finally given by

$$\eta_{\text{rad}}^{\star} = \frac{F k_{\text{r}}}{F k_{\text{r}} + k_{\text{nr}}}. \tag{2.22}$$

Compared to the intrinsic radiative efficiency, it can be both enhanced or reduced depending on the actual microcavity strength. Hence, the external quantum efficiency is influenced by the position of the emitter inside the OLED stack.

Outcoupling Efficiency An even stronger influence of the emitter position on the EQE is observed for the last factor in Eq. 2.19: The outcoupling efficiency provides a measure for the amount of light that is actually emitted by the OLED with respect to the photons generated internally. Due to the difference in the refractive indices of the organic layers, the electrodes, the substrate, and the surrounding air, around 80% of the generated light is typically trapped inside bottom-emitting OLEDs when using conventional glass substrates.[94] This value holds for optimized devices in which the emitting dipoles are located in the maximum of the optical field. If their position is outside the field maximum, the efficiency can decrease further.[37;68]

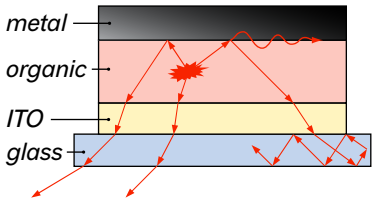

Figure 2.12: Cross-section through an OLED stack. Emitted light is refracted and reflected at the interfaces due to different refractive indices. The wavy line indicates surface plasmon polaritons.

The effect is illustrated in Fig. 2.12. Due to the higher refractive indices of the organic layers and ITO compared to the glass substrate, total internal reflection keeps the modes inside the device. Furthermore, coupling of the emitting dipoles to the electrode excites surface plasmons, which are also a strong loss mechanism.[37]

Measurable Quantities In experiment, the external quantum efficiency is calculated by measuring the angular dependent spectral radiant intensity $I_{\text{e}}(\vartheta, \lambda)$ as a function of the applied current density J:

$$\text{EQE}(J) = \frac{2\pi q}{Jhc} \int_\vartheta \int_\lambda \lambda I_{\text{e}}(\vartheta, \lambda) \sin\vartheta d\vartheta d\lambda, \tag{2.23}$$

Here, ϑ is the viewing angle, q the elementary charge, h the Planck constant, and c the speed of light. Obviously, the EQE depends on the current density J and is, therefore, also related to the luminance

L. Typically, the efficiency decreases with increasing current density, which is denoted as efficiency roll-off. As roll-off is the main interest of this work, it will be discussed in more detail in Chapter 3.

Although the external quantum efficiency is a good measure for understanding and comparing the physics behind different samples, the luminous efficacy (LE) is more interesting for applications. It is a photometric quantity and reads:

$$\mathrm{LE}(J) = \frac{2\pi K_\mathrm{m}}{JV} \int_\vartheta \int_\lambda U(\lambda) I_\mathrm{e}(\vartheta, \lambda) \sin\vartheta d\vartheta d\lambda. \tag{2.24}$$

In comparison to the radiometric EQE, the LE is weighed with the sensitivity of the human eye $U(\lambda)$, and furthermore includes the photopic constant K_m, which denotes the maximum luminous efficacy of a green emitter at 555 nm wavelength.[53;95]

Emitter Orientation Emission can be described as radiation from a dipole antenna. This is related to the fact that an exciton consists of two charge carriers. Emission then occurs when an electron from the LUMO recombines with a hole in the HOMO. According to the location of HOMO and LUMO in the molecule, transition dipoles are found in certain direction of the molecule. Typically, the transition dipoles are thought of having fixed positions compared to the symmetry axis of the molecule.[96] However, recent investigations showed that the dipole moment may also fluctuate.[97]

Until recently, OLED emitters were assumed to have an isotropic orientation. This implies that the dipoles radiate into all directions with the same probability. In order to couple light efficiently out of the OLED stack, horizontal orientation of the emitting dipoles is preferred because vertical dipoles emit their light mainly in plane of the device. Hence, they largely excite surface plasmon polaritons.[53]

In order to investigate the transition dipole orientation, the spectral power density $K(\lambda, u)$ that was introduced in Eq. 2.21 is split into transverse magnetic (TM, p-polarized) and transverse electric (TE, s-polarized) components:

$$K = aK_\mathrm{TM,v} + (1-a)(K_\mathrm{TM,h} + K_\mathrm{TE,h}). \tag{2.25}$$

The left term describes emission from vertical (v) dipoles while the right term denotes emission from horizontal (h) dipoles. The ratio of vertical to horizontal dipoles is expressed in the anisotropy factor a, which takes values of (0, 0.33, 1) for (horizontal, isotropic, vertical) dipole orientation.

Regarding phosphorescent compounds, Schmidt *et al.* were the first to find an emitter with preferential horizontal orientation.[92] Since then, different phosphorescent emitters were studied and anisotropy factors ranging from 0.22 to 0.40 have been found.[78;96;98–101] Theoretical calculations showed that the EQE on conventional glass substrates could be enhanced by a factor of 1.5 to up to 35 % when using an emitter with completely horizontal orientation.[102] Using optimized emitters with a radiative efficiency of 1 could increase the EQE

even further to 45 %.[96] Although such emitters have not been found yet, an EQE of 32 % has been demonstrated by Kim *et al.* using the phosphorescent compound bis(2-phenylpyridine)iridium(III)(2,2,6,6-tetramethylheptane-3,5-diketonate) ($Ir(ppy)_2(tmd)$), which possesses preferential horizontal orientation with $a = 0.22$ and a very high radiative efficiency of $\eta_{rad} = 0.96$.[78]

3 Theory of Efficiency Roll-Off

Efficiency Roll-Off describes the efficiency loss of an OLED with increasing current density. This chapter introduces the figures of merit to quantify and compare the roll-off of different devices and gives an overview about the best achieved efficiencies at high brightness to date. The underlying processes are discussed in detail with a focus on phosphorescent dyes. Finally, the influence of the different processes is discussed and the scope of this work is outlined.[1]

3.1 Current Status

The efficiency roll-off can be quantified by the critical current density J_0, which represents the current density at which the EQE drops to half of its maximum value.[12] Thus, devices with strong roll-off will have low critical current densities. J_0 is a useful measure to compare the roll-off of different OLEDs. However, in efficient fluorescent OLEDs as well as in phosphorescent devices with short lifetimes, J_0 can often not be reached without driving the device into a regime where material degradation sets in. Therefore, the critical current density $J_{90\%}$ is introduced, i.e., the current at which the EQE drops to 90 % of its maximum value.

Figure 3.1a shows the maximum external quantum efficiency of selected monochrome and white OLEDs reported in the literature as a function of $J_{90\%}$.[2] The data is divided into phosphorescent, fluorescent, and hybrid devices, where hybrid refers to OLEDs using both phosphorescent and fluorescent emitters. High efficiencies above 15 % are mainly achieved by devices based on phosphorescent emitters. For these, however, the EQE rolls off to 90 % of its maximum at currents as low as $1-30\,\mathrm{mA/cm^2}$, which corresponds to a luminance of $1000-10\,000\,\mathrm{cd/m^2}$, i.e., to luminance values that will be required for applications in OLED in lighting. Fluorescent materials instead achieve much higher critical current densities in the range of $50-1000\,\mathrm{mA/cm^2}$, but external quantum efficiencies remain below 10 %.

Concerning white light emission, phosphorescent emitters outperform fluorescent approaches in efficiency, but suffer from the lowest critical current densities. Hybrid approaches have been used to increase device stability and to decrease the roll-off, but for current densities up to $500\,\mathrm{mA/cm^2}$, truly low roll-off has so far only been achieved in fully fluorescent devices.

For fluorescent, monochrome devices, no difference in the average roll-off can be observed with regard to the emitted color. For phospho-

[1] Predominant parts of this chapter are published in Ref. 11. Reprinted with permission. Copyright 2013, Wiley VCH.

[2] Data selected in March 2013.

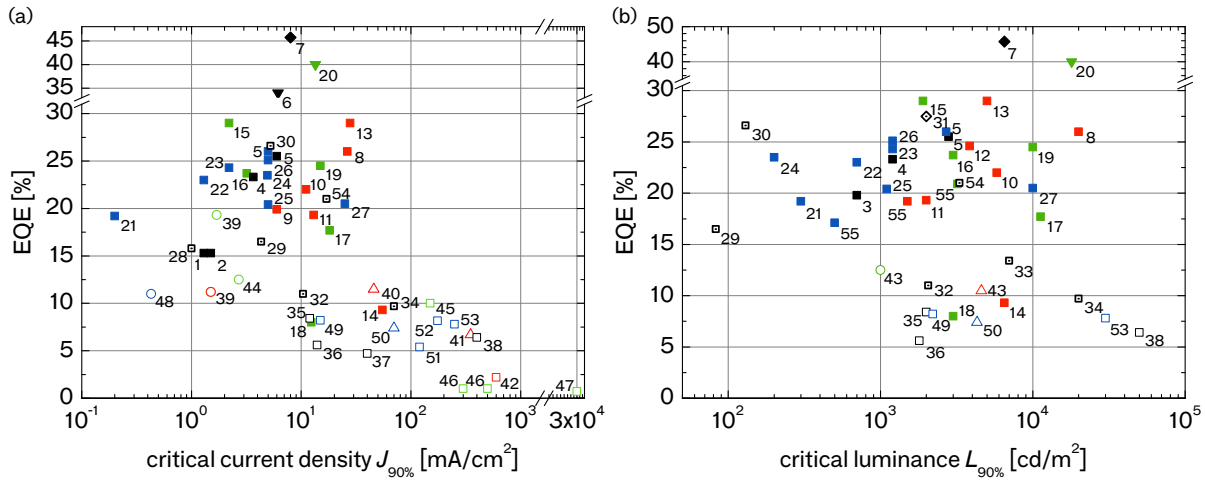

Figure 3.1: External quantum efficiency (EQE) versus (a) critical current density $J_{90\%}$ and (b) critical luminance $L_{90\%}$ for various OLEDs reported in the literature. Color of symbols represents the color of emitted light, black symbols stand for white-emitting OLEDs. Phosphorescent (■), fluorescent (□), and hybrid approaches using both phosphorescent and fluorescent emitters (⊡) are denoted. The use of flat outcoupling structures (▼), TADF emitters (●), TTA (▲), and tandem devices (⧫) to improve efficiency is also marked. Further information on the definition of EQE, $J_{90\%}$, and $L_{90\%}$ and a list of all references can be found in App. A.

rescent OLEDs, however, blue-emitting devices tend to have the highest roll-off. This can be attributed to the usually very poor chemical stability of the blue-emitting phosphors, which affects measurements of the efficiency at high current densities (further information can be found in Sec. 3.2.3).

For practical applications, the roll-off in efficiency with increasing luminance will be more relevant than the roll-off with current density. The maximum EQE is therefore further compared as a function of the critical luminance $L_{90\%}$ (i.e., the luminance, at which the EQE has dropped to 90 % of its maximum value) for selected fluorescent and phosphorescent OLEDs (cf. Fig. 3.1b). Although $L_{90\%}$ of fluorescent OLEDs could only be extracted from a limited number of publications, it is obvious that the average critical luminance is relatively similar for fluorescent and for phosphorescent materials, with typical $L_{90\%}$ being in the range of 1000 and 10 000 cd/m^2. The relatively low critical luminance of fluorescent OLEDs results from their lower current efficiencies compared to phosphorescent devices which mean that higher current densities are necessary to achieve the same brightness as in phosphorescent devices.

In many cases, in particular for lighting applications, the luminous efficacy (LE) which is given by the luminous power output over the electrical power input (cf. Eq. 2.24) is more relevant than the EQE and can be more directly compared to performance measures of other light sources. However, the roll-off of the LE is not only caused by the reduction in EQE with increasing brightness, but also by resistive losses, which are proportional to EQE/V.[10] These resistive losses are due to energy barriers, low charge-carrier mobilities of the involved materials, and a high sheet resistance of the electrodes and lead to a much higher roll-off in LE than in EQE. Resistive losses are minimized in devices with very steep luminance-voltage characteristics, i.e., in devices where the luminance increases rapidly with voltage. This can be achieved by using doped charge-transport layers, materials with

	EQE [%]	LE [lm/W]	$J_{90\%}$ [mA/cm^2]	$L_{90\%}$ [cd/m^2]	Reference
Red	25.3	64	26.3	20000	103 ([8] in Fig. 3.1)
Green	39.5	83	13.5	18000	75 ([20] in Fig. 3.1)
Blue	22.4	34	5	2700	104 ([5] in Fig. 3.1)
White	27.2	74	6	–	8 ([6] in Fig. 3.1)

Table 3.1: Devices with outstanding EQE and LE at 5000 cd/m^2 from scientific literature for red, green, blue, and white devices. All devices incorporate phosphorescent emitters. Furthermore, the critical current density $J_{90\%}$ and critical luminance $L_{90\%}$ are listed. The green and white devices contain flat outcoupling structures.

high charge-carrier mobility, and electrodes with low sheet resistance. As the LE roll-off thus reflects the superposition of several different effects, some of which are external to the physical process inside the device, it will be focussed on EQE roll-off as the more physical quantity throughout this thesis.

The performance of a few devices with outstanding efficiency at high brightness (5000 cd/m^2 is taken as a reference) is summarized in Table 3.1. Very high EQE and LE values of 39.5 % and 83 lm/W, respectively, have been achieved in a green OLED using a highly efficient OLED stack and a thin-film outcoupling structure on flexible plastic substrate.[75] For red OLEDs, the highest efficiencies were obtained by increasing microcavity effects in the OLED using either an additional silver layer on the ITO ground electrode or using top-emitting OLED design.[67;103] In blue OLEDs, the highest LE and EQE that have been achieved at 5000 cd/m^2 lie far behind the red and green devices.[104] The combination of red, green, and blue emitters in a white OLED led to LE up to 74 lm/W, when a periodic outcoupling structure is attached.[8] Furthermore, fluorescent OLEDs which show no detectable EQE roll-off across the entire measurement range (i.e., up to 30 000 mA/cm^2 or 30 000 cd/m^2) have been reported.[105;106]

3.2 *Processes Leading to Roll-Off*

The roll-off in EQE with increasing current density is the result of an interaction of many different processes, which influence one or more factors in Eq. 2.19: While the spin factor is usually assumed to remain constant, the electrical efficiency γ can be subject to a change in charge balance with increasing voltage and the outcoupling efficiency η_{out} might be influenced by a shift of the recombination zone. However, the roll-off is assumed to be most dramatic for the radiative efficiency $\eta^{\star}_{\text{rad}}$, which can be affected by various different bimolecular annihilation processes. In the following subsections, these mechanisms and effects influencing the other factors in Eq. 2.19 will be discussed in detail.

To provide an overview, the scheme in Figure 3.2 summarizes the different processes. In this scheme, bimolecular processes are illustrated by lines connecting electrons (e^-), holes (h^+), triplet excitons (T), or singlet excitons (S); open circles denote the destruction of a particle (i.e., an e^-, h^+, T, or S), closed circles denote their creation, and the absence of a circle means that the respective particle is preserved. Excitons are formed by an electron and a hole (exciton formation, EF). Singlets can be quenched (i.e., destroyed) by polarons[3] (singlet-

[3] When a charge carrier travels along a solid, it polarizes the surrounding molecules. This forms a quasi-particle, which is known as polaron.[16]

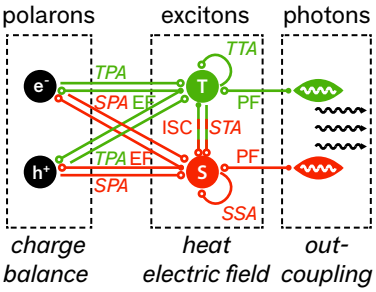

Figure 3.2: Schematic illustration of possible mechanisms leading to efficiency roll-off in OLEDs. The different particles involved are electrons (e^-), holes (h^+), singlets (S, red), and triplets (T, green). Connecting lines indicate whether a particle is destroyed (open circle), created (full circle), or preserved (no circle). The mechanisms involved are charge imbalance, bimolecular quenching processes such as TPA/SPA, SSA, STA, TTA, exciton dissociation under the influence of heat or an electric field, and the outcoupling of the created photons. Mechanisms that might depend on current density and would thus influence the roll-off are shown in italics. For completeness, exciton formation (EF), intersystem crossing (ISC), and photon formation (PF) are also shown.

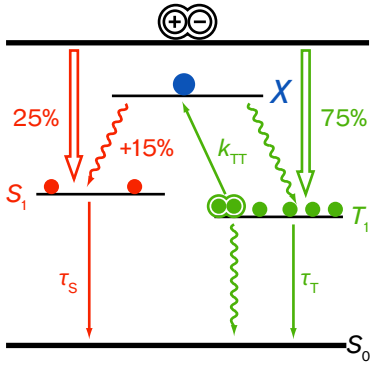

Figure 3.3: Illustration of spin-statistics in electrically driven OLEDs. Figure adapted from Ref. 108.

polaron annihilation, SPA), by other singlets (singlet-singlet annihilation, SSA), or by triplets (singlet-triplet annihilation, STA), while triplets can get quenched by polarons (triplet-polaron annihilation, TPA) or other triplets (triplet-triplet annihilation, TTA). Furthermore, singlets can convert into triplets by ISC. Generated excitons might be dissociated by heat or in an applied electric field. Finally, the created photons are coupled out of the layer stack.

3.2.1 *Triplet-Triplet Annihilation*

TTA is mostly relevant to the efficiency roll-off in phosphorescent OLEDs. The first phosphorescent OLED, which was reported by Baldo *et al.* in 1998, used 2,3,7,8,12,13,17,18-octaethyl-21H,23H-porphine platinum (PtOEP) as the emitter molecule.[27] In this first publication it was already suggested that the observed decrease in EQE at high currents is caused by a bimolecular quenching process. At this time, the authors supported their suggestion by showing that the excited-state lifetime of triplet excitons in PtOEP decreased for increasing currents. Although bimolecular quenching indeed plays a relevant role in PtOEP based devices, it has been shown later that the early interpretation of the decreased lifetime was not entirely accurate. In the following years, Baldo and co-workers investigated the efficiency roll-off and in particular TTA in detail for various phosphorescent host-guest systems.[12]

Since then, TTA is probably the most widely-studied mechanism involved in the efficiency roll-off of OLEDs. The TTA effect itself was in fact known long before the development of phosphorescent OLEDs and was first noticed during observations of TTA induced delayed fluorescence in organic crystals in 1962.[35;107] Due to the long lifetime of excited triplet states (in the microsecond range), the probability for these excitons to annihilate is much higher than for singlet states, which have radiative lifetimes in the nanosecond range. Figure 3.3 schematically shows the possible creation and decay pathways of singlet (red) and triplet (green) excitons. During electrical excitation, charge carriers usually form singlet and triplet excitons with a 25 % to 75 % ratio (cf. Sec. 2.5.2).

In TTA, the annihilation of two triplet states leads to an intermediate state X, which can be transferred—according to spin statistics—into one singlet, three triplet, or five quintet states. The quintet states are usually higher in energy than the two initial triplet states and can thus be neglected.[35] Possible pathways are therefore:

$$T_1 + T_1 \xrightarrow{k_{TT}} X \begin{cases} \xrightarrow{75\%} T_n + S_0 \rightarrow T_1 + S_0 \\ \xrightarrow{25\%} S_n + S_0 \rightarrow S_1 + S_0 \end{cases} \tag{3.1}$$

where k_{TT} is the rate constant describing the kinetics of the TTA process. The total fraction of triplet excitons that can be converted into singlet excitons by multiple TTA processes is 15 %.[108] For fluorescent materials TTA may therefore increase the device efficiency (cf. up triangles in Figure 3.1).[35;108–110] In phosphorescent systems any

singlet exciton formed during the TTA process can quickly transfer back into a radiative triplet excited state via ISC, however, at least one triplet exciton will be lost in the process. Depending on the excited state lifetime, current density, and, hence, on the triplet density, TTA may significantly decrease the efficiency of phosphorescent OLEDs.

In the following, it is mainly focussed on TTA in phosphorescent materials. In OLEDs, the emitter molecules are often doped into a host material to avoid self-absorption and concentration quenching and, thus, to achieve efficient luminescence (cf. Sec. 2.5.1).[39] In such host-guest systems, efficient exciton confinement on the guest requires that the host material has a higher triplet energy level than the emissive guest molecules. Especially for blue phosphorescent emitters, this requirement is sometimes difficult to fulfill. Therefore, host materials with resonant or even lower triplet levels are also used and at least moderate quantum efficiencies are still achieved.[111;112] In these host-guest systems, different forms of TTA can occur, namely between two excited guests, between host and guest, or between two excited host triplets.[113] In the following, the different TTA mechanisms and how their presence can be detected are described. Focus lies especially on guest-guest annihilation as this process is assumed to be the dominant one in most OLEDs. Furthermore, host-guest TTA and host-host TTA can only be observed indirectly. Thus, only few publications exist that specifically investigate these TTA processes.

Guest-Guest Annihilation TTA can be observed using time-resolved photoluminescence (PL) or electroluminescence (EL) measurements. The time evolution of the density of guest molecules in the triplet state $n_\mathrm{T}(t)$ after pulsed excitation is described by the general rate equation:[12;13]

$$\frac{d}{dt} n_\mathrm{T}(t) = -\frac{n_\mathrm{T}(t)}{\tau_\mathrm{T}} - \frac{1}{2} k_\mathrm{TT} n_\mathrm{T}(t)^2. \tag{3.2}$$

Here, the first term describes the conventional and ideally radiative monoexcitonic decay with the triplet lifetime τ_T and the second term accounts for the biexcitonic annihilation with the TTA rate k_TT. Thus, TTA increases non-linearly with increasing triplet densities. The factor ½ accounts for the fact that one of two triplet excitons is lost during annihilation. Equation 3.2 can be solved to

$$n_\mathrm{T}(t) = \frac{n_{\mathrm{T}_0}}{\left(1 + n_{\mathrm{T}_0} \frac{k_\mathrm{TT}\tau_\mathrm{T}}{2}\right) \mathrm{e}^{t/\tau_\mathrm{T}} - n_{\mathrm{T}_0} \frac{k_\mathrm{TT}\tau_\mathrm{T}}{2}}, \tag{3.3}$$

where n_{T_0} is the initial triplet exciton density. In order to take electrical excitation into account, a creation term of the form $\frac{J}{qw}$ can be added to Eq. 3.2, where J is the current density, q is the electron charge, and w is the width of the emission zone.[12] Here, an exciton formation zone with a rectangular shape is assumed.

Under steady state conditions, the EQE of an OLED can be calculated from Eq. 3.2 to

$$\frac{\mathrm{EQE}}{\mathrm{EQE}_0} = \frac{J_0}{4J}\left(\sqrt{1+8\frac{J}{J_0}}-1\right), \text{ with} \tag{3.4}$$

$$J_0 = \frac{4wq}{k_{\mathrm{TT}}\tau_{\mathrm{T}}^2} \tag{3.5}$$

describing the critical current density, i.e., the current density where $\mathrm{EQE} = \frac{\mathrm{EQE}_0}{2}$ with EQE_0 the external quantum efficiency at currents low enough so that TTA is negligible. Using the values for k_{TT} and τ_{T} obtained from transient measurements, it is then possible to calculate J_0. With this, the EQE of an OLED and its roll-off with increasing current density can be predicted.

TTA can only occur if two triplet excitons are in close proximity. In principle, triplets can move towards each other through Dexter or Förster energy transfer. In literature, both transfer processes are discussed to cause TTA,[40;41;114;115] but recent findings propose that only Dexter transfer takes place.[116] Especially concerning iridium-cored compounds, mainly Dexter transfer has shown to contribute to TTA and will therefore be presented in more detail in the following.[40;114;116;117]

Dexter energy transfer can be described as a diffusion based exchange following a random walk and the associated k_{TT} can be approximated as

$$k_{\mathrm{TT}} = 8\pi DR \tag{3.6}$$

with the diffusion constant D and the effective interaction distance R, over which the two excited states annihilate.[16;117–119] This distance can be approximated by an average 3D lattice constant.[120] Equation 3.6 implies that k_{TT} does not depend on excitation density unless there is an indirect dependence through the diffusion constant. It should furthermore be noted that, unless there is no energy barrier between host and guest, R depends on the guest concentration and that therefore Dexter transfer based TTA is enhanced in highly concentrated host-guest systems.[41] In the phosphorescent system 4,4′,4″-tris(N-carbazolyl)-triphenylamine (TCTA):$\mathrm{Ir(ppy)_3}$, the guest-guest distance at a typical doping concentration of 9.3 mol % is 2.9 nm assuming cubic closed packing.[117] This is larger than the typical Dexter interaction distance of two excited states (cf. Sec. 2.3).[16] Hence, diffusion based energy transfer can only reach substantial levels in such a system if there is no energy barrier between host and guest or if the guest molecules aggregate.

Host-Guest Annihilation The general rate equation derived for guest-guest annihilation (Equation 3.2) describes TTA correctly only if the energy transfer within the host-guest system is a fully exothermic process and the triplet density on the host is negligible.[12] For tris(8-hydroxyquinolinato)aluminum ($\mathrm{Alq_3}$):PtOEP and CBP:$\mathrm{Ir(ppy)_3}$, where the energy differences between host and guest are below 200 meV,

early work of Baldo *et al.* already revealed that this is not necessarily the case and in fact the measured PL transients cannot be accurately described with Eq. 3.3.[12] This deviation was attributed to interaction between host and guest resulting from the small triplet energy difference. To account for this, a TTA process involving both host (H) and guest (G) molecules was suggested:

$$T_1^{\mathrm{H}} + T_1^{\mathrm{G}} \rightarrow X \rightarrow \begin{cases} T_1^{\mathrm{H}} + S_0^{\mathrm{G}} \\ S_0^{\mathrm{H}} + T_1^{\mathrm{G}}. \end{cases} \tag{3.7}$$

The intermediate bimolecular state X relaxes to one excited state molecule (either on host or guest) and to one ground state molecule.

In balanced host-guest systems, the host triplet density is expected to be very low compared to the guest triplet density due to the efficient Dexter energy transfer to the lower lying guest triplet, even though the triplet lifetime on the non-phosphorescent host is usually orders of magnitude higher than on the guest molecules. However, if the difference in triplet energy between guest and host is small, back-transfer of triplet excitons from guest to host can result in a non-negligible triplet density on the host.[111;121] Furthermore, at very high excitation density, an increased host singlet density is expected as all guest molecules are already saturated with triplet excitons. These excess host singlet excitons may transfer their energy to excited guest triplets, exciting them into a higher triplet state T_n^{G}. This intermediate state can then relax into the first excited triplet state while transferring the excess energy via Dexter transfer to the host, thus yielding a host triplet state T_1^{H}:[113]

$$S_1^{\mathrm{H}} + T_1^{\mathrm{G}} \rightarrow S_0^{\mathrm{H}} + T_n^{\mathrm{G}}, \tag{3.8a}$$

$$T_n^{\mathrm{G}} + S_0^{\mathrm{H}} \rightarrow T_1^{\mathrm{G}} + T_1^{\mathrm{H}}. \tag{3.8b}$$

This energy transfer is only possible if $T_n^{\mathrm{G}} - T_1^{\mathrm{G}} > T_1^{\mathrm{H}}$ and therefore only happens for host materials with a low triplet energy.

Host-Host Annihilation With few exceptions,[119;122] host-host TTA has not been studied in any detail in the past. During host-host TTA, two host triplet excitons annihilate thus reducing the overall triplet density and, hence, also decreasing the number of triplets, which can be transferred to guest molecules:

$$T_1^{\mathrm{H}} + T_1^{\mathrm{H}} \rightarrow X \rightarrow \begin{cases} T_1^{\mathrm{H}} + S_0^{\mathrm{H}} \\ S_1^{\mathrm{H}} + S_0^{\mathrm{H}}. \end{cases} \tag{3.9}$$

The host triplet density in exothermic host-guest systems is low due to efficient Dexter energy transfer to the guest. Therefore, the contribution of host-host TTA compared to other annihilation processes is expected to be small in these systems. If host and guest have resonant energy levels, the situation differs. Furthermore, host-host TTA might also play an important role in OLEDs making use of the

triplet harvesting concept.[123] In these devices, triplet states diffuse through a fluorescent emitting host towards a region doped with phosphorescent emitter molecules.[124–129] During this process, parasitic host-host annihilation of the diffusing triplets might occur but experimental evidence remains elusive at this stage.

3.2.2 *Triplet-Polaron Interaction*

The annihilation of excited triplet states with free or trapped charge carriers is possible via the following processes:[12;13;16;130]

$$T_1 + h^+ \xrightarrow{k_{\mathrm{TP,h}}} S_0 + h^{+\star}, \tag{3.10}$$

$$T_1 + e^- \xrightarrow{k_{\mathrm{TP,e}}} S_0 + e^{-\star}. \tag{3.11}$$

Here, it is distinguished between electrons e^- and holes h^+ and their respective annihilation rates $k_{\mathrm{TP,h}}$ and $k_{\mathrm{TP,e}}$. The star denotes higher excited states. In an alternative picture, TPA can be described as quenching of triplets with doublets D (the spin-state of the polaron), which form a triplet-doublet pair (T, D). This pair then transforms into the singlet ground state S_0 and an excited doublet $D^\star$, which can either relax into a ground state doublet or auto-ionize into a free charge carrier and a ground state neutral trap:[130;131]

$$T_1 + D \leftrightarrow (T, D) \rightarrow S_0 + D^\star. \tag{3.12}$$

Like the previous annihilation processes, quenching of triplet states by charge carriers has been first observed in anthracene crystals.[131–133] Bouchriha *et al.* found that in an anthracene crystal quenching rates of trapped holes are three orders of magnitude higher than for free holes, which was attributed to their different mobility.[131] As shown in Eq. 3.12, the triplet-doublet pair does not necessarily decay into $S_0 + D^\star$. Bouchriha *et al.* calculated that most often the triplet is in fact only scattered but not quenched by the hole. Furthermore, the authors also observed detrapping of holes by triplet excitons, which leads to a current enhancement. The interaction distance for these processes, however, is believed to be on the order of the nearest neighbor molecular distance.[131]

TPA occurs mainly by Förster transfer and is described by the general rate equation:[13]

$$\frac{d}{dt} n_{\mathrm{T}}(t) = -\frac{n_{\mathrm{T}}(t)}{\tau_{\mathrm{T}}} - k_{\mathrm{TP}} n_{\mathrm{P}}(t) n_{\mathrm{T}}(t), \tag{3.13}$$

where $n_{\mathrm{P}}(t)$ is the polaron density. Here, it is assumed that the electron and hole conductivity in the EML differ by orders of magnitude, which is the case for most organic semiconductors, in particular when doped with emitter molecules.[13] If this assumption is not fulfilled, a factor of 2 should be included in order to account for quenching by both charge carrier species.[29]

The current transport in organic molecular solids is often described by the SCLC theory (see Sec. 2.4).[55] A detailed investigation of TPA

under SCLC transport conditions can be found in Ref. 13. Here, it is assumed for simplification that charge carriers are homogenously distributed inside the EML and recombine via Langevin recombination with the rate k_L.[51] The polaron density can then be expressed by the following rate equation:[29;31]

$$\frac{dn_P}{dt} = \frac{J}{qw} - k_L n_P^2, \tag{3.14}$$

$$k_L = \frac{q(\mu_e + \mu_h)}{\epsilon_0 \epsilon_r}, \tag{3.15}$$

with the elementary charge q, the mobility $\mu_{e/h}$, the relative permittivity ϵ_r, and the permittivity of free space ϵ_0.

3.2.3 *Further Processes Influencing Roll-Off*

Field-Induced Quenching Field-induced quenching was first observed in 1972 for thin-films of poly-N-vinylcarbazole (PVK) that showed a reduction in PL intensity when a high voltage was applied to electrodes surrounding the film.[134] In OLEDs, Kalinowski and Stampor *et al.* later investigated the underlying mechanism of electric field-induced quenching in more detail using small-molecule OLEDs comprising Alq_3.[135;136] The authors measured the PL of thin Alq_3 films to which an electrical field modulated with a sinusoidal signal was applied. The quenching has been interpreted as dissociation of excited states into free charges, which (partially) escape the EML, but the exact mechanism remains controversial: Evidence for field-assisted hopping of excited states within their local environment has been found.[136] However, continuous diffusion in the Coulomb field of the respective counter-charge according to the 3D Onsager model of geminate recombination has also been suggested.[130;137;138] Further studies gave evidence for field-induced quenching and found that the amount of quenching depends on the properties of the involved materials, such as the exciton lifetime, the exciton binding energy, the initial electron-hole separation distance, the Onsager radius, and the layer thickness.[110;139–141]

Changes in Charge Carrier Balance Besides quenching of excitons, the efficiency of the exciton generation process itself may also be dependent on the current density, thus representing a further potential source of efficiency roll-off. This can for instance be caused by a change in charge carrier balance. At low current densities, charge imbalances are relatively common in OLED structures since the energy barriers inside the layer stack are different for electrons and holes. As a result, an initial increase in external quantum efficiency with current is often found.[46;142–144] At higher currents and applied voltages, this imbalance often decreases as injection barriers are easier to overcome.[145;146] In contrast, if the injection barriers are field dependent, the charge balance may also deteriorate with increasing voltage, which would increase the efficiency roll-off.[147;148]

Early contributions to the understanding of the influence of changes in charge carrier balance on the efficiency roll-off were made by Giebink *et al.*[148] Using time-resolved experiments, the authors investigated the importance of charge balance effects for a range of OLED structures. For the phosphorescent emitter PtOEP, it is assumed that the very quick roll-off is mainly due to exciton quenching. This is reasonable because of the long triplet lifetime of PtOEP (56 s).[12;148] Instead, for $Ir(ppy)_3$, offering a much lower triplet lifetime of around 1 s, charge imbalance sets in at approximately 100 mA/cm^2. However, charge balance is not an intrinsic property of a certain host-guest system, but depends on all used materials and should be determined for each OLED layer stack anew.

Joule Heating Joule heating is caused by the Ohmic losses occurring during charge injection and transport and can influence the efficiency roll-off in a similar way as the annihilation processes described above.[56;149–153] Management of Joule heating is particularly important for large-area devices as well as for high-brightness applications like lasers. As thermal phenomena occur alongside with the above mentioned quenching processes, care has to be taken to avoid falsely attributing thermal quenching to other annihilation processes. This can be achieved, among other means, by varying the size of the active area of the device or the thermal contact between sample and environment.

Outcoupling Efficiency A change in charge balance upon increasing the current density can lead to a change in the location or profile of the emission zone. In this case, the outcoupling efficiency will depend on the applied voltage. In state-of-the-art small-molecule OLEDs, such changes in outcoupling efficiency will not play a major role as thin (around 20 nm) emission layers are usually used. In polymer OLEDs, however, considerably thicker emission layers are used (up to approximately 100 nm) and van Mensfoort *et al.* demonstrated that the maximum of the center of the emission zone in such OLEDs can shift by up to 50 nm when increasing the applied voltage by 2 V.[154] Such strong changes can also be expected to influence the efficiency roll-off although the influence can be both positive and negative depending on the original position of the emission zone within the OLED microcavity.

Device Degradation Finally, it shall be clarified that device degradation during one measurement cycle can reduce the efficiency at high current densities and thus result in an apparent EQE roll-off.[13;155;156] Especially when using phosphorescent blue emitters with poor chemical stability, e.g., bis[(4,6-difluorophenyl)pyridinato-N,C^2](picolinato)-iridium(III) (FIrpic) or iridium(III)bis(4',6'-difluorophenylpyridinato)-tetrakis(1-pyrazolyl)borate (FIr6), the luminance can decrease with increasing voltage.[157;158] This behavior is usually irreversible and

strongly depends on the speed of the measurement and can therefore significantly falsify roll-off measurements.

3.3 *Interplay of the Various Processes*

In the following, the influence and relative importance of the processes introduced above is discussed. In literature, opinions diverge on this matter and giving a definite answer is impossible as the relative importance of the different processes depends on the actual material system and layer structure. Nevertheless, quantifying each process is helpful in order to determine where most effort should be invested in the future to increase the efficiency at high brightness levels.

Figure 3.4 shows simulated IQE values for an OLED comprising the phosphorescent host-guest system TCTA:Ir(ppy)$_3$ taking the bimolecular quenching processes TTA and TPA into account. These results were obtained by solving the rate equations for the triplet density,[13]

$$\frac{dn_\mathrm{T}}{dt} = k_\mathrm{L} n_\mathrm{P}^2 - \frac{n_\mathrm{T}}{\tau_\mathrm{T}} - \frac{1}{2} k_\mathrm{TT} n_\mathrm{T}^2 - k_\mathrm{TP} n_\mathrm{P} n_\mathrm{T}, \tag{3.16}$$

and polaron density according to Eq. 3.14. The figure shows the triplet and polaron densities calculated using the rate constants $k_\mathrm{TT} = 3 \times 10^{-12}\,\mathrm{cm}^3/\mathrm{s}$, $k_\mathrm{TP} = 3 \times 10^{-13}\,\mathrm{cm}^3/\mathrm{s}$, $k_\mathrm{L} = 8.31 \times 10^{-11}\,\mathrm{cm}^3/\mathrm{s}$,[4] and $\tau_\mathrm{T} = 1.58\,\mathrm{s}$.[13] The IQE is then calculated from these densities as the ratio of radiatively decaying singlets over the number of injected electrons: $\mathrm{IQE} = \frac{n_\mathrm{T}}{\tau_\mathrm{T}} / \left(\frac{J}{qw}\right)$. For simplification, light outcoupling is not considered and hence IQE rather than EQE data is presented. Moreover, the electric and radiative efficiencies are set to 1 at low current density (cf. Eq. 2.19). Furthermore, the contribution of each triplet decay process is computed as a function of the applied current density. The IQE thus coincides with the contribution of the radiative triplet decay $k_\mathrm{T} n_\mathrm{T}$.

[4] Assuming that holes are transported on TCTA with $\mu_\mathrm{h} = 1.6 \times 10^{-4}\,\mathrm{cm}^2/\mathrm{Vs} \gg \mu_\mathrm{e}$ and $\epsilon_\mathrm{r} = 3.5$.[159]

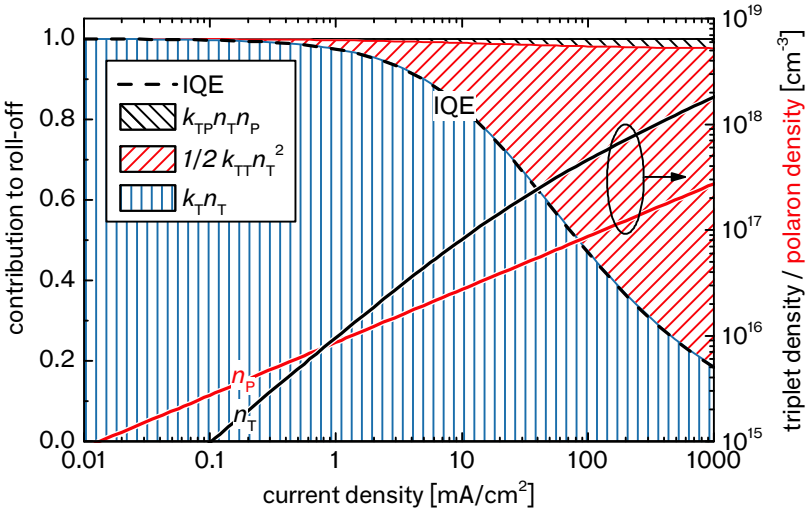

Figure 3.4: Simulated internal quantum efficiency (IQE) (dashed line) as a function of the current density for a phosphorescent OLED based on TCTA:Ir(ppy)$_3$. Triplet- and polaron densities (lines) are calculated according to Eqs. 3.16 and 3.14 using the annihilation rates mentioned in the text. Hatched areas indicate the relative contribution of TTA and TPA as well as of the emission to the overall exciton decay.

At current densities below 1 mA/cm^2, the polaron density is larger than the triplet density and TPA is thus largest in the very low current regime (not visible in the graph). However, TTA is expected to be the dominating quenching process across the entire current range investigated for systems that are comparable to the one shown here.[12;13] Note that in contrast to this finding, other publications argue that TPA dominates over TTA in phosphorescent devices.[122;160;161] One explanation for this difference is that the probability for TTA depends on the charge trapping characteristics of the host-guest system: When the emitter molecules constitute a trapping site for polarons within the host, accelerated TPA can be expected which in turn reduces the relative importance of TTA.[110]

In the roll-off simulations in Figure 3.4 only bimolecular quenching processes are considered. Kalinowski *et al.* compared the influence of exciton-polaron quenching and exciton dissociation by electric fields on the roll-off.[138] Dissociation is most important at medium field strengths of around 10^6 V/cm as it saturates at higher fields. Its influence is generally smaller than the influence of exciton-polaron interaction and thus exciton dissociation under an electric field plays a minor role within the practically relevant current regime. Changes in charge balance might lead to significant roll-off, but this is unfortunately difficult to predict as theoretical modeling of charge transport remains challenging for the complex multi-layer systems used in today's OLEDs.[162] An alternative is to estimate the electrical efficiency using optical modeling of the emission spectrum[68] or direct measurement with a suitable time-resolved setup.[148] However, as the influence on the efficiency roll-off strongly depends on the precise layer stack, no general statement can be made. In conclusion, efforts to reduce EQE roll-off should focus on minimizing TTA and on designing OLED stacks in which charge balance is independent of the applied voltage.

3.4 *Scope of this Work*

As discussed in the previous section, TTA is the dominating annihilation process underlying efficiency roll-off in most phosphorescent OLEDs. In order to modify the strength of TTA, the definition of the critical current density J_0 under the TTA model (Eq. 3.5) shall again be considered. Three factors that influence the roll-off are visible: The width of the emission zone w, the TTA rate constant k_{TT}, and the triplet lifetime τ_T. This thesis aims at modifying these three parameters in order to reduce the roll-off based on TTA.

It was shown in Eq. 2.20 that the intrinsic emitter lifetime can be modified through the Purcell effect. Therefore, τ_T is studied in Chapter 5 as a function of the OLED microcavity strength. Chapter 6 focusses on the emission zone width w. Here, three different structures are explored that may increase the emission zone width. Finally, the TTA rate constant k_{TT} is measured for different phosphorescent emitters in Chapter 7. It is found that some compounds tend to

aggregate, which increases k_{TT}. Therefore, the amount of aggregation is studied varying the matrix material and changing the processing parameters.

Although TTA may be overlapped by other processes such as charge carrier imbalance, the three investigations performed in this work give an important insight into molecular and device design and help improving the high-brightness performance of OLEDs.

4 Experimental Methods

This chapter briefly describes the experimental methods. First, the sample preparation by means of thermal evaporation in UHV is presented along with the used device structure. Second, measurement techniques are outlined including thin-film and OLED characterization. The last section gives an overview about the materials used and their main properties.

4.1 Sample Preparation

All samples in this thesis are prepared by thermal evaporation in UHV. This holds for both organic materials and metal electrodes. Three different evaporation tools are used that are all attached to a glovebox: two single chamber systems and a multi chamber tool consisting of nine individual chambers, which are connected via a large substrate handler. The multi chamber tool handles single samples with a size of 2.5×2.5 cm^2 and is used for evaporation of single layers.

The single chamber tools are able to fabricate up to 36 different samples at ones on a substrate of 15×15 cm^2 size. The samples are arranged in a 6×6 matrix. A system of masks allows an individual evaporation to each column and row so that processing parameters such as layer thickness, concentration, and material can be wedged systematically. All OLEDs in this thesis are fabricated in the single chamber tool. The general structure of all evaporation systems is similar and described as follows.

A schematic illustration of an evaporation chamber is shown in Fig. 4.1. The chambers are evacuated to a base pressure of $5 \times 10^{-9} - 5 \times 10^{-7}$ mbar. Materials are filled into ceramic crucibles that are heated while the evaporation rate is controlled by quartz crystal monitors. If the desired evaporation rate of typically 0.3 to 2.0 Å/s is reached, a shutter is opened, which allows the organic vapor to condense on the substrate. A mask that is attached directly below the substrate defines the area. Co- and triple-evaporations are possible by heating several crucibles in parallel.

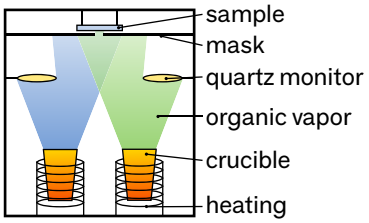

Figure 4.1: Schematic illustration of an evaporation chamber.

Materials are evaporated onto 1 mm thick glass substrates that are cleaned prior to use. Figure 4.2 shows the layout of a common device structure used for OLEDs. Glass substrates are pre-coated with 90 nm thick indium tin oxide (ITO) fingers with a sheet resistance of 25 Ω/square, which serve as transparent electrode. Subsequently, the organic layers are evaporated and finished by a highly reflecting metal electrode. The overlap of bottom and top electrode defines the active area, which has a size of approximately 6 mm^2. Each sample consists

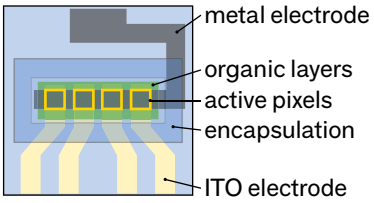

Figure 4.2: Schematic illustration of the sample layout. The active pixel area (yellow frame) is defined by the overlap of ITO bottom and metal top electrode.

of four individual pixels that can be addressed independently. In order to avoid contamination of the organic materials by moisture and oxygen, the samples are encapsulated with glass lids in nitrogen atmosphere directly after evaporation using an epoxy resin. For OLEDs, an additional desiccant acting as getter, which binds penetrating water, is put below the encapsulation glass.

4.2 Measurement

4.2.1 Thin-Film Characterization

For thin-film characterization, single layers of the respective materials are deposited on bare glass substrates and are furthermore encapsulated.

Photoluminescence and Absorbance Excitation and photoluminescence spectra are recorded using a luminescence spectrometer (Fluoromax, Horiba Jobin Yvon). Here, the sample is illuminated under a certain angle with monochromatic light from a Xenon arc lamp. The light is detected by a photomultiplier in reflection geometry, again using a monochromator. First, an excitation spectrum is recorded at the maximum of the PL spectrum. The PL spectrum is then measured at the maximum of the excitation spectrum. This process is repeated until the maxima of excitation and emission remain constant.

Absorbance is measured with a two beam difference spectrometer (UV-3101, Shimadzu). The recorded wavelength typically ranges from 300−800 nm.

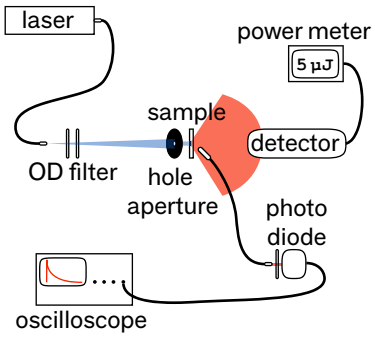

Figure 4.3: Schematic illustration of the transient PL setup.

Transient Photoluminescence The following procedure is applied in order to measure transient photoluminescence (see Fig. 4.3): Samples are excited with a nitrogen laser (MNL 200, Lasertechnik Berlin) at 337 nm. The pulse duration is typically 1.3 ns and the operation frequency is 20 Hz. A circular mask is attached to the sample in order to enable a constant illumination area. The PL signal is collected by a fibre and passed to a silicon photodiode (PDA 10A-EC, Thorlabs). The fibre is mounted slanted to the substrate normal so that transmission of incoming laser light onto the detector is avoided. A color filter that is attached to the photodiode furthermore suppresses transmitted UV light. The signal is averaged over at least 256 events and is finally displayed by an oscilloscope (infinium, Hewlett Packard). The pump exciton density n_{exc} is varied by putting optical density (OD) filters in front of the sample and is calculated by

$$n_{\mathrm{exc}} = \frac{\eta_{\mathrm{T}}\lambda}{Adhc} \cdot E_0 \cdot \left(1 - \mathrm{e}^{-\alpha d}\right). \tag{4.1}$$

Here, η_{T} is the efficiency of triplet exciton formation,[1] λ the wavelength of the laser, A the illuminated area, d the sample thickness, h the Planck constant, and c the speed of light. Furthermore, the sample absorption is accounted for using Lambert-Beer law with E_0 the pulse energy and α the absorption coefficient of the thin-film (cf. Eq. 2.14).

[1] The laser pulse mainly excites the matrix singlet states. These are quickly transferred to the guest, where they relax to the triplet state via ISC. Host singlet emission is in the ns-regime and, thus, negligible compared to the much more intense guest triplet emission in the µs-regime. Hence, η_{T} is assumed to be unity.

The pulse energy is measured through a bare glass substrate with a power meter (1835-C, Newport) and a suitable detector head (318J09B, Newport).

The triplet exciton density n_T that is present in the film is calculated assuming that $n_T = n_{exc}$ at small pump intensity (cf. the linear regime in Fig. 7.7a). Furthermore, the density of guest molecules n_G in a host-guest system is given by

$$n_G = \frac{\rho}{M} N_A \cdot \Gamma \tag{4.2}$$

with the density ρ and molar mass M of the guest, the Avogadro constant N_A, and the guest concentration Γ in mol %.

X-Ray Diffraction X-ray reflectometry (XRR) is used to measure film thickness and roughness and grazing incidence X-ray diffraction (GIXRD) to explore the film structure. Both measurements are conducted by Dr. Lutz Wilde at Fraunhofer IPMS-CNT, Dresden. The XRD tool (D8 Discover, Bruker) uses Cu-K_α radiation ($\lambda = 1.54$ Å) and a scintillation counter. Figure 4.4a and b show the used geometries. XRR measurements are conducted in Bragg-Brentano geometry, where the incident angle ω equals the reflection angle 2θ. The measurement range covers small angles from $2\theta = 0°$ to 5°, where interference occurs mainly at the layer interfaces and not on the lattice planes. Spectra are fitted with the software REFSIM (Version 2.0, Bruker 1999) in order to extract film thickness and roughness.

For GIXRD, the incident angle is kept constant at a very small angle of approximately $\omega \approx 0.2°$ while 2θ is scanned from $3-90°$ (cf. Ref. 163 for more details). Additionally, the background is measured at a smaller incident angle so that the light is totally reflected at the interface between air and organic thin-film. All measurements are background-corrected.

Furthermore, 2D grazing incidence wide-angle X-ray scattering (GIWAXS) is measured by Dr. Chris Elschner at the Stanford Synchrotron Radiation Lightsource (SSRL), beamline 11-3, at an energy of 12 735 eV. Here, a 2D image plate detects scattered X-rays both in out-of-plane and in-plane direction, which enables knowledge of the crystal orientation. GIWAXS data are isotropically converted to q-values and are further analyzed using the software WxDiff.

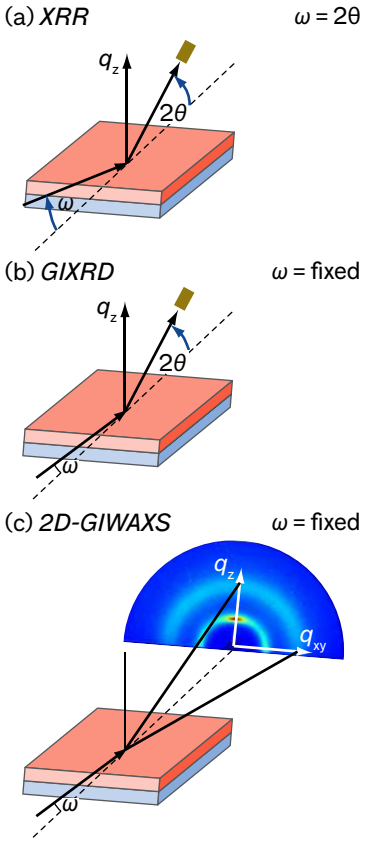

Figure 4.4: Geometries used for X-ray spectroscopy measurements. (a) Bragg-Brentano geometry for XRR ($\omega = 2\theta$) and (b) GIXRD (ω is fixed and 2θ is varied); both use a point detector. (c) 2D-GIWAXS using a 2D image plate as detector.[164]

4.2.2 OLED Characterization

Efficiency Measurement Current density-voltage-luminance and spectral radiance are recorded in an automated measurement system consisting of a source-measure unit (SMU) (SM2400, Keithley), a silicon photodiode, and a calibrated spectrometer (CAS140CT, Instrument Systems GmbH). The efficiencies can be estimated from those measurement data assuming a Lambertian angular characteristic.[2]

Typically, the Lambertian characteristic is only a rough estimate and OLEDs may heavily deviate from this behavior, especially in strong microcavities or when built in the optical minimum. There-

[2] For a Lambertian light source, the luminance follows $L(\vartheta) = L_0 \cos(\vartheta)$ with the angle ϑ between observer and substrate normal, and the luminance L_0 measured perpendicular to the substrate.

fore, a spectro-goniometer is used to measure the angular dependent spectra. The OLED is positioned on a rotatable stage and is driven by an SMU (SM2400, Keithley). A portable fibre spectrometer (USB4000, Ocean Optics) detects the spectral irradiance as a function of the angle. Spectra are measured from 0° to 90° in steps of 5°. Now, the EQE and LE are calculated according to Eqs. 2.23 and 2.24. If not stated otherwise, all efficiencies throughout this thesis are calculated taking this angular correction into account.

Transient Electroluminescence For transient electroluminescence measurements, 50 s long voltage pulses are applied to the sample at a frequency of 100 Hz using a pulse generator (8114A, Hewlett Packard). Transient EL is recorded with a Streak camera (Hamamatsu C5680) while an oscilloscope (infinium, Hewlett Packard) monitors the applied voltage pulse. Additionally, the voltage drop over a 50 Ω resistance that is connected in parallel to the OLED is detected in order to control the current through the device.[165]

4.3 Materials

All materials are purchased commercially and are further purified by high-vacuum gradient sublimation prior to use.

4.3.1 Electrodes, Transport Materials, and Blockers

The OLEDs that are studied throughout this work are built in bottom-emitting configuration. This means that the light is coupled out through the glass substrate. Therefore, 90 nm transparent ITO with an average transmission of around 92 % in the visible wavelength regime is used as anode.[23] On the other side, 100 nm thick layers of Al or Ag are employed as highly reflecting cathodes. Ag possesses a higher reflectivity in the red and green wavelength regime than Al and can therefore increase the outcoupling efficiency for red- and green-emitting OLEDs.[166]

In order to inject charges from the electrodes, either very thin injection layers or doped transport layers are used. The injection layers are composed of the inorganic materials molybdenum trioxide (MoO_3)[167;168] for hole injection and lithium fluoride (LiF)[169] for electron injection.

Using doped transport layers also enables Ohmic hole injection. Here, the organic p-dopant 2,2′-(perfluoronaphthalene-2,6-diylidene)-dimalononitrile (F_6-TCNNQ)[66;73] is doped into the hole transporting materials N,N,N′,N′-tetrakis(4-methoxyphenyl)-benzidine (MeO-TPD)[74;170] or 2,2′,7,7′-tetrakis(N,N′-di-p-methylphenylamino)-9,9′-spirobifluorene (Spiro-TTB).[62;73] Both HTLs show a similar conductivity of 1.5×10^{-4} S/cm and 1.3×10^{-4} S/cm, respectively, at a doping concentration of 4 wt %.[74] For electron injection and transport, 4,7-diphenyl-1,10-phenanthroline (BPhen) is doped 1 : 1 with the alkali metal Cs, which reaches a conductivity of 2×10^{-5} S/cm.[171]

If doped transport layers are used, blocker materials are introduced in order to keep charges and excitons inside the EML. Therefore, either pure layers of the matrix materials or specific blocking materials are used such as the hole-transporting 2,2′,7,7′-tetrakis-(N,N-diphenylamino)-9,9′-spirobifluorene (Spiro-TAD)[172] or the electron-transporting bis-(2-methyl-8-quinolinato)(4-phenylphenolate)-aluminium(III) ($BAlq_2$)[173].

4.3.2 *Materials of the Emission Layer*

The investigation of phosphorescent iridium emitters is one key part of this thesis. Seven different compounds are studied in Chapter 7: tris(2-phenylpyridine)iridium(III) ($Ir(ppy)_3$), bis(2-phenylpyridine)-(acetylacetonate)iridium(III) ($Ir(ppy)_2(acac)$), tris(2-(1-cyclohexenyl)pyridine)iridium(III) ($Ir(chpy)_3$), bis(2-(9,9-dihexylfluorenyl)-1-pyridine)-(acetylacetonate)iridium(III) ($Ir(dhfpy)_2(acac)$), bis(2-phenylbenzothiazolato)(acetylacetonate)iridium(III) ($Ir(BT)_2(acac)$), bis(2-methyldibenzo[f,h]quinoxaline)(acetylacetonate)iridium(III) ($Ir(MDQ)_2(acac)$), and tris(1-phenylisoquinoline)iridium(III) ($Ir(piq)_3$). The properties of all these emitters are discussed in more detail in Section 7.2. The structure formulas are shown in Fig. 7.1 and the PL spectra in Fig. 7.2.

Furthermore, the blue emitter bis(4′,6′-difluorophenylpyridinato)-tetrakis(1-pyrazolyl)borate (FIr6) is used in Sec. 6.4.[156;174] Figure 4.5 shows its chemical structure and PL spectrum. FIr6 has a triplet energy of 2.72 eV and is one of the most efficient pure blue emitters.[175–177]

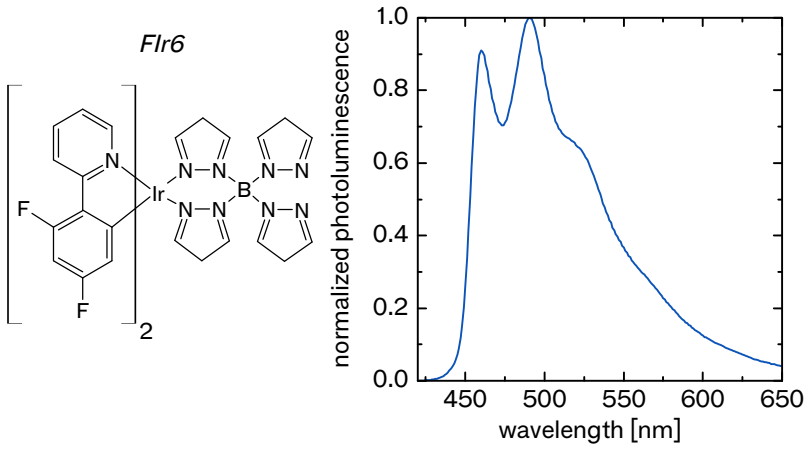

Figure 4.5: Chemical structure and PL spectrum of the blue emitter FIr6.

The emitter compounds are doped into matrix materials in order to avoid concentration quenching.[39] Throughout this thesis, seven different matrix materials are used: 4,4′,4″-tris(N-carbazolyl)-triphenylamine (TCTA)[159;178;179], 1,1-bis[(di-4-tolylamino)phenyl]cyclohexane (TAPC)[180;181], 4,4′-bis(carbazol-9-yl)biphenyl (CBP)[121;181], N,N′-di(naphthalen-1-yl)-N,N′-diphenyl-benzidine (NPB)[181], N,N′-di-1-naphthalenyl-N,N′-diphenyl-[1,1′:4′,1″:4″,1‴-quaterphenyl]-4,4‴-diamine (4P-NPD)[125], 2,2′,2″(1,3,5-benzenetriyl)tris-(1-phenyl-1H-

benzimidazole) (TPBi)[179;182;183], and 2-(diphenylphosphoryl)spirofluorene (SPPO1)[143;184;185]. The chemical structures are shown in Fig. 4.6. TCTA, TAPC, 4P-NPD, and NPB primarily transport holes, while TPBi and SPPO1 favor electron transport. CBP is known as ambipolar material offering similar conduction properties for electrons and holes, which will be further discussed in Sec. 6.3.[186;187]

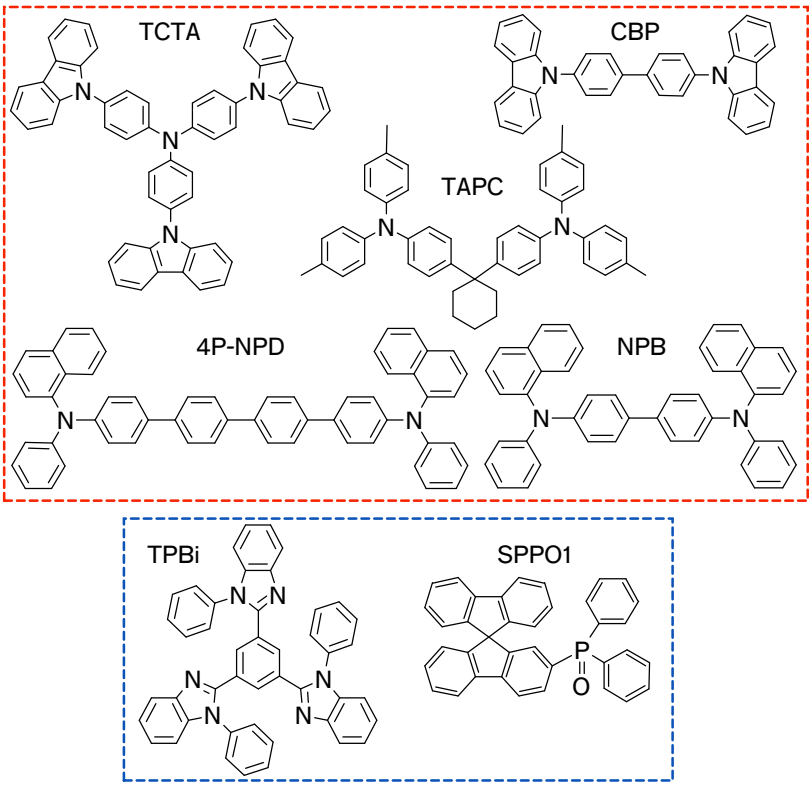

Figure 4.6: Chemical structures of the used host materials. Red and blue frames indicate hosts that primarily conduct holes and electrons, respectively.

5 Influence of the Optical Environment

The exciton density and, hence, the efficiency roll-off depend on the emitter lifetime, which can be influenced by the optical environment around the emitting dipoles. This chapter studies the effect by varying the distance between emitter and metal cathode for two OLED stacks. Each contains a phosphorescent emitter: either the red-emitting Ir(MDQ)$_2$(acac) or the green-emitting Ir(ppy)$_3$. A strong influence of emitter position and orientation on roll-off is observed. The measurements are modeled by TTA theory, yielding the critical current density and the TTA rate constant. By further simulating the roll-off as a function of emitter-cathode distance, emissive dipole orientation, and radiative efficiency, design principles for optimal high-brightness performance are developed.[1]

5.1 Introduction

Placing the emitter within a strong microcavity or in close proximity to metal surfaces can considerably reduce the effective triplet lifetime.[68] For instance, improved roll-off has been demonstrated for top-emitting OLEDs, where the presence of a stronger microcavity[2] than in conventional bottom-emitting structures shortens the emitter lifetime.[189] Further reports showed a reduction in emitter lifetime by placing gold nanoparticles in close proximity (15–20 nm) to the EML.[190]

Song *et al.* found some evidence that the roll-off also correlates with the distance between emitter and reflecting metal cathode.[191] However, they did not analyze this effect quantitatively, and probably additional quenching mechanisms overlapped with TTA in their study because the efficiency roll-off observed for large distances between emitter and cathode was higher than expected from the TTA model.

In the following, the influence of the OLED microcavity strength on emitter lifetime and, thus, roll-off is studied in more detail. The optical environment is varied by changing the distance of the emitter molecules from the reflecting metal cathode. Furthermore, two different Ir-complexes are used as emitter in order to investigate the effect of the emitter orientation. Finally, simulations of efficiency roll-off reveal further insight into design principles for efficient OLED stacks.

5.2 Influence of Emitter-Cathode Distance

Schematics of the OLED layer stacks investigated in this study are shown in Fig. 5.1. Stack A contains the red-emitting Ir(MDQ)$_2$(acac) in an NPB matrix while Stack B is based on the green-emitting Ir(ppy)$_3$ in a double-EML consisting of the hole-transporting TCTA and the electron-transporting TPBi. The distance of the EML to the metal cath-

[1] Part of this chapter is published in Refs. 11 and 188, respectively. Reprinted with permission. Copyright 2013/2014, Wiley VCH.

[2] Compared to bottom-emitting OLEDs, the microcavity in top-emitting devices is strengthened due to metal contacts used on both sides of the active layers.

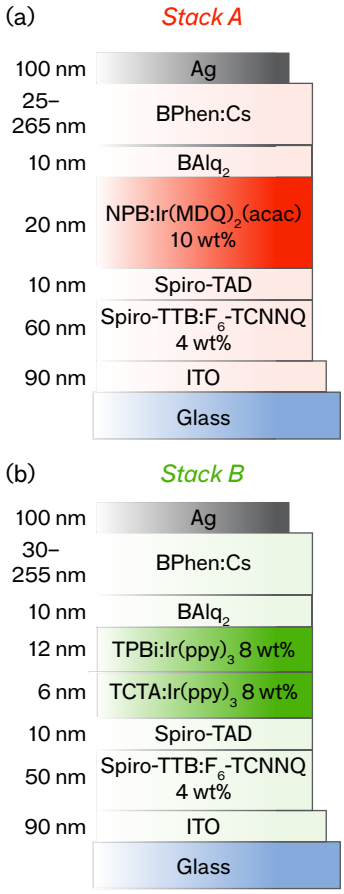

Figure 5.1: Structure of (a) the red-emitting $Ir(MDQ)_2(acac)$-based OLEDs (Stack A) and (b) the green-emitting $Ir(ppy)_3$-based OLEDs (Stack B) investigated in this study. The thickness of the BPhen:Cs ETL is varied over a broad range as indicated.

ode is varied by changing the thickness of the ETL over a broad range (Stack A from 25 to 265 nm and Stack B from 30 to 255 nm). Doped transport layers are employed to ensure that all samples have similar electrical performance despite their significantly different overall thickness.[58] In fact, up to a current density of $3\,mA/cm^2$, identical current-voltage characteristics are observed for all ETL thicknesses (cf. Fig. 5.2a). At higher current densities, a slight decrease of the current density with increasing ETL thickness is observed due to imperfect doping.

Figure 5.2b shows the measured EQE of all samples as a function of the ETL thickness. The EQE values are taken at a current density of $0.5\,mA/cm^2$, where TTA rates are negligible. The outcoupling efficiency varies depending on the position of the emitter with respect to the electromagnetic field supported by the OLED stack, which leads to pronounced EQE maxima and minima for certain ETL thicknesses.[68] The devices at the two EQE maxima are in the following referred to as first maximum device (for the lower ETL thickness) and second maximum device (for the thicker ETL). The highest EQE values are achieved at an ETL thickness of 265 nm for $Ir(MDQ)_2(acac)$ and at 205 nm for $Ir(ppy)_3$, which corresponds to the second maximum in both cases. The fact that the EQE of the second maximum device is higher than that of the first maximum device is a result of the high radiative efficiency of $Ir(MDQ)_2(acac)$ and $Ir(ppy)_3$.[68]

Figure 5.3 shows the EQE as a function of the current density J for four $Ir(MDQ)_2(acac)$ devices with different ETL thickness. All four datasets are normalized to the efficiency at low current densities where TTA is negligible. The EQE roll-off indeed shows a pronounced variation between devices, but, contrary to previous reports, no direct proportionality between roll-off and ETL thickness can be seen.[191]

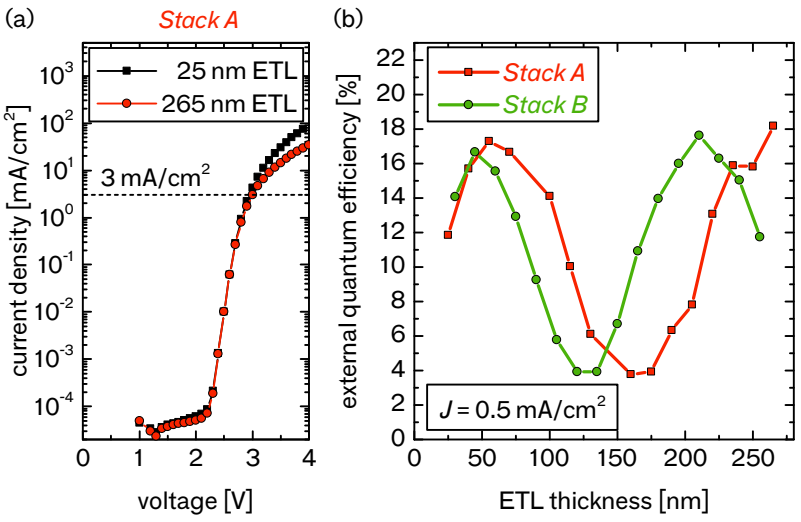

Figure 5.2: (a) Current density-voltage characteristics of the two $Ir(MDQ)_2(acac)$-based OLEDs with thinnest/thickest BPhen:Cs layer. (b) External quantum efficiency as a function of ETL thickness for the red- and green-emitting OLEDs shown in Fig. 5.1 at an applied current density of $0.5\,mA/cm^2$. Lines are guides to the eye.

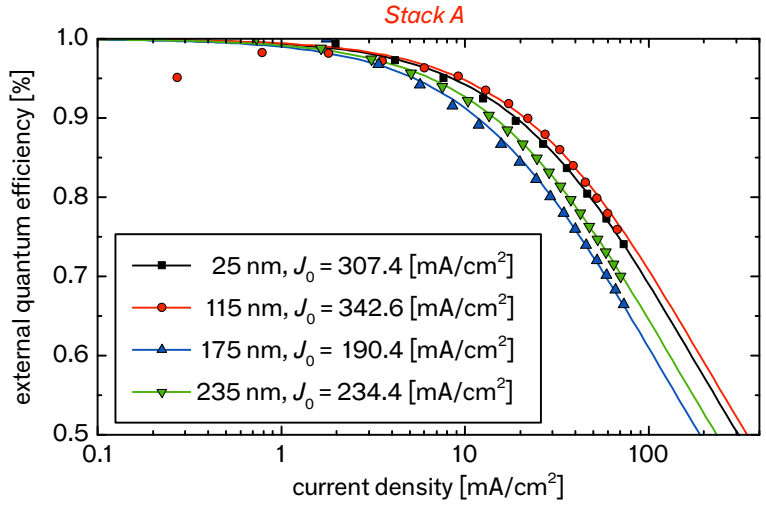

Figure 5.3: Normalized EQE versus current density for several red-emitting OLEDs (Stack A) with different ETL thicknesses. Experimental data (points) and fits according to Eq. 3.4 (lines).

A good measure for the roll-off is the critical current density J_0, i.e., the current density at which the EQE has decreased to half of its initial value.[12] However, a direct measurement of J_0 is usually not possible or meaningful because very high current densities would have to be applied, which would lead to device degradation.[47] Therefore, the measured EQE vs. J data are fitted by Eq. 3.4, yielding J_0 as a measure of roll-off. Figure 5.4 summarizes the extracted J_0 values for both samples as a function of ETL thickness. For the $Ir(MDQ)_2(acac)$-based device, the highest critical current density and, thus, the lowest roll-off is observed for ETL thicknesses close to the first EQE maximum (cf. Fig. 5.2b), i.e., for ETL thicknesses of 50–100 nm. The lowest J_0 value is obtained at 160 nm, close to the optical minimum.[3] The behavior is different for the $Ir(ppy)_3$-based devices: Here, the highest J_0 (lowest roll-off) is obtained when the emitter molecules are in close proximity to the metal cathode (thin ETL), while J_0 stays relatively constant for ETL thicknesses above 100 nm. For both emitters, critical current densities between 150 and 350 mA/cm^2 are achieved, which are typical values for state-of-the-art OLEDs.[11]

[3] Note that the sample at 145 nm ETL thickness was not measureable leading to a high leap at this point.

5.3 *Emitter Lifetime and Orientation*

To establish why the $Ir(MDQ)_2(acac)$-based OLEDs behave differently than the $Ir(ppy)_3$ devices, the change in triplet lifetime with ETL thickness is measured.[4] Therefore, the devices are electrically excited with 50 µs long rectangular voltage pulses (rise/fall time < 10 ns) and the decay in luminance after the end of the pulse duration is recorded. The current density is kept below 3 mA/cm^2 to ensure comparable electrical behavior for all ETL thicknesses (cf. Fig. 5.2a) and to avoid TTA. Figure 5.5 shows two typical transients for the red-emitting OLEDs with ETLs of different thicknesses. All devices show a mono-exponential decay; non-exponential processes such as TTA, TPA, or delayed exciton generation are not observed.[13,71] The triplet lifetime

[4] Measurement of emitter lifetime and the following extraction of the orientation is performed by Philipp Liehm (TU Dresden).

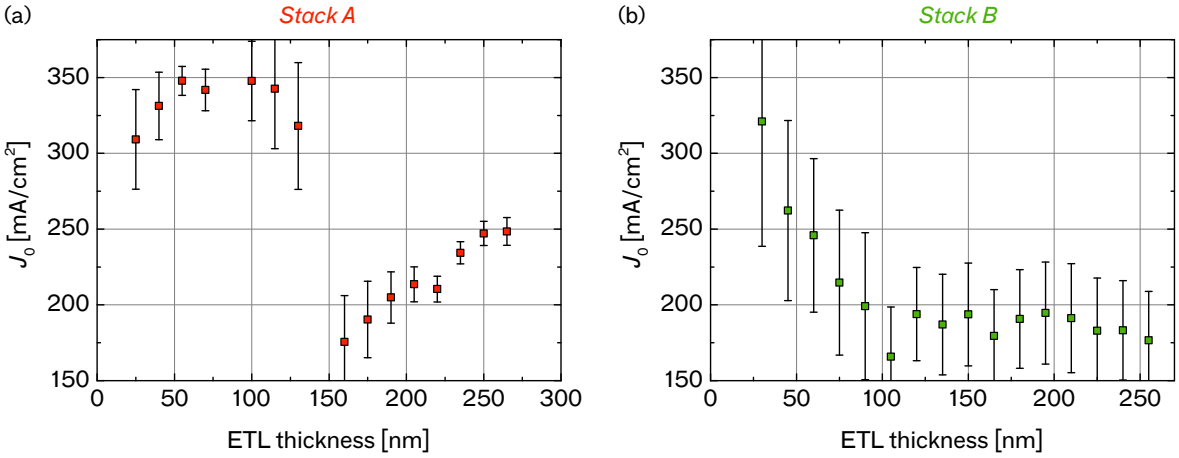

Figure 5.4: Critical current density J_0 as a function of ETL thickness, obtained from fits to the EQE vs. J data using Eq. 3.4. Error bars represent uncertainty of the fit. Data is shown for OLEDs based on (a) Ir(MDQ)$_2$(acac) and (b) Ir(ppy)$_3$.

of the device is extracted by fitting a mono-exponential decay function including a constant background. The inverse of the measured lifetimes, namely the decay rates $k^\star = 1/\tau^\star$, of all Ir(MDQ)$_2$(acac)- and Ir(ppy)$_3$-based samples are summarized in Fig. 5.6 (open symbols).

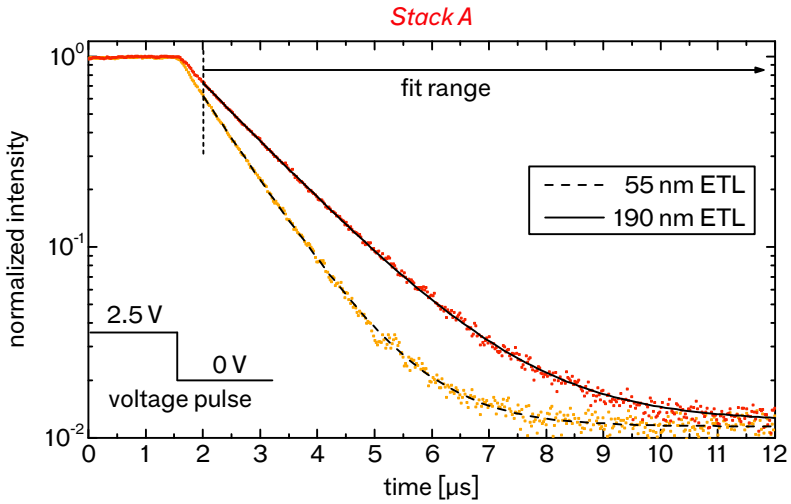

Figure 5.5: Transient electroluminescent intensity data of two typical samples based on Ir(MDQ)$_2$(acac) after excitation with a 50 µs long voltage pulse of 2.5 V (points). The data are fitted to a mono-exponential decay function (including a constant background) to extract the triplet lifetime $\tau^\star$ (lines).

The measured triplet decay rates versus ETL thickness data are then fitted to Eq. 2.20, performing a least-square optimization of k_r, k_{nr}, and a (Fig. 5.6, solid lines). For Ir(ppy)$_3$-based OLEDs, the fit reveals an isotropic dipole orientation of $a = 0.33 \pm 0.03$. By contrast, the transition dipoles of the Ir(MDQ)$_2$(acac) molecules in the red-emitting OLEDs clearly show a preferential horizontal orientation ($a = 0.21 \pm 0.03$); assuming an isotropic orientation for these devices leads to significant deviations between model and experiment for thin ETLs (cf. the dashed line in Fig. 5.6a).

All fit parameters are summarized in Tab. 5.1. According to these fits, both emitters exhibit comparable intrinsic radiative efficiencies of

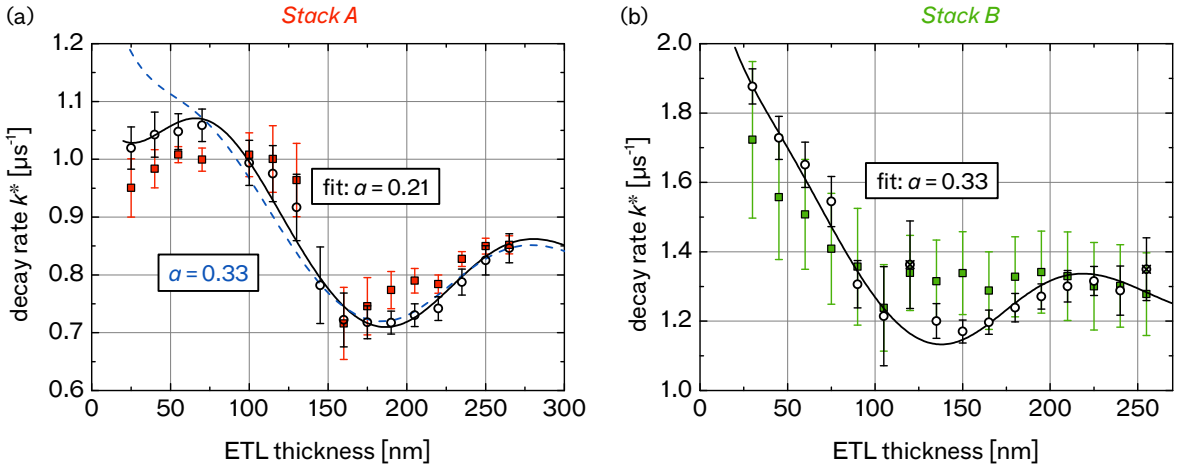

Figure 5.6: Directly measured decay rates $k^\star$ (white circles, error bars represent uncertainty of the fit to time-resolved intensity data) and decay rates extracted from fitted J_0 values (colored squares, errors bars according to Fig. 5.4) for OLEDs based on (a) $Ir(MDQ)_2(acac)$ and (b) $Ir(ppy)_3$. The directly measured decay rates are fitted according to the model described in Sec. 2.5.2 (Eq. 2.20; solid lines; crossed symbols represent data that are excluded from the fitting routine) yielding the anisotropy factor a. For comparison, the dashed line in (a) shows the expected behavior if the emissive dipoles of $Ir(MDQ)_2(acac)$ were oriented isotropically.

$\eta_{rad} \approx 0.7$. Emitter orientation and radiative efficiency are consistent with values obtained in previous measurements.[68;91–93;98;102] However, in the past, time-resolved measurements of transition dipole orientations have been limited to optical excitation,[92;93] under which location and width of the emission zone are different than under electrical excitation. Measuring orientation under electrical excitation more closely resembles the situation in a real device and ensures to obtain the average orientation of exactly those emitter molecules that contribute to the electroluminescence generated by the device.

5.4 *Correlation of Roll-Off and Orientation*

Using the obtained fits, the measured critical current densities from Sec. 5.2 can be properly explained. These J_0 values are scaled according to Eq. 3.5 ($\sqrt{J_0} \propto k^\star$) to obtain the effective decay rates $k^\star$ (Fig. 5.6, solid symbols). A clear correlation between roll-off and triplet lifetime is observed for both emitters, i.e., the data extracted from J_0 are in good agreement with the fits obtained from transient electroluminescence measurements. Moreover, with knowledge of the emitter orientation, the observed differences in roll-off behavior between the two emitters can be explained: Due to their isotropic orientation, the decay rate of $Ir(ppy)_3$ molecules is considerably increased when these are in close proximity to the metal cathode. Therefore, the roll-off in $Ir(ppy)_3$-based devices decreases as the distance between emitter and electrode diminishes, in agreement with previous observations.[191] For $Ir(MDQ)_2(acac)$, however, the preferential horizontal transition

Table 5.1: Extracted fit parameters for OLEDs containing $Ir(MDQ)_2(acac)$ or $Ir(ppy)_3$: anisotropy factor a, radiative decay rate k_r, non-radiative decay rate k_{nr}, radiative efficiency η_{rad}, and TTA rate constant k_{TT}.

	a	k_r [µs^{-1}]	k_{nr} [µs^{-1}]	η_{rad}	k_{TT} [cm^3/s]
$Ir(MDQ)_2(acac)$	0.21 ± 0.03	0.58 ± 0.03	0.24 ± 0.03	0.71 ± 0.06	$(1.9 \pm 0.2) \times 10^{-12}$
$Ir(ppy)_3$	0.33 ± 0.03	0.92 ± 0.04	0.36 ± 0.04	0.72 ± 0.03	$(6.0 \pm 1.2) \times 10^{-12}$

dipole orientation leads to a minimal roll-off at an ETL thickness in the range of 50–100 nm.

The decay rates estimated from J_0 mostly agree with the direct measurements within their experimental uncertainty. Remaining deviations are probably caused by the presence of other quenching mechanisms that have not been taken into account here but that may also influence the efficiency roll-off. Especially for thin ETLs, quenching is higher than expected. As shown in Fig. 5.2a, the current-voltage characteristics slightly differ at high voltage for devices with different ETL thickness, which can lead to reduced charge balance at high voltages for certain devices.

In the following, Eq. 3.5 is used to extract the TTA rate constant k_{TT} from the measured critical current densities and the effective decay rates. The width of the exciton formation zone is assumed to be $w = 10$ nm for both device structures as this value has been previously measured for similar OLED stacks based on EMLs of TCTA:Ir(ppy)$_3$.[13] This yields $k_{TT} = (1.9 \pm 0.2) \times 10^{-12}$ cm^3/s for Ir(MDQ)$_2$(acac) and $k_{TT} = (6.0 \pm 1.2) \times 10^{-12}$ cm^3/s for Ir(ppy)$_3$. For the latter, a value of $k_{TT} = (3 \pm 2) \times 10^{-12}$ cm^3/s has previously been obtained for a similar OLED stack using transient decay measurements at high excitation densities.[13] Compared to Ir(MDQ)$_2$(acac), Ir(ppy)$_3$ shows a higher TTA rate, which is probably due to its stronger tendency to form aggregates (cf. Chapter 7).[117;142]

Note that measurements of k_{TT} usually require time-resolved measurements at high excitation densities, which can introduce device degradation. The method suggested here is instead based on a combination of decay time measurements at low excitation densities with measurements of the efficiency roll-off.

5.5 *Simulation of Roll-Off*

Thin-film optical simulations based on a source dipole model and transfer matrix approach are frequently used to optimize light extraction (outcoupling) from OLEDs, but up to now they ignore efficiency roll-off. Instead, the thickness of all layers in a device is usually only optimized for low brightness levels. However, the optimum thickness may change at high brightness because the decay rate and, thus, the fraction of excitons lost to TTA or other quenching mechanisms that scale with the exciton density generally depend on the layer thickness. In the following, optical simulations[5] of EQE and decay rate (both as a function of ETL thickness) are combined with calculations of the efficiency roll-off, using the Ir(MDQ)$_2$(acac)-based OLEDs (Stack A) as an example.

[5] Optical simulations using a transfer matrix approach are performed by Philipp Liehm (TU Dresden).

Figure 5.7 shows the simulated EQE of Stack A over the ETL thickness for different current densities. At low current density, the second maximum device shows the highest efficiency, according to the experimental observation in Fig. 5.2b. As the efficiency roll-off depends on the position of the emitter within the OLED microcavity, a first maximum device shows a different roll-off behavior than a

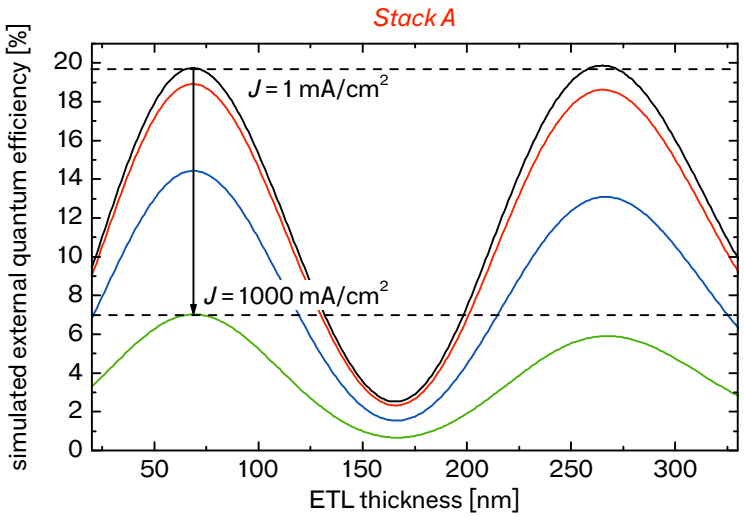

Figure 5.7: Simulated EQE of Stack A as a function of the ETL thickness for current densities of 1, 10, 100, and 1000 mA/cm^2. While at a low current density the second maximum device is slightly more efficient than the first maximum device, the efficiency of the latter is less reduced at high current densities.

second maximum device. In our example (Stack A), the decay rate $k^\star$ and, thus, the critical current density J_0 is higher in the first maximum leading to a weaker roll-off compared to the second maximum (cf. Fig. 5.4a). Therefore, the first maximum device is more efficient at high current densities than the second maximum device.

Whether the first or the second maximum is more suitable depends on the electroluminescence spectrum, the radiative efficiency and the orientation of the emitter molecules, as well as on other factors including the reflectivity of the cathode.

5.5.1 *Influence of the Electroluminescence Spectrum*

In order to enable efficient white OLED design at high brightness, the influence of the electroluminescence spectrum is investigated in more detail by calculating the dependence of the EQE on current density and ETL thickness for varying spectra. Optical simulations of EQE and $k^\star$ vs. ETL thickness are performed using the fit parameters from Tab. 5.1. The EQE roll-off is then calculated according to Eq. 3.4 using the values of k_{TT} and w as determined in Sec. 5.4.

Figure 5.8a shows three different spectra that are used for the simulation: A red, a yellow, and a blue spectrum. The red spectrum resembles the PL spectrum of Ir(MDQ)$_2$(acac), whereas for the other two colors the Ir(MDQ)$_2$(acac) spectrum is artificially shifted into the yellow and blue region so that their maxima are positioned at 550 nm and 450 nm, respectively. Figure 5.8b shows the calculated critical current density J_0 of the three devices in dependence of the ETL thickness d_{ETL}. The local minima and maxima of J_0 shift to smaller ETL thicknesses when changing the emission from red to blue. This is due to the concurrent shift of the total radiated power F that is forced by the decreasing cavity length for constructive/destructive interference. Moreover, the behavior of J_0 at small microcavities differs strongly: For the red spectrum, a maximum J_0 of 394 mA/cm^2

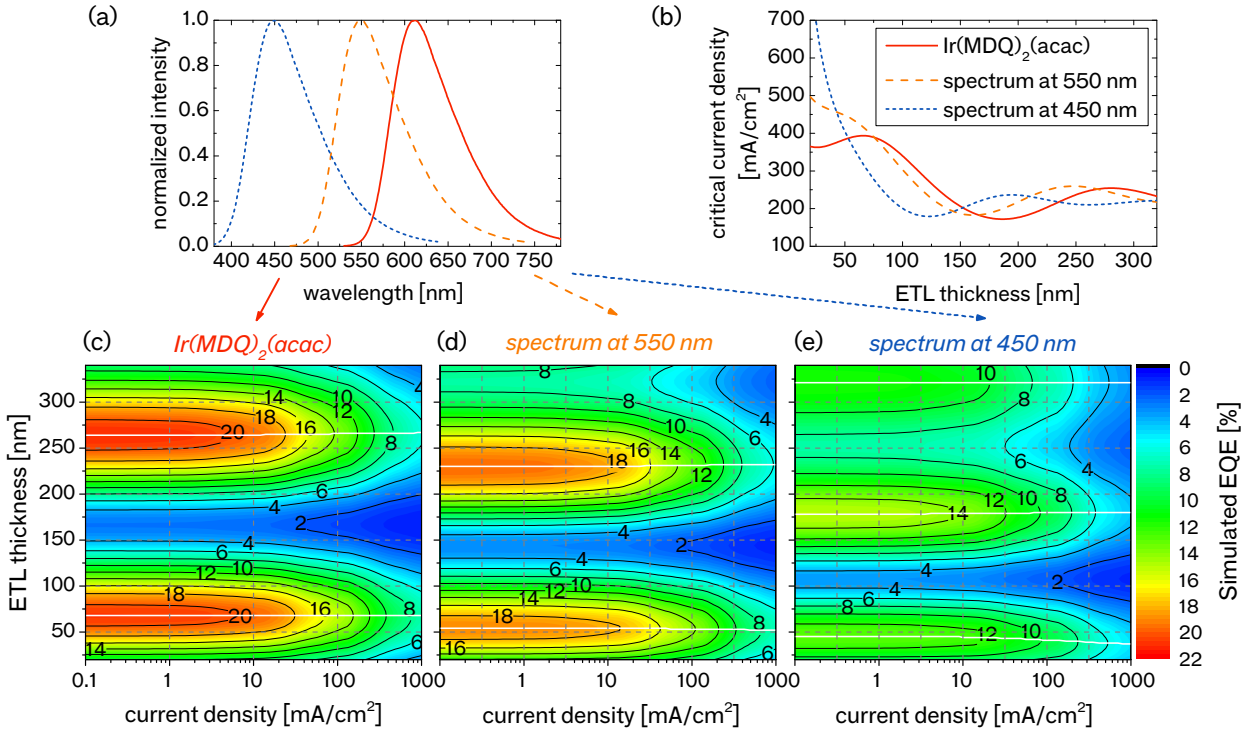

Figure 5.8: Optical simulation and subsequent calculation of efficiency roll-off of Stack A. (a) PL spectra of the three samples. The maximum of $Ir(MDQ)_2(acac)$ is shifted from its original position at 612 nm to 550 nm and 450 nm. (b) Critical current density J_0 as calculated from the simulated decay rates. (c-e) Simulated EQE (z-scale) as a function of ETL thickness and current density J for the three different spectra. White lines indicate the ETL thickness in optical maximum.

is obtained at an ETL thickness of 66 nm. For the yellow and blue spectra, instead, this first maximum vanishes and J_0 increases with decreasing ETL thickness reaching more than 800 mA/cm^2 for the blue spectrum at $d_{\mathrm{ETL}} < 22$ nm. However, designing OLED stacks with very low ETL thickness is not suitable as the coupling of the emitter dipoles to the metal electrode leads to surface plasmons, which strongly decrease the EQE.

To further correlate roll-off with efficiency at different cavity thicknesses, Figs. 5.8c-e show the EQE as a color map for varying ETL thickness over a wide current range between 0.1 and 1000 mA/cm^2. The ETL thickness necessary to obtain maximum EQE decreases with decreasing emission wavelength. Furthermore, the absolute EQE decreases with the spectral shift due to the increasing absorption of the silver cathode in the blue wavelength regime.[166]

At low current density, the second maximum device is most efficient for all colors. With increasing brightness, however, the efficiency of the second maximum decreases faster than the efficiency of the first maximum so that already at 5 mA/cm^2 for the red spectrum (90 mA/cm^2 for the blue spectrum) the first maximum sample becomes more efficient. Additionally, the ETL thickness in the optical maximum is marked by white lines. With increasing current density, the ETL thickness changes slightly for the red and remarkably for the blue spectrum. In the latter, the first maximum shifts from $d_{\mathrm{ETL}} = 45$ nm to 37 nm over the calculated current density regime. Here, the effect is strongest for the first maximum of the blue sample

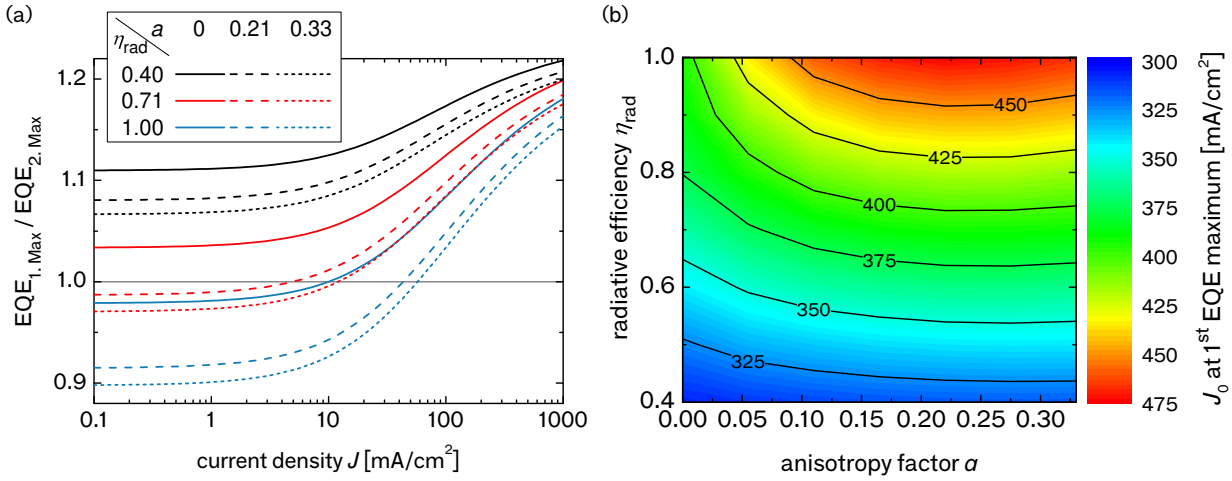

Figure 5.9: Optical simulation of efficiency roll-off for OLEDs based on Stack A for varying anisotropy factor a and radiative efficiency η_{rad} assuming a constant intrinsic decay rate of $k = 0.816\,s^{-1}$ and the emission spectrum of $Ir(MDQ)_2(acac)$. (a) Ratio of EQE for first maximum devices over EQE of second maximum devices as a function of the current density J. Values above 1 indicate that the first maximum device is more efficient. (b) Critical current density J_0 of first maximum devices (z-scale) as a function of η_{rad} and a.

due to the steepest slope of J_0 vs. d_{ETL}. Applying these findings to the design of highly efficient OLED stacks, the operational current regime should always be taken into account; the maximum EQE can not only switch from first to second maximum (or vice-versa), but the ETL thicknesses of the maxima also require different values for different targeted current density.

5.5.2 *Influence of Orientation and Radiative Efficiency*

The influence of the anisotropy factor and radiative efficiency of the emitter on the roll-off is now studied in more detail. Figure 5.9a shows the ratio of the calculated EQE of the first maximum device over the EQE of the second maximum device as a function of current density. The simulation is performed for hypothetical phosphorescent emitters with different anisotropy factors ($0 \leq a \leq 0.33$) and radiative efficiencies ($0.4 \leq \eta_{rad} \leq 1$), again on Stack A with the red spectrum. For the actual material parameters of $Ir(MDQ)_2(acac)$ ($a = 0.21$, $\eta_{rad} = 0.71$), the second maximum device is more efficient up to a current density of $5\,mA/cm^2$ as already observed in Fig. 5.8c. Concerning the anistropy factor, the EQE of the first maximum device would increase if the emitters were oriented more horizontally because losses from coupling of vertically oriented dipoles to the metal electrode are reduced. Therefore, building second maximum devices becomes less suitable for horizontal emitters already at very low current densities. For emitters with high radiative efficiency, however, second maximum devices would become more efficient not only for low, but also for rather high brightness levels (e.g., up to $56\,mA/cm^2$ for an emitter with $a = 0.33$, $\eta_{rad} = 1$).

To systematically evaluate how the emitter orientation and radiative efficiency influence the roll-off, the critical current density J_0 is calculated for the first maximum devices of Stack A as a function of emitter orientation and radiative efficiency (Fig. 5.9b). For a given emitter orientation, the critical current density is highest for the high-

est radiative efficiency. This is related to the increase of η_{rad} in decay rate at small ETL thickness (cf. Fig. 8 in Ref. 68): If the radiative efficiency is high, the total decay rate of the emitter is dominated by the effective radiative decay rate, which in turn strongly increases in close proximity to the metal contact, thus reducing the roll-off. For low radiative efficiencies, instead, η_{rad} mainly resembles the non-radiative decay rate k_{nr}, and the influence of the Purcell factor F vanishes so that $\tau^\star$ becomes τ. Therefore, the roll-off of less efficient emitters can only weakly be influenced by strengthening the OLED microcavity.

The influence of orientation, however, is less obvious: J_0 remains relatively constant for different values of a if η_{rad} is low, while for $\eta_{rad} = 1$ a clear maximum of J_0 is obtained at an intermediate value of $a \approx 0.22$. The different behavior for low and high η_{rad} is caused by the strong shift in ETL thickness required to position the emitter molecules at the first maximum of the field. For instance, when changing a from 0 to 0.33 (at $\eta_{rad} = 1$), the respective ETL thickness changes by 18 nm. Considering the properties of $Ir(MDQ)_2(acac)$, the average orientation of the transition dipoles in the material is close to the optimum with regard to the roll-off. However, the roll-off performance would improve further if an emitter with a higher radiative efficiency becomes available, which will of course also increase the absolute EQE.

A similar behavior is also found for Stack B containing $Ir(ppy)_3$ as emitter. However, at this stage, the dependence of EQE and roll-off on a and η_{rad} cannot be generalized because especially the reflectivity of the metal electrode has a pronounced influence on the EQE and the decay rates. Efficient device design therefore always requires optical simulation of the particular OLED stack.

5.6 Conclusion

In conclusion, efficiency roll-off is strongly influenced by the position and orientation of the emitter molecules within the OLED microcavity.[6] An exception are emitters with very low radiative efficiency, but those are generally of little interest. The relation between efficiency roll-off and distance between emitter molecules and metal cathode was investigated in detail for OLEDs based either on $Ir(MDQ)_2(acac)$ or on $Ir(ppy)_3$. A distinctly different behavior was observed for the two types of emitter molecules. By performing time-resolved electroluminescence measurements and optical modeling on the same set of OLEDs, these differences could be correlated to different orientations of the emissive dipoles for the two types of emitters. OLEDs based on $Ir(ppy)_3$, which is oriented isotropically, show the lowest roll-off if the emitter is positioned close to the metal cathode. $Ir(MDQ)_2(acac)$, instead, is preferentially horizontally oriented. As a result, lowest roll-off is observed when the emitter is located close to the first optical maximum of the electromagnetic field. Due to the clear relation between roll-off and emitter orientation, the roll-off analysis introduced here can in principle be used to perform an independent in-situ

[6] The influence of the OLED microcavity on the roll-off has recently been also approved by Wehrmeister *et al.*[161]

measurement of emitter orientation. However, this requires that the contribution of roll-off mechanisms other than TTA can be neglected.

The findings are important to guide the optimization of OLEDs towards even higher efficiency at high brightness: First, the good agreement between the decay rates estimated from measured critical current densities and the decay rates measured directly indicates that TTA is indeed the dominant mechanism for efficiency roll-off in these OLEDs.[7] Other possible roll-off mechanisms show a different dependence on decay rate and, hence, their presence would cause strong deviations between the two sets of decay rates. Second, the distance of the emitter molecules from the metal contact of the OLED should be selected according to the emitter spectrum, orientation, radiative efficiency, and the current regime in which the OLED is intended to be operated. For OLEDs based on horizontally oriented emitters with lower radiative efficiency, the first optical maximum is typically more efficient for all brightness levels. Stacks based on isotropic emitters with high radiative efficiency show higher EQE for second maximum devices at low currents, where no roll-off is observed. When going to high-brightness applications, however, most emitters perform best in first maximum devices, as the decay rate for these is often higher than in second maximum devices.

Decreasing the emitter lifetime by changing the optical environment is not only useful for reducing the roll-off caused by TTA: Increasing the Purcell factor reduces the exciton density in general—both for triplets and singlets. Therefore, the proposed method can reduce the influence of all processes that scale with the exciton density, i.e. SSA, STA, SPA, and TPA.

[7] Note that, in a very recent publication, TPA was suggested to be the dominant mechanism leading to roll-off for an OLED similar to stack A comprising an EML with NPB:Ir(MDQ)$_2$(acac).[161] However, the different transport materials used can lead to very different polaron densities, which may make TPA much more efficient in their devices than TTA.

6 Influence of the Emission Profile

The spatial exciton distribution inside the emission layer is described by the emission profile of an OLED. This chapter focusses on the derivation and modification of the emission profile in order to decrease the local exciton density and, thus, improve the efficiency roll-off. First, a method is developed that allows experimental extraction of the spatial exciton distribution. Therefore, a thin sensing layer that locally quenches excitons is introduced into the EML at varying positions. A comprehensive theory based on the diffusion equation enables fitting the measured data and extracting the emission profile with nanometer spatial resolution. As a proof-of-principle, the method is applied to an EML comprising the ambipolar host material CBP and the green emitters Ir(ppy)$_2$(acac) and Ir(ppy)$_3$, respectively. It is found that exciton formation occurs in a narrow region close to the ETL. In order to explore EML structures that might broaden the emission profile, double and mixed emission layers are studied thereafter. Here, a hole and an electron transporting matrix are either positioned beside each other or mixed into one another. A narrow emission profile is found in the double EML, whereas the emission profile of the mixed EML strongly depends on the ratio of the chosen matrix materials. The results indicate that broad exciton distribution across the whole EML is hard to achieve in any of the three EML structures.

6.1 Preliminary Considerations

6.1.1 Exciton Generation and Diffusion

The exciton density in OLEDs is generally highest within the generation zone, both for phosphorescent and fluorescent host-guest systems.[1] Therefore, one strategy to improve the roll-off behavior is to reduce the exciton density by broadening the generation zone.

However, emission and annihilation not only occur within the generation region, but, due to exciton diffusion, across a region that is in many cases much broader. This total emission zone is described as emission profile and resembles the spatial distribution of the exciton density.

In the following, the shape of the emission profile shall be investigated in more detail. The time-independent spatial distribution of the exciton density $n(x)$ in one dimension is given by the steady-state diffusion equation with the diffusion constant D (cf. Eq. 2.16):

$$D\frac{\partial^2 n(x)}{\partial x^2} - \frac{n(x)}{\tau} + G(x) = 0. \tag{6.1}$$

$G(x)$ denotes the profile where exciton generation takes place. In OLEDs, this generation profile can be modelled by electrical simulations. For instance, Mesta *et al.* modelled the generation profile of a multilayer white OLED by means of Monte Carlo simulations.[192] They found a narrow generation region in the middle of the EML at

[1] A minor part of this section is published in Ref. 11. Reprinted with permission. Copyright 2013, Wiley VCH.

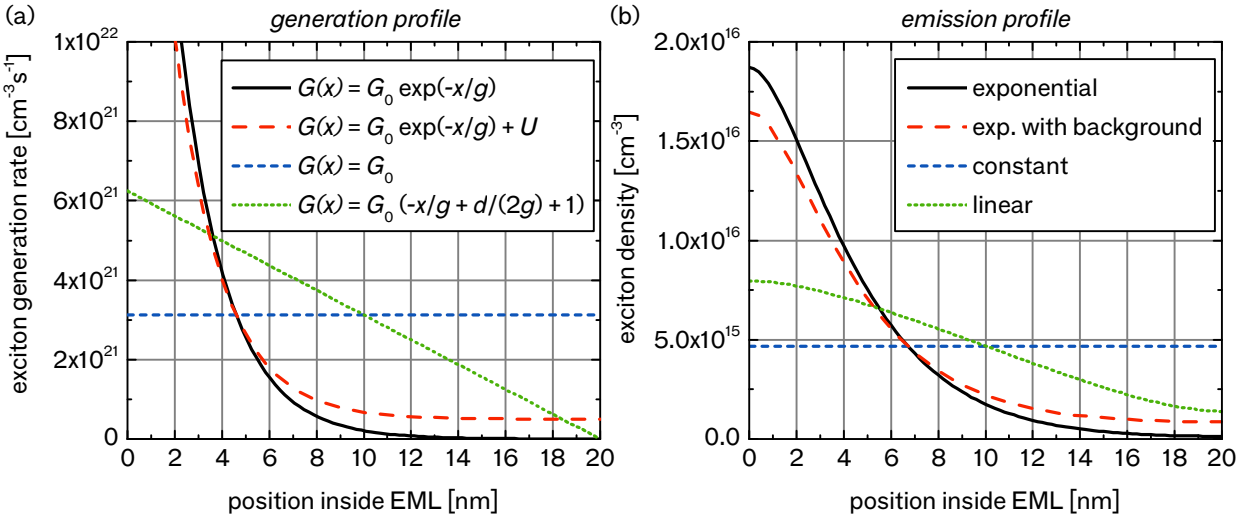

Figure 6.1: (a) Generation profiles $G(x)$ for exponential, exponential with background, constant, and linear exciton formation inside the EML. (b) Calculated emission profiles of the four different functions in (a) after solving Eq. 6.1 (see App. B.1 for the derivation of the emission profiles and the definition of G_0; $d = 20\,\text{nm}$; $l = 3\,\text{nm}$; the generation width $g = 2\,\text{nm}$ for the exponential profiles and 10 nm for the linear profile; $U = 5 \times 10^{20}\,\text{cm}^{-3}\text{s}^{-1}$).

the interface between the different emission layers and an intrinsic interlayer. The generation profile is roughly resembled by an exponential shape, where the maximum is positioned at the layer border. Schober performed drift-diffusion simulations on the same OLED layer stack and obtained a similar exciton generation zone.[193]

However, as exciton generation cannot be directly measured, the shape of the generation zone is mostly approximated. Figure 6.1a shows four different generation profiles $G(x)$ for an EML width of $d = 20\,\text{nm}$. For all profiles, the total exciton generation rate k_{Gen} in the EML is kept constant.[2] In literature, a constant profile is often assumed (blue line). Due to the typically different mobility for electrons and holes, a linear profile or an exponential shape appear more realistic. Both profiles contain a characteristic generation width g. Furthermore, an exponential generation profile with a constant background is also depicted as electron or hole traps inside the EML often lead to trap-assisted charge recombination.[194;195] These traps may be introduced by the emitter, which mostly provides a higher HOMO or lower LUMO level than the matrix.

The excitons that are generated within the emission layer diffuse with the diffusion length $l = \sqrt{D\tau}$ until they decay with an average emitter lifetime τ. This decay position is resembled by the emission profile (i.e., the exciton density n as a function of the position x inside the EML). Figure 6.1b shows the resulting emission profiles as calculated in App. B.1 assuming reflecting boundary conditions[3] on both sides of the EML, $l = 3\,\text{nm}$, and the width of the EML $d = 20\,\text{nm}$. A constant generation profile also leads to a constant emission profile. The emission profile of the linear generation profile is flattened at the interface to the blockers. The same also holds for the exponential profiles: diffusion leads to decreased exciton density at $x = 0$ and increased density in regions where only few excitons are generated.

[2] The exciton generation rate $k_{\text{Gen}} = \int_0^d G(x)dx = 6.2 \times 10^{15}\,\text{cm}^{-2}\text{s}^{-1}$ corresponds to a current density of $1\,\text{mA/cm}^2$ via $k_{\text{Gen}} = \frac{\nu}{q} J$ with ν as exciton formation probability (set to 1 here).[13]

[3] $\frac{\partial}{\partial x} n(0) = 0$ and $\frac{\partial}{\partial x} n(d) = 0$.

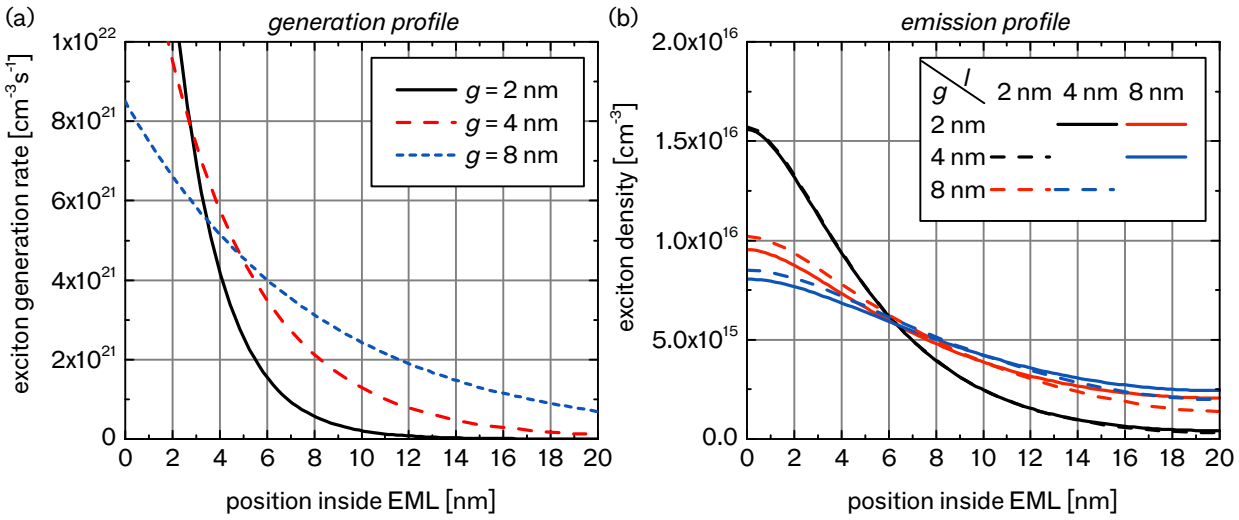

Figure 6.2: (a) Different exponential generation profiles with varying generation width g. (b) Calculated emission profile of the different generation profiles for varying diffusion lengths l.

Measurements of the generation profile indicate that in most EML structures which incorporate host materials with very different hole and electron mobility, the generation profile has an exponential shape.[196–200] Therefore, the exponential emission profile is investigated in more detail in the following. Figure 6.2a shows three exponential generation profiles with different generation widths g from 2 to 8 nm. Again, the total exciton generation rate is kept constant. Figure 6.2b shows the respective emission profiles upon varying the diffusion length in the same range as g from 2 to 8 nm. For $g = l$ no analytic solution is possible (cf. the denominator in Eq. B.5c). Comparing two curves with the same color, a small difference is visible between the influence of g and l despite both processes following exponential laws: A long diffusion length leads to a more homogeneous exciton distribution than a broad generation profile. This becomes especially obvious when the difference between g and l is high. For very long diffusion lengths $l \to \infty$ the emission profile gets constant independent of the shape of the generation profile.

The influence of diffusion strongly depends on the OLED structure. In fluorescent materials, singlet exciton diffusion lengths of around 5 nm have been found for NPB and 4P-NPD.[199;201] The triplet exciton diffusion length is in principle expected to be higher due to its longer lifetime. However, in efficient phosphorescent systems, where the emitter is highly diluted into a matrix material, triplet diffusion should hardly occur as the Förster and Dexter transfer lengths are only a few nm.[39;47] Here, the assumption that a measured emission profile resembles the generation profile is reasonable. However, many emitter molecules tend to aggregate (cf. Chapter 7) leading to local triplet migration also in efficient host-guest systems.

The above investigations neglect all quenching processes and, therefore, only hold for low exciton densities. Of course, the influence of quenching processes would be very interesting regarding the shape of the emission profile with increasing current density. Annihilation

processes could be included into Eq. 6.1 as additional terms, but then the equation could only be solved numerically.[12;13;148;202]

For the sake of simplicity, many authors assume an emission profile with a rectangular shape and a width w to simplify calculation of the roll-off—a simplification that will also be used in the following sections.[4] Here, w is approximated by dividing the total exciton density by the maximum exciton density, located at x_{max} (see Fig. 6.3):

$$w = \frac{\int_0^d n(x)dx}{n(x_{max})}. \tag{6.2}$$

This simplification should be handled with care as many quenching processes (such as TTA) depend quadratically on the exciton density. Hence, using a rectangular profile would overestimate the influence of these quenching processes.

[4] Note that this rectangular emission zone width is the same that has already been introduced in Eq. 3.5 to quantify the roll-off based on TTA.

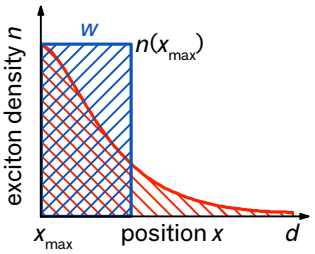

Figure 6.3: Illustration of the emission zone width w compared to an exponential emission profile. The overall exciton density is kept constant.

6.1.2 *Width of the Emission Zone*

In small molecule OLED structures, the emission zone is typically rather narrow (around 2 to 10 nm), which is ascribed to preferential electron or hole conduction in most EML materials.[13;71;98;203] In polymer OLEDs, instead, broader zones are found.[154;204]

Here, the influence of the emission zone width on the exciton density and, hence, the efficiency roll-off is studied in more detail concentrating on TTA (or TTA and TPA) as only loss mechanisms. In Figure 6.4a, the triplet exciton density n_T is calculated as a function of w for different current densities. Without any loss mechanisms, the solution of the steady-state triplet density equation[5] results in an indirect proportionality of n_T to w (dashed lines in Fig. 6.4a). When TTA is taken into account, deviations become visible (solid lines), which are, for low current densities, only observed for small emission zone widths. With increasing current density, however, TTA becomes also significant for broader emission zones. Nevertheless, the influence of TTA vanishes for $w \to \infty$. In state-of-the-art OLED stacks, where the EML is rarely broader than 20 nm and >10 mA/cm^2 are needed for high-brightness applications, w approximating the full EML width is essential to reduce losses due to exciton quenching, but experimentally not so often observed.

[5] The steady-state triplet density is given by $0 = \frac{J}{qw} - \frac{n_T}{\tau}\left(-\frac{1}{2}k_{TT}n_T^2\right)$, assuming $\tau = 1.5\,\mu s$ and $k_{TT} = 3 \times 10^{-12}\,cm^3/s$ for all calculations in this section.

The dependence of the critical current density J_0 on w is illustrated in Fig. 6.4b. Under the TTA model, J_0 is proportional to w (cf. Eq. 3.5). Taking additionally TPA into account, the dependence of J_0 on w becomes more complex.[202] Here, broadening the emission zone results in a sharper increase in J_0 for small widths compared to large ones.

Furthermore, the roll-off in EQE is calculated for different values of w between 2 and 20 nm taking TTA, or TTA and TPA into account (Figure 6.5).[6] As expected, the critical current density increases by the same factor under the TTA model from 19 to 190 mA/cm^2, and from 18 to 162 mA/cm^2 under the TTA/TPA-model. Deviations between

[6] Calculations based on the TTA model are performed according to Eq. 3.4. For the model combining TTA and TPA, SCLC theory is assumed and calculations are performed according to Ref. 13 (Eq. 12 therein); $k_P = 3 \times 10^{-13}\,cm^3/s$.

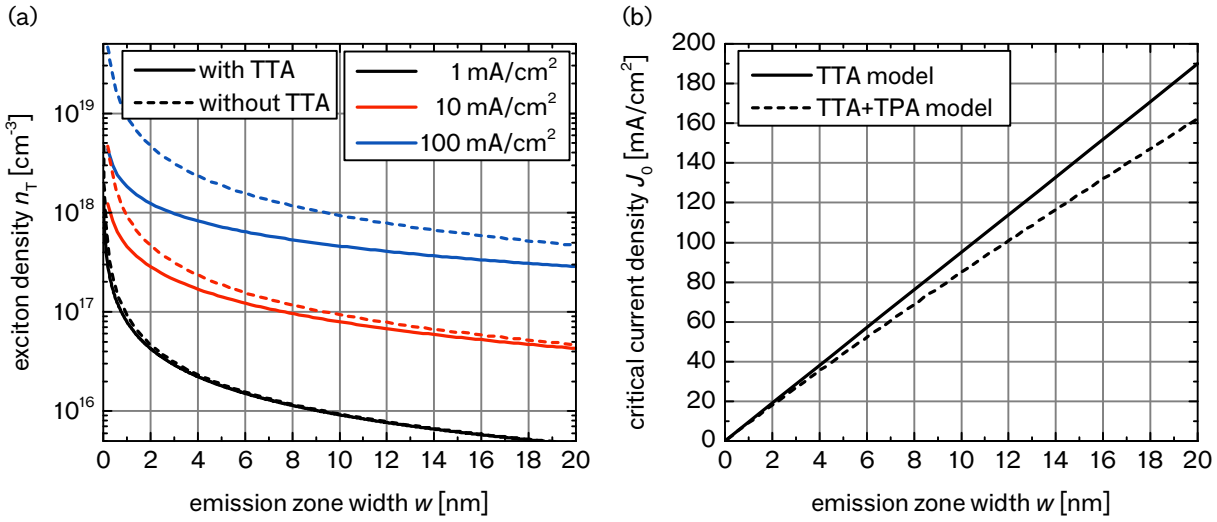

Figure 6.4: (a) Triplet exciton density n_T as a function of w for different current densities J without (dashed lines) and with (solid lines) TTA. (b) Critical current density J_0 in dependence of the emission zone width w taking TTA (solid line) or TTA and TPA (dashed line) as loss channels into account.

the two models become more apparent at high current densities as the influence of TPA increases with J (cf. Fig. 3.4).

Depending on the OLED structure, the emission zone may not stay constant over the whole current regime, but broaden with increasing current density.[148;154] To illustrate this effect on the efficiency roll-off, the change in EQE with current density is calculated for a case where the emission zone broadens with increasing current density. If an exponential broadening is assumed (cf. the blue dotted line in Fig. 6.5),[7] the EQE curve shows an s-kink at a current density of approximately $10\,\mathrm{mA/cm^2}$ for both quenching models (red lines). Such s-shaped EQE-current density curves are reported from time to time and have been mainly attributed to changes in charge balance with increasing current density.[205–208] However, according to the simulations, a broadening in the emission zone might also explain these deviations.

[7] The emission zone width increases from 2 nm at $J < 1\,\mathrm{mA/cm^2}$ to 20 nm at $J > 300\,\mathrm{mA/cm^2}$: $w(J) = 20\,\mathrm{nm} \cdot \left(1 - 0.9 \cdot \mathrm{e}^{-J/(50\ \mathrm{mA/cm^2})}\right)$.

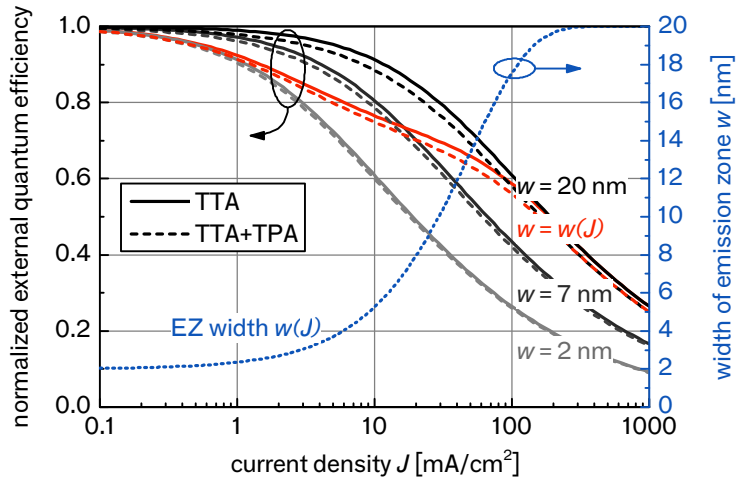

Figure 6.5: Normalized EQE vs. current density for emission zones of different width w under the TTA model (solid lines) or the combined TTA/TPA model (dashed lines). The roll-off is shifted to higher current densities for broader emission zones. The blue dotted curve represents an assumed broadening of the emission profile with increasing current density from 2 to 20 nm. For this case, the EQE vs. current density curve shows an s-kink at a current density of approximately $10\,\mathrm{mA/cm^2}$ (red lines).

6.1.3 *Dependence on the Structure of the Emission Layer*

In typical OLED structures, the EML consists of a matrix material, which is either preferentially electron or preferentially hole transporting. Therefore, the emission zone in these so-called *single EML* (S-EML) devices is located on one side of the EML and, hence, is rather thin. Figure 6.6 shows four different approaches to broaden the emission zone compared to the S-EML configuration. The introduction of *double EMLs* (D-EML) leads to a significant broadening.[157;187;209–211] Here, a preferentially electron transporting and a preferentially hole transporting matrix are both doped with the emitter material and positioned on top of each other so that the emission zone is located at the interface of both materials. In this configuration excitons are able to diffuse into both materials. Although giving a somewhat broader emission profile, D-EMLs still suffer from a relatively narrow emission zone due to the sharp interface between the matrix materials. *Mixed-EMLs* (M-EML) consisting of a single layer that comprises a mixture of a hole and an electron transporting matrix material provide a broader emission zone and, thus, improve the roll-off further.[212–214] Recently, promising roll-off and broad emission profiles have been shown for *graded EMLs* (G-EML), i.e., for EMLs where the mixing ratio between the two matrix materials is continuously adjusted from the bottom to the top of the EML by changing the evaporation rate of each material during co-evaporation.[144;215–217] One drawback of the M-EML and the G-EML concepts is that the emission profile strongly depends on the conductivity of the used materials which means that proper adjustment of HOMO and LUMO levels and of the mobilities is crucial. Furthermore, the ratio of the two materials can influence the mobility by several orders of magnitude, thus strongly affecting the overall efficiency as well as the roll-off characteristics.[72;157;158;205;206;213;218] Finally, *ambipolar matrix materials*, which provide similar mobilities for electrons and holes, have the potential to reduce roll-off while avoiding complex fabrication steps.[219–222]

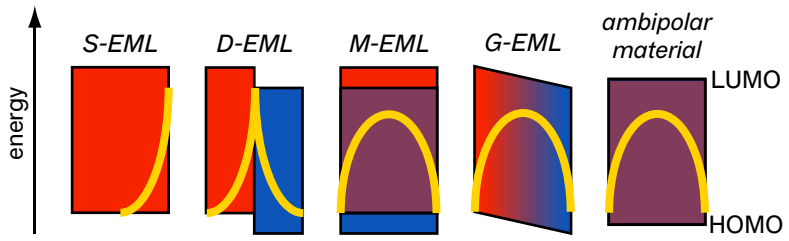

Figure 6.6: Illustration of different strategies to broaden the emission zone. Hole and electron transporting matrix materials (red and blue, respectively) are either used on their own (S-EML), put next to each other (D-EML), mixed into one another (M-EML), or mixed with a gradient profile (G-EML). Furthermore, ambipolar materials, which conduct both electrons and holes equally well, can be used. Yellow lines roughly indicate the expected emission profiles for each case.

All EML design possibilities mentioned above bear the potential to broaden the emission zone. As D-EML, M-EML, and G-EML make device fabrication more complex, the use of an ambipolar matrix material seems to be the most promising route. However, further research is required to develop ambipolar host materials with suitable energy levels, especially for blue emitters.

6.2 Measurement of the Emission Profile

6.2.1 Method

The measurement of the emission profile is of great interest not only regarding the reduction of efficiency roll-off, but also for optical modelling to improve light outcoupling. In literature, two different methods are proposed:

The first method utilizes the change in outcoupled emission upon varying the emitter position. The position of the emitting dipoles is extracted by measuring the angular resolved emission spectra of the device and fitting these spectra by means of optical simulations. This method has been well approved for polymer OLEDs, where the light-emitting polymer layer is rather thick (around 100 nm).[154;197;198;204;223] Recently, promising results were also presented for small-molecule OLEDs with thin EMLs (around 20 nm), and even for multi-color OLEDs, but the resolution still does not exceed 5 nm.[192;224]

The second method consists of a thin sensing layer that locally quenches the emission.[13;71;186;213;225–227] The amount of quenched excitons is mapped by inserting this layer at different positions inside the EML (see Figure 6.7). Although sample fabrication is more complex compared to the first method, this approach has the advantage of high spatial resolution and no need for optical simulations. Therefore, all investigations on the emission zone width in this thesis are performed by the sensing layer method.

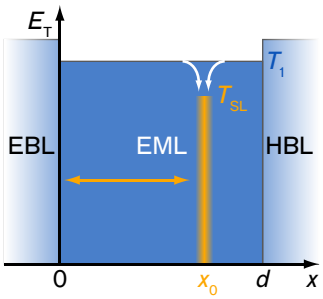

Figure 6.7: Illustration of the sensing method: A thin layer of a material with a lower triplet energy T_{SL} than the emitter is inserted at different positions x_0 inside the EML. The triplet excitons are then locally quenched by the sensor.

6.2.2 Mathematical Description

In order to evaluate the measured sensing intensities, the influence of the sensor on the exciton distribution in the emission profile is described for the case of an infinitely thin sensing layer. Lebental *et al.* discussed the aspect of the "invasiveness" of the sensing layer on charge and exciton distribution.[228] Two extreme cases may arise: A non-invasive quencher, which shows no influence on excitons and charges, but also does not quench the emission and, therefore, is not suitable as sensor. The other case is a strongly invasive quencher that quenches all excitons reaching the sensor, but might influence both the exciton distribution and the charge transport. The reality might fall somewhere in between, but its mathematical description is not straightforward. The following calculations illustrate the effect of a strongly invasive quencher on the local exciton density by splitting the solution of the diffusion equation (Eq. 6.1) into two regions, left (l) and right (r) of the sensing layer, which is positioned at x_0:

$$n(x) = \begin{cases} n_l(x) & (0 \leq x \leq x_0) \\ n_r(x) & (x_0 \leq x \leq d). \end{cases} \tag{6.3}$$

Again, reflecting boundary conditions are considered at the interface between the EML and the blockers (i.e., at $x = 0$ and $x = d$). The strongly invasive quencher assumes that all excitons at x_0 are

quenched, giving rise to two further boundary conditions: $n_1(x_0) = 0$ and $n_r(x_0) = 0$ that guarantee continuousness of $n(x)$ at x_0.

The solution of the above equation for the case of a constant and an exponential generation profile (with and without background) is given in App. B.2. Figures 6.8a and b illustrate the solution for three different sensing layer positions. The result shows that the exciton density around x_0 is strongly reduced compared to the case without sensing layer (black line). The width of the quenched intensity strongly depends on the diffusion length l. Dashed lines in Fig. 6.8a illustrate that short l lead to a more local quenching compared to long l.

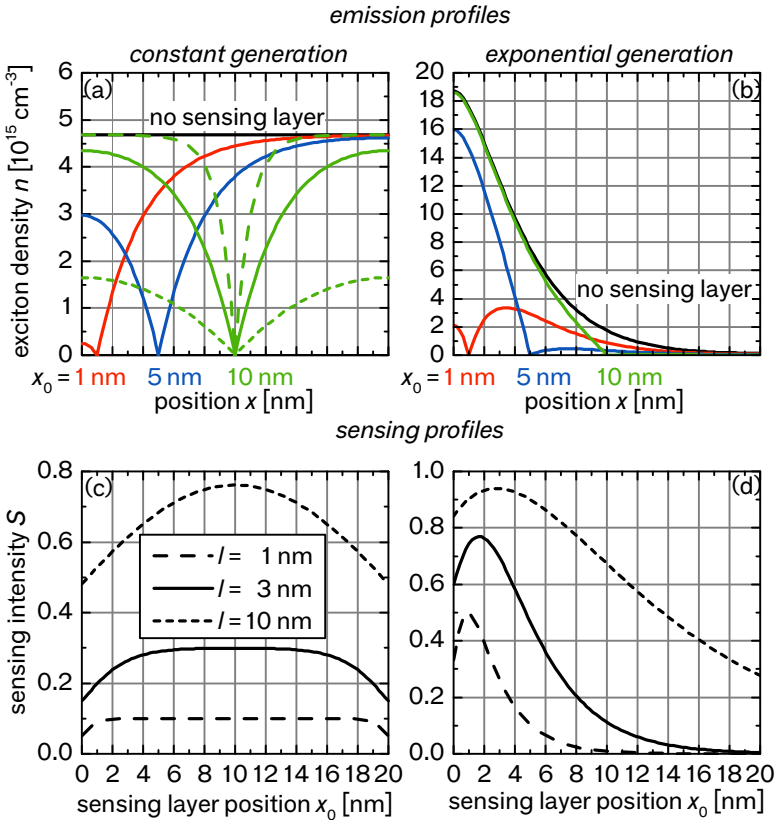

Figure 6.8: Emission profiles upon inserting a strongly invasive sensing layer at different positions x_0 assuming (a) a constant and (b) an exponential generation profile; $l = 3\,\text{nm}$, $g = 2\,\text{nm}$. A variation of the diffusion length l from 1 to 10 nm is shown exemplary with dashed lines in (a) at a sensing layer position of $x_0 = 10\,\text{nm}$ (legend in (c)). The respective sensing profiles $S(x_0)$ are plotted in (c) and (d) for different l (for equations see App. B).

In order to later extract the emission profile from the measured spectral radiant intensity of the OLEDs with varying sensing layer position, the so-called sensing profile $S(x_0)$ is introduced. This profile resembles the integral of the simulated emission profiles for all sensor positions and is calculated as follows:

$$S(x_0) = \frac{\epsilon - \epsilon_{\text{SL}}(x_0)}{\epsilon}, \tag{6.4}$$

$$\epsilon = \int_0^d n(x)dx, \qquad \epsilon_{\text{SL}}(x_0) = \int_0^{x_0} n_1(x)dx + \int_{x_0}^d n_r(x)dx. \tag{6.5}$$

Here, ϵ and ϵ_{SL} denote the integrated emission profiles with and without sensing layer (SL), respectively (see App. B.3).

Figures 6.8c and d show the calculated sensing profiles for different diffusion lengths. Compared to the emission profiles, the sensing profiles decrease at both interfaces because the amount of quenchable excitons decreases with increasing proximity of the sensing layer to the blockers. The exponential generation profile hence leads to a local maximum some nanometers apart from the blocker. A long diffusion length increases this behavior leading to a more roundly shaped sensing profile, where the maximum is shifted to the center of the EML. Furthermore, the absolute intensity of S is higher for long diffusion lengths than for short ones because more excitons reach the quencher.

In experiment, often an exponential generation profile with a constant background is found, which besides the diffusion length furthermore contains the parameters g and B. B denotes the ratio of the background intensity to the number of excitons that are formed in the exponential profile and is 1 for very high background (resembling a constant profile) and 0 for negligible background (resembling a purely exponential profile). Figure. 6.9 shows the influence of g and B on the sensing profile. An increase of the generation width g leads to a decreased maximum that is shifted more to the center of the EML. Furthermore, a broad generation width leads to a slightly stronger decrease of the intensity close to the blockers. Increasing background intensity changes the ratio between the maximum and the background.

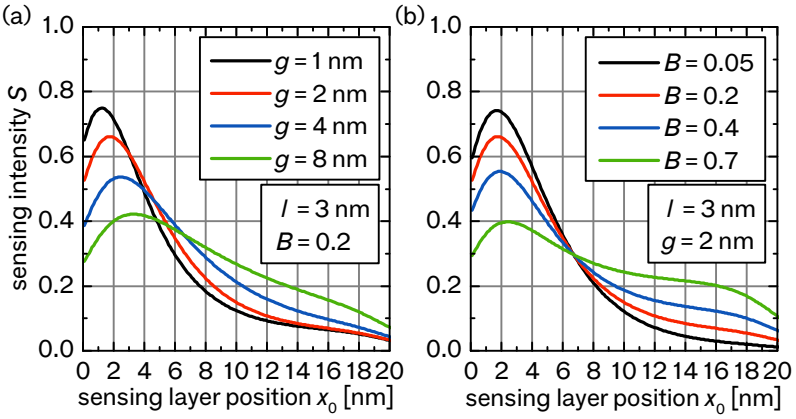

Figure 6.9: Sensing intensity $S(x_0)$, calculated by Eq. B.10 for an exponential generation profile with background upon varying (a) the generation width g, and (b) the background intensity B.

Despite the only marginally different influence of g and l on the emission profile (cf. Fig. 6.2b), the influence on the sensing profile is very different: while the maximum intensity increases with increasing l, it decreases with increasing g; B instead mainly influences the ratio between maximum and background. Therefore, extraction of the three parameters from fitting of experimental data should be possible.

The above investigations are restricted to the limiting case of a strongly invasive quencher. In reality, the efficiency of the sensing layer depends on the thickness and doping concentration of the quencher. Furthermore, the chosen material and applied current density matter. All these properties could be included into the mathe-

matical description by attributing the sensing layer a certain capture efficiency.[200;228] However, this efficiency is hardly accessible in experiment and is, therefore, out of the scope of this thesis. Note that the capture efficiency of the sensing layer is different from the capture length, which describes the radius within which excitons are quenched. The above investigations are performed assuming a capture length of 0 nm meaning that only excitons which actually diffuse to the sensing layer are quenched and that the sensor cannot "actively" attract excitons.

6.2.3 *Experimental Realization and Evaluation*

In order to yield reliable results, the sensing layer has to fulfill different requirements: (i) it must not influence the electrical properties of the device, (ii) triplet excitons should be efficiently quenched, (iii) the capture length has to be small in order to achieve high spatial resolution, and (iv) the influence of microcavity effects should be excluded.

(i) In order to avoid influence of the sensing layer on charge transport, very thin layer thicknesses below 1 nm are chosen, which do not form a closed layer. Still, the influence of the sensor on current transport should be checked for each experiment individually by comparing the JV-curves of samples with and without quencher.

(ii) Efficient triplet quenching can be achieved by using a quencher with a sufficiently lower triplet energy than that of the emitter. Both, a fluorescent and a phosphorescent sensing layer are practicable. A fluorescent quencher has the advantage of omitting additional emission, which simplifies the extraction of the quenched emission from the measured spectral radiant intensity. However, the triplet lifetimes of fluorescent materials are typically in the range of milliseconds leading to very high triplet densities on the quencher. As the sensing layer should be very thin, saturation of the quenching molecules may then already occur at low current densities.

(iii) To guarantee a small capture length, the sensing layer method is only applied to phosphorescent emitter systems, where the triplet energy is mainly exchanged via Dexter transfer. The interaction distance is in the range of 1 nm giving rise for small capture lengths of the sensing layer and, therefore, high spatial resolution.[45]

(iv) In order to minimize different outcoupling between the samples, the thickness of the transport layers should be designed such that a similar outcoupling efficiency for all quencher positions is ensured. Alternatively, this influence may also be taken into account by weighing the measured emission intensity with respectively modelled spectra for each sensing layer position.[228]

In experiment, the exciton densities are not directly accessible. Instead, the spectral radiant intensity of samples with and without sensing layer is measured. For illustration, Fig. 6.10a shows the spectrum of an OLED with and without sensor in forward direction, where $Ir(ppy)_2(acac)$ is used as emitter and $Ir(MDQ)_2(acac)$ as sensor.[8]

[8] For the device structure see Fig. 6.11. The sensing layer is positioned at $x_0 = 14$ nm.

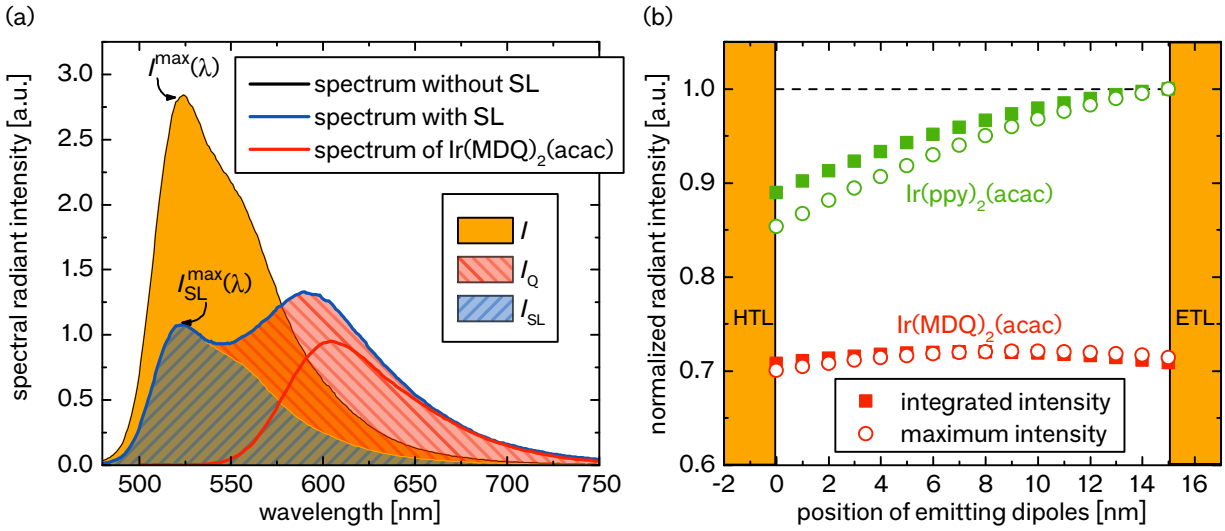

Figure 6.10: (a) Illustration of the derivation of the sensing profile. As an example, the spectral radiant intensity of an OLED with and without sensing layer (SL) is shown together with the simulated EL spectrum of Ir(MDQ)$_2$(acac) in forward direction. Different colors indicate the intensity I of the reference, the intensity I_{SL} of all excitons that are not quenched, and the intensity I_Q of the quenched intensity. (b) Simulated radiant intensity at 0° of the same layer stack assuming Ir(ppy)$_2$(acac) or Ir(MDQ)$_2$(acac) as emitter as a function of the position of the emitting dipoles. Values of the integrated intensity are normalized to the maximum of the green stack, whereas the curves of the maximum intensities are normalized to the respective maxima of the integrated intensity for red and green individually.

In the sensing layer sample, the green emission from Ir(ppy)$_2$(acac) is strongly reduced compared to the reference device and red emission from the Ir(MDQ)$_2$(acac) sensor appears. The sensing profile may now be derived from

$$S(x_0) = \frac{I - I_{SL}(x_0)}{I}, \tag{6.6}$$

where I is the intensity of the reference sample, and $I_{SL}(x_0)$ is the signal from the excitons in the sensing layer device that are not quenched. Note that the radiant intensities I and $I_{SL}(x_0)$ are directly proportional to the exciton densities ϵ and $\epsilon_{SL}(x_0)$, respectively (cf. Eq. 6.5), if constant outcoupling efficiency for all samples is ensured. Instead of $I - I_{SL}(x_0)$, the light $I_Q(x_0)$ that is emitted from the sensor may be measured. However, as shown in the following paragraph, different outcoupling between the light from the emitter and the light from the sensor can falsify the results. Furthermore, the calculation of $I_{SL}(x_0)$ and $I_Q(x_0)$ takes much effort as the reference spectrum has to be scaled for every single spectrum in order to calculate the integrals. For simplification, the intensity at a fixed wavelength, e.g. the maximum $I^{max}(\lambda) - I_{SL}^{max}(\lambda)$, may also be chosen. Here, care must be taken that the quencher does not radiate at the same wavelength as the emitter. In this case, using Ir(MDQ)$_2$(acac) as sensor, no emission from the sensing layer is observed at the maximum of the green emitters (cf. the simulated EL spectrum of the same sample using Ir(MDQ)$_2$(acac) as emitter that is also depicted in Fig. 6.10a).

Both methods using integrated and maximum intensities require a constant shape of the emitter spectrum for all sensing layer positions. As an example for the influence of different outcoupling, Fig. 6.10b shows the simulated radiant intensity in forward direction of the reference OLED using either Ir(ppy)$_2$(acac) or Ir(MDQ)$_2$(acac) as emitter for different positions of the emitting dipoles.[9] Closed symbols show the integrated spectral radiant intensity, normalized to the maximum value. As the OLED microcavity is optimized for the green emitter,

[9] Simulations using a transfer-matrix model[68] were performed by Cornelius Fuchs (TU Dresden).

the intensity of the samples with $Ir(MDQ)_2(acac)$ is strongly reduced. Here, $I_Q(x_0)$ would indeed differ from $I - I_{SL}(x_0)$ and should not be taken for extraction of the sensing profile. However, the intensity of the red samples is much more uniform over the entire EML than the intensity of the green samples, which decreases by 10% when shifting the emitter position from the HBL to the EBL side of the EML. This shift may directly influence the extracted sensing profile. Measuring the maximum values of the spectra instead of the integrated intensity, a slight difference is observed. Nevertheless, the comparison of the spectral radiant intensities at a fixed wavelength seems to be sufficiently accurate compared to other uncertainties of the sensing layer method. The above considerations are made for spectra measured in forward direction and only hold if the angular dependency of all samples is similar. Generally, the spectra should be integrated over all angles or measured in an Ulbricht sphere.

6.3 *Ambipolar Matrix Materials*

In this section, the sensing layer method is applied to an OLED with an ambipolar matrix material in order to (i) prove the experimental functionality of the extraction of the shape and width of the emission zone via this method and to (ii) verify whether ambipolar matrix materials can help in broadening the emission zone. The most prominent ambipolar material is probably CBP, which offers hole and electron mobilities of $2 \times 10^{-3}\,cm^2/(V\,s)$ and $3 \times 10^{-4}\,cm^2/(V\,s)$, respectively.[187] Wang *et al.* reported very high EQE and low roll-off for devices based on an EML with an ambipolar CBP matrix and the green emitter $Ir(ppy)_2(acac)$: An EQE of up to 22% was achieved at $10\,000\,cd/m^2$ and the critical current density was as high as $J_{90\%} \approx 15\,mA/cm^2$.[75,229] The low roll-off of the device suggests that the emission zone may be relatively broad. In the following, this stack is reproduced and taken as an example for ambipolar matrix materials, and a closer investigation on the shape and width of the emission profile is performed.[10]

[10] A minor part of this section is published in Ref. 98. Reprinted with permission. Copyright 2012, AIP.

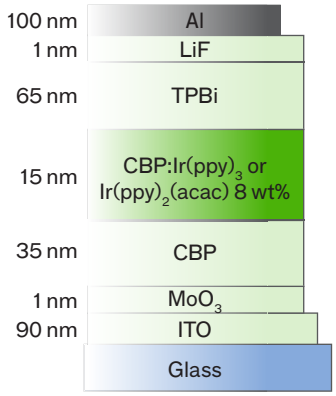

Figure 6.11: Structure of green OLEDs with the ambipolar matrix material CBP and the emitters $Ir(ppy)_2(acac)$ or $Ir(ppy)_3$.

6.3.1 *Device Performance*

Figure 6.11 shows the structure of the investigated OLEDs. In contrast to other samples in this thesis, intrinsic transport layers are used here. Hence, blocking layers are not necessary. Efficient injection into the transport materials from the contacts is ensured by using thin injection layers (MoO_3 and LiF, respectively). The EML consists of 15 nm CBP doped with 8 wt% of either $Ir(ppy)_2(acac)$ or $Ir(ppy)_3$. The two materials differ in their molecular orientation[98] as well as in their ability to form aggregates[142] (cf. Chapter 7.2).

The current density-voltage characteristics are shown in Fig. 6.12a. Similar behavior is observed for both devices, which leads to the conclusion that both emitters have a similar influence on the current transport. Compared to OLEDs with doped transport layers, the

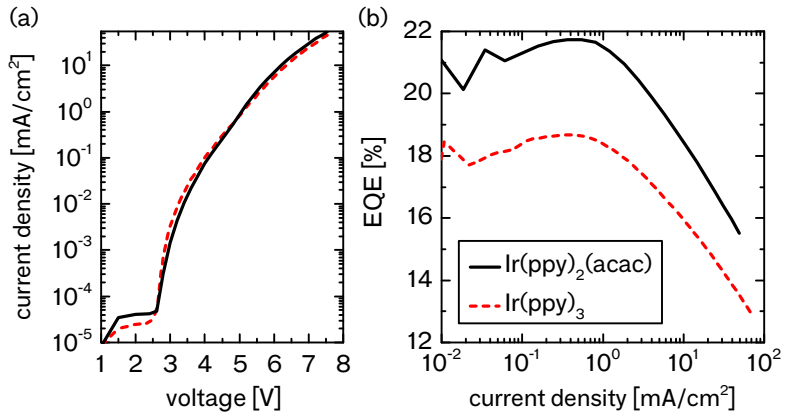

Figure 6.12: (a) Current density-voltage characteristics and (b) EQE as functions of the current density for the OLEDs from Fig. 6.11.

intrinsic transport layers lead to flatter JV-curves. Furthermore, the very low HOMO energy of CBP (−6.0 eV) represents a significant barrier to hole injection and increases the operation voltage of these devices.[121] Nevertheless, a very high EQE is achieved with 21.4 % and 18.1 % at 1000 cd/m^2 for Ir(ppy)$_2$(acac) and Ir(ppy)$_3$, respectively (see Fig. 6.12b). The higher EQE for Ir(ppy)$_2$(acac) is related to the preferential horizontal dipole orientation of this molecule.[98]

6.3.2 *Influence of the Sensing Layer*

In order to measure the emission profile, a 0.5 nm thin sensing layer is inserted at different positions within the emissive layer consisting of 10 wt% Ir(MDQ)$_2$(acac) doped into CBP (see Fig. 6.13). The red emitter Ir(MDQ)$_2$(acac) has a lower triplet energy level than both green emitters and, thus, should efficiently quench the emission. The samples are produced in two different runs, one for Ir(ppy)$_2$(acac) and one for Ir(ppy)$_3$. The sensing layer is inserted at 12 different positions x_0. For an absolute comparison and for calculating the sensing profile, samples without sensor are produced in the same run. Therefore, a high comparability between samples without and with sensing layer at different positions is achieved.

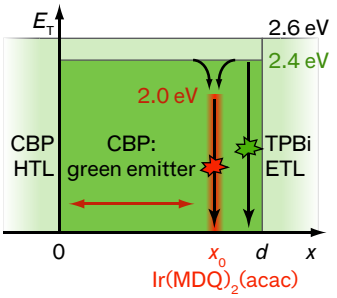

Figure 6.13: Application of the sensing method to the OLED structure in Fig. 6.11: The red-emitting sensor Ir(MDQ)$_2$(acac) is inserted at different positions x_0 inside the EML. It provides a lower triplet energy level than both green emitters and, thus, efficiently quenches excitons.

Figure 6.14 shows the electrical performance of devices with and without sensing layer. In contrast to the measurement in Fig. 6.12a, the current density using Ir(ppy)$_3$ as emitter is here lower compared to the Ir(ppy)$_2$(acac) devices, which is due to typical run-to-run variations of about 10 %. For both emitters, a marginally lower current density is observed when the sensing layer is positioned close to the ETL side or in the center of the EML. This suggests that electrons may be trapped by Ir(MDQ)$_2$(acac), which has already been observed in similar systems using TPBi as HBL and Ir(MDQ)$_2$(acac) as emitter and is related to similar LUMO energies.[71] Hole transport, on the other hand, is not influenced, which is proven by the constant JV-curves when inserting the sensing layer close to the HTL.

The influence of the sensing layer on the emitted spectrum is illustrated in Fig. 6.15 for the case of Ir(ppy)$_2$(acac) as emitter at different

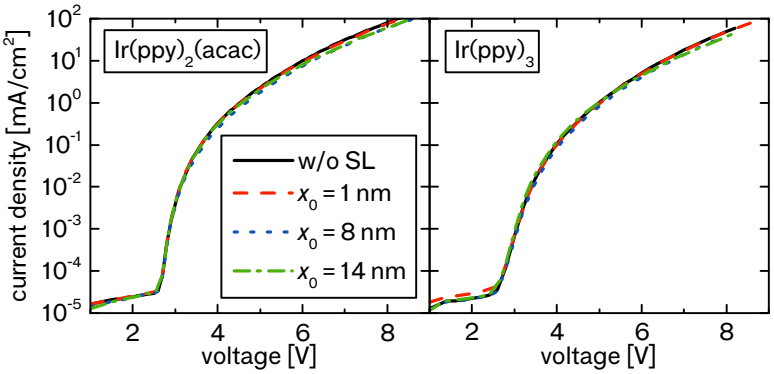

Figure 6.14: Current density as a function of the voltage for selected devices with and without sensing layer (SL) for the emitters $Ir(ppy)_2(acac)$ and $Ir(ppy)_3$.

applied current densities. Strong quenching of the green emission and concurrent emission from the red $Ir(MDQ)_2(acac)$ sensor is observed when the sensing layer is positioned close to the ETL. With increasing current density, the quenched amount slightly decreases, which could be due to a shift in the emission zone. Saturation of the sensor is excluded as the number of $Ir(MDQ)_2(acac)$ sites is approximately one order of magnitude higher than the total exciton density within the EML even at the highest applied current density.[11] If the sensing layer is positioned close to the HTL, the amount of quenched excitons increases with increasing current density. At low current density ($\leq 1.5\,mA/cm^2$), however, no quenching is observed for $x_0 < 5\,nm$. This gives further evidence that hole trapping by the sensing layer is not present in these devices. The above observations hold for both $Ir(ppy)_2(acac)$ and $Ir(ppy)_3$ and prove that $Ir(MDQ)_2(acac)$ efficiently quenches the local green emission.

In the following, the influence of a change in light outcoupling is studied by integrating over the whole measured spectrum for each sensing layer position. In theory, constant radiant intensity of all samples is achieved if the following two prerequisites are fulfilled: (i) the sensor converts 100 % of the quenched excitons into photons and (ii) the light emitted from the sensor underlies a similar outcoupling efficiency as the emitter. Figure 6.16 shows the integrated spectra of

[11] The density of $Ir(MDQ)_2(acac)$ molecules is $n_G = 6.5 \times 10^{19}\,cm^{-3}$ (cf. Eq. 4.2); concerning the sensor thickness $d_{SL} = 0.5\,nm$, then $n_G \cdot d_{SL} = 3.3 \times 10^{12}\,cm^{-2}$; the density of generated excitons at $46\,mA/cm^2$ is roughly $\epsilon = \tau \cdot k_{Gen} = 4.4 \times 10^{11}\,cm^{-2}$.

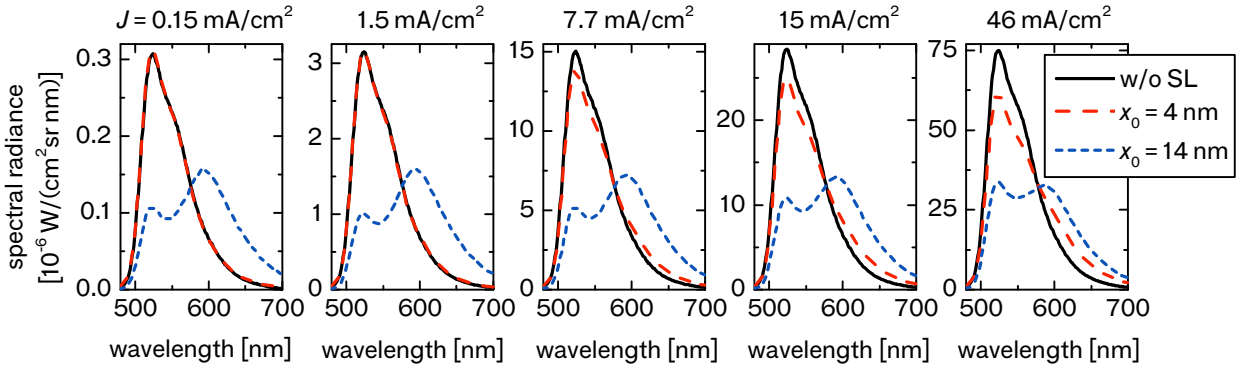

Figure 6.15: Spectra of exemplary samples with and without sensing layer (SL) at different applied current densities using $Ir(ppy)_2(acac)$ as emitter.

all measured samples using $Ir(ppy)_2(acac)$ as emitter at three different current densities. For each sensing layer position two pixels on the same sample are measured. The data are normalized to samples without sensor, which are plotted at $x_0 = 0\,\text{nm}$. At $1.5\,\text{mA/cm}^2$, a slight increase of intensity is observed when the sensing layer is positioned close to the HTL, which originates from increased green emission. This additional intensity vanishes with increasing current density when quenching sets in. For all current densities, a clear decrease of the radiant intensity by up to 20 % is observed when the sensing layer is positioned close to the ETL. This is related to the strong quenching of the green emission and concurrent red emission from the sensor at this EML side. As the outcoupling efficiency of the red emission is significantly weaker compared to that of the green emission (cf. Fig. 6.10b) the overall outcoupling efficiency decreases with increasing quenching intensity.

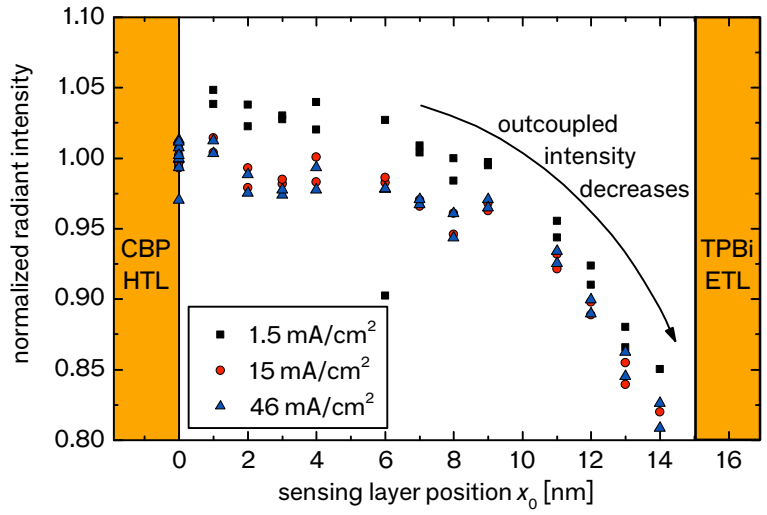

Figure 6.16: Radiant intensity at different applied current densities obtained by integrating over the measured spectra for different sensing layer positions x_0, normalized to the intensity of samples without sensor (plotted at $x_0 = 0\,\text{nm}$) using $Ir(ppy)_2(acac)$ as emitter.

Concluding, CBP:$Ir(MDQ)_2(acac)$ is a suitable sensor for this OLED material structure, which efficiently and locally quenches the excitons, while barely influencing the electrical properties. In order to neglect the outcoupling effects in the following investigations, the reduction of the green emission is measured rather than the concurrent sensor emission.

6.3.3 *Emission Profile*

To derive the emission profiles, the absolute radiance $I_{\text{SL}}^{\text{max}}(x_0)$ and I^{max} of each sample with and without sensing layer, respectively, is measured at the maximum of the green emission, where $\lambda_{\text{max}} = 524\,\text{nm}$ in the case of $Ir(ppy)_2(acac)$ and $\lambda_{\text{max}} = 515\,\text{nm}$ for $Ir(ppy)_3$. The sensing profile is then calculated as discussed previously from Eq. 6.6. To calculate I^{max}, the mean value of eight measured samples is taken. Figure 6.17 shows the sensing profiles for both OLED stacks

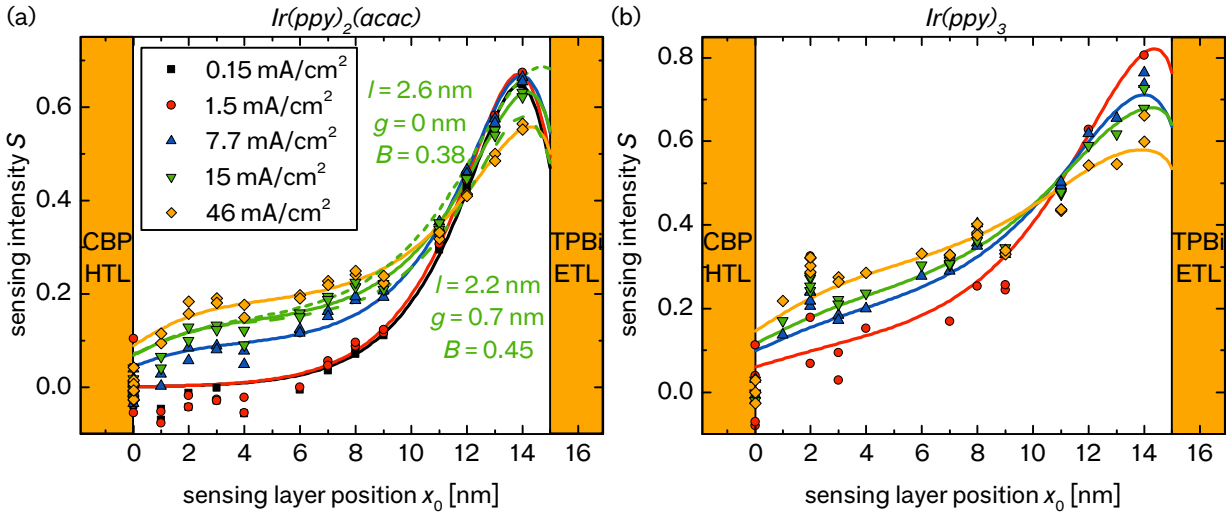

Figure 6.17: Measured sensing profiles for (a) $Ir(ppy)_2(acac)$ and (b) $Ir(ppy)_3$ at different applied current densities (points), and fits according to Eq. B.10 (lines). Fit parameters are given in Table 6.1. Dashed lines exemplary show the error margins for the fit at $15\,mA/cm^2$.

containing either $Ir(ppy)_2(acac)$ or $Ir(ppy)_3$ at different applied current densities. Data points at $x_0 = 0\,nm$ correspond to samples without sensing layer. Both emitters show a similar profile: the emission zone is mainly located at the CBP/TPBi-interface suggesting that hole transport through the EML is favored compared to electrons, which is reasonable considering the by one order of magnitude different mobilities.[187] Furthermore, depending on the current density, a constant background is observed. The $Ir(ppy)_3$ samples show high leakage currents and many flickering pixels, which resulted in stronger scattering of the radiance. Hence, higher deviations between the data points are observed.

In order to characterize the profiles in more detail, they are fitted according to Eq. B.10 and to the derivation given in Sec. 6.2.2 with an exponential profile that contains a constant background. The fit parameters are given in Table 6.1 along with their fit errors. As an example for the derived errors, dashed lines in Fig. 6.17a show the margins for the fit at $15\,mA/cm^2$. Deviations are already observed for sub-nanometer changes of the fit parameters and are especially visible in the exponential part of the profile. The error increases with increasing background and decreasing generation width g, because a g below 1 nm only significantly influences the shape of the curve between its maximum and the ETL, where no measured data are available. However, very accurate fitting is possible due to the already discussed different influence of l and g on the height of the maximum (cf. Figs. 6.8d and 6.9a).

The diffusion length l is higher for $Ir(ppy)_3$ (3.2–3.5 nm) compared to $Ir(ppy)_2(acac)$ (1.6–2.5 nm), which could be due to the stronger molecular aggregation of $Ir(ppy)_3$ that opens a channel for exciton diffusion not only on the host but also on the guest molecules.[142] The relatively small diffusion length could be explained with an exciton generation directly on the emitter molecules. Neglecting

J [mA/cm^2]	$Ir(ppy)_2(acac)$ l [nm]	g [nm]	B	$Ir(ppy)_3$ l [nm]	g [nm]	B
0.15	1.55 ± 0.10	1.75 ± 0.20	0.02 ± 0.02	–	–	–
1.5	1.65 ± 0.10	1.7 ± 0.2	0.02 ± 0.02	3.2 ± 0.5	0.3 ± 1.0	0.21 ± 0.09
7.7	2.20 ± 0.20	0.9 ± 0.3	0.29 ± 0.06	3.4 ± 0.3	0.5 ± 0.5	0.37 ± 0.13
15	2.40 ± 0.20	0.5 ± 0.5	0.42 ± 0.06	3.5 ± 0.4	0.2 ± 0.5	0.43 ± 0.10
46	2.45 ± 0.30	0.3 ± 0.5	0.54 ± 0.06	3.5 ± 0.5	0.2 ± 0.5	0.58 ± 0.11

Table 6.1: Extracted parameters l, g, and B from fits of Eq. B.10 to the data displayed in Fig. 6.17.

aggregation, the distance between two $Ir(ppy)_3$ molecules in the investigated host-guest system can be calculated to roughly 2.5 nm assuming cubic closed packing. This is higher than the Förster or Dexter transfer length on $Ir(ppy)_3$ so that exciton migration is improbable.[39;47] The same behavior is also expected for the structurally similar $Ir(ppy)_2(acac)$.

Overall, l increases for both emitters with increasing current density, which is contrary to the expectation: The neglection of annihilation processes should lead to decreasing diffusion length with increasing current density.[199] However, Wünsche *et al.* also observed an increase in the 4P-NPD triplet diffusion length with increasing current density and suggested that it could be related to the increase in charge carrier mobility with increasing current density.[200]

The width of the exponential generation zone g decreases with increasing current density. For $Ir(ppy)_2(acac)$, no background is observed at current densities below 1.5 mA/cm^2. Instead, a slightly negative sensing intensity is measured, which is related to the increased radiance of these samples when containing a sensing layer compared to the reference devices as observed in Fig. 6.16. With increasing current density, the background intensity strongly increases so that at 46 mA/cm^2, more than 50 % of the excitons are created homogeneously throughout the EML and not within the exponential profile.

Figure 6.18 shows the energy level diagram of the OLED. As discussed earlier, the preferential hole transport of CBP leads to exciton formation at the TPBi interface. Yun *et al.* found that holes are efficiently trapped by the emitters $Ir(ppy)_2(acac)$ and $Ir(ppy)_3$ in CBP due to the big difference in HOMO energy levels between host and guest.[72;230] For $Ir(ppy)_3$, having the highest HOMO energy, the observed effect was slightly stronger compared to $Ir(ppy)_2(acac)$. Electron transport, however, remained unaffected by the emitter. This hints at a possible explanation for the increased background at high current density: because electrons are hardly injected into the EML at low voltages, excitons are only formed at the EML/TPBi interface. With increasing voltage, however, electron injection and transport on CBP or the emitter, respectively, are facilitated. Finally, the electrons recombine with the trapped holes leading to the observed constant background, which is slightly higher in the case of $Ir(ppy)_3$, where stronger hole trapping is expected. An explanation for the decreasing

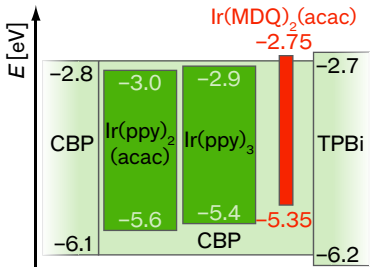

Figure 6.18: HOMO and LUMO energy levels of the OLED structure in Fig. 6.11.

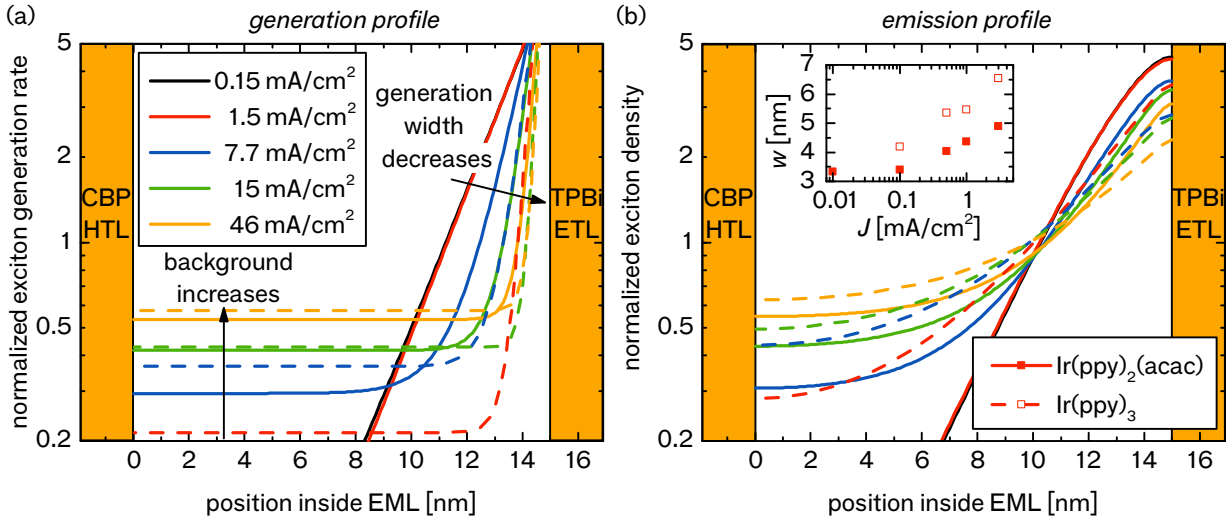

Figure 6.19: Calculated (a) generation and (b) emission profiles for $Ir(ppy)_2(acac)$ (solid lines) and $Ir(ppy)_3$ (dashed lines) extracted from the sensing profiles in Fig. 6.17 normalized to the total generation rate k_{Gen} (i.e. the applied current density). Note that a logarithmic scale has been chosen in order to distinguish more clearly between the individual curves. Inset in (b): emission zone width w as a function of the current density for $Ir(ppy)_2(acac)$ (■) and $Ir(ppy)_3$ (□).

generation width g with increasing current density, however, remains elusive from this energy level point of view.

Now, the generation and emission profiles of the OLEDs may be calculated from the extracted fit parameters. Figure 6.19 shows the respective results, derived from Eqs. B.1d and B.5c. For both emitters, the generation width decreases with increasing current density, while the background increases. For $Ir(ppy)_3$, both behaviors are more pronounced than for $Ir(ppy)_2(acac)$. As a result, the emission profiles of $Ir(ppy)_3$ are flatter leading to a broader emission zone.

To quantify the different influence of the two emitters, the simplified emission zone width w is calculated according to Eq. 6.2 and plotted in the inset of Fig. 6.19b: the width ranges from 3 to 7 nm. Furthermore, w broadens with increasing current density and is slightly higher for $Ir(ppy)_3$ compared to $Ir(ppy)_2(acac)$.

In contrast to literature,[124;231–233] where the exciton formation zone in CBP is often assumed to be centered and relatively broad due to the ambipolar conduction properties of CBP, a narrow emission zone close to the ETL is found here. However, the estimated w fits well to the study of Giebink *et al.*, who calculated the width of the emission zone in a CBP:$Ir(ppy)_3$ OLED to 3–12 nm, also increasing with increasing current density.[148] Furthermore, Adachi *et al.* showed that the exciton formation zone in CBP:$Ir(ppy)_3$-based OLEDs depends on the barriers which the charge carriers have to overcome by varying the transport materials adjacent to the EML.[186]

Deviations to literature results may arise from two important simplifications that have been made in order to extract the emission profile: First, TTA has been neglected in the fitting routine, and second, a strongly invasive sensor has been assumed that quenches all arriving excitons, yet does not actively capture them. Disregarding TTA can lead to an underestimation of l. In fact, a higher l of 6.8 nm has been proposed in literature for the same system[12] also neglecting

[12] CBP:$Ir(ppy)_3$; the current density at which the measurement was conducted is not given.

annihilation processes.[234] However, the authors assumed a delta-shaped generation zone, which is contrary to the observations here and possibly enables an overestimation of their value. Furthermore, exciton diffusion strongly depends on whether excitons are formed on the matrix or on the emitter. Here, exciton generation on the emitter is probable, giving rise to very short diffusion lengths. However, the formation process is influenced by the energy levels of the materials adjacent to the EML and, hence, cannot directly be compared to the above-mentioned literature results. In addition, the parameters extracted here should at least be independent of TTA at low current densities. The second assumption could be verified in further experiments by varying the doping concentration of the sensor. However, sensing intensities of up to 80 % are measured using only 10 wt % sensor concentration giving rise to very high quenching efficiencies. Further studies on the exact mechanism go beyond the scope of the investigations here.

In conclusion, the developed sensing layer method shows a very high accuracy enabling sub-nanometer extraction of the diffusion length and of the shape and width of the emission profile. Furthermore, evidence has been given that ambipolar matrix materials do not generally help in broadening the emission zone width. The shape and width of the emission profile not only depends on the chosen material system, which influences charge transport and exciton diffusion, but also on the applied current density.

6.4 Double- and Mixed Emission Layers

The previous section showed that ambipolar matrix materials do not generally help in broadening the emission zone. In Sec. 6.1.3 and Figure 6.6, double- and mixed emission layers (D-EML and M-EML, respectively) have been introduced, which also might broaden the EML. For both structures high efficiencies and low roll-off have been proposed in literature.[157;187;209;212–214] In this section, these structures shall be compared regarding their width of the emission zone and their roll-off behavior.

The investigated OLED layer stack is presented in Fig. 6.20. The EML consists of the two matrix materials TAPC and SPPO1, which transport holes and electrons, respectively, and are either positioned next to each other (D-EML) or mixed into one another (M-EML). In the M-EML device, the doping ratio $x : y$ of TAPC : SPPO1 is varied in order to balance the hole and electron mobility. As emitter, the blue phosphorescent FIr6 is used, which is doped with 20 wt % into the matrix. The layout is chosen according to preliminary studies on this stack that already proposed different emission layer widths between D-EML and M-EML.[235]

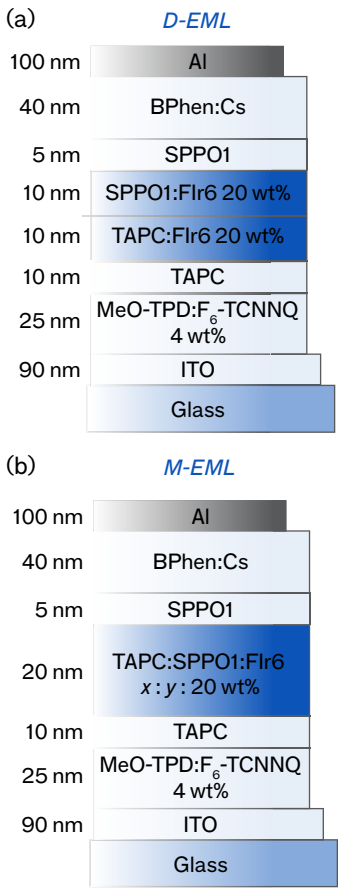

Figure 6.20: Structure of the investigated OLEDs: (a) D-EML and (b) M-EML device. For M-EML, the ratio of the two matrix materials $x : y$ is varied.

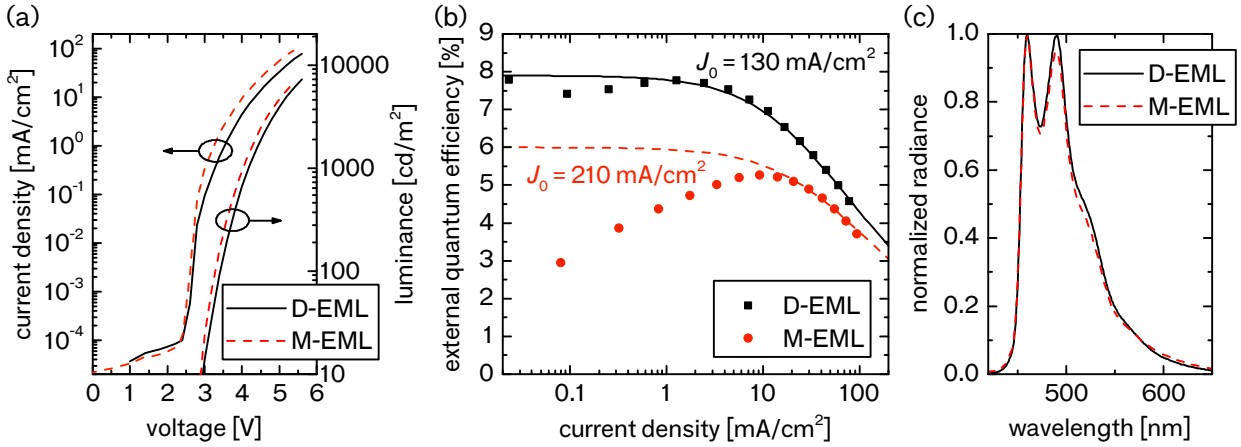

Figure 6.21: Performance of OLEDs containing either D-EML or M-EML (cf. Fig. 6.20). (a) Current density (left) and luminance (right) vs. voltage. (b) Measured external quantum efficiency (dots) and fits according to Eq. 3.4 (lines). (c) Normalized spectral radiance at 15.4 mA/cm^2.

6.4.1 *Emission Profile*

First, the D-EML is compared to the M-EML, where $x : y$ is 1 : 1. Figure 6.21 shows the performance of the two devices. The current density through the M-EML device is enhanced by roughly a factor of two compared to the D-EML. This behavior has been observed in many materials, both in literature[212;216] and in further own experiments (see App. C.3), and is related to reduced energy barriers for one type of charge carrier. As will be shown later, holes and electrons are not injected uniformly into the M-EML so that exciton formation takes place at the interface to the blocker and transport on one of the two matrix materials is negligible. This behavior also leads to a slightly higher luminance in the M-EML at a constant voltage compared to the D-EML.

The external quantum efficiency of both EML structures is shown in Fig. 6.21b.[13] The D-EML device shows an overall improved efficiency with a maximum of 7.8 % compared to the M-EML, which only reaches 5.3 % at maximum. Here, a strong initial increase of the efficiency up to a current density of 9 mA/cm^2 is observed, which can be attributed to a high charge carrier imbalance at low voltages. The EQE is fitted in the high current regime using Eq. 3.4 in order to extract the critical current density. For the D-EML, $J_0 = 130\,\mathrm{mA/cm^2}$ is obtained, whereas this value is strongly enhanced to $J_0 = 210\,\mathrm{mA/cm^2}$ in the M-EML device. For these samples, the fit can only be treated as a rough approximation because the high charge carrier imbalance at small voltages impedes exact fitting. Furthermore, it is unknown whether charge imbalance might also play a role at high voltages and, lastly, other processes like TPA that might also contribute to the roll-off are neglected. However, enhanced J_0 in M-EML compared to D-EML has also been observed by Erickson *et al.* using Ir(ppy)$_3$ as emitter and TCTA and BPhen as matrix materials and was appointed to an increased emission zone width.[227]

[13] All EQE values throughout this section are calculated assuming Lambertian angular characteristics. This is valid as long as the roll-off characteristics are compared. Furthermore, the angular dependency of the emission should stay relatively constant for all investigated samples, because only the position of the emission zone is shifted between the different samples, while the overall cavity length is kept constant.

Figure 6.21c shows spectra of the two samples. They differ slightly for the M-EML shows a minimally narrower spectrum compared to the D-EML. This suggests that the location of the emission zone in the M-EML is shifted towards the metal cathode where smaller distances strengthen the outcoupling of the blue light.

In the following, the position and width of the emission zone of both EML structures shall be compared. Therefore, the sensing layer method is applied to both sample structures. The sensor again consists of a 0.5 nm thick layer of 10 wt % $Ir(MDQ)_2(acac)$-doped host, where the host is the respective matrix material (either TAPC, SPPO1, or TAPC:SPPO1). Due to restrictions in the production process, the samples are produced in three different runs. One run contains 16 different sensing layer positions for the M-EML. Here, the samples from Fig. 6.21 are chosen as reference, because the sensing layer run does not contain any reference samples without sensor. For the D-EML, two runs are produced, in which the sensor is shifted through one of the two matrix materials at eight different positions. These two runs furthermore contain each eight reference samples without sensor. However, the performance of all D-EML and M-EML samples show strong run-to-run variations (for more details see App. C.1). The lack of reference devices for the M-EML samples may lead to wrong absolute sensing intensities $S(x_0)$. Therefore, the measured data will only be discussed qualitatively and the developed fitting routine will not be applied. Finally, the sensor slightly influences the current transport in the M-EML, where decreased current density is observed if the sensor is positioned close to the HBL (see App. C.2).

Figure 6.22 shows the measured sensing profiles of the M-EML and D-EML devices at three different current densities. The M-EML shows a relatively homogeneous distribution of the sensing intensity. The highest intensity is observed close to the SPPO1 HBL. This leads to the conclusion that a 1 : 1 mixture of TAPC and SPPO1 favors hole transport, which is reasonable because the hole mobility of TAPC is 200 times higher than the electron mobility of SPPO1.[14] With increasing current density, the profile becomes flatter due to enhanced electron transport through the M-EML.

In the D-EML, exciton formation takes place near the interface between the two matrix materials TAPC and SPPO1. However, different profiles are observed within the two materials: In TAPC, the intensity quickly decreases when the sensor is positioned closer to the blocker. This decrease is much weaker in SPPO1 and additionally shows a strong dependency on current density, which is not observed in the TAPC-part. This suggests that electron transport at low voltages is limited, leading to the concurrent shift of the exciton generation zone to the SPPO1-part of the EML. With increasing voltage, electron transport is enhanced so that the generation zone slightly shifts towards the EBL and broadens, which is also in agreement with the observation in the M-EML. The different shape of the sensing profiles in TAPC and SPPO1 could be furthermore related to different diffusion lengths in the two materials. However, a long diffusion length should

[14] Hole mobility of TAPC: $\mu_h = 1 \times 10^{-2}\,cm^2/(V\,s)$, electron mobility: $\mu_e = 5 \times 10^{-5}\,cm^2/(V\,s)$.[143;236]

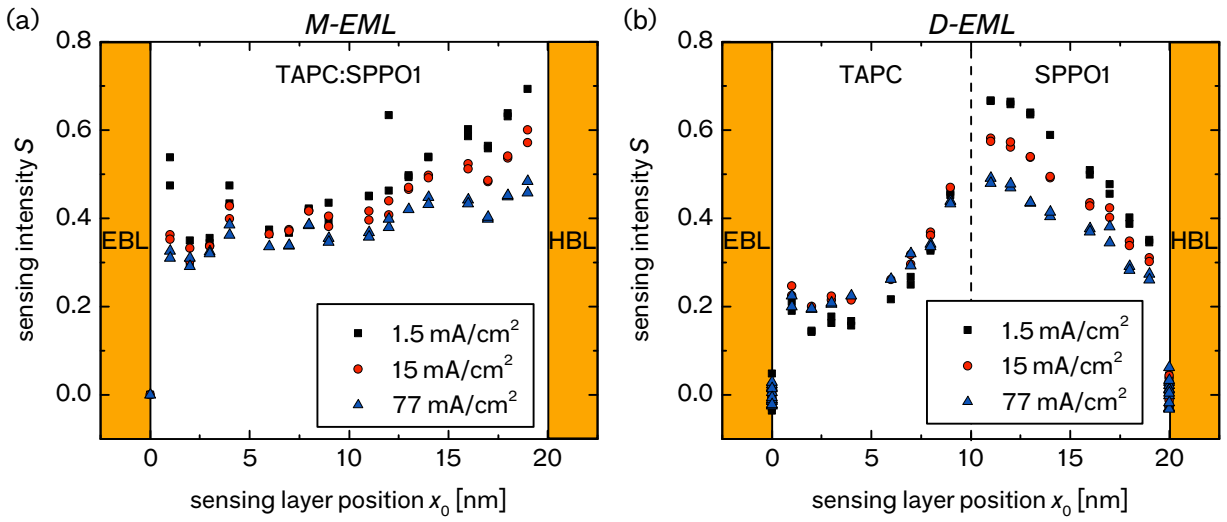

Figure 6.22: Measured sensing profiles for (a) M-EML and (b) D-EML at different current densities. Data at 0 nm show the reference without sensing layer (data points at 20 nm in (b) are the references for the sensing layer samples with $x_0 > 10$ nm).

also lead to a reduced sensing intensity close to the blockers, which is not observed here (cf. Fig. 6.8).

For both device structures, a fit of the sensing profiles would require a reasonable assumption for the underlying generation profile. For the M-EML, an exponential profile with a constant background could be a valid assumption due to the still more than one order of magnitude differing mobilities for electrons and holes. In the D-EML, however, the generation profile cannot be described by one of the profiles that have been suggested in Sec. 6.1.1. Instead, a Gaussian distribution may be chosen. Erickson *et al.* provided a model to calculate the charge carrier density in graded EMLs.[227] This model could possibly also be applied to the D-EML and M-EML structures here. However, as the measured sensing intensities underlie strong run-to-run variations, no further quantitative evaluation is performed in this work.

Overall, the width of the emission zone is broader in the M-EML compared to the D-EML. However, exciton formation in the M-EML takes place close to the SPPO1 HBL and not in the center of the EML, which leads to changes in the spectral radiance. As the SPPO1 triplet energy (2.8 eV)[185] is only slightly higher than the triplet energy of the blue emitter FIr6 (2.72 eV)[156], excitons could possibly diffuse into SPPO1 where they decay non-radiatively. This could be a reason for the overall lower efficiency of the M-EML compared to the D-EML. Furthermore, the sensing profiles can also explain the high initial increase in EQE: At low voltages, electron injection into the EML (or already into the SPPO1 HBL) is hindered leading to a massive holes surplus. With increasing voltage, the electron transport is facilitated enhancing the charge balance and, therefore, the EQE. In the D-EML, excitons are only formed when electrons are transported via the SPPO1 matrix leading to a higher turn-on voltage, but also an enhanced charge balance. However, it is expected that the ratio of

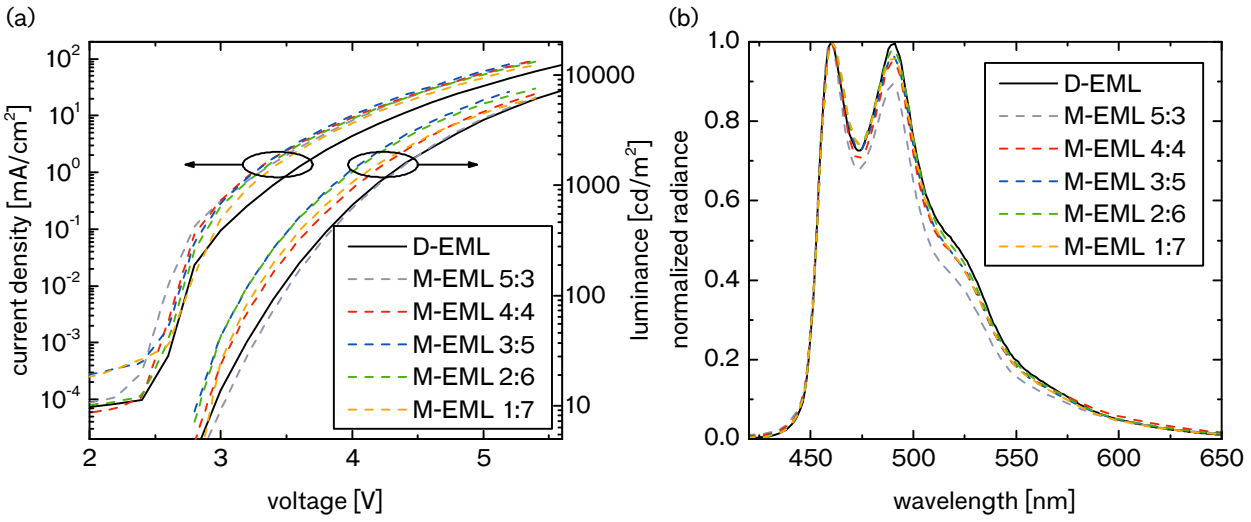

Figure 6.23: (a) Current density (left) and luminance (right) vs. voltage and (b) normalized spectral radiance at 15.4 mA/cm^2 for D-EML (solid line) and M-EML (dashed lines) with different ratios $x : y$ of TAPC:SPPO1.

the two matrix materials in the M-EML may strongly influence the charge carrier balance. Here, an increased SPPO1 content may shift the exciton generation zone more to the center of the EML. In the following, the influence of the matrix ratio is studied in more detail.

6.4.2 *Influence of the Matrix Ratio*

The matrix ratio $x : y$ is varied from slightly increased TAPC content of 5 : 3 over 4 : 4 (the same ratio as in the previous subsection) up to increased SPPO1 contents of 3 : 5, 2 : 6, and 1 : 7 (all ratios by weight). Figure 6.23 shows the performance of all samples compared to the D-EML device. The current density is enhanced for all M-EML samples and the current onset at low voltages decreases with increasing TAPC content. At higher voltages, however, the highest current density is achieved at a ratio of 3 : 5. The luminance follows a similar voltage behavior as the current density, with the exception that the 5 : 3 sample shows the lowest overall luminance.

The M-EML spectra in Fig. 6.23b show a spectral narrowing and the centers of mass shift towards smaller wavelengths with increasing TAPC content, which indicates that the exciton generation zone shifts closer to the cathode and possibly also narrows. Of all samples, the D-EML device shows the broadest spectrum and the highest green contribution. As shown in Fig. 6.22, the emission profile is located in the center of the EML, but is slightly shifted towards the HBL. As the small-wavelength peak in all M-EML spectra is more pronounced, it can be deduced that even at a matrix ratio of 1 : 7 the generation zone lies closer to the HBL than to the EBL because an emission profile close to the EBL should lead to a more green-emphasized spectrum than that of the D-EML.

The EQE vs. current density of all samples is shown in Fig. 6.24. The highest EQE is obtained for the M-EML with a matrix ratio of 2 : 6. Here, increasing SPPO1 content leads to increasing efficiency

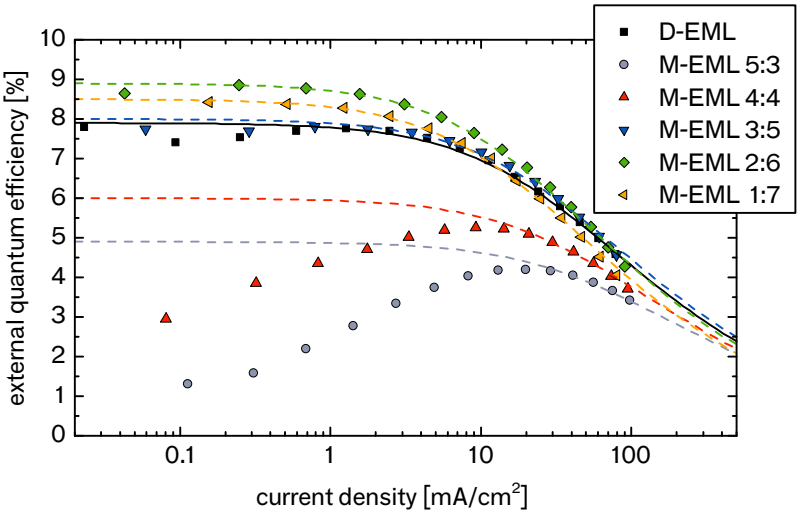

Figure 6.24: Measured external quantum efficiency (dots) and fits according to Eq. 3.4 (lines) for D-EML (solid line) and M-EML (dashed lines) with varying matrix ratio.

device	J_0 [mA/cm^2]
D-EML	130
M-EML 5 : 3	(310)
M-EML 4 : 4	(210)
M-EML 3 : 5	140
M-EML 2 : 6	90
M-EML 1 : 7	80

Table 6.2: Critical current density J_0 extracted from fits of Eq. 3.4 to the EQE data shown in Fig. 6.24.

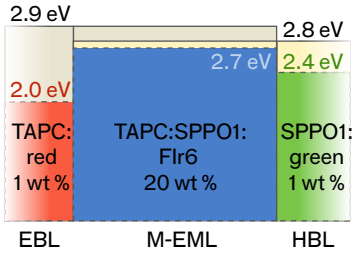

Figure 6.25: EBL/EML/HBL structure of M-EML samples using doped blockers. Lines show the triplet energy levels of all materials used.

and better charge balance at low voltages. A high TAPC content as in the sample with the 5 : 3 ratio instead decreases the overall efficiency and leads to an even steeper EQE increase at low voltages than the previously discussed 4 : 4 sample.

Again, the measured data are fitted by Eq. 3.4 assuming TTA as the only mechanism leading to roll-off in order to extract the critical current densities J_0 (see Table 6.2). While in the D-EML $J_0 = 130\,\mathrm{mA/cm^2}$, increasing TAPC content seems to strongly enlarge J_0, which would suggest a broadened emission zone. However, this is contradictory to the observations from the emission spectra and is probably related to the strong charge imbalance, which impedes accurate fitting in these devices. Increasing SPPO1 content, instead, diminishes J_0. Here, a broadening of the emission zone would have been expected due to the better charge balance and the shift of the spectrum to the center of the EML.

In the following, the position and width of the emission profile shall be determined more precisely. The measurement of the emission profile of all samples using the sensing layer method would require an individual sample run for each M-EML composition resulting in high productions costs. Instead, only one new sample run is produced where the blocking layers for four different matrix ratios are doped with a phosphorescent sensor. The sensor again provides a lower triplet energy level than the emitter and, thus, allows mapping of the triplet excitons which are located close to the blocking layer. As EBL sensor, TAPC is doped with 1 wt % of the red emitter Ir(MDQ)$_2$(acac) and, as HBL sensor, SPPO1 is doped with 1 wt % of the green emitter Ir(ppy)$_3$ (see Fig. 6.25). Samples are produced such that either the HBL or the EBL is doped. Furthermore, the sample run contains reference samples without doped blockers.

Figure 6.26 shows the emission from the doped blockers for all samples at a current density of 15.4 mA/cm^2 along with the PL spectra of Ir(MDQ)$_2$(acac) and Ir(ppy)$_3$ for comparison. The blocker emission

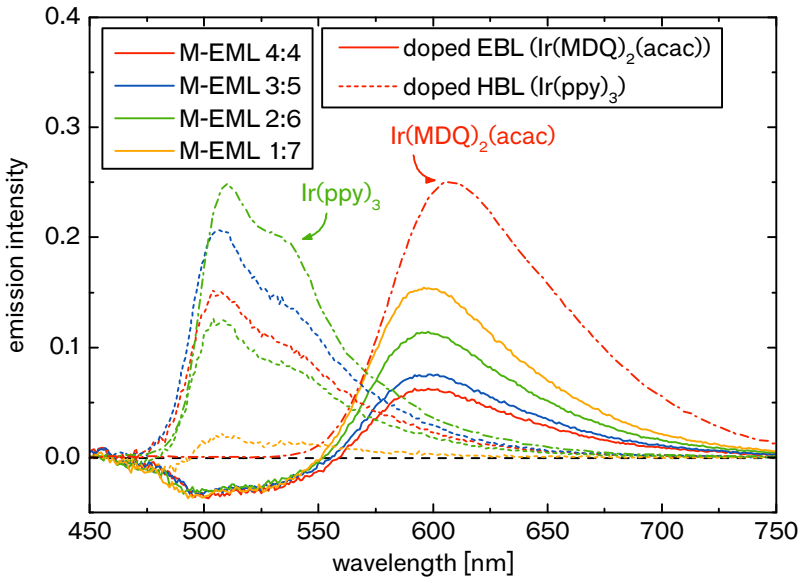

Figure 6.26: Spectral emission of the doped blockers at varying M-EML ratio. The intensity is calculated by subtracting the spectrum of the reference from the spectral radiance of M-EML samples with doped blockers at a current density of 15.4 mA/cm^2. Spectra are normalized to the first blue maximum at 460 nm prior to calculating the difference. For comparison, the PL spectra of $Ir(MDQ)_2(acac)$ and $Ir(ppy)_3$ are given as dash-dotted lines.

is calculated by, first, normalizing all spectra to the maximum of the blue emitter at 460 nm and, second, subtracting the reference spectra from the spectra of the devices with doped blockers. Compared to the PL spectra of the dopants, the emission is slightly blue-shifted due to the OLED microcavity. At a matrix ratio of 4 : 4, emission from both blockers is detected, which is in agreement with the emission profile in Fig. 6.22a. Although the samples do not permit a quantitative comparison between the emission from HBL and EBL due to the differently chosen sensor materials, it can be deduced that the green sensor exhibits higher intensity because the sensing profile is more intense at the HBL side (cf. Fig. 6.22a). With increasing SPPO1 content, the green emission from the HBL decreases, whereas the red emission from the EBL increases. This is attributed to a shift of the emission zone towards the EBL. At a ratio of 1 : 7, only little green emission from the HBL is detected whereas red emission is observed for all samples. This indicates that the emission zone may indeed shift from one EML side to the other. The negative intensity observed in the green spectral part for samples with doped EBL could be related to contamination of the reference samples with the green emitter during evaporation.

Overall, the results deduced from the spectra in Fig. 6.23b and the observations from the doped blockers are opposing: The spectra from Fig. 6.23b suggested that the exciton generation zone in the M-EML shifts with increasing SPPO1 content from the HBL towards the EBL, but does not markedly cross the center of the EML. The experiment with the doped blockers instead indicates that the generation zone shifts from the HBL to the EBL. The different observations could be a consequence of the challenging preparation of the mixed EML films, where the obtained doping concentrations cannot only vary from run to run, but can also change throughout the thickness of the EML. Here,

a larger error might be introduced. Furthermore, the high deviations between equal samples (cf. App. C.1) may falsify the obtained results. In addition, the blue emitter FIr6 is known as an instable compound leading to fast emitter degradation when high current densities are applied, which might contribute to the contrasting observations.[235] Therefore, further investigations of the D-EML and M-EML structure using the more stable green emitter $Ir(ppy)_3$ are given in App. C.3 for comparison.

Finally, some general conclusions may be drawn: The M-EML structure seems to generally increase the current density compared to the D-EML due to reduced energy barriers as typically only one sort of charge carriers needs to be injected into an M-EML. However, this also leads to exciton formation close to one of the blocking layers. The measurement of the emission profile and the investigations using doped blockers indicate that the emission profile in M-EML devices might indeed be broader compared to D-EML, which is caused by the less confined charge exciton formation region. The spatial exciton distribution in the M-EML, however, strongly depends on the mixing ratio of the two hosts.

6.5 Summary and Outlook

In this chapter, a method is developed that enables extraction of the emission profile with nanometer spatial resolution. The emission profile represents the spatial distribution of the excitons inside the EML including exciton generation and diffusion. In order to measure the emission profile, a small sensor that locally quenches the excitons is introduced at varying positions inside the EML. Evaluating the emission spectra for each sensor position then allows mapping of the spatial exciton distribution. For a quantitative evaluation of the results, the experimental quenching process is mathematically described by solving the diffusion equation for samples with and without sensor. The influence of the sensing layer is attributed for by assuming that all excitons reaching the sensor are quenched. Finally, the measured sensing intensities are fitted allowing extraction of the exciton generation profile, the diffusion length, and the shape and width of the emission profile.

The sensing method is applied to three different EML systems, namely, an ambipolar EML, a double EML, and a mixed EML. The system containing an ambipolar matrix material was chosen as a proof-of-principle, where all prerequisites of the sensing method were tested before extracting the emission profile. It was assured that the sensor does not influence the electrical properties of the OLED, that effects due to different outcoupling can be neglected, and that excitons are only locally quenched. Yet, one assumption could not be guaranteed, namely, that all excitons that reach the sensor are quenched. This would require further experiments, in which the doping concentration of the sensor is systematically varied. If total quenching of all excitons would be present, an increased sensor

concentration would not alter the results of the extracted sensing profiles.

It was found that in the ambipolar systems CBP:Ir(ppy)$_2$(acac) and CBP:Ir(ppy)$_3$, excitons are generated within an exponential profile close to the electron transport layer. The width of this generation zone is very narrow and decreases with increasing current density. Furthermore, the triplet diffusion lengths of CBP:Ir(ppy)$_2$(acac) and CBP:Ir(ppy)$_3$ were extracted. Interestingly, very small lengths of 2.4 nm and 3.5 nm were observed at 15 mA/cm^2, respectively, which is much lower than typically reported in literature. The small diffusion lengths suggest that excitons are generated on the emitter molecules impeding wide Dexter-driven exciton diffusion on the guest due to the higher triplet energy level of CBP. As will be further discussed in Chapter 7, the higher diffusion length of CBP:Ir(ppy)$_3$ could be related to the property of Ir(ppy)$_3$ to form aggregates. Overall, the width of the emission zone increases with increasing current density from 0.2 to 50 mA/cm^2, in CBP:Ir(ppy)$_2$(acac) from 3 to 5 nm, and in CBP:Ir(ppy)$_3$ from 4 to 7 nm. Broadening of the emission zone with increasing current density has been barely discussed up to now but can lead to unusual kinks in the efficiency-current density curves. Although CBP is typically stated as an ambipolar material in literature, which should result in very broad exciton formation across the whole EML, a very narrow emission zone was observed here. Concluding, an ambipolar material alone does not guarantee well-balanced charge carrier densities within the EML, because energy barriers and the conduction properties of the emitter molecules influence the region of exciton formation as well.

In order to find other structures that might broaden the emission zone, double and mixed emission layers comprising the blue emitter FIr6 embedded in the primarily hole transporting TAPC and the primarily electron transporting SPPO1 are studied qualitatively using the sensing method. In the D-EML structure, exciton formation is a very local process located at the interface between the two matrix materials and leading to a narrow emission zone. The M-EML instead helps in broadening the emission zone due to the spatially non-defined generation zone, which expands over larger regions of the EML. However, the shape and width of the emission profile strongly depends on the chosen materials as the exciton formation region is defined by the HOMO and LUMO levels, the conductivity, and the doping concentrations of the matrices and the emitter. Here, a variation of the ratio of the two matrix materials revealed a shift of the exciton generation zone across the EML. Finding an optimal M-EML structure that ensures a broad emission profile requires much experimental optimization or a profound electrical simulation. Both are challenging due to the need for high precision evaporation tools and knowledge of all relevant material constants, respectively.

In the future, further structures should be investigated in order to find optimal emission layers with a very broad exciton distribution. Promising results have already been reported using graded emission

layers (cf. Fig. 6.6).[227] While the authors extracted the emission profile of their graded OLED structure using the sensing layer method as well, an analysis of their data is missing so that their extracted width of around 80 nm can only be regarded as a rough estimation. Fitting the results and a detailed discussion of the influence of the sensor could verify this large emission zone width.

Broadening the exciton distribution in OLEDs will lead to lower local exciton densities and, thus, can reduce all exciton-driven quenching processes. However, the efficiency roll-off due to exciton annihilation is typically overlapped by an imperfect charge carrier balance. Therefore, independent measurement of the charge balance and, especially, the avoidance of charge imbalance should be studied in more detail.

7 Influence of Molecular Aggregation

The triplet-triplet annihilation rate constant, which is one of the factors determining the strength of efficiency roll-off, can be altered by aggregation of emitter molecules. This chapter studies the extent of aggregation in seven phosphorescent iridium-cored emitters, three of which possess a homoleptic and four a heteroleptic structure. Using steady-state and time-resolved spectroscopy, an increased aggregate formation within the homoleptic compounds is found. A variation of the matrix material shows only weak influence on aggregation, except for the emitter Ir(ppy)$_3$, where a strong increase of TTA is observed when doping the emitter into the host TPBi. Furthermore, the influence of the processing conditions is studied. Increasing the substrate temperature and decreasing the deposition rate leads to slightly stronger aggregation. Changing the underlying layer from glass to TCTA strongly decreases TTA due to a weaker aggregate formation. In addition, X-ray diffraction measurements reveal that Ir(ppy)$_3$ and Ir(ppy)$_2$(acac) form small crystallites with a preferred orientation, both in pure layers and when embedded into a host.

7.1 Introduction

The triplet-triplet annihilation rate k_{TT} is a material property describing how efficient TTA between two emitter molecules takes place.[1] It mainly depends on the interaction radius of two triplet excitons and, hence, on the distance between emitter molecules. Previous investigations on host-guest systems with state-of-the-art phosphorescent emitters suggest that the guest molecules show a tendency to aggregate within the EML,[39;43;117;237–240] leading to high local exciton densities and fast Dexter TTA. In this context, the term aggregation usually describes molecular clustering rather than the formation of physical dimers. To minimize Dexter based TTA, the average distance between emitter molecules should be as large as possible and, thus, aggregation in particular needs to be avoided. To achieve this, both molecular design approaches and customized OLED stacks have been pursued.

[1] Parts of this section are published in Ref. 11. Reprinted with permission. Copyright 2013, Wiley VCH.

Reineke *et al.* suggested that molecules with lower dipole moments have a reduced tendency to form aggregates.[142] For phosphorescent emitter molecules this was shown by comparing the two rather similar green emitting compounds Ir(ppy)$_3$ and Ir(ppy)$_2$(acac), each doped into TCTA at a concentration of 8 wt %. Time-resolved PL measurements revealed that the TTA rate in the Ir(ppy)$_2$(acac) blend amounts to only 70 % of the TTA rate in the Ir(ppy)$_3$-based blend, which is consistent with the much lower dipole moment[2] μ_D of Ir(ppy)$_2$(acac).[241] The observed differences in TTA correlate with the roll-off behavior of complete devices, i.e., an improved roll-off has been observed for Ir(ppy)$_2$(acac)-based OLEDs.[142] It seems likely that due to enhanced

[2] The dipole moments of Ir(ppy)$_2$(acac) and Ir(ppy)$_3$ are 1.91 D and 6.26 D, respectively.

aggregation of emitters with large dipole moments, devices based on such emitters generally tend to suffer from increased roll-off.

One way to increase the average intermolecular distance of emitter molecules and, thus, reduce Dexter-based TTA rates is the introduction of large dendrons into fluorescent or phosphorescent complexes.[40;114;239;242–246] Namdas *et al.* synthesized different $Ir(ppy)_3$-cored dendrimers that provide a core to core distance in neat layers of up to 23 Å.[40] With increasing molecular size, k_{TT} was indeed found to decrease by more than one order of magnitude. Instead of optimizing the chemical structure of the emitter molecule, another way to reduce aggregation consists of engineering the device stack appropriately. Here, improved roll-off behavior can be achieved by introducing intrinsic interlayers between thin emitting layers which can reduce exciton transfer in the direction perpendicular to the substrate.[43;47;247–250]

Effects of aggregation cannot only be seen in transient measurements, but are also visible in the PL spectra of the material. Increasing the emitter concentration leads to spectral broadening and, thus, reduces the visibility of the individual vibronic bands, which is attributed to enhanced aggregation of emitter molecules.[39] Furthermore, emitter aggregation was revealed using microscopic methods including TEM, AFM, STM, or fluorescence microscopy.[117;237–239] As the typical cluster size of phosphorescent emitters that are embedded in a matrix material and produced via thermal evaporation is only in the range of around 10 nm, the resolution of the microscopic technique has to be very high.

Throughout this chapter, the influence of the molecular properties of the emitter is studied in more detail. Therefore, seven different iridium compounds are embedded into matrix materials at varying doping concentrations. The samples are investigated by steady-state luminescence measurements, time-resolved spectroscopy, and X-ray diffraction. Furthermore, the matrix material and the deposition parameters are varied in order to find systematic relations between molecular film structure and the formation of aggregates.

If not stated otherwise, organic thin-films are fabricated by thermal evaporation with a thickness of 20 nm on glass substrates that are further encapsulated.

7.2 *Aggregation of Homoleptic and Heteroleptic Emitters*

In this section, seven different phosphorescent iridium (III) complexes are studied, where three of the emitters possess a homoleptic structure $Ir(C–N)_3$ and four a heteroleptic structure $Ir(C–N)_2(acac)$ containing an acetylacetonate (acac) ligand. Here, (C–N) is a charged cyclometalating ligand. The chemical structures are shown in Fig. 7.1. All materials show strong spin-orbit coupling due to the central heavy metal iridium atom, resulting in efficient intersystem crossing and, thus, phosphorescence.

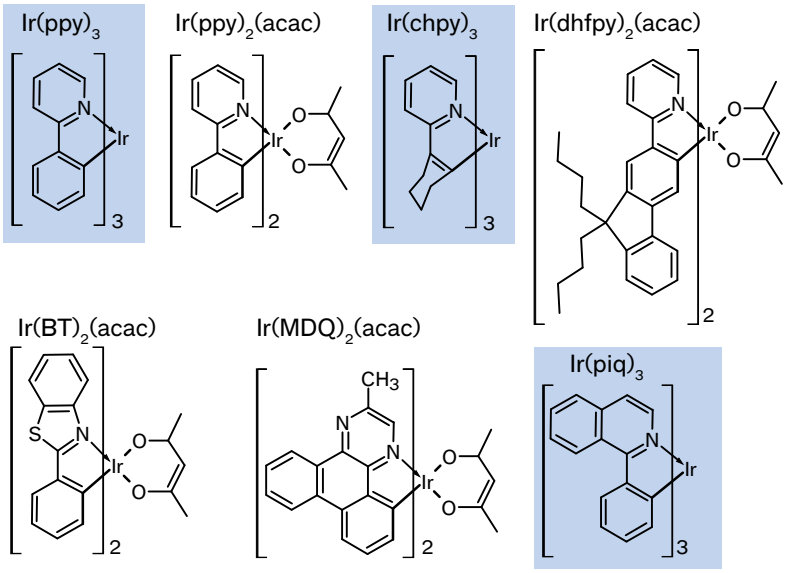

Figure 7.1: Chemical structures of the investigated homoleptic (marked in blue) and heteroleptic emitters.

7.2.1 *Photoluminescence Measurements*

Figure 7.2 shows the PL spectra of the host-guest systems at an emitter concentration of approximately 1 mol %. Emitter aggregation is weak at this doping concentration and the emitters are suspected to be well separated from each other by the matrix molecules. The respective host materials are selected in terms of efficient energy transfer from host to guest and are given in Table 7.1 together with the wavelength of the emission maximum. TCTA with a triplet energy $E_T = 2.8\,\text{eV}$ is used for the green emitters $Ir(ppy)_3$ and $Ir(ppy)_2(acac)$,[142;179] CBP ($E_T = 2.6\,\text{eV}$) for the yellow-emitting $Ir(chpy)_3$, $Ir(dhfpy)_2(acac)$, and $Ir(BT)_2(acac)$,[179;251–253] and NPB ($E_T = 2.3\,\text{eV}$) for the red emitters $Ir(MDQ)_2(acac)$ and $Ir(piq)_3$.[173;181;254] The emission color is roughly related to the molecular size, where an increased electron delocalization on larger ligands leads to reduced transition energies.[255] Overall, the spectra are composed of clear vibronic subbands (except for the emitter $Ir(MDQ)_2(acac)$).

emitter	matrix	λ_1 [nm]	Γ_1 [mol %]	Γ_2 [mol %]
$Ir(ppy)_3$	TCTA	511	1.1	9.0
$Ir(ppy)_2(acac)$	TCTA	519	1.2	9.7
$Ir(chpy)_3$	CBP	537	0.7	7.5
$Ir(dhfpy)_2(acac)$	CBP	556	0.4	4.6
$Ir(BT)_2(acac)$	CBP	560	0.7	7.0
$Ir(MDQ)_2(acac)$	NPB	601	0.7	7.3
$Ir(piq)_3$	NPB	618	0.7	7.1

Table 7.1: Selected matrix materials, doping concentrations Γ_1 and Γ_2, and wavelength λ_1 of the emission maximum at concentration Γ_1. Homoleptic emitters are marked in blue.

In the following, thin-films with higher doping concentrations, Γ_2, are prepared (see Table 7.1). As an example, Fig. 7.3a shows the normalized emission intensity of $Ir(ppy)_3$ as a function of the wavelength for 0.7, 9.0, and 22.1 mol %. The spectrum shows a significant red-shift with increasing doping concentration and the vibronic

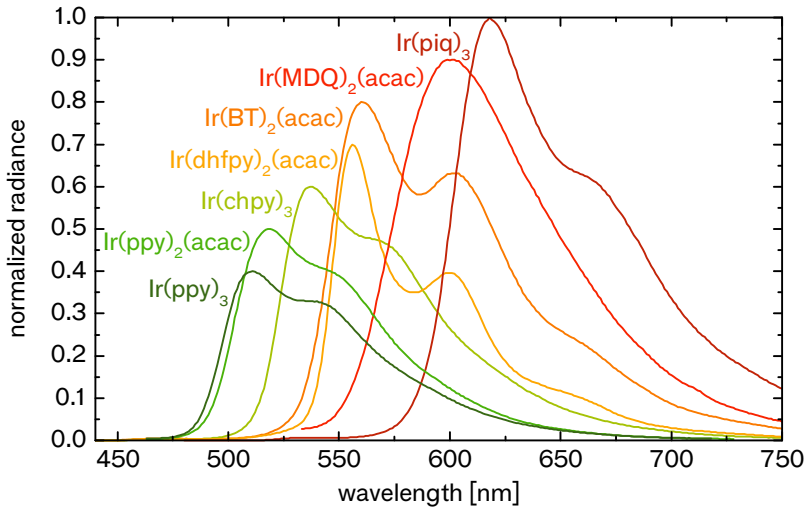

Figure 7.2: Photoluminescence spectra of the investigated phosphorescent emitters, doped with concentration Γ_1 into a matrix material (cf. Table 7.1). Spectra are normalized to different intensities for better visualization.

transitions become less distinguishable. Furthermore, the spectrum broadens significantly and thus reduces the visibility of the individual vibronic bands, which is shown in Fig. 7.3b by normalizing the wavelength to the wavelength of the emission maximum. In literature, spectral broadening and red-shift have been previously observed for $Ir(ppy)_3$ and FIrpic and were attributed to increased aggregation of emitter molecules.[39;117] However, this effect was not observed for $Ir(ppy)_2(acac)$ and for the red emitter bis[2-(2′-benzothienyl)-pyridinato-N,C3′](acetylacetonate)iridium(III) ($Ir(Btp)_2(acac)$).[39;142]

In order to investigate the spectral behavior of the different emitters and to find out which processes lead to spectral changes on the molecular scale, all spectra are calculated as a function of energy by dividing by E^2 ($I(E) \propto I(\lambda)/E^2$).

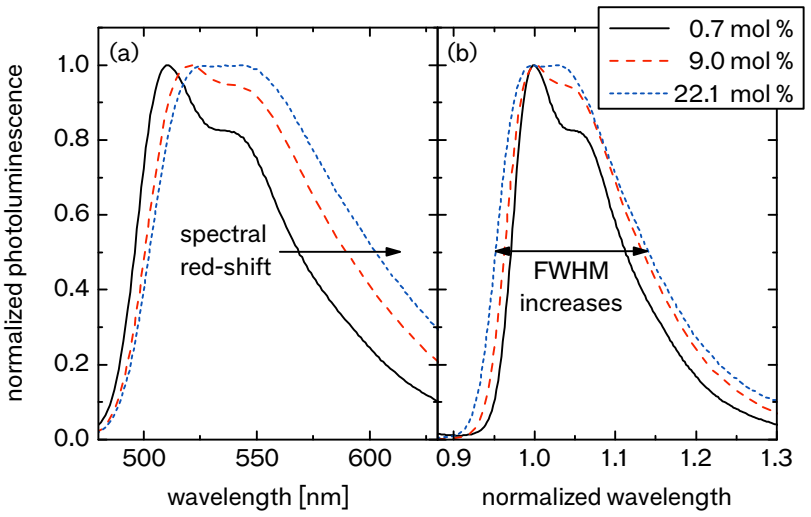

Figure 7.3: Photoluminescence spectra of TCTA:$Ir(ppy)_3$ at varying emitter concentration. (a) demonstrates the spectral red-shift whereas in (b) the wavelength is normalized to the emission maximum in order to illustrate spectral broadening with increasing concentration.

The radiative recombination rate of a transition depends on the third power of the energy by

$$k_\mathrm{r} = \frac{\mu_\mathrm{TDM}^2 n^3 E^3}{3\pi\epsilon_0\hbar^4 c^3}, \tag{7.1}$$

with the transition dipole moment μ_TDM and the refractive index n.[256] Therefore, the spectra $I(E)$ are furthermore divided by E^3. This rescaled emission intensity is now proportional to the density of states of the vibronic subbands of the molecular transition, which allows fitting of the vibronic transitions to the emission spectra.[129;257] Each line $I_\nu(E)$ is affected by an individual Gaussian broadening accounting for an energetic modulation of the density of states due to the environment:[256]

$$I_\nu(E) \propto \frac{\mu_\mathrm{TDM}^2 n^3 E^3}{3\pi\epsilon_0\hbar^4 c^3} \frac{1}{\sqrt{2\pi}\sigma_\nu} \mathrm{e}^{-\left(\frac{E-E_\nu}{\sqrt{2}\sigma_\nu}\right)^2}. \tag{7.2}$$

The first term describes the radiative recombination from Eq. 7.1.[257] The analysis is based on a Poisson progression of the vibronic lines. Finally, the emission spectra are fitted to

$$\begin{aligned} f(E) &= \sum_{\nu=0}^{\nu=5} f_\nu(E), \quad \text{with} \\ f_\nu(E) &= \frac{S^\nu \mathrm{e}^{-S}}{\nu!} \cdot \frac{b}{\sqrt{2\pi}\sigma_\nu} \mathrm{e}^{-\left(\frac{E-E_{00}+\nu\hbar\omega}{\sqrt{2}\sigma_\nu}\right)^2}, \end{aligned} \tag{7.3}$$

where the first factor accounts for the Poisson distribution of the individual lines and the other term describes the Gaussian broadening of the individual states. According to Kasha's rule, electronic transitions occur from the lowest excited state $E_{0\mathrm{e}}$ into one of the vibronic states of the ground state $E_{\nu\mathrm{g}}$. The probability of a certain transition depends on the overlap of the vibronic wave functions (Franck-Condon principle). This is schematically illustrated in Fig. 7.4. Here, the molecular deformation between ground and excited state determining the transition probability is described by the Huang-Rhys factor s, which serves as the argument of the Poisson progression in Eq. 7.3. The factor b is a normalization constant. All lines are equally distributed with a line distance of $\hbar\omega$ and possess an individual broadening σ_ν.

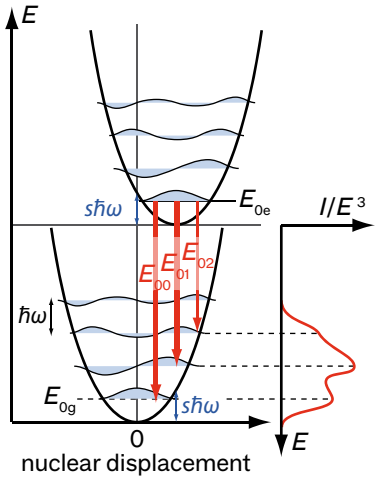

Figure 7.4: Illustration of the molecular transitions from excited state, e, into a vibronic band of the ground state, g, according to the Franck-Condon principle. Right: corresponding spectrum $I(E)/E^3$ as a function of energy.

In the following, all measured spectra are fitted with a least-squares algorithm. After selecting a suitable fit region where only emission from the emitter is observed, start values for E_{00}, s, and $\hbar\omega$ are determined from the measured spectra. Next, the start values are optimized in the fitting routine while keeping all σ_ν constant and small in order to distinguish properly between the individual lines. Then, the standard deviations are fitted one after another[3] resulting finally in extraction of E_{00}, the Huang-Rhys factor s, the line distance $\hbar\omega$, and the standard deviation of the lines σ_ν. Furthermore, the center of mass $\langle E \rangle$ is calculated according to

$$\langle E \rangle = E_{00} - S\hbar\omega. \tag{7.4}$$

[3] σ_4 and σ_5 are kept constant at approximately the value of σ_3 because the measured spectra often exclude the low-energy region of E_{04} and E_{05} or show only weak resolution in this regime (cf. Fig. 7.5).

This is a better measure of the spectral red-shift than the typically used wavelength of the maximum intensity, which neglects changes in the spectral shape and prohibits direct conclusions onto the molecular transitions.

As an example, Figure 7.5 shows the emission intensity of TCTA: $Ir(ppy)_3$ at 1.1 mol % as a function of energy (dashed line) together with the fit to the Poisson progression and the individual lines $f_\nu(E)$. Here, the fit region is selected from 1.74 to 2.70 eV in order to exclude emission that is not related to the emitter.[4] Note that the fit can even be extrapolated to a region $E < 1.74$ eV as the position and intensity of the higher vibronic transitions result from the Poisson distribution.

[4] Emission from the matrix is detected in the blue wavelength regime at 3.05 eV and again as an artefact in the infrared regime at doubled wavelength, which originates from the monochromator's wavelength selection.

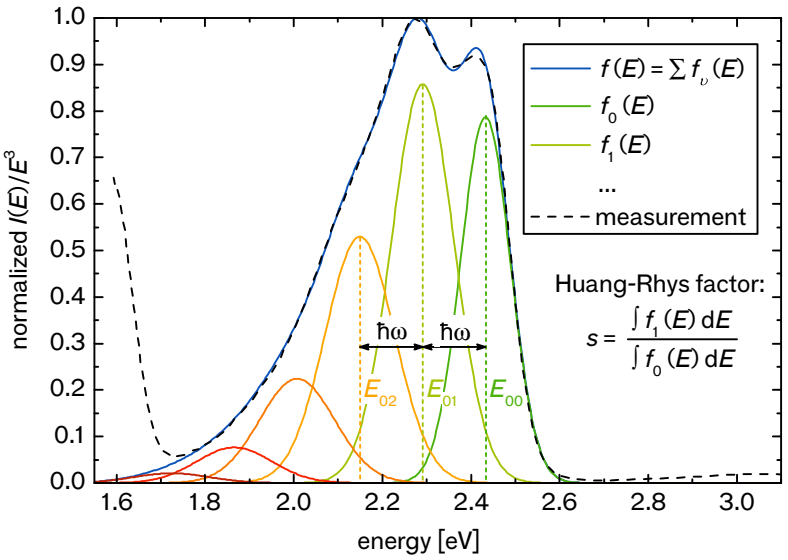

Figure 7.5: Emission intensity of TCTA:$Ir(ppy)_3$ (0.7 mol %, dashed line) as a function of energy and divided by E^3. The resulting fit of the spectrum to a Poisson progression (blue, cf. Eq. 7.3) and the individual vibronic transitions are shown as solid lines.

The fitted parameters are collected in Fig. 7.6a for all seven emitters at the lower doping concentration Γ_1 (see Table 7.1). The fundamental transition E_{00} ranges from 2.43 eV for $Ir(ppy)_3$ to 2.00 eV for $Ir(piq)_3$, whereas the center of mass shifts approximately 0.1−0.2 eV towards red. With the exception of $Ir(MDQ)_2(acac)$, the Huang-Rhys factor s exceeds 1, indicating that the transition f_1 into the first vibronic sublevel is more intense than the fundamental transition f_0 (cf. Fig. 7.5). The standard deviation σ_ν increases with the vibronic subband number. The line distance $\hbar\omega$ is similar for all emitters ranging from 130 to 158 meV, although a smaller $\hbar\omega$ is observed for the homoleptic emitters. Finally, a full width at half maximum (FWHM) of 280 to 420 meV is observed.

In order to investigate the change of fit parameters X with increasing doping concentration Γ, the relative parameters ΔX are calculated according to

$$\Delta X = \frac{X_2 - X_1}{\Gamma_2 - \Gamma_1} \cdot \frac{1}{X_1}. \tag{7.5}$$

Here, 2 and 1 denote the higher and lower concentrated sample, respectively (see Table 7.1). Hence, ΔX describes the change of a

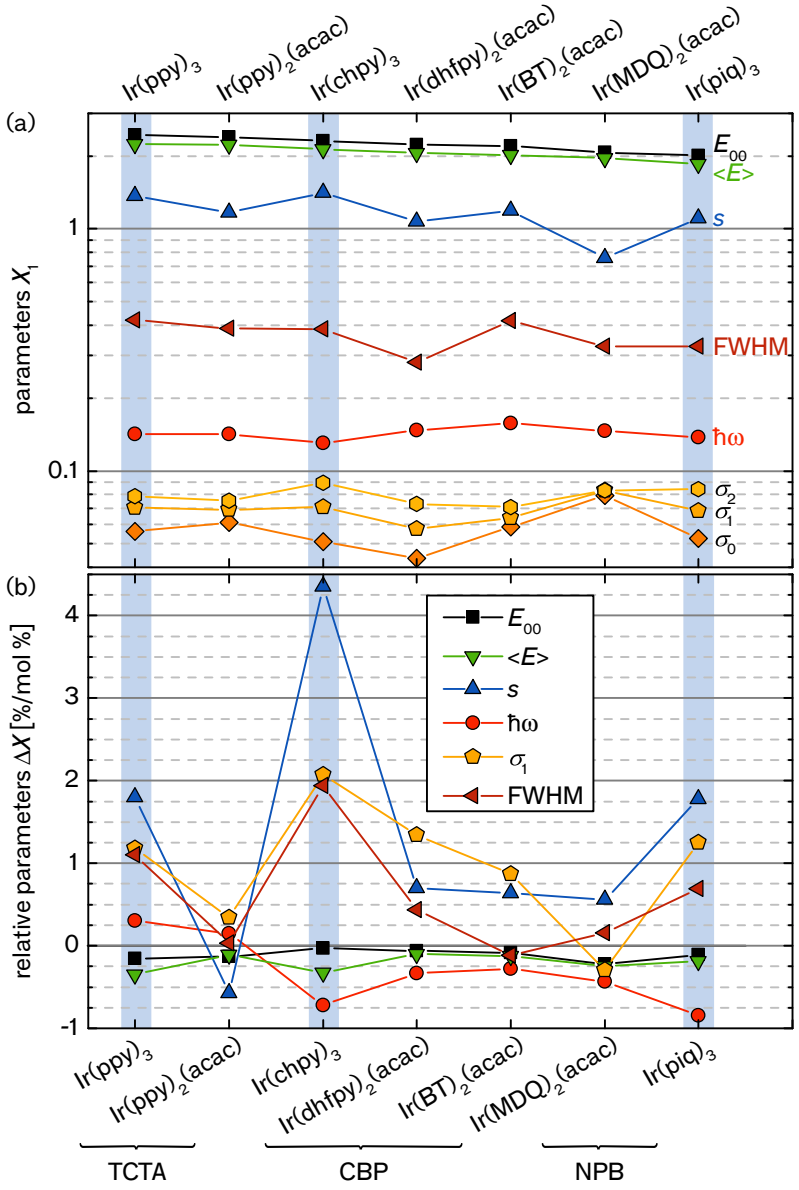

Figure 7.6: Spectroscopic parameters accessed by fitting the emission intensity $I(E)/E^3$ of seven different emitters to the Poisson progression in Eq. 7.3. (a) Absolute values at Γ_1 doping concentration (see Table 7.1). The parameters E_{00}, $\langle E \rangle$, FWHM, $\hbar\omega$, and σ_ν are given in eV; s is dimensionless. (b) Relative change ΔX of the parameters with increasing doping concentration. Values are calculated according to Eq. 7.5 and are given in % per mol %. For clarity, only σ_1 is given here. Blue bars mark the homoleptic emitters.

parameter compared to the value X_1 it takes at concentration Γ_1 per concentration increase. Note that this approach assumes a linear dependency of the parameters on the doping concentration, which may not be true for all materials and parameters. However, it allows a rough comparison between the properties of the different compounds.

A negative change of the center of mass $\langle E \rangle$ corresponds to a red-shift of the spectrum, which is observed for all emitters. However, the effect is only significant for $Ir(ppy)_3$, $Ir(chpy)_3$, and $Ir(MDQ)_2(acac)$. A very large effect is instead observed in the FWHM, where the homoleptic emitters show a significant broadening. The question now arises which parameters defining the molecular transition lead to the observed red-shift and spectral broadening.

Having a look at ΔE_{00}, Δs, $\Delta\hbar\omega$, and $\Delta\sigma_1$ in Fig. 7.6b, the strongest change with increasing doping concentration is observed for the

Huang-Rhys factor, where the homoleptic emitters show a significant increase of s. The distance $\hbar\omega$ between the individual subbands slightly increases for $Ir(ppy)_3$ and $Ir(ppy)_2(acac)$, whereas it decreases for the other emitters. However, this influence is rather small compared to the change in s. The change in σ_ν is only shown for the most prominent transition f_1, but similar results are obtained for other vibronic lines. Here, the homoleptic compounds show again the strongest change, where a significant increase of the linewidth is observed. Therefore, the overall broadening of the FWHM is mainly related to the increase of s and is additionally supported by the broadening of the subbands. The red-shift of the spectra is also related to the increasing s, but is furthermore overlapped by the shift of the fundamental transition E_{00} in the case of $Ir(ppy)_3$, $Ir(ppy)_2(acac)$, and $Ir(MDQ)_2(acac)$.

How can we now understand the parameter changes on a molecular scale? The strong increase of the Huang-Rhys factor for the homoleptic compounds hints to an increased molecular deformation[5] of the excited state with increasing concentration. However, this conclusion is based on the underlying model of excited states from single molecules, which might not be feasible anymore as the environment of a molecule at high concentration is different from the environment of spatially well-separated molecules. Another, more probable, explanation is that the spectra are composed of many single spectra originating from molecular aggregation. The particular strong increase in σ_ν for the homoleptic emitters also indicates the formation of aggregates. Compared to well separated emitters, which are only surrounded by matrix molecules, an emitter located in an aggregate experiences a stronger variation in its surrounding and, thus, in the density of states. This can lead to shifts of the fundamental transition and to broadening of the substates. Furthermore, the formation of dimers is possible, which are known to cause red-shifts.[16] The electronic transitions can also exhibit changes if the electron density of two excited states overlaps. In any case, the spectra cannot be fitted with a single set of vibronic lines anymore but are overlapped by spectra of different transition species. Instead, an ensemble of vibronic transitions should be applied. Concluding, the strong change of the Huang-Rhys factor and the broadening linewidth with increasing doping concentration indicate molecular aggregation in the homoleptic compounds.

[5] The molecular deformation can be described by the reorganization energy $\lambda = s\hbar\omega$ (cf. Fig. 7.4).[258]

7.2.2 *Time-Resolved Spectroscopy*

Using time-resolved spectroscopy, the effect of the molecular structure on efficiency roll-off can be studied by investigating the strength of triplet-triplet annihilation in the respective materials. Therefore, all samples are excited by a pulsed nitrogen laser providing an excitation wavelength of 337 nm, while measuring the sample radiation with a fast photodiode. Using optical density filters, the excitation density is varied over three orders of magnitude. For details of the measurement

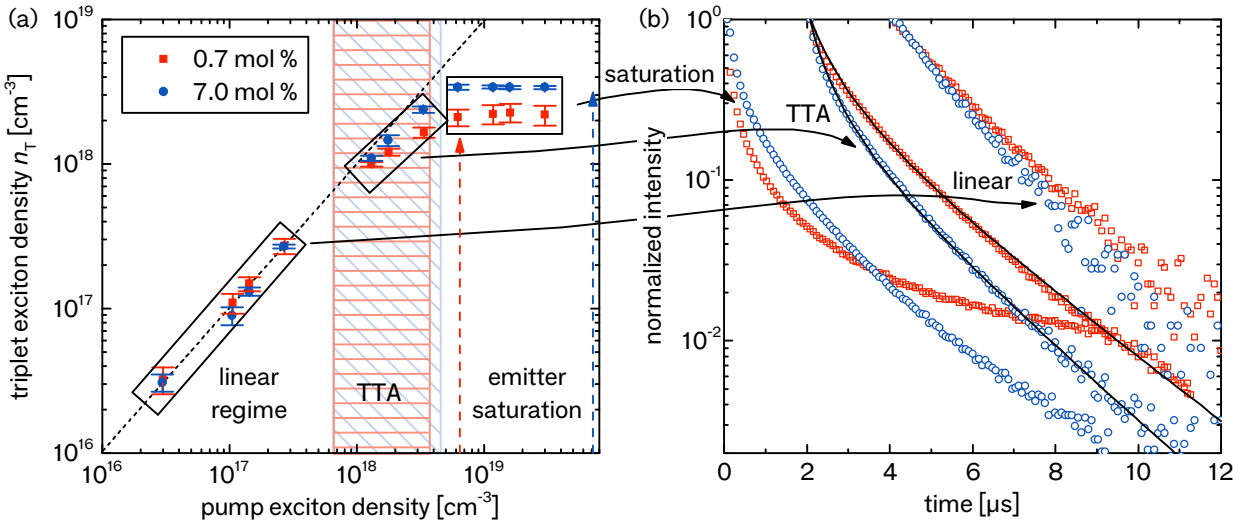

Figure 7.7: Time-resolved measurements of $Ir(BT)_2(acac)$: (a) Triplet exciton density as a function of the pump exciton density. Hatched squares indicate the TTA regime. Dashed arrows mark the density of emitter molecules. (b) Exemplary transients from all three regimes indicating monoexponential decay inside the linear regime, TTA, and emitter saturation. Transients are shifted in time for better visualization. Black lines indicate fits according to Eq. 3.3.

setup and the determination of the pump and triplet exciton density, refer to Sec. 4.2.1.

Figure 7.7a shows the triplet exciton density as a function of the pump density for the CBP:$Ir(BT)_2(acac)$ host-guest system. In total, three different regimes are distinguishable: A linear regime at low pump intensities, a TTA regime at intermediate excitation, and a saturation regime at strong pumping. The linear increase indicates that one absorbed photon leads to one exciton. With increasing excitation, the distance between the excitons decreases and interaction sets in—namely, triplets are quenched due to TTA leading to a deviation from the linear decay. At very high pump densities above around $7 \times 10^{18}\,\mathrm{cm}^{-3}$, the signal becomes constant due to saturation of the emitter.

The measurements are again performed for low and high emitter concentration. For the sample with low guest concentration, the emitters saturate at lower excitation density and the maximum triplet exciton density is reduced. Interestingly, the onset of emitter saturation directly correlates with the density of emitter molecules only in the case of the lower concentrated sample (cf. the dashed arrows indicating the guest density, calculated according to Eq. 4.2). At higher concentration, saturation sets already in before reaching the actual guest density.[165] A similar picture is observed for the other emitters.

Figure 7.7b shows some exemplary transients from each regime at two different guest concentrations. In the linear regime, the radiative decay follows a monoexponential function. With onset of TTA, the initial decay is fastened and a deviation from the monoexponential behavior is observed. Finally, in the saturation regime, not only TTA but also other processes are observed. For the example of $Ir(BT)_2(acac)$, host-guest interaction could explain the long-living feature in the 0.7 mol % sample.[113] Here, excitons are not anymore completely confined on the low concentrated guest molecules, but might also reside on the host. The long lifetime of the host triplet state then leads

to a much slower decay, which is observed after an initial strong TTA contribution.

For further evaluation of emitter aggregation, only transients from the TTA regime are selected. All curves are fitted according to Eq. 3.3 yielding the TTA rate constant k_{TT} and the intrinsic emitter lifetime τ. Table 7.2 summarizes the two parameters as a function of the triplet exciton density n_T. TTA is reduced in the lower concentrated sample resulting in a smaller k_{TT}, whereas the triplet lifetime is slightly higher. Within the investigated TTA regime, k_{TT} and τ remain constant within the margin of the errors so that a mean value is calculated for all following investigations.[13]

Table 7.2: Fit parameters from the transient measurements of $Ir(BT)_2(acac)$ in the TTA regime: guest concentration Γ, triplet exciton density n_T, TTA rate k_{TT}, and triplet lifetime τ.

Γ [mol %]	n_T [10^{18} cm^{-3}]	k_{TT} [10^{-12} cm^3/s]	τ [s]
0.7	1.65 ± 0.13	2.01 ± 0.47	2.2 ± 1.0
	1.21 ± 0.07	1.90 ± 0.52	2.2 ± 0.3
	1.00 ± 0.03	2.01 ± 0.47	2.2 ± 0.3
7.0	2.38 ± 0.13	2.72 ± 0.57	2.0 ± 0.3
	1.46 ± 0.13	2.81 ± 0.59	1.9 ± 0.3
	1.09 ± 0.04	2.37 ± 0.55	1.7 ± 0.3

Time-resolved measurements are performed for all host-guest systems.[6] As an example, Fig. 7.8 shows transient measurements and corresponding fits for two different $Ir(chpy)_3$ concentrations. The $Ir(chpy)_3$ host-guest system is selected here because the quality of the fits displays the strengths and weaknesses of the underlying TTA method as will be discussed subsequently. At 0.7 mol %, a relatively slow decay with a lifetime of 3.8 s is measured. Furthermore, the fit shows severe deviations from the data at the initial decay from 0−2 s, which becomes especially obvious at high excitation density. At 7.5 mol % concentration, the fits resemble the data well and the intrinsic decay time is only 2.3 s.

The depicted transients illustrate the limit of the underlying TTA model: While at high concentration TTA seems to be the dominant process allowing reasonable fitting of the measured data, stronger deviations at low emitter concentration suggest that further physical processes might play a role. As indicated previously, high excitation densities can lead to excitons remaining on the host because no free guest can be found. This holds particularly for low guest concentrations and small energy differences between host and guest.

Deviations between fit and data are not only found for the lower concentrated $Ir(chpy)_3$ sample, but also for $Ir(dhfpy)_2(acac)$, both at 0.4 and 4.6 mol %. Note that the concentrations of the $Ir(dhfpy)_2(acac)$-samples are significantly lower compared to the other samples, which render the host-guest interaction reasonable. Furthermore, both emitters are doped into the host CBP, for which host-guest TTA has already been observed with the green-emitting $Ir(ppy)_3$ as guest.[113] Although the triplet energies of $Ir(chpy)_3$ and $Ir(dhfpy)_2(acac)$ are smaller compared to $Ir(ppy)_3$, an interaction between CBP and the two emitters might still be possible.[7] The other four investigated emit-

[6] For $Ir(MDQ)_2(acac)$, the measurements are only performed in the TTA and saturation regime, which impedes a calculation of the triplet exciton density. Therefore, $Ir(MDQ)_2(acac)$ is omitted in the comparison of the emitters.

[7] For further investigation on the energy transfer between host and guest, the host emission and guest absorption could be analyzed in terms of a Poisson progression as well. This would give information on the deformation energy and, thus, the transition between the lowest excited states of host and guest.[129]

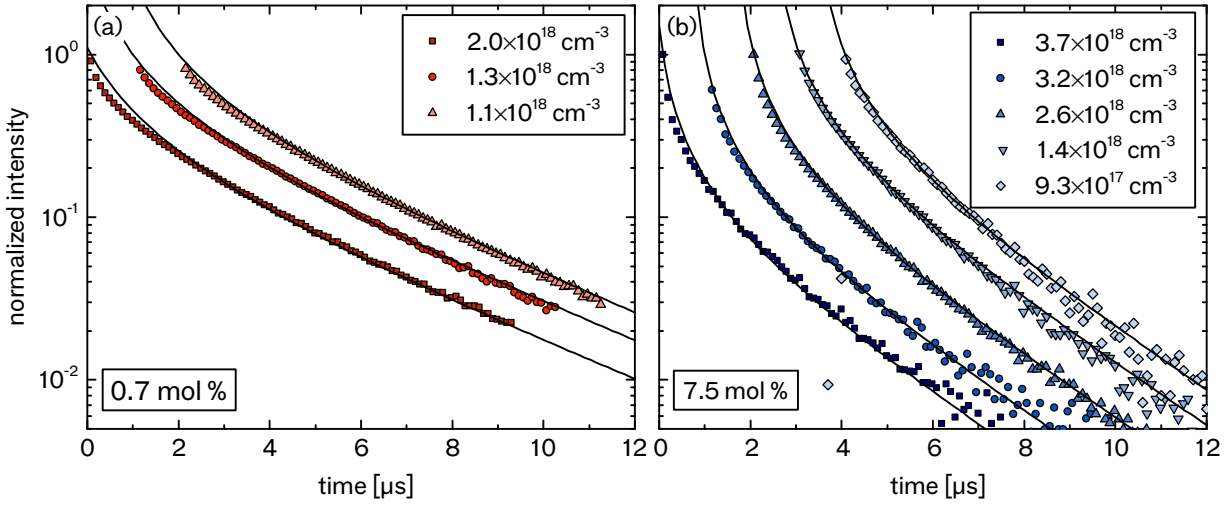

Figure 7.8: Transients of CBP:Ir(chpy)$_3$ at (a) 0.7 mol % and (b) 7.5 mol %. All transients are measured in the TTA regime. Data are shifted in time for better visualization, where the initial triplet exciton density decreases from left to right (values of n_T are given in the legend). Black lines indicate fits according to Eq. 3.3.

ters are doped into TCTA and NPB, respectively, leading to a more exothermic energy transfer. Therefore, reasonable fits are achieved in these systems.

The average triplet lifetimes of all systems are summarized in Fig. 7.9b. The emitters show a lifetime of around 2 s, which slightly decreases with increasing emitter concentration. This has been previously observed in other phosphorescent host-guest systems and is related to concentration quenching due to dipole-dipole interactions.[39] The probable host-guest interaction in CBP:Ir(dhfpy)$_2$(acac) and CBP:Ir(chpy)$_3$ causes longer decay times of 3.8−5.5 s in these systems. In addition, broader error margins account for the stronger deviations between data and fit. In literature, decay times of 1.5 s for Ir(ppy)$_3$ and Ir(ppy)$_2$(acac), 1.1 s for Ir(piq)$_3$ (concentrations correspond to the higher concentrated samples), and 2.0 s for Ir(chpy)$_3$ (in solution) are found, which are all slightly lower compared to the results obtained here.[13;142;251]

Figures 7.9a and c show the absolute and relative TTA rates k_{TT} and Δk_{TT} as calculated according to Eq. 7.5. The TTA rates increase for all emitters with increasing doping concentration. The lowest rate is observed for TCTA:Ir(ppy)$_3$ at 1.1 mol % with 8×10^{-13} cm^3/s. For Ir(ppy)$_2$(acac), Ir(chpy)$_3$, and Ir(dhfpy)$_2$(acac), a similar k_{TT} of around 1×10^{-12} cm^3/s is measured at the lower concentrated samples, whereas Ir(BT)$_2$(acac) and Ir(piq)$_3$ show much higher TTA rates with k_{TT} up to 3.3×10^{-12} cm^3/s. The strongest increase of k_{TT} with increasing concentration is observed for Ir(ppy)$_3$ and Ir(chpy)$_3$. While literature suggests that Ir(chpy)$_3$ may suppress TTA compared to Ir(ppy)$_3$ due to its rigid and bulky cycloalkene units,[251] very similar results for the two materials are instead obtained. A difference is mainly observed in the relative TTA rate, but the error margins are very large and do not allow direct conclusions.

For Ir(ppy)$_3$, being an archetype phosphorescent emitter that is well studied in literature, several TTA rates can be found with TCTA

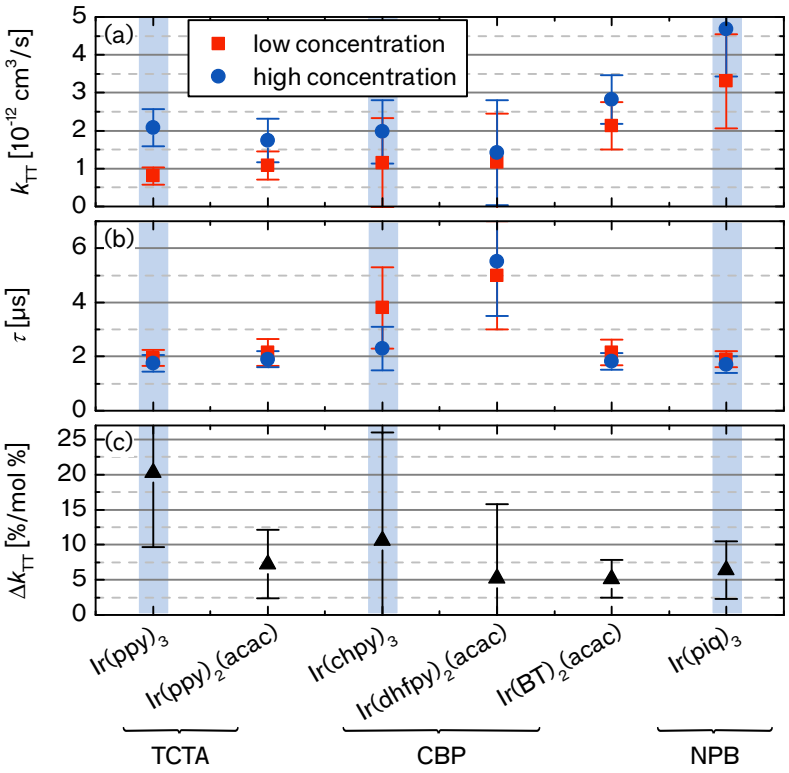

Figure 7.9: Parameters describing the strength of triplet-triplet annihilation in phosphorescent host-guest systems. (a) TTA rate constant k_{TT} and (b) triplet lifetime τ at low and high concentrations. (c) Relative change Δk_{TT} of the TTA rate with increasing doping concentration calculated according to Eq. 7.5 and given in % per mol %. Blue bars mark the homoleptic emitters.

as host and with doping concentrations similar to the here used 9.0 mol %. The values range from $0.7-5.2 \times 10^{-12}$ cm^3/s, which include also the result of this thesis.[13;142;165] However, given the fact that the literature values range over nearly one order of magnitude, the overall reliability of the experiment is questionable. Furthermore, literature shows that k_{TT} of Ir(ppy)$_2$(acac) is lower compared to Ir(ppy)$_3$ at a concentration of 9.7 mol %, which is also observed here.[142] However, this only holds for the higher concentration in this work.

Further deviations to literature are found for NPB:Ir(piq)$_3$, where a value of $k_{TT} = 1.4 \times 10^{-12}$ cm^3/s was measured at 20 wt %, which is much lower than the values extracted here.[13] Baldo *et al.* studied the influence of the doping concentration of the exotherm host-guest system CBP:PtOEP.[12] Comparable to the results of this thesis, they found an increase of the TTA rate with increasing concentration, which can be explained by the reduced distance between two emitter molecules enhancing diffusion-based annihilation. Whether aggregation of emitter molecules further contributes to TTA shall be discussed at the end of this chapter together with the results from other experimental investigations.

7.2.3 *X-Ray Diffraction*

Molecular aggregation of light-emitting compounds often coincides with the formation of crystalline phases.[259] Crystallinity can be well studied using X-ray diffraction techniques because the wavelength of

X-rays resembles the molecular and inter-molecular distances. Studies of the film morphology may not only give valuable insight into aggregation but also on molecular orientation, which is nowadays highly discussed in terms of enhancing the outcoupling efficiency in OLEDs.[92;96;98;99;102] However, up to now, structure analysis of organic semiconductors by means of X-ray diffraction has mainly been applied for the evaluation of charge and exciton transport in thin-film transistors or photovoltaics.[164;260;261] In fact, the light-emitting structures used in OLEDs have rarely been addressed yet.

In conventional specular geometry, the penetration depth of X-rays in organic material is several m, which is orders of magnitude higher compared to the typical layer thickness of organic thin-films. In order to get valuable information from the organic films and not from the underlying substrate, grazing-incidence geometry is used here, where the incident angle ω between ray and sample is kept very small. This leads to total reflection at the interface between thin-film and substrate and furthermore reduces possible damage of the organics by the X-rays due to a broad spreading of the ray over the sample. The specular geometry is here only used for X-ray reflection (XRR) measurements, which allow evaluation of film thickness and roughness.[8]

[8] XRR and GIXRD measurements are carried out by Dr. Lutz Wilde at Fraunhofer IPMS, Center Nanoelectronic Technologies, Dresden.

For the investigations, $Ir(ppy)_3$ and $Ir(ppy)_2(acac)$ are selected as well-studied examples providing different properties regarding their probable tendency to form aggregates and their different transition dipole orientation.[98;142] Both are either doped into CBP or TCTA. Further analysis of the other emitters was not possible due to limited time and facility access. Again, the doping concentration is varied—this time from pure matrix layers over 8, 20, and 50 wt % concentrations up to pure emitter layers (cf. Table 7.3 for concentrations in mol %). All samples are prepared on glass substrates with a nominal thickness of 50 nm and are measured without encapsulation at ambient conditions. Previous studies showed that the molecular arrangement and, hence, X-ray measurements, are not influenced by storage and measurement in air.[163]

Figure 7.10 shows the X-ray reflectivity of both emitters doped into the host TCTA (solid lines). Distinct oscillations are observed for all samples—so-called Kiessig fringes that are formed by interference and contain information about the layer thickness and roughness.[262] The layer thickness d depends on the distance of the fringes and

Table 7.3: Doping concentration Γ of mixed TCTA:guest layers in mol % and fit results from XRR measurements yielding the layer thickness d and roughness ξ.

	Ir(ppy)$_3$			*Ir(ppy)$_2$(acac)*		
material	Γ [mol %]	d [nm]	ξ [nm]	Γ [mol %]	d [nm]	ξ [nm]
guest	100	51.8	(0.1)	100	46.1	(0)
TCTA:guest 50 wt %	53.1	39.2	0.3	55.3	46.0	0.4
TCTA:guest 20 wt %	22.1	40.2	0.5	23.6	50.3	0.7
TCTA:guest 8 wt %	9.0	42.1	0.6	9.7	51.4	0.7
TCTA	100	41.6	0.5			

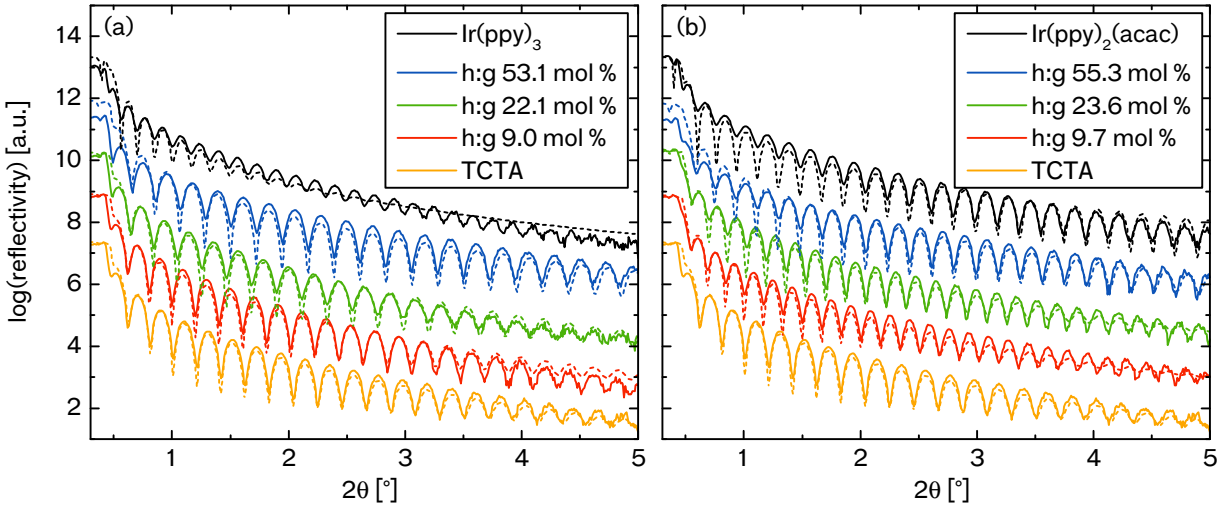

Figure 7.10: X-ray reflectivity as a function of the angle 2θ for thin-film layers of (a) $Ir(ppy)_3$ and (b) $Ir(ppy)_2(acac)$ as guest (g) mixed with the host (h) TCTA at different concentrations. Measurements (solid lines) and fits (dashed lines) of the different concentrations are split in intensity for better visualization.

[9] The density of $Ir(ppy)_2(acac)$ is unknown and is approximated by the density of $Ir(ppy)_3$.

can be precisely determined by fitting the curves (dashed lines, cf. Sec. 4.2.1).[263] Table 7.3 shows the results, which lie between 40 and 50 nm. Deviations compared to the nominal thickness of 50 nm that should have been evaporated appear mainly due to an incorrect density of the materials.[9] Uncertainties in the tooling factors can lead to further deviations. All layers are relatively smooth with a roughness ξ below 1 nm. Stronger variations in the surface height would lead to a smaller amplitude and less fringes. The TCTA host layer shows a roughness of 0.5 nm, which stays relatively constant when small amounts of the emitters are doped into the host. At 50 wt %, the films become slightly smoother. For the pure emitter layers, fits indicate very smooth films with a roughness below 0.1 nm. However, these values should be handled with great care because the fit shows large deviations from the measurement, especially for $Ir(ppy)_3$. Comparing the XRR data of $Ir(ppy)_3$ to $Ir(ppy)_2(acac)$ and TCTA, a lower amplitude is observed for $Ir(ppy)_3$ and the fringes blur at smaller angles. Contrary to the fit, both observations are related to an increased film roughness, which would indicate crystallization of the $Ir(ppy)_3$ film. XRR measurements are furthermore performed for $Ir(ppy)_3$ and $Ir(ppy)_2(acac)$ doped into CBP (data not shown here). A slightly increased roughness is observed for the CBP-doped systems, but still the mixed layers are very smooth.

In the following, grazing incidence X-ray diffraction (GIXRD) measurements are performed in out-of-plane direction. Figures 7.11a and b show the results for $Ir(ppy)_3$ and $Ir(ppy)_2(acac)$, respectively, as well as for their mixture into TCTA at different concentrations. The pure emitter films show a distinct peak at around 11°, which indicates that the emitters form crystallites. In addition, a weak shoulder at approximately 22° originating from diffusely scattered radiation hints to further amorphous regions or could be related to the glass substrate.[163] In contrast, the XRD spectra of TCTA and CBP show only

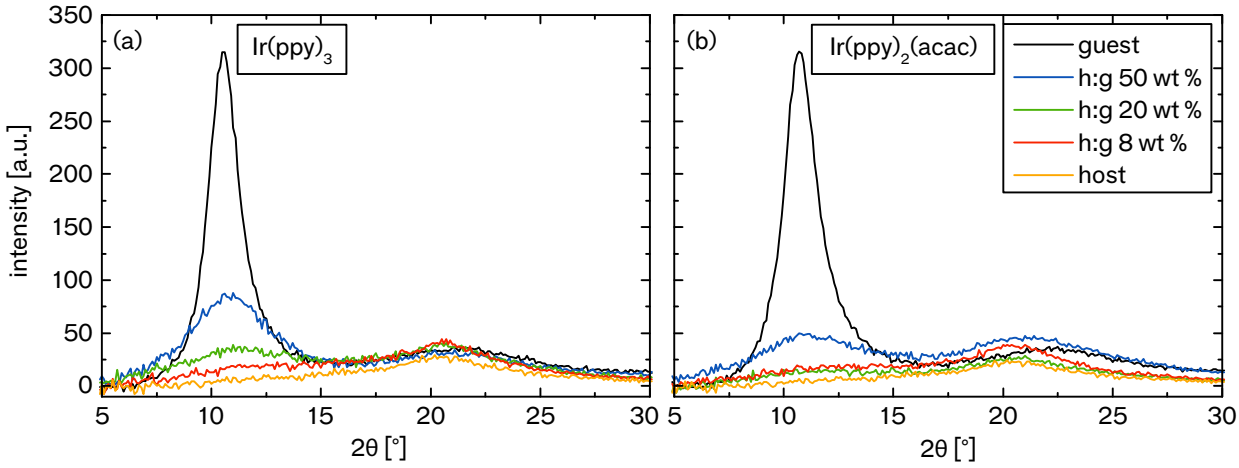

Figure 7.11: XRD measurements of thin-films containing (a) $Ir(ppy)_3$ or (b) $Ir(ppy)_2(acac)$ (g) doped into TCTA (h), respectively. The data is scaled with the layer thickness.

this shoulder leading to the conclusion that both matrix materials are amorphous. If the emitters are now doped into one of the two matrix materials, the diffraction peak at 11° decreases, but is still present down to a doping concentration of 20 wt %. At 8 wt %, a concentration that is typically used in OLEDs, the peak is hardly observed anymore. Nevertheless, the presence of the peak in the higher concentrated samples discloses that $Ir(ppy)_3$ and $Ir(ppy)_2(acac)$ form crystalline grains also when embedded into a matrix. This suggests that both emitters form aggregates in the film.

According to Bragg's law, the diffraction angle θ is inversely proportional to the distance d of the repeating structures:

$$n\lambda = 2d \sin\theta, \tag{7.6}$$

where n is an integer. In order to extract the peak position and FWHM, all spectra are fitted with two Gauss functions (see Fig. 7.12). This ensures that the peak at 22°, which is caused by diffusely scattered radiation, does not interfere with the position of the main peak. The fit results and standard deviations are summarized in Table 7.4.

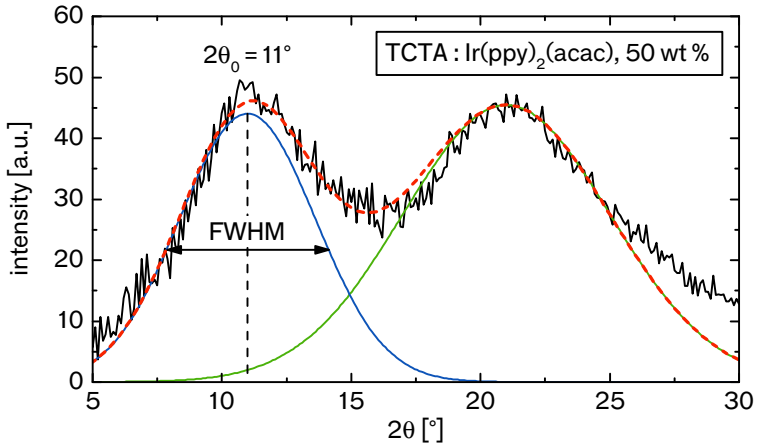

Figure 7.12: GIXRD spectrum of TCTA:$Ir(ppy)_2(acac)$ at 50 wt % (black line) together with a fit (red dashed line) that is composed of two individual Gauss functions, one for each observed peak.

	Ir(ppy)$_3$		*Ir(ppy)$_2$(acac)*	
material	$2\theta_0$ [°]	L_c [nm]	$2\theta_0$ [°]	L_c [nm]
guest	10.60 ± 0.01	4.38 ± 0.04	10.82 ± 0.02	3.81 ± 0.07
TCTA:guest 50 wt %	10.75 ± 0.02	2.07 ± 0.03	10.99 ± 0.06	1.43 ± 0.04
TCTA:guest 20 wt %	10.95 ± 0.06	1.49 ± 0.04	12.40 ± 0.10	1.24 ± 0.05
CBP:guest 50 wt %	10.86 ± 0.01	2.46 ± 0.03	10.98 ± 0.01	2.26 ± 0.03
CBP:guest 20 wt %	11.08 ± 0.05	2.22 ± 0.09	11.17 ± 0.07	2.09 ± 0.11

Table 7.4: Diffraction angle $2\theta_0$ of the main reflex and coherence length L_c calculated from the peak width via the Scherrer equation (Eq. 7.7). Errors represent the standard deviation of the fits.

Compared to the Ir(ppy)$_3$ peak, which is found at 10.60°, the peak in Ir(ppy)$_2$(acac) is positioned at 10.82°, which would indicate a slightly stronger packing in real space if both materials would possess the same crystal structure.[10]

In experiment, the diffraction peak shifts to higher angles when reducing the emitter concentration, which, hints to a compression of the emitter aggregates with increasing host proportion. This compression could be imagined as an increase in surface tension when the emitter aggregates become smaller due to the strong intermolecular attraction that is evoked by the emitter's dipole-dipole potential.

Berger *et al.* and Takayasu *et al.* investigated the crystal structure of Ir(ppy)$_3$.[264;265] Both found that Ir(ppy)$_3$ crystallizes in the acentric tetragonal space group $P\bar{4}2_1c$. Single crystals were grown upon vacuum sublimation, which is analogously to the thin-film evaporation used here.[11] Thus, it is expected that the Ir(ppy)$_3$ single crystal data may be compared to its thin-film structure.

The powder pattern of Ir(ppy)$_3$ is displayed in Fig. 7.13a (provided by Berger *et al.*, Ref. 264). Two peaks are observed at the angle of the thin-film diffraction peak: A smaller peak originating from the (101)-plane at 10.42° and the most intense peak of the spectrum at 10.82°, which is correlated to the (220)-plane. Note that Takayasu *et al.* measured a slightly larger crystallite size, so that the (220)-peak is positioned at 10.72° in their powder pattern.[265] Although neither peak fits exactly to the observed thin-film peak, it is probable that the latter originates from reflection at the (220)-plane. The reasons are twofold: First, the (220)-peak is the most intense one of the whole spectrum, and, second, this peak fits much better for decreasing Ir(ppy)$_3$ concentrations, where $2\theta_0$ increases.

Figure 7.13b shows the crystal packing of the Ir(ppy)$_3$ unit cell, which contains eight molecules. The C_3 symmetry axis of Ir(ppy)$_3$ and its high dipole moment lie roughly parallel to c pointing in the direction of the nitrogen atoms. Each four molecules can be grouped together to form a tetramer, where each two molecules alter in chirality (see Fig. 7.13c). Hence, their permanent dipole moments oppose in direction.[264]

For Ir(ppy)$_2$(acac), no suitable crystal structure has been measured yet.[12] Therefore, it cannot be evaluated whether the Ir(ppy)$_2$(acac) thin-film diffraction peak, which is very similar to Ir(ppy)$_3$, originates from the same diffraction plane.

[10] The stronger packing is supported by the fact that Ir(ppy)$_2$(acac) is slightly smaller than Ir(ppy)$_3$ (cf. Table 7.5).[99]

[11] Note that Ir(ppy)$_3$ shows polymorphic character. Breu *et al.* measured a different crystal structure for single crystals that had been grown by slow evaporation from solution.[266]

[12] So far, it was only measured for single crystals that were grown from solution.[267] As already discussed, their structure may strongly deviate from thin-film structure and shall not be taken for evaluation here.

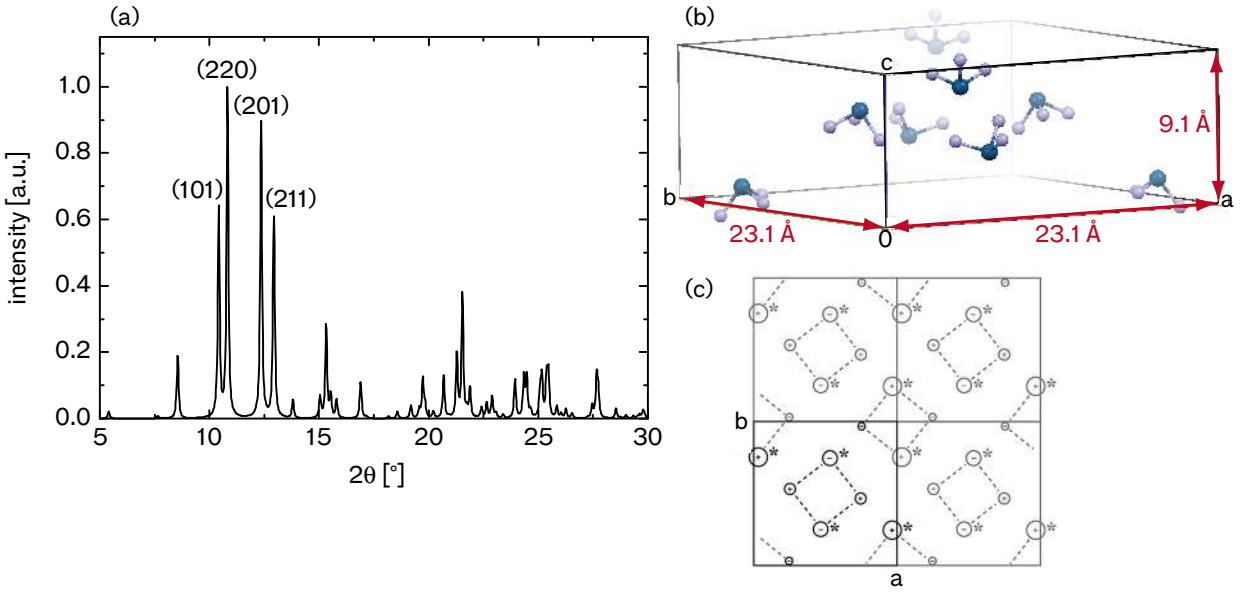

Figure 7.13: (a) Powder pattern of $Ir(ppy)_3$ with indication of the four main peaks. (b) Packing diagram of $Ir(ppy)_3$ showing the unit cell containing eight molecules. Molecules are outlined by their iridium cores and the three nitrogen atoms. The spatial depth of the molecules is indicated by decreasing color intensity. (c) Four unit cells with tetramers of $Ir(ppy)_3$, displayed along c. Large/small circles correspond to higher/lower lying $Ir(ppy)_3$ molecules. $(+/-)$-signs indicate the direction of the permanent dipole moment of the molecule, which is approximately parallel to the c-axis. Crystallographic data for (a,b) and the figure of part (c) are taken from Ref. 264. Reprinted with permission. Copyright 2010, Wiley VCH.

In order to compare the amount of molecular aggregation between the two emitters, the size of crystallite grains is approximated with the Scherrer equation, which correlates the FWHM $\Delta(2\theta_0)$ of the diffraction peak (located at $2\theta_0$) with the coherence length L_c:[164]

$$L_c = \frac{K\lambda}{\cos((2\theta_0)/2)\Delta(2\theta_0)}. \tag{7.7}$$

Here, λ denotes the wavelength of the X-rays and K is a shape factor that is approximated here as 1. The FWHM and $2\theta_0$ are determined by fitting the spectra with two Gauss functions (cf. Fig. 7.12) and the results are given in Table 7.4.

The coherence length is 4.4 nm for $Ir(ppy)_3$ and 3.8 nm in the case of $Ir(ppy)_2(acac)$. Furthermore, it decreases when embedding the emitters into the hosts.[13] For all host-guest combinations, L_c is higher for $Ir(ppy)_3$ compared to $Ir(ppy)_2(acac)$ and for using CBP instead of TCTA as host. A longer coherence length correlates with larger crystallite grains and therefore hints that $Ir(ppy)_3$ forms larger aggregates than $Ir(ppy)_2(acac)$, as has been previously suggested by Reineke *et al.*[142] However, the calculated coherence length gives only a lower limit for the size of aggregates, which could effectively be much larger. For instance, a distortion of the molecular arrangement due to cumulative disorder yields very small grain sizes although molecular arrangement is still present. Despite the absence of a clear diffraction peak in the 8 wt % samples, aggregation could still be present because diffraction on the (220)-plane is omitted if the grain size becomes too small. However, as the diffraction peak is still visible at 20 wt %, a significant amount of aggregates must be larger than the unit cell, which contains eight molecules.

Up to now, only the out-of-plane direction is studied by GIXRD. In order to find out more about the orientation of the molecules, 2D graz-

[13] Note that only the coherence length in out-of-plane direction is calculated giving a hint on the extension of the aggregates perpendicular to the substrate. The in-plane extension, however, could be different.

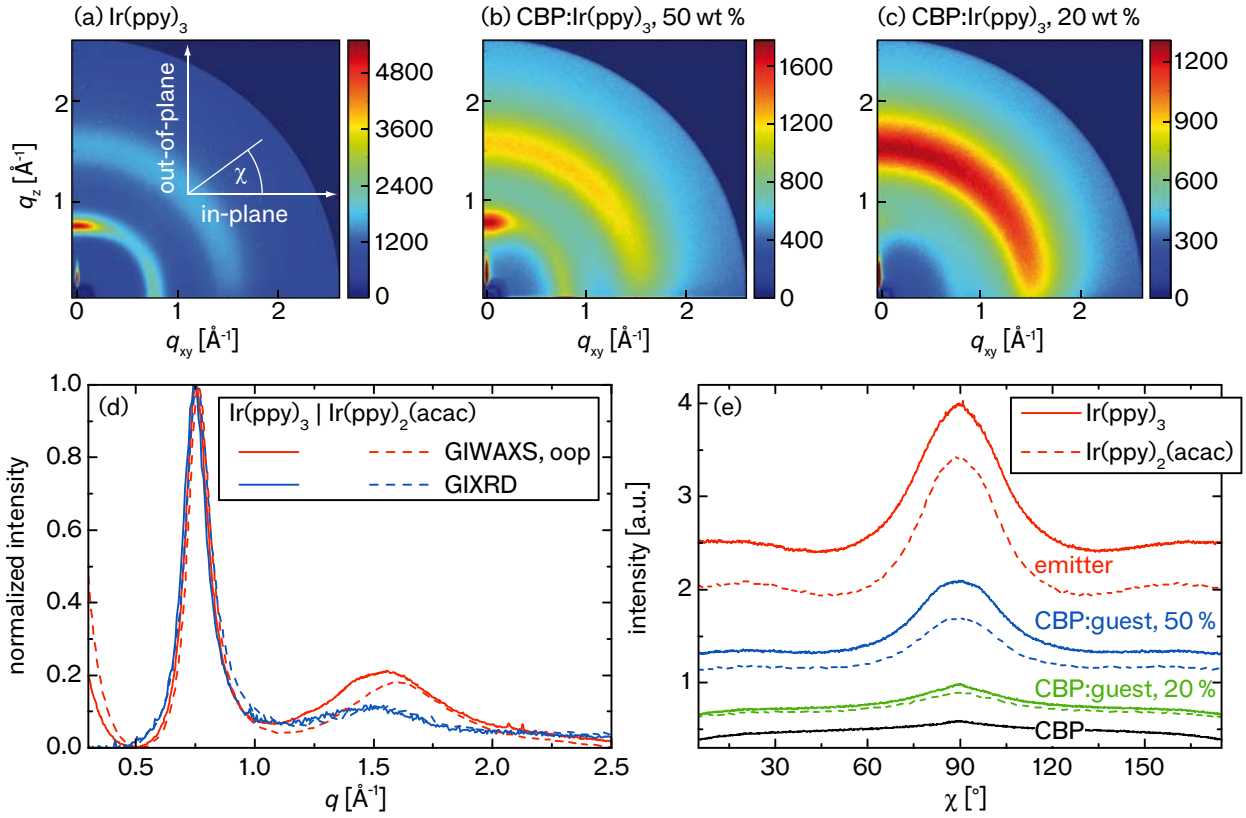

Figure 7.14: 2D-GIWAXS measurements on (a) $Ir(ppy)_3$, (b) CBP:$Ir(ppy)_3$, 50 wt %, and (c) CBP:$Ir(ppy)_3$, 20 wt %. (d) Comparison of the out-of-plane (oop)-component, calculated by summation over all χ between 80 and 100°, to the GIXRD-measurements. (e) Intensity of the inner ring as a function of the angle χ by summation over $0.6\,\text{Å}^{-1} \leq q \leq 1.0\,\text{Å}^{-1}$.

[14] Measurements are carried out by Chris Elschner (TU Dresden) at the Stanford Synchrotron Radiation Lightsource, CA, USA.

[15] The peak at very small q_z and $q_{xy} = 0$ results from the incident radiation.

ing incidence wide-angle X-ray scattering (GIWAXS) measurements are performed on pure $Ir(ppy)_3$, $Ir(ppy)_2(acac)$, and CBP films and on the respective host-guest systems with 50 and 20 wt %.[14] Exemplary data for $Ir(ppy)_3$-doped systems are shown in Fig. 7.14. Here, q_z denotes the out-of-plane direction and q_{xy} the in-plane direction. The scattering vector q_z relates to the diffraction angle 2θ via [263]

$$q_z = \frac{2\pi}{\lambda}\left(\sin\omega + \sin\left(2\theta - \omega\right)\right). \tag{7.8}$$

An isotropic orientation of the crystallites is visible as a ring in the 2D-measurements, whereas spots indicate a strong orientation. [164] In Figs. 7.14a–c, a broad halo ring is observed at $q = 1.5\,\text{Å}^{-1}$, which is related to the second peak in GIXRD measurements at around 22° and confirms the assumption of diffusely scattered radiation due to amorphous regions. [163] More interesting, a peak is detected in out-of-plane direction with further intensity along a ring.[15] The same observations are made for $Ir(ppy)_2(acac)$ (see Fig. D.1 in App. D). Figure 7.14d shows the out-of-plane component by a summation over the polar angle χ from $80° < \chi < 100°$ in comparison to the GIXRD measurements. The first diffraction peak from GIXRD is clearly reproduced. Slight deviations are visible in the width of the first peak and stronger deviations in intensity of the second peak. These deviations are mainly attributed to the missing background information for the GIWAXS data and, thus, incorrect normalization. Furthermore, the

summation over certain polar angles leads to changing intensity of the first peak compared to the second. Nevertheless, the measurements allow a qualitative comparison.

In order to illustrate the orientation of this Bragg peak, Fig. 7.14e shows a summation over all q from $0.6\,\text{Å}^{-1}$ to $1.0\,\text{Å}^{-1}$ as a function of the polar angle χ. In out-of-plane direction ($\chi = 90°$), the peak has a FWHM of approximately 30° and its shape is very similar for $Ir(ppy)_3$ and $Ir(ppy)_2(acac)$. In addition, the peak is also preserved in the mixed layers (see Figs. 7.14b and c). The pure emitter layers further show a slight increase in intensity in in-plane direction, which vanishes when decreasing the emitter concentration and which is not present in the pure CBP film. The following section now discusses the results in more detail.

7.2.4 *Conclusions on Emitter Orientation*

2D-GIWAXS measurements show that $Ir(ppy)_3$ and $Ir(ppy)_2(acac)$ crystallites are textured. More precisely, a comparison of the $Ir(ppy)_3$ GIXRD-data with its powder spectrum reveals that the Bragg peak at 10.60° results from reflection on the (220)-plane. This peak is mainly found in out-of-plane direction with a further, but strongly reduced, intensity in-plane. This indicates that $Ir(ppy)_3$ crystallites are predominantly oriented with the (220)-plane parallel to the substrate. Hence, the $Ir(ppy)_3$ symmetry axis points roughly parallel to the substrate as illustrated in Fig. 7.15. The order is relatively low and the crystallite size is small, but still a preferential orientation is visible. Furthermore, this orientation is also preserved when embedding the emitter into a matrix, at least for the investigated concentrations above 20 wt %. The XRD-measurements for $Ir(ppy)_2(acac)$ show very much the same results and emitter orientation is also present for $Ir(ppy)_2(acac)$. However, due to missing knowledge on its crystal structure, the exact molecular orientation with respect to the substrate remains unknown.

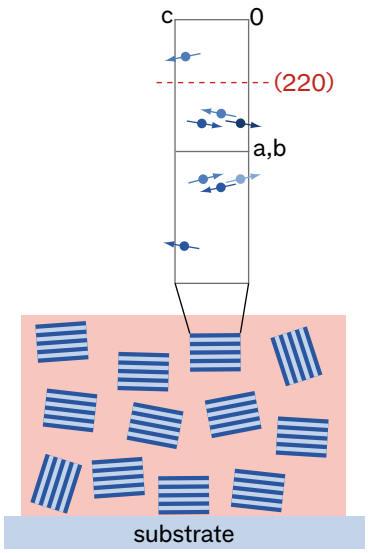

Figure 7.15: Schematic illustration of the orientation of $Ir(ppy)_3$ crystallites when embedded in a matrix. The top shows the crystal structure of the unit cell with the (220)-plane parallel to the substrate. The emitter symmetry axis and its permanent dipole moment, which both point into the direction of the arrows, are oriented roughly in-plane. The spatial depth of the molecules is indicated by decreasing color intensity.

The finding of molecular orientation (i.e., orientation of the permanent dipoles) of both iridium compounds is very interesting when comparing to the orientation of their transition dipole moments: $Ir(ppy)_2(acac)$ transition dipoles embedded with 8 wt % into a CBP matrix exhibit a preferential horizontal orientation with an anisotropy factor of $a = 0.23$, but $Ir(ppy)_3$ dipoles are found to be isotropically oriented ($a = 0.33$) (see Chapter 5 and Ref. 98). Hence, the orientation of the emitter does not necessarily imply an orientation of the transition dipoles.

The orientation of the transition dipole moment is observed in many established iridium compounds and its origin is currently strongly debated in the OLED community. Very recently, two different approaches were reported: Graf *et al.* suggested that the different orientation of the two emitters originates from their different dipole-dipole potential (cf. Table 7.5).[99] The strong potential between $Ir(ppy)_3$ molecules is correlated to an increased aggregation, which

leads to a reduced influence of the emitter orientation by the environment. For all other emitters studied by Graf *et al.* (the very same seven compounds that are investigated throughout this chapter), a preferential horizontal orientation is found and attributed to spontaneously induced London forces between the emitter and the matrix causing anisotropy.

In another study, Kim *et al.* investigated the transition dipole orientation of one homoleptic and three heteroleptic emitters: The homoleptic compound showed isotropic orientation whereas the heteroleptic compounds were preferentially horizontally aligned.[96] Performing quantum chemical calculations, the authors found that all emitters form supramolecules together with their host materials (consisting of NPB and bis(4,6-(3,5-di-(3-pyridyl)phenyl))-2-methylpyrimidine (B3PYMPM)). While these supramolecules arrange in a more or less linear fashion and lie flat on the substrate, the emitter in the middle of the two matrix molecules aligns with its symmetry axis perpendicular to the substrate. The key difference between the homoleptic and the heteroleptic emitters is the orientation of their transition dipoles with respect to the symmetry axis: The heteroleptic emitters possess a dipole moment perpendicular to the symmetry axis, which in the supramolecular environment leads to horizontally oriented dipoles. The transition dipoles of the homoleptic compound, instead, are slanted by an angle of 67.6° from the symmetry axis leading to isotropic dipole orientation.

Note that the term 'isotropic' dipole orientation might be misleading in this context. In the optical measurement of the transition dipole moment only the *ratio* of horizontal to vertical dipoles may be determined (cf. Sec. 2.5.2). An anisotropy factor of 0.33 could, on one hand, indicate that the molecule is not oriented and that the transition dipoles point randomly in all directions. On the other hand, it could also indicate that the emitter is oriented but that its transition dipoles are slanted by an angle of 55° with respect to the substrate normal.[16]

[16] The angle is calculated by Christian Hänisch (TU Dresden).

The GIWAXS measurements support the hypothesis of Kim *et al.* that the iridium compounds are oriented with respect to the substrate. However, in contrast to their report, molecular orientation is here especially observed for pure emitter layers and seems to be an intrinsic property of the material growth. Quantum chemical calculations may show how the transition dipoles are oriented in $Ir(ppy)_3$ and $Ir(ppy)_2(acac)$ with respect to their symmetry axis.[17] If these two molecules show the same trend as the four emitters studied by Kim *et al.*, the origin of emitter orientation may then not only be governed by the formation of supramolecules with the matrix, but also by intrinsic orientation of the emitters within aggregates and the respective orientation of the aggregate on the substrate.

[17] According to a very recent publication by Moon *et al.*, the three transition dipole moments of $Ir(ppy)_3$ point from the iridium core to the three ligands and are mutually orthogonal.[101] Hence, this leads to the observed isotropic orientation.

7.2.5 Comparison of the Different Methods—Emitter Aggregation

Finally, the results from the individual measurement techniques shall be compared with focussing on molecular aggregation. The steady-

state PL measurements showed a red-shift and broadening of the spectra with increasing doping concentration for all emitters. The effect was quantified by applying a Poisson progression to the spectra and, thus, calculating the vibronic transitions. A difference between homoleptic and heteroleptic compounds was found, where the homoleptic compounds showed a stronger change in the Huang-Rhys factor and in the individual broadening of the lines upon increasing emitter concentration. This was explained by the stronger aggregate formation of the homoleptic emitters.

The time-resolved measurements drew a slightly different picture. TTA was strongest in $Ir(piq)_3$, whereas $Ir(ppy)_3$ and, to some smaller extend, $Ir(chpy)_3$ exhibited the largest change in k_{TT} with increasing concentration. Taking both observations, the highest absolute k_{TT} and the strongest change with increasing concentration, together, aggregation of the homoleptic compounds could again be the reason. However, the measurements underlie high errors and deviations are observed compared to literature.

The X-ray measurements directly revealed the formation of small crystallites for both $Ir(ppy)_3$ and $Ir(ppy)_2(acac)$ at concentrations above 20 wt %. Although the coherence length of these crystallites was rather small with around 2 nm at 20 wt %, it is expected that the aggregates themselves are larger. A comparison of $Ir(ppy)_3$ with $Ir(ppy)_2(acac)$ showed slightly larger crystallites for $Ir(ppy)_3$. However, the molecular diameter of $Ir(ppy)_3$ is also higher compared to $Ir(ppy)_2(acac)$ so that the larger crystallites do not directly imply a stronger aggregation for $Ir(ppy)_3$ (cf. Table 7.5).

Overall, emitter aggregation was observed by all three methods and probably takes place for all iridium compounds. Differentiating its extent, however, is rather complicated. Nevertheless, taking all measurements into account, aggregation seems to be more pronounced for homoleptic emitters. The remaining question is now, what the underlying mechanisms are.

So-called Keesom forces describe the attraction between two molecules arising from their permanent dipole moment μ_D, which is given in Table 7.5.[99] Reineke *et al.* already related the stronger aggregation of $Ir(ppy)_3$ compared to $Ir(ppy)_2(acac)$ to its higher dipole moment.[142] Indeed, the dipole moments of the investigated homoleptic compounds are all higher than those of the heteroleptic ones, which for the latter is also related to the used acac ligand.[268] The attraction between two molecules, however, is described by the dipole-dipole potential U, which not only depends on the dipole moment, but also on the distance R between the two molecules:[269]

$$U \propto -\frac{\mu_{D,1}^2 \mu_{D,2}^2}{R^3}. \tag{7.9}$$

The potential U_{GG} for two equal guest (G) molecules is calculated in Table 7.5 relative to the potential of $Ir(ppy)_3$ while approximating R with the molecule's diameter. The highest potential is found for $Ir(ppy)_3$. For $Ir(piq)_3$, the potential yields 40 % compared to $Ir(ppy)_3$ and for all other emitters the amount is less than 10 %. Although

the potential is highest for the homoleptic emitters, the difference between the potentials of $Ir(chpy)_3$ and $Ir(ppy)_2(acac)$ is marginal. Moreover, the attraction between any two emitters should be compared to the potential U_{GH} arising between guest and host, which is also displayed in Table 7.5. As all three hosts possess low dipole moments ($\mu_{D,TCTA}$ =0.00 D, $\mu_{D,CBP}$ =0.03 D, and $\mu_{D,NPB}$ =0.84 D)[18], the potential between host and guest is negligible and attraction, thus, takes only place between two emitters.

[18] Values are calculated by Reinhard Scholz (TU Dresden), performing density functional theory (DFT) with a B3LYP functional.

Table 7.5: Selected properties of phosphorescent emitters. Values of the emitter's diameter R and the dipole moment μ_D are taken from Ref. 99. The dipole-dipole potentials between two emitter molecules U_{GG} and between emitter and host U_{GH} are calculated relative to the potential of $Ir(ppy)_3$ using Eq. 7.9. Homoleptic emitters are marked with a blue background.

emitter	R [Å]	μ_D [D]	$U_{GG}/U_{Ir(ppy)_3}$	$U_{GH}/U_{Ir(ppy)_3}$
$Ir(ppy)_3$	11.4	6.40	1.00	0.00
$Ir(ppy)_2(acac)$	11.0	1.66	0.07	0.00
$Ir(chpy)_3$	11.6	2.02	0.09	0.00
$Ir(dhfpy)_2(acac)$	17.7	1.16	0.01	0.00
$Ir(BT)_2(acac)$	12.6	1.76	0.06	0.00
$Ir(MDQ)_2(acac)$	13.8	1.75	0.04	0.00
$Ir(piq)_3$	13.5	5.20	0.40	0.01

Different studies reported on spectral changes upon dipole interactions of highly polar guests.[270–272] For instance, Baldo *et al.* reported on spectral red-shifts with increasing fraction of a polar molecule due to the formation of ordered domains.[273] Within these domains, dipole-dipole interactions lead to an energetic reduction of the transition and, thus, a red-shift with increasing domain size. However, this is not correlated with spectral broadening and, therefore, can be ruled out here. If the guest is instead uniformly mixed into the host, a red-shift of energy should depend linearly on the guest concentration. Spectral broadening is instead caused if the guests are randomly oriented.[273] Furthermore, spectral red-shift within aggregates may result from exciton migration to the lowest energetic state. In this case, a spectrum should shift with decreasing temperature, which has at least for the case of NPB:$Ir(MDQ)_2(acac)$ not been observed.[274]

The observations throughout this section suggest that several processes may overlap leading to both red-shift and spectral broadening. Hence, although aggregation may be driven by the mutual attraction of two dipoles, it cannot explain the differences observed in experiment alone. Instead, also the molecular structure might play a role. Possibly, the three equal ligands in the homoleptic compounds allow a closer packing compared to heteroleptic molecules. Another idea is that the acetylacetonate ligand may omit aggregation. However, more investigations on the chemical structure and arrangement are necessary, e.g. by DFT calculations, to elucidate the origin of aggregation.

7.3 *Influence of the Matrix Material*

In the former section, molecular aggregation was observed for homoleptic compounds, which exhibited a strong dipole-dipole potential

compared to the potential between emitter and matrix. In order to find ways to decrease emitter aggregation, the influence of the matrix material shall be studied in more detail, again by photoluminescence and time-resolved measurements. $Ir(ppy)_3$ and $Ir(ppy)_2(acac)$ are selected for the matrix study due to their similar structure, which should facilitate comparability. Both materials are doped into TCTA (cf. previous section), TPBi, and CBP. Furthermore, the red-emitting $Ir(MDQ)_2(acac)$ is doped into four different hosts, namely TCTA, TPBi, NPB, and 4P-NPD. The chemical structures of all used host materials are shown in Fig. 4.6. Table 7.6 displays the used concentrations in mol %.

emitter	matrix	Γ_1 [mol %]	Γ_2 [mol %]	$U_{GH}/U_{Ir(ppy)_3}$
$Ir(ppy)_3$	TCTA	1.1	9.0	0.00
$Ir(ppy)_3$	TPBi	1.0	8.0	0.93
$Ir(ppy)_3$	CBP	0.7	6.1	0.00
$Ir(ppy)_2(acac)$	TCTA	1.2	9.7	0.00
$Ir(ppy)_2(acac)$	TPBi	1.1	8.7	0.07
$Ir(ppy)_2(acac)$	CBP	0.8	6.6	0.00
$Ir(MDQ)_2(acac)$	TCTA	1.0	9.5	0.00
$Ir(MDQ)_2(acac)$	TPBi	0.8	8.5	0.05
$Ir(MDQ)_2(acac)$	NPB	0.7	7.4	0.00
$Ir(MDQ)_2(acac)$	4P-NPD	1.0	9.5	0.00

Table 7.6: Doping concentrations Γ_1 and Γ_2, and the relative dipole-dipole potential $U_{GH}/U_{Ir(ppy)_3}$ between guest and host of all investigated host-guest systems. Blue backgrounds mark the systems that have been studied in Section 7.2.

In comparison to all other matrix materials, TPBi possesses a rather high dipole moment ($\mu_{D,TPBi} = 5.99\,D$), whereas the dipole moment of 4P-NPD is equal to the structurally similar compound NPB ($\mu_{D,4P\text{-}NPD} = 0.84\,D$).[19] Here, TPBi is the most interesting host because it offers a dipole-dipole potential between host and guest that is similar to the potential between two guest molecules (see Table 7.6).

On the other hand, it is known from solutions that the polarity of the solvent strongly influences the spectrum of the emitter, where typically a red-shifted[20] spectrum is observed for highly polar solvents.[106;275–277] This effect has later also been found in organic thin-films by Bulović *et al.*, where it is called solid-state solvation effect.[271] The authors doped the highly polar [2-methyl-6-[2-(2,3,6,7-tetrahydro-1H,5H-benzo[*ij*]quinolizin-9-yl) ethenyl]-4H-pyran-4-ylidene]propane-dinitrile (DCM2) at a fixed concentration into a co-host of the polar Alq_3 and the non-polar N,N'-diphenyl-N,N'-bis(3-methylphenyl)-1,1'-biphenyl-4,4'-diamine (TPD). By changing the ratio between the two hosts, the spectrum exhibited a red-shift with increasing fraction of the more polar Alq_3. Further evidence of solid-state solvation was found subsequently.[42;278] Madigan *et al.* could finally confirm that the effect is not necessarily attributed to guest aggregation, but simply an analogue to the theory of solvatochromism in liquids.[279]

[19] Dipole moments are again calculated by Reinhard Scholz (TU Dresden), performing DFT with a B3LYP functional.

[20] Note that the direction of the energetic shift depends on the difference between the chromophore's dipole moments in ground and excited state.[275]

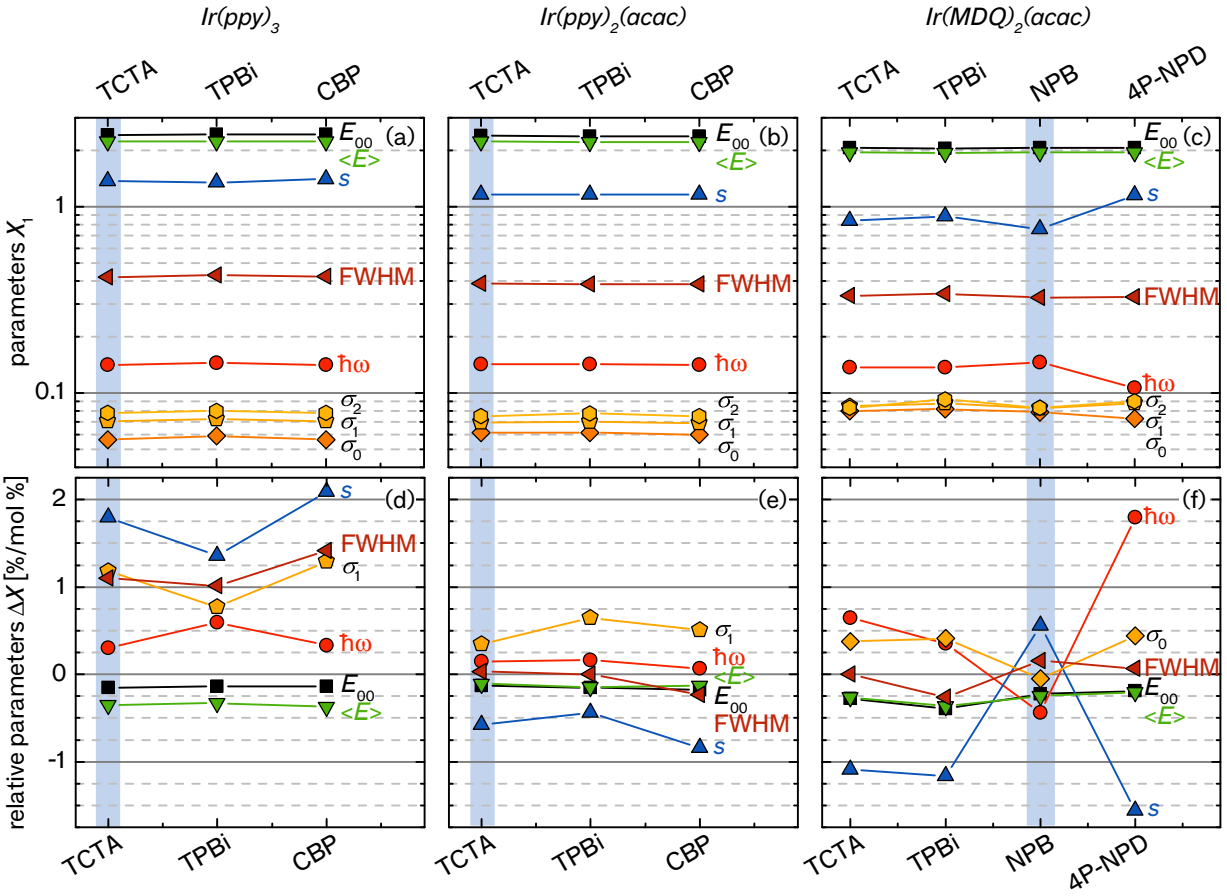

Figure 7.16: Spectroscopic parameters of (a,d) $Ir(ppy)_3$, (b,e) $Ir(ppy)_2(acac)$, and (c,f) $Ir(MDQ)_2(acac)$ doped into different host materials. Data are accessed by fitting the emission intensity $I(E)/E^3$ to the Poisson progression in Eq. 7.3. (a-c) Absolute values at Γ_1 doping concentration (see Table 7.6). The parameters E_{00}, $\langle E \rangle$, FWHM, $\hbar\omega$, and σ_ν are given in eV; s is dimensionless. (d-f) Relative change ΔX of the parameters with increasing doping concentration. Values are calculated according to Eq. 7.5 and are given in % per mol %. Blue bars mark the hosts that were used in Sec. 7.2.

7.3.1 *Photoluminescence Measurements*

In the following, PL spectra of low and highly doped host-guest systems are measured and analyzed in terms of a Poisson progression as explained in Sec. 7.2.1. Figure 7.16 displays the fitted parameters X_1 at low concentration and the relative parameters ΔX upon increasing concentration as calculated by Eq. 7.5. At low concentration, the spectra barely change for all chosen matrix materials. Only for $Ir(MDQ)_2(acac)$, a stronger variation is observed when using 4P-NPD. Here, the Huang-Rhys factor s is higher than 1, whereas for all other hosts the fundamental transition is most efficient, leading to $s < 1$. Instead, the line distance $\hbar\omega$ is reduced in 4P-NPD.

With increasing doping concentration, the fit parameters change by up to 2 % per mol % (cf. Fig. 7.16d-f). For $Ir(ppy)_3$, slight differences regarding the three matrix materials are observed: Using TPBi, the lowest Δs and $\Delta\sigma_1$ are measured. The FWHM increases for all used hosts with increasing concentration, where the highest increase is observed for CBP, which also shows the strongest change in s and σ_1. Whereas for $Ir(ppy)_2(acac)$ the parameter changes are overall small, $Ir(MDQ)_2(acac)$-doped systems exhibit stronger differences between the used hosts. Specifically, the Huang-Rhys factor decreases for

$Ir(MDQ)_2(acac)$ with increasing doping concentration when using TCTA, TPBi, or 4P-NPD, but increases when using NPB. For 4P-NPD, moreover, a large increase in $\hbar\omega$ and the lowest Δs are observed. However, considering the differences of Δs, $\Delta\sigma_1$, and the FWHM that were observed in Fig. 7.6 between the seven emitters, the influence of the matrix material on those parameters is much smaller.

From the observed data, a particular strong influence of the solid-state solvation effect can be ruled out as the highly polar TPBi did not lead to stronger spectral shifts than the other hosts. In the case of $Ir(ppy)_3$, TPBi even causes the smallest red-shift and broadening. The strongest influence is instead observed for CBP, which possesses the lowest dipole moment. Possibly, the similar dipole-dipole potential between two $Ir(ppy)_3$ molecules and $Ir(ppy)_3$ and TPBi could in fact reduce the aggregate formation. However, this theory does not hold for the other emitters, where the differences between the matrix materials cannot directly be correlated to their different dipole-dipole potential.

7.3.2 *Time-Resolved Spectroscopy*

The influence of the matrix material on triplet-triplet annihilation is furthermore studied in time-resolved measurements using $Ir(ppy)_3$ and $Ir(ppy)_2(acac)$ as emitters. Transients of $Ir(ppy)_3$-doped hosts are depicted in Fig. 7.17. The initial triplet exciton density is kept constant at $2-2.5 \times 10^{18}\,cm^{-3}$ enabling direct comparability of the curves. The decay is very similar when using TCTA and CBP as hosts: At low concentration, only a small deviation from monoexponential decay is observed during the first microseconds. Then, at higher concentration, the curves exhibit a faster initial decay and a slightly decreased lifetime. In contrast, using TPBi as matrix, a quick initial decay is already observed at 1 wt % and becomes even faster with increasing guest concentration. In addition, the decay of the triplet density decelerates after a few microseconds leading to a much longer lifetime, especially for the 8 wt % sample. Interestingly, this strong

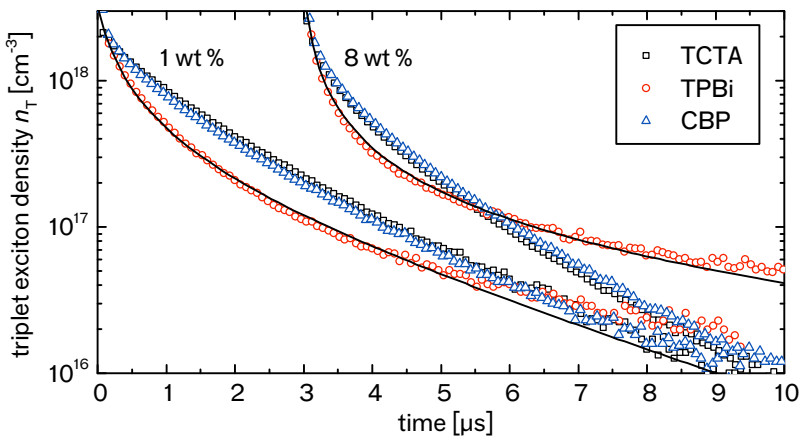

Figure 7.17: Transient decay of $Ir(ppy)_3$ doped with 1 wt % (left) and 8 wt % (right) into different hosts. Curves are selected in terms of similar initial triplet exciton density. Lines show fits of the TPBi:$Ir(ppy)_3$ data to Eq. 3.3.

influence of the matrix TPBi on the phosphorescent decay is not observed for $Ir(ppy)_2(acac)$ as will be shown later.

The transients of all host-guest combinations are again measured at different pump intensities. Curves with a pump density lying in the TTA regime (cf. Fig. 7.7a) are fitted to Eq. 3.3 yielding the triplet lifetime τ and the TTA rate k_{TT}. The average parameters of each sample are summarized as a function of emitter concentration in Figure 7.18. The triplet lifetime is approximately 2 s and decreases with increasing concentration. Only TPBi:$Ir(ppy)_3$ forms an exception yielding $\tau = 2.8$ s at 1 mol % and 12 s at 8 mol %. This system furthermore possesses the highest TTA rates, which are around 2.5 times higher compared to TCTA and CBP. The large error bars express stronger deviations between the measurement and fit (see the lines in Fig. 7.17) and indicate that TTA is probably not the only mechanism underlying the decay in these samples. Using $Ir(ppy)_2(acac)$, the highest lifetime is measured in CBP, which also shows a stronger increase of k_{TT} with increasing concentration.

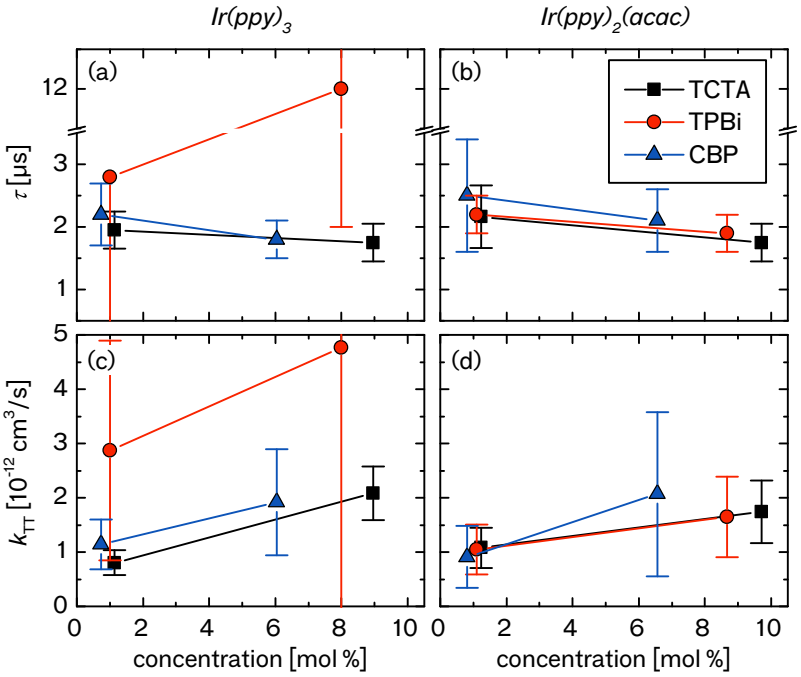

Figure 7.18: (a,b) Triplet lifetime τ and (c,d) triplet-triplet annihilation rate constant k_{TT} as a function of emitter concentration for (a,c) $Ir(ppy)_3$ and (b,d) $Ir(ppy)_2(acac)$, doped into different matrix materials.

Compared to the other hosts, the strong influence of TPBi on the annihilation processes occurring in $Ir(ppy)_3$ is surprising and has not been published for any other host-guest combination before.[21] For $Ir(ppy)_2(acac)$, the matrix influence on TTA is much less but the results from time-resolved and steady-state measurements are congruent. Namely, the matrix CBP shows both the strongest change in the PL spectrum and the highest increase of the TTA rate upon increasing concentration. Unfortunately, the experimental observations of the different matrix materials are ambiguous and furthermore reveal only little influence of the matrix (except for the case of TPBi:$Ir(ppy)_3$ transients).

[21] Note that similar differences between TCTA and TPBi doped with $Ir(ppy)_3$ have also been observed by Sebastian Reineke at Massachusetts Institute of Technology, USA.

7.4 *Influence of Processing Parameters*

As the study of the different matrix materials disclosed only little influence of the host on the formation of emitter aggregates, it shall now be clarified whether and how guest aggregation can be controlled by different processing parameters. Studies showed that aggregation in thin-films is not only observed for thermal evaporation, but also for spin-coating.[238;240;280] Here, layer formation may be influenced by the solvent and spin speed.[281] However, all materials explored throughout this thesis are deposited via thermal evaporation and, hence, focus lies on methods applicable to vacuum deposition. This contains substrate heating, change of deposition rate, and the influence of underlying layers.

All investigations in this section are performed on the well-known model system TCTA:$Ir(ppy)_3$. The doping concentration is kept fixed at 9 mol % and the layer thickness is always 20 nm.

7.4.1 *Substrate Heating*

In organic photovoltaics, material segregation at elevated substrate temperatures is widely utilized to fabricate bulk heterojunction solar cells.[282–284] However, for OLED fabrication, substrate heating is barely used up to now.[22] Gong *et al.* nicely demonstrated phase separation of TPBi:1,4-bis(benzothiazole-vinyl) benzene (BT)-films upon heating using scanning tunneling microscopy.[285] Heating furthermore led to broadening of the PL spectra and to a decrease in PL quantum efficiency, which is indicating emitter aggregation. Additionally, Smith *et al.* observed aggregation of $Ir(ppy)_3$ in CBP after heating to 80 °C by AFM and luminescence microscopy.[237] Surprisingly, aggregation was only observed for blends containing 6 wt % of $Ir(ppy)_3$, but not for 12 wt %.

[22] A minor part of this section is published in Ref. 11. Reprinted with permission. Copyright 2013, Wiley VCH.

Very recently, Mayr *et al.* demonstrated that the glass transition temperature of the host influences emitter orientation of the fluorescent emitter 3-(2-benzothiazolyl)-7-(diethylamino)coumarin (Coumarin 6), where increased horizontal orientation was measured for hosts with high glass transition temperatures.[286] The authors explain their observation by a stronger molecular motion on the surface if the substrate temperature (here: room temperature) is close to the glass transition temperature of the host. Related to this finding, higher substrate temperatures could enhance molecular motion and, hence, also increase the formation of aggregates. However, the observed effect was very small for phosphorescent iridium-compounds, which the authors relate to their high molecular weights. Concluding, the direct effect of substrate heating on TTA has not been investigated so far.

In the following, the temperature of the glass substrate is varied during evaporation from 25 °C to 140 °C. Higher temperatures would exceed the glass transition temperature of TCTA (approximately 150 °C), which could lead to stronger changes in morphology

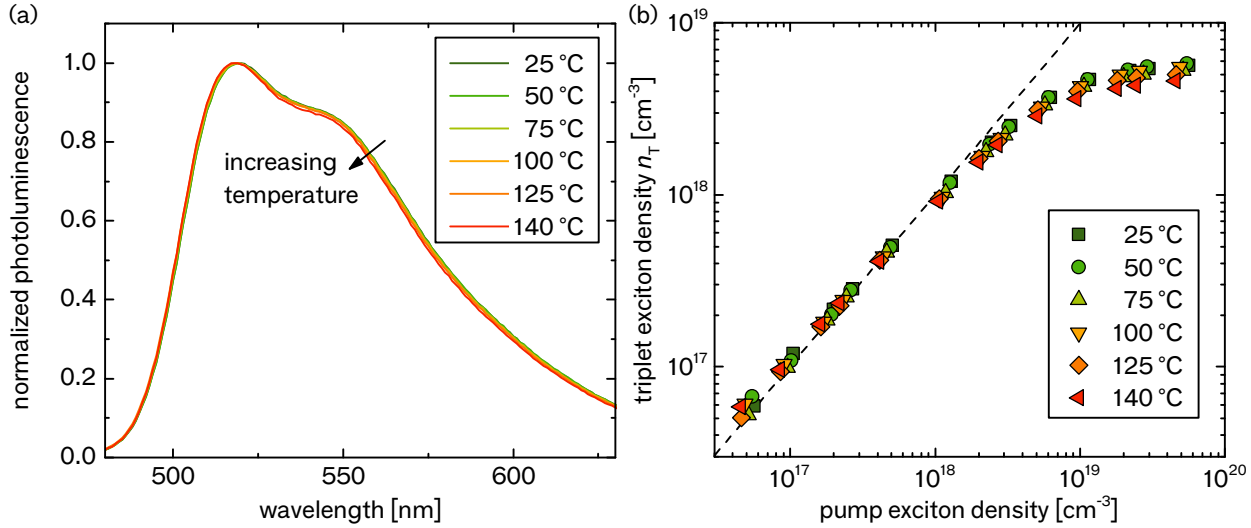

Figure 7.19: Influence of substrate temperature on emission of TCTA:Ir(ppy)$_3$ at 9 mol %. (a) Normalized PL intensity and (b) triplet exciton density n_T as a function of the pump exciton density governed by time-resolved PL measurements.

and is therefore omitted.[287] All samples are fabricated on one substrate within one fabrication run. Evaporation is started at the highest temperature in order to avoid heating of already prepared samples. Figure 7.19a shows the normalized PL spectra of all samples. A very small blue-shift with increasing temperature is observed, but the overall effect is marginal. The absolute intensity instead stays constant up to 75 °C and then decreases with higher temperatures (see Fig. D.2a in App. D). This could in fact hint to aggregation and exciton annihilation, respectively.

Time-resolved measurement of the PL intensity shall clarify whether an effect of the substrate temperature can be observed. Figure 7.19b shows the triplet exciton density as a function of the pump intensity for all applied temperatures. Small differences are observed: the final triplet exciton density that is reached in the saturation regime decreases above 50 °C with increasing temperature. The transients in the TTA regime are again fitted by Eq. 3.3 with a constant lifetime of 1.75 s. Figure 7.20a shows the extracted TTA rates. A slight increase of k_{TT} with increasing temperature is observed. The overall effect, however, is again small spreading from 1.74×10^{-12} cm^3/s at room temperature to 2.08×10^{-12} cm^3/s at 140 °C. Nevertheless, the smaller triplet density at high excitation and the higher TTA rate indicate that aggregation of Ir(ppy)$_3$ is increased at higher deposition temperatures. This is a result of the increased potential energy of the molecules, which renders molecular motion more effective.

As aggregation in host-guest systems is undesirable, substrate cooling during deposition of the film might help to obtain a more even distribution of guest molecules throughout the host matrix. Recently, it was shown that agglomeration of the p-dopant MoO_3 in CBP, which typically occurs at room temperature, can be suppressed by cooling the substrate to 120 K.[288] However, substrate cooling has

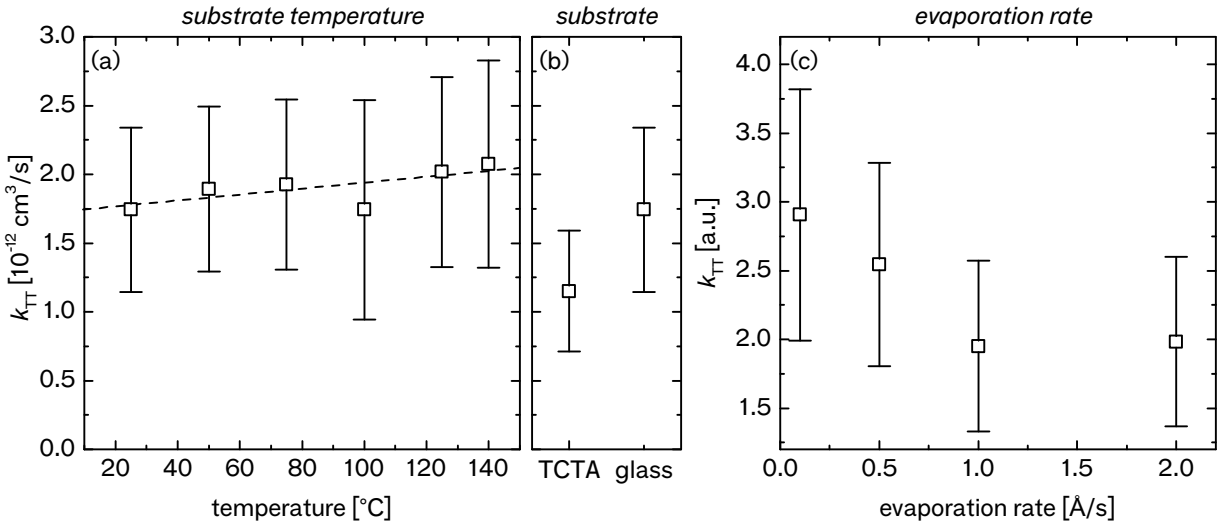

Figure 7.20: Triplet-triplet annihilation rate k_{TT} of TCTA:Ir(ppy)$_3$ (9 mol %) (a) as a function of the substrate temperature, (b) for different underlying layers, and (c) upon varying the deposition rate. The dashed line in (a) shows a linear fit.

not yet been applied to phosphorescent emitters and should be tested in future.

7.4.2 *Underlying Layer*

Yokoyama *et al.* pointed out that horizontal orientation of vacuum deposited amorphous films is independent of the underlying substrate and occurs both in neat layers and embedded into a matrix material.[287;289] This is caused by weak van der Waals interaction between two organic molecules, which is still higher than the interaction between organic molecules and the substrate. Whether this independence of orientation on the substrate also holds for the formation of guest aggregates when embedded into a host shall be investigated in this section.

Typically, spectroscopic properties of organic light-emitting thin-films are studied by depositing the material onto glass substrates as has also been done for all previous investigations throughout this chapter. In devices, however, the EML is typically applied on top of other organic layers, which might lead to different growth conditions. In the following, a 20 nm thick TCTA:Ir(ppy)$_3$-layer is deposited at a concentration of 9 mol % onto a 20 nm thick TCTA layer.

While no change in the shape of the PL spectrum is observed (see Fig. D.2b in App. D), stronger deviation in the transient response is measured. Figure 7.20b shows the extracted TTA rates of both samples. Compared to the layer deposition onto TCTA, fabrication on glass leads to an increase of k_{TT} by 51 %. This effect is large compared to the influence of the substrate temperature. An explanation could be a different strong formation of the polycrystalline Ir(ppy)$_3$ aggregates.[23] This effect, however, seems to be rather large given the fact that both underlying layers are amorphous and possess a low surface energy.[290] As a consequence, both substrates should interact only weakly with the organic molecules.

[23] Influences due to a changed microcavity or waveguiding effects introduced by the additional organic layer can be excluded as they would only alter the emitter lifetime, which is not observed here (cf. Chapter 5).

Although this effect is only studied for one host-guest system and one concentration, it shows that k_{TT} values of thin-films evaporated on glass cannot directly be applied to the same layers incorporated in an OLED. Instead, the processing conditions for single layers should meet the conditions in actual devices.

7.4.3 *Evaporation Rate*

In a study of Liu *et al.*, the authors observed an increasing PLQY and enhanced current transport with increasing evaporation rate in devices containing the planar molecule bis(10-hydroxybenzo[h] quinolinato)beryllium ($Bebq_2$) as emitter.[291;292] The effect was attributed to enhanced aggregate formation of $Bebq_2$ at slow deposition. Similarly, Cheng *et al.* observed an increased film roughness and material decomposition by AFM and XPS measurements of Alq_3 thin-films when decreasing the evaporation rate from 1.33 to 0.05 Å/s.[293] Indeed, it is reasonable to assume that aggregate formation is a matter of speed and depends on how fast molecules which are deposited on top of other molecules can 'fix' these underlying molecules in their position. However, it remains elusive at which time scales molecular rearrangement takes place.

In the previous sections, all layers have typically been evaporated at a rate of 0.3 Å/s. In order to study the influence of the evaporation rate on the formation of aggregates in host-guest systems, TCTA:$Ir(ppy)_3$ layers are fabricated varying the rate from 0.1 to 2 Å/s. Rates exceeding this range are either not controllable with the used quartz crystal monitors or would waste material.

The shape of the PL spectra is unaffected by the deposition rate (see Fig. D.2c in App. D), which has also previously been found for the case of Alq_3.[291] Figure 7.20c shows the TTA rates extracted from time-resolved measurements as a function of the evaporation rate.[24] Interestingly, k_{TT} decreases by approximately 30 % when the rate is increased by one order of magnitude from 0.1 to 1 Å/s. At a higher rate of 2 Å/s, k_{TT} remains constant. This suggests that enhanced $Ir(ppy)_3$ aggregate formation takes place at slow evaporation rates. The result supports the above mentioned findings and furthermore shows that the evaporation rate not only influences aggregate formation in single layers but also in doped systems.

[24] Note that only relative k_{TT}-values are displayed in Fig. 7.20c because the absolute triplet exciton density is not measured here.

7.5 *Summary and Implications of Aggregation on Efficiency Roll-Off*

Based on a previous report that identified different emitter aggregation in the two structurally similar compounds $Ir(ppy)_2(acac)$ and $Ir(ppy)_3$,[142] the extent of aggregate formation is studied for three homoleptic and four heteroleptic emitters. Three different techniques have been applied varying the doping concentration of the emitters. Photoluminescence measurements revealed a spectral broadening and red-shift for all investigated compounds, which was quantified by fit-

ting the spectra to a Poisson progression. As a result, the homoleptic emitters showed a strong increase of the Huang-Rhys factor and of the line broadening, which suggests the formation of aggregates.

Next, triplet-triplet annihilation was studied in the films using time-resolved spectroscopy. Again, the homoleptic emitters showed either high absolute TTA rates or a strong change of their rate upon increasing concentration. Both could be a result of guest aggregation. However, the measurement underlies high uncertainties and stronger deviations between data and fit were observed.

In order to find out more about the structure and size of the aggregates, X-ray diffraction measurements were performed on $Ir(ppy)_3$ and $Ir(ppy)_2(acac)$ systems. Interestingly, both emitters form polycrystalline grains. A calculation of the coherence length revealed that the molecular order is spanning over only a few nanometers. Furthermore, no crystallites could be observed at a doping concentration of 8 wt %, which would reflect the situation in OLEDs. Although it is expected that aggregates are also present at this concentration, either their size is too small or the order is not high enough to reveal diffraction peaks.

It was suggested that the aggregate formation of the homoleptic compounds may be related to their higher dipole-dipole potential compared to their heteroleptic counterparts. In the case of $Ir(chpy)_3$, however, the potential is only marginally higher than for the heteroleptic emitters. Therefore, it is suggested that also the molecular structure itself may be an origin for aggregation. Here, a wider range of emitters should be studied, such as heteroleptic compounds with ligands other than acetylacetonate or with higher dipole-dipole potentials.

When comparing the three methods, still many uncertainties remain. The steady-state PL spectroscopy is very easy to apply, but redshift and spectral broadening may be caused by numerous processes that are not easy to distinguish. Comparing emitters by time-resolved spectroscopy is generally more promising, especially because it directly reflects the influence of aggregation on efficiency roll-off in OLEDs. XRD, however, seems to be rather unsuitable for studying aggregation because the crystal order, especially at the concentrations relevant to OLEDs, is not high enough. This is expected to hold also for other iridium-cored phosphors.

For further investigations, the range of investigated doping concentrations should be extended. On the one hand, the different effects leading to spectral shifts could be better differentiated.[273] On the other hand, it would establish whether TTA increases with increasing concentration simply due to the reduced distance between two emitters or in fact due to aggregate formation. Although pure emitter layers scarcely luminesce, the knowledge of their spectrum and TTA rates would give an upper limit and a better basis for discussion.

Next, the influence of the matrix material was studied. Changing the host for $Ir(ppy)_3$ from TCTA to TPBi resulted in a strong increase of TTA, both in the emitter lifetime and in the TTA rate constant.

Using this structure in an OLED would result in a critical current density of only $0.5\,\mathrm{mA/cm^2}$. This is surprisingly low compared to the observed roll-off in Fig. C.4, where $J_0 = 245\,\mathrm{mA/cm^2}$ for a D-EML comprising TCTA:$\mathrm{Ir(ppy)_3}$/TPBi:$\mathrm{Ir(ppy)_3}$. Unfortunately, no data for TPBi:$\mathrm{Ir(ppy)_3}$ single EMLs is available. For all other matrix materials, however, the influence of the host was much less compared to the differences observed between the seven emitters.

Last, the influence of three processing parameters was studied in PL and time-resolved measurements. A variation of the substrate temperature during layer deposition suggests an increased emitter aggregation with increasing temperature due to enhanced diffusive motion of the molecules. Therefore, substrate cooling during evaporation might be helpful. However, the overall influence of substrate temperature is relatively low. Instead, a variation of the underlying material revealed a much stronger influence, where less TTA was observed when the host-guest system is fabricated on top of another organic layer compared to a bare glass substrate. Furthermore, small evaporation rates were found to increase aggregate formation. In order to find out how molecular aggregates are exactly formed, a further variation of the layer thickness from sub-monolayer thickness on might be helpful.

From the three processing conditions that were studied, evaporating the layers onto a cooled substrate and with a high evaporation rate are possibilities that are also applicable in practice. Changing the underlying material, however, is only possible as long as the optical and transport properties are preserved. Therefore, further material screening would be necessary including a systematic variation of, e.g., the dipole moment, the glass transition temperature, or the orientation of the underlying layer.

Finally, the extracted parameters from time-resolved measurements are used to discuss how emitter aggregation influences efficiency roll-off. Considering Eqs. 3.4 and 3.5, not only k_{TT} plays a role, but also the intrinsic emitter lifetime, which is less influenced by aggregation. In order to compare the potential behavior of the materials when incorporated into OLEDs, Fig. 7.21 shows the normalized EQE as a function of the current density based on the extracted parameters and assuming $w = 5\,\mathrm{nm}$. Here, the higher concentrated samples are selected because those reflect the real situation in devices.

The smallest roll-off is observed for the two green emitters $\mathrm{Ir(ppy)_3}$ and $\mathrm{Ir(ppy)_2(acac)}$. In contrast to previous findings,[142] no difference between the two emitters is found because the decreased k_{TT} of $\mathrm{Ir(ppy)_2(acac)}$ is cancelled out by its longer lifetime. All other emitters show a stronger roll-off. Especially for $\mathrm{Ir(dhfpy)_2(acac)}$, a critical current density of only $7\,\mathrm{mA/cm^2}$ is observed. This is related to its very long lifetime, which may not be a property of the emitter itself but may be influenced by the host. Nevertheless, this effect would cause a strong roll-off when embedding $\mathrm{Ir(dhfpy)_2(acac)}$ into real devices. Indeed, an increased roll-off was detected when raising the $\mathrm{Ir(dhfpy)_2(acac)}$ concentration in two-color OLEDs that contained

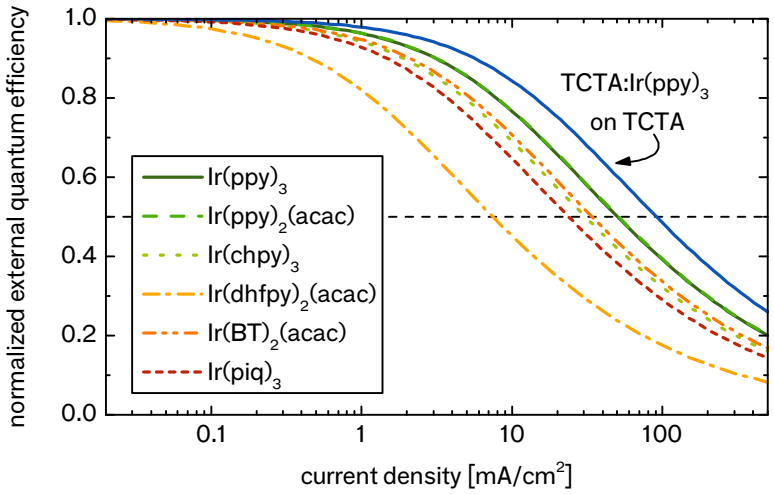

Figure 7.21: Simulated normalized EQE of the six host-guest systems studied in Sec. 7.2.2 at concentration Γ_2, calculated by Eq. 3.4 and assuming $w = 5\,\text{nm}$. The parameters k_{TT} and τ are taken from the higher concentrated samples in Fig. 7.9. Furthermore, the roll-off of the TCTA:Ir(ppy)$_3$ sample on TCTA as underlying layer is displayed.

an emission layer with a mixture of Ir(ppy)$_3$ and Ir(dhfpy)$_2$(acac).[127] In addition, a critical current density of only $5\,\text{mA/cm}^2$ was measured for CBP:Ir(dhfpy)$_2$(acac) OLEDs at Γ_2 doping concentration.[252] Further evidence for the strong roll-off in Ir(dhfpy)$_2$(acac)-based pin-OLEDs was given by Simone Hofmann (TU Dresden), who embedded the emitter with 8 wt % into TCTA and measured $J_0 \approx 20\,\text{mA/cm}^2$ (unpublished).

Table 7.7 summarizes the critical current densities at low and high concentration that could be achieved when embedding the six emitters into OLEDs. J_0 is calculated according to Eq. 3.5 neglecting a change of the lifetime due to microcavity effects and further assuming $w = 5\,\text{nm}$. Interestingly, J_0 does not always decrease with increasing concentration as would have been expected from emitter aggregation. For instance, Ir(chpy)$_3$, for which aggregate formation is strongly expected, shows an increase of J_0 by more than 60 %. Hence, it is very important to avoid processes that may increase the emitter lifetime such as host-guest interactions. Although taking hosts with higher triplet energies may introduce energy barriers and, thus, can lead to higher voltages, an exothermic energy transfer is critical for achieving low roll-off.

emitter	J_0 [mA/cm^2] at Γ_1	J_0 [mA/cm^2] at Γ_2
Ir(ppy)$_3$	104	50
Ir(ppy)$_2$(acac)	64	51
Ir(chpy)$_3$	19	31
Ir(dhfpy)$_2$(acac)	11	7
Ir(BT)$_2$(acac)	33	34
Ir(piq)$_3$	27	24

Table 7.7: Calculated critical current density J_0 at low and high concentration (Γ_1 and Γ_2, respectively) using Eq. 3.5 and the values of k_{TT} and τ from Fig. 7.9; $w = 5\,\text{nm}$. Homoleptic emitters are marked with a blue background.

8 Summary and Outlook

This chapter summarizes the results of the thesis and describes the interplay of optical environment, emission profile, and emitter aggregation with regard to efficiency roll-off. It outlines future challenges that have to be addressed in order to further improve the efficiency at high brightness. In addition, the results on emitter orientation are summarized and discussed.

8.1 Summary of Roll-Off Investigations

In this thesis, three processes that influence the exciton density have been studied: (1) the optical environment, which influences the effective lifetime, (2) the width and shape of the emission profile, and (3) emitter aggregation, which increases the TTA rate. Although the investigations focussed on triplet-triplet annihilation in phosphorescent OLEDs, all three studies are also applicable to fluorescent compounds. Hence, both triplet and singlet densities may be influenced, which, in the end, cannot only decrease TTA but also reduce processes such as singlet-singlet, singlet-triplet, singlet-polaron, and triplet-polaron annihilation. This enables an enhancement of efficiency at high brightness for a broad range of emitters and OLED structures.

The optical environment determines the strength of the OLED microcavity, which influences the radiative decay rate via the Purcell effect. Varying the strength of the microcavity by changing the distance between emitter and reflective metal electrode, a large variation of the emitter lifetime by more than 50 % was observed. This is directly reflected in the roll-off, where the critical current density could be doubled. Simulation of the efficiency roll-off showed that especially the radiative decay rate strongly influences the critical current density. Finally, design principles have been developed to improve efficiency roll-off by optical simulation. Here, the current regime, at which the OLED shall be operated should always be taken into account because optimal layer thickness changes with the applied current density.

The emission profile describes the spatial exciton distribution inside the emission layer. It is based on the exciton formation region and diffusion. In this thesis, a method is developed that allows extraction of the emission profile shape and width with nanometer spatial resolution. This is achieved by inserting a very thin sensing layer that locally quenches excitons at varying positions inside the EML. The emission spectra of these devices are modelled solving the diffusion equation, which allowed extraction of the exciton formation region and of the diffusion length. The method was applied to three different

EML structures using either an ambipolar host, a D-EML, or an M-EML. For the ambipolar host, $Ir(ppy)_3$ and $Ir(ppy)_2(acac)$, respectively, were doped into CBP. The extracted emission profile was located at the ETL-side of the EML and was rather narrow. In fact, the conduction properties of CBP for holes and electrons still differ too much to enable broad exciton formation in the middle of the EML. Furthermore, the M-EML showed broader exciton formation compared to the D-EML. A proper adjustment of the two matrix materials concerning transport properties, e.g. by varying the mixing ratio, could lead to a broad exciton distribution across the whole EML.

Previous publications suggested that emitter molecules tend to aggregate at the concentrations used in OLEDs. Aggregation leads to strong annihilation of excited states and, thus, increases roll-off. Here, aggregation is studied for a broad range of emitters and matrix materials by PL and transient measurements under variation of the guest doping concentration. Compared to heteroleptic emitters, homoleptic compounds tend to aggregate stronger, which may be related to their higher dipole-dipole potential and their molecular structure. The matrix material, however, showed less influence on aggregation. Furthermore, processing conditions were investigated, where increased annihilation was observed for increasing substrate temperature and low evaporation rates. In addition, the underlying layer seems to be crucial, where stronger TTA was found on glass compared to an organic thin-film.

8.2 *Improving the High-Brightness Performance Further*

The local exciton density mainly depends on the emitter lifetime and the spatial exciton distribution. Furthermore, annihilation processes may strongly influence the total exciton density. Regarding TTA, which typically is the most prominent process affecting roll-off, the lifetime goes quadratic with the critical current density, while all other factors show a linear dependency (cf. Eq. 3.5). Therefore, a decrease of lifetime would lead to the highest improvement.

Compared to the first phosphorescent emitters, which showed lifetimes of around 100 s,[25;26;294;295] the introduction of heavy metal atoms could strongly decrease the lifetime to the current state-of-the-art of around 1 s.[28;267;296–298] An empirical description by Yersin *et al.* showed that the intrinsic lifetime of organo-transition metal complexes can only be reduced to around 0.75 s.[299] Decreasing the lifetime using microcavity effects as proposed in Chapter 5 always goes along with a change of the outcoupling efficiency. Therefore, optimization of the lifetime by changing the optical environment is limited. Instead, avoiding processes that may increase the lifetime, e.g. host-guest interaction, are critical.

The investigations in Chapter 6 showed that the emission zone width is still rather small in state-of-the-art OLEDs. Here, much room for improvement is possible. This can be achieved by broadening the exciton generation region. Therefore, further concepts such as graded

EMLs should be developed with the help of electrical simulation tools. A proper prediction of the exciton formation region would not only help in reducing the roll-off but also in optimizing the outcoupling efficiency. However, broadening the generation zone is not only based on the mobilities and energy levels of host and guest, but also of all surrounding materials. For instance, exchanging the ETL TPBi of the ambipolar stack in Fig. 6.11 by a material with higher electron mobility might shift the generation zone more to the middle of the EML. An analogous increase of the diffusion length, which would also broaden the emission zone, would be accompanied by the drawback of increased exciton annihilation. Furthermore, increasing the diffusion length is mainly achieved by embedding the guest into a host with resonant triplet energy, which would then also increase the lifetime.

Different possibilities to avoid aggregation and, thus, reduce exciton annihilation have been proposed in Chapter 7. However, the mechanism of aggregate formation is still not fully understood. DFT calculations or Monte Carlo simulations of a set of molecules could give further insight. High prospect was also given by incorporating efficient phosphorescent compounds into dendrimers. Here, the matrix material may be fully avoided and the molecular distance is only determined by the size of the dendron.

Efficiency roll-off is not only based on high exciton densities, but also on many other mechanisms. Especially a proper investigation of the charge carrier balance offers much room for improvement. Here, studies should include both better theoretical predictions and accurate measurement techniques for determining the charge balance.

In recent years, much attention has been drawn to thermally activated delayed fluorescence (TADF)[76;87;89;300;301] and to triplet harvesting (TH)[125–129]. Both methods enable up to 100 % internal quantum efficiency despite using fluorescent emitters. Triplet excitons are utilized either by transferring them to a phosphor (TH) or by converting them back to singlets (TADF). The triplet state of the used fluorescent emitters and hosts possesses a lifetime in the range of 100 s up to milliseconds.[302] Therefore, TTA is an important issue in these devices, which limits the efficiency at high brightness (see the achieved EQE–$J_{90\%}$ values of TADF, marked by circles in Fig. 3.1). For both concepts, the triplet lifetime could be modified with the method proposed in Chapter 5. This would require (1) an exact measurement of the triplet lifetime and (2) according optical modelling. For EMLs comprising TADF emitters, the roll-off could furthermore be strongly reduced by increasing the emission zone width as studied in Chapter 6. In addition, further investigations, especially in the direction of molecular design, are necessary to make OLEDs based on these two methods competitive.

8.3 Concluding Words on Emitter Orientation

Horizontal orientation of the transition dipole moment has the prospect to strongly increase the efficiency of OLEDs. In Chapter 5, theoretical modelling showed that not only the absolute outcoupling efficiency depends on emitter orientation but also the roll-off. This results from the dependency of the radiative decay rate on the direction of light emission with respect to the microcavity structure. Conversely, measurement of the roll-off for different OLED microcavities and concurrent optical modelling could be used to determine the anisotropy factor.

In Chapter 7, thin-films of $Ir(ppy)_3$ and $Ir(ppy)_2(acac)$ were studied using GIXRD and GIWAXS. Both compounds form small crystallites that show a preferential orientation in out-of-plane direction. Doping the emitters with 20 wt % into a matrix, the crystallite size decreases with decreasing concentration but the ordering and orientation retain. Comparing the thin-film diffraction data of $Ir(ppy)_3$ with its powder spectrum suggests that $Ir(ppy)_3$ molecules are oriented with their permanent dipole moment roughly perpendicular to the substrate.

For phosphorescent emitters, anisotropy factors of $0.22 < a < 0.40$ have been measured to date.[78;96;98–101] In order to fully exploit the power of orientation, emitters with much lower anisotropy factors have to be found. A first step to explore those compounds is to gain a deeper knowledge on the mechanism that leads to orientation. DFT simulations,[96] single-molecule spectroscopy,[97;303] or scanning tunneling microscopy[304–306] might help in this context. In addition, experiments could test whether the orientation may be influenced during layer deposition. Here, substrate temperature, evaporation speed, and underlying layers should be tested. Further possibilities include evaporation onto tilted substrates and systematic variation of the surrounding host molecules.[101;286]

A Appendix to Theory of Efficiency Roll-Off

Derivation of EQE and $J_{90\%}$

All EQE values represent maximum values achieved by the device, except for Ref. [6,37,38], where values are taken at 1000 cd/m^2. Values for $J_{90\%}$ from Ref. [4,6,10,18,24,29,30] are calculated from J_0. Values for $J_{90\%}$ from Ref. [22,37,38] are calculated from current efficiency measurements assuming that the spectrum remains constant with increasing current density. Values for $J_{90\%}$ from Ref. [34,38,45,47,53] represent rough estimates and could possibly be much higher. Note that tandem devices can have a maximum internal quantum efficiency of 200 %.

References

[1] Y. Sun, S. R. Forrest, *Applied Physics Letters* 91, 263503 (2007).

[2] Y. Sun, S. R. Forrest, *Organic Electronics* 9, 994 (2008).

[3] C. W. Seo, J. Y. Lee, *Thin Solid Films* 520, 5075 (2012).

[4] H. Sasabe, J. Takamatsu, T. Motoyama, S. Watanabe, G. Wagenblast, N. Langer, O. Molt, E. Fuchs, C. Lennartz, J. Kido, *Advanced Materials* 22, 5003 (2010).

[5] S.-J. Su, E. Gonmori, H. Sasabe, J. Kido, *Advanced Materials* 20, 4189 (2008).

[6] S. Reineke, F. Lindner, G. Schwartz, N. Seidler, K. Walzer, B. Lüssem, K. Leo, *Nature* 459, 234 (2009).

[7] Y. Chen, J. Chen, D. Ma, D. Yan, L. Wang, *Applied Physics Letters* 99, 103304 (2011).

[8] a) R. Meerheim, R. Nitsche, K. Leo, *Applied Physics Letters* 93, 043310 (2008). b) R. Meerheim: *Quanteneffizienz und Langzeitstabilität monochromer organischer Leuchtdioden.* PhD Thesis, Technische Universität Dresden (2009).

[9] C.-H. Chien, F.-M. Hsu, C.-F. Shu, Y. Chi, *Organic Electronics* 10, 871 (2009).

[10] Y.-L. Tung, S.-W. Lee, Y. Chi, Y.-T. Tao, C.-H. Chien, Y.-M. Cheng, P.-T. Chou, S.-M. Peng, C.-S. Liu, *Journal of Materials Chemistry* 15, 460 (2005).

[11] J. Kwak, Y.-Y. Lyu, H. Lee, B. Choi, K. Char, C. Lee, *Journal of Materials Chemistry* 22, 6351 (2012).

[12] D. H. Kim, N. S. Cho, H.-Y. Oh, J. H. Yang, W. S. Jeon, J. S. Park, M. C. Suh, J. H. Kwon, *Advanced Materials* 23, 2721 (2011).

[13] a) S. Hofmann, M. Thomschke, P. Freitag, M. Furno, B. Lüssem, K. Leo, *Applied Physics Letters* 97, 253308 (2010). b) S. Hofmann, M. Thomschke, P. Freitag, M. Furno, B. Lüssem, K. Leo, *Proc. Solid-State and Organic Lighting*, SOThA1 (2010).

[14] J.-R. Koo, S. J. Lee, G. W. Hyung, D. W. Im, H. S. Yu, J.-H. Park, K. H. Lee, S. S. Yoon, W. Y. Kim, Y. K. Kim, *AIP Advances* 2, 012117 (2012).

[15] D. Tanaka, H. Sasabe, Y.-J. Li, S.-J. Su, T. Takeda, J. Kido, *Japanese Journal of Applied Physics* 46, L10 (2007).

[16] Y. Tao, Q. Wang, C. Yang, C. Zhong, J. Qin, D. Ma, *Advanced Functional Materials* 20, 2923 (2010).

[17] S. Reineke, T. C. Rosenow, B. Lüssem, K. Leo, *Advanced Materials* 22, 3189 (2010).

[18] C. Adachi, R. Kwong, S. R. Forrest, *Organic Electronics* 2, 37 (2001).

[19] Z. B. Wang, M. G. Helander, J. Qiu, D. P. Puzzo, M. T. Greiner, Z. W. Liu, Z. H. Lu, *Applied Physics Letters* 98, 073310 (2011).

[20] Z. B. Wang, M. G. Helander, J. Qiu, D. P. Puzzo, M. T. Greiner, Z. M. Hudson, S. Wang, Z. W. Liu, Z. H. Lu, *Nature Photonics* 5, 753 (2011).

[21] S. O. Jeon, K. S. Yook, C. W. Joo, J. Y. Lee, *Applied Physics Letters* 94, 13301 (2009).

[22] H. Sasabe, E. Gonmori, T. Chiba, Y.-J. Li, D. Tanaka, S.-J. Su, T. Takeda, Y.-J. Pu, K. Nakayama, J. Kido, *Chemistry of Materials* 20, 5951 (2008).

[23] S.-J. Su, H. Sasabe, T. Takeda, J. Kido, *Chemistry Of Materials* 20, 1691 (2008).

[24] H.-H. Chou, C.-H. Cheng, *Advanced Materials* 22, 2468 (2010).

[25] Y. Chen, J. Chen, Y. Zhao, D. Ma, *Applied Physics Letters* 100, 213301 (2012).

[26] S. O. Jeon, S. E. Jang, H. S. Son, J. Y. Lee, *Advanced Materials* 23, 1436 (2011).

[27] J. Lee, J.-I. Lee, J. Y. Lee, H. Y. Chu, *Organic Electronics* 10, 1529 (2009).

[28] M. E. Kondakova, J. C. Deaton, T. D. Pawlik, D. J. Giesen, D. Y. Kondakov, R. H. Young, T. L. Royster, D. L. Comfort, J. D. Shore, *Journal of Applied Physics* 107, 014515 (2010).

[29] Y. Chen, F. Zhao, Y. Zhao, J. Chen, D. Ma, *Organic Electronics* 13, 2807 (2012).

[30] J. Ye, C.-J. Zheng, X.-M. Ou, X.-H. Zhang, M.-K. Fung, C.-S. Lee, *Advanced Materials* 24, 3410 (2012).

[31] a) T. C. Rosenow, M. Furno, S. Reineke, S. Olthof, B. Lüssem, K. Leo, *Journal of Applied Physics* 108, 113113 (2010). b) T. C. Rosenow: *White Organic Light Emitting Diodes.* Technische Universität Dresden, PhD Thesis (2010).

[32] Y. Sun, N. C. Giebink, H. Kanno, B. Ma, M. E. Thompson, S. R. Forrest, *Nature* 440, 908 (2006).

[33] F. Zhao, Z. Zhang, Y. Liu, Y. Dai, J. Chen, D. Ma, *Organic Electronics* 13, 1049 (2012).

[34] K. S. Yook, S. O. Jeon, C. W. Joo, J. Y. Lee, *Applied Physics Letters* 93, 073302 (2008).

[35] Z. Zhang, Q. Wang, Y. Dai, Y. Liu, L. Wang, D. Ma, *Organic Electronics* 10, 491 (2009).

[36] Y. Yang, T. Peng, K. Ye, Y. Wu, Y. Liu, Y. Wang, *Organic Electronics* 12, 29 (2011).

[37] Y.-C. Tsai, J.-H. Jou, *Applied Physics Letters* 89, 243521 (2006).

[38] M.-F. Lin, L. Wang, W.-K. Wong, K.-W. Cheah, H.-L. Tam, M.-T. Lee, M.-H. Ho, C. H. Chen, *Applied Physics Letters* 91, 073517 (2007).

[39] H. Uoyama, K. Goushi, K. Shizu, H. Nomura, C. Adachi, *Nature* 492, 234 (2012).

[40] J. P. Spindler, W. J. Begley, T. K. Hatwar, D. Y. Kondakov, *SID Symposium Digest of Technical Papers*, 30.4 (2009).

[41] Y. Zhang, S. Forrest, *Physical Review Letters* 108, 267404 (2012).

[42] T. Matsushima, C. Adachi, *Applied Physics Letters* 89, 253506 (2006).

[43] C. Rothe, A. Werner, O. Fadhel, M. Limmert, T. W. Canzler, J. Birnstock, *SID Symposium Digest of Technical Papers*, 35.2 (2009).

[44] H. Tanaka, K. Shizu, H. Miyazaki, C. Adachi, *Chemical Communications* 48, 11392 (2012).

[45] K. Okumoto, H. Kanno, Y. Hamaa, H. Takahashi, K. Shibata, *Applied Physics Letters* 89, 063504 (2006).

[46] H. Nakanotani, H. Sasabe, C. Adachi, *Applied Physics Letters* 86, 213506 (2005).

[47] T. Matsushima, C. Adachi, *Applied Physics Letters* 92, 063306 (2008).

[48] S. Y. Lee, T. Yasuda, H. Nomura, C. Adachi, *Applied Physics Letters* 101, 093306 (2012).

[49] Y.-J. Pu, G. Nakata, F. Satoh, H. Sasabe, D. Yokoyama, J. Kido, *Advanced Materials* 24, 1765 (2012).

[50] H. Fukagawa, T. Shimizu, N. Ohbe, S. Tokito, K. Tokumaru, H. Fujikake, *Organic Electronics* 13, 1197 (2012).

[51] N. Matsumoto, T. Miyazaki, M. Nishiyama, C. Adachi, *The Journal of Physical Chemistry C* 113, 6261 (2009).

[52] Y.-M. Jeon, J.-Y. Lee, J.-W. Kim, C.-W. Lee, M.-S. Gong, *Organic Electronics* 11, 1844 (2010).

[53] K. H. Lee, L. K. Kang, J. Y. Lee, S. Kang, S. O. Jeon, K. S. Yook, J. Y. Lee, S. S. Yoon, *Advanced Functional Materials* 20, 1345 (2010).

[54] C.-J. Zheng, J. Wang, J. Ye, M.-F. Lo, X.-K. Liu, M.-K. Fung, X.-H. Zhang, C.-S. Lee, *Advanced Materials* 25, 2205 (2013).

[55] Y. Zhao, J. Chen, D. Ma, *ACS Applied Materials & Interfaces* 5, 965 (2013).

B Appendix to Emission and Sensing Profiles

B.1 Emission Profiles

In Section 6.1.1, four different generation profiles have been introduced:

$$G(x) = G_0 \qquad \text{(constant)}, \tag{B.1a}$$

$$G(x) = G_0 \left(-\frac{x}{g} + \frac{d}{2g} + 1 \right) \qquad \text{(linear)}, \tag{B.1b}$$

$$G(x) = G_0 \mathrm{e}^{-x/g} \qquad \text{(exponential)}, \tag{B.1c}$$

$$G(x) = G_0 \mathrm{e}^{-x/g} + U \qquad \text{(exp. with background)}. \tag{B.1d}$$

Here, G_0 is defined individually for each profile in order to secure that $k_{\mathrm{Gen}} = \int_0^d G(x)dx$:

$$G_0 = \frac{k_{\mathrm{Gen}}}{d} \qquad \text{(constant)}, \tag{B.2a}$$

$$G_0 = \frac{k_{\mathrm{Gen}}}{d} \qquad \text{(linear)}, \tag{B.2b}$$

$$G_0 = \frac{k_{\mathrm{Gen}}}{g(1 - \mathrm{e}^{-d/g})} \qquad \text{(exponential)}, \tag{B.2c}$$

$$G_0 = \frac{k_{\mathrm{Gen}} - Ud}{g(1 - \mathrm{e}^{-d/g})} \qquad \text{(exp. with background)}. \tag{B.2d}$$

g denotes the width of the generation profile, d the EML thickness, and U the background.

The homogenous solution of the steady-state diffusion equation (given in Eq. 6.1) is

$$n_{\mathrm{h}}(x) = C_1 \mathrm{e}^{x/l} + C_2 \mathrm{e}^{-x/l}, \tag{B.3}$$

where l is the diffusion length: $l = \sqrt{D\tau}$. Now, the inhomogeneous differential equation is solved for each generation profile. It is assumed that excitons are blocked at the border to the blocking layers giving rise to the boundary conditions

$$\frac{\partial}{\partial x} n(0) = 0 \quad \text{and} \quad \frac{\partial}{\partial x} n(d) = 0, \tag{B.4}$$

from which the constants C_1 and C_2 are derived. Finally, the following emission profiles are obtained:

$$n(x) = G_0\tau \tag{B.5a}$$

(constant),

$$n(x) = \frac{G_0\tau}{g}\left[\frac{l(1-\mathrm{e}^{d/l})}{\sinh(d/l)}\cosh\left(\frac{x}{l}\right) + l\mathrm{e}^{x/l} - x + g + \frac{d}{2}\right] \tag{B.5b}$$

(linear),

$$n(x) = \frac{lgG_0\tau}{l^2-g^2}\left[\frac{\mathrm{e}^{d/l}-\mathrm{e}^{-d/g}}{\sinh(d/l)}\cosh\left(\frac{x}{l}\right) - \mathrm{e}^{x/l} - \frac{g}{l}\mathrm{e}^{-x/g}\right] \tag{B.5c}$$

(exponential),

$$n(x) = \frac{lgG_0\tau}{l^2-g^2}\left[\frac{\mathrm{e}^{d/l}-\mathrm{e}^{-d/g}}{\sinh(d/l)}\cosh\left(\frac{x}{l}\right) - \mathrm{e}^{x/l} - \frac{g}{l}\mathrm{e}^{-x/g}\right] + U\tau \tag{B.5d}$$

(exponential with background).

B.2 *Emission Profiles Including a Sensing Layer*

In oder to include the effect of the quencher, the solution of the diffusion equation is split into two functions $n_\mathrm{l}(x)$ and $n_\mathrm{r}(x)$ (see Eq. 6.3), where

$$n_\mathrm{l}(x) = C_1^\mathrm{l}\mathrm{e}^{x/l} + C_2^\mathrm{l}\mathrm{e}^{-x/l} + n_\mathrm{p}^\mathrm{l}(x), \quad \text{and} \tag{B.6a}$$

$$n_\mathrm{r}(x) = C_1^\mathrm{r}\mathrm{e}^{x/l} + C_2^\mathrm{r}\mathrm{e}^{-x/l} + n_\mathrm{p}^\mathrm{r}(x), \tag{B.6b}$$

with $n_\mathrm{p}(x)$ as the particular solution of the respective generation profile.

The four constants C_1^l, C_2^l, C_1^r, and C_2^r are derived from the boundary conditions

$$\frac{\partial}{\partial x}n_\mathrm{l}(0) = 0, \quad \frac{\partial}{\partial x}n_\mathrm{r}(d) = 0, \quad n_\mathrm{l}(x_0) = 0, \quad \text{and} \quad n_\mathrm{r}(x_0) = 0. \tag{B.7}$$

The solution assuming either a constant or an exponential generation profile with and without background finally reads with $A = (lgG_0\tau)/(l^2-g^2)$:

$$n_\mathrm{l}(x) = G_0\tau\left[1 - \frac{\cosh(x/l)}{\cosh(x_0/l)}\right]$$

$$n_\mathrm{r}(x) = G_0\tau\left[1 - \frac{\mathrm{e}^{-2d/l}\mathrm{e}^{x/l} + \mathrm{e}^{-x/l}}{\mathrm{e}^{-2d/l}\mathrm{e}^{x_0/l} + \mathrm{e}^{-x_0/l}}\right] \tag{B.8a}$$

(constant generation profile),

$$n_\mathrm{l}(x) = A\left[\frac{\mathrm{e}^{x_0/l} + \frac{g}{l}\mathrm{e}^{-x_0/g}}{\cosh(x_0/l)}\cosh\left(\frac{x}{l}\right) - \mathrm{e}^{x/l} - \frac{g}{l}\mathrm{e}^{-x/g}\right]$$

$$n_\mathrm{r}(x) = A\left[\frac{\mathrm{e}^{-d/g}\mathrm{e}^{-d/l}\mathrm{e}^{x_0/l} + \frac{g}{l}\mathrm{e}^{-x_0/g}}{\mathrm{e}^{-2d/l}\mathrm{e}^{x_0/l} + \mathrm{e}^{-x_0/l}}\left(\mathrm{e}^{-2d/l}\mathrm{e}^{x/l} + \mathrm{e}^{-x/l}\right)\right. \tag{B.8b}$$

$$\left. -\mathrm{e}^{-d/g}\mathrm{e}^{-d/l}\mathrm{e}^{x/l} - \frac{g}{l}\mathrm{e}^{-x/g}\right]$$

(exponential generation profile),

$$
\begin{aligned}
n_1(x) &= \frac{\cosh(x/l)}{\cosh(x_0/l)}\left[A\left(\mathrm{e}^{x_0/l}+\frac{g}{l}\mathrm{e}^{-x_0/g}\right)-U\tau\right] \\
&\quad - A\left(\mathrm{e}^{x/l}+\frac{g}{l}\mathrm{e}^{-x/g}\right)+U\tau \\
n_\mathrm{r}(x) &= \frac{\mathrm{e}^{-2d/l}\mathrm{e}^{x/l}+\mathrm{e}^{-x/l}}{\mathrm{e}^{-2d/l}\mathrm{e}^{x_0/l}+\mathrm{e}^{-x_0/l}}\left[A\left(\mathrm{e}^{-d/g}\mathrm{e}^{-d/l}\mathrm{e}^{x_0/l}+\frac{g}{l}\mathrm{e}^{-x_0/g}\right)\right. \\
&\quad \left.-U\tau\right] - A\left(\mathrm{e}^{-d/g}\mathrm{e}^{-d/l}\mathrm{e}^{x/l}+\frac{g}{l}\mathrm{e}^{-x/g}\right)+U\tau \\
&\quad \text{(exponential generation profile with background).}
\end{aligned}
\tag{B.8c}
$$

B.3 Sensing Profiles

The sensing profiles $S(x_0)$ are calculated from the integrated emission profiles ϵ and ϵ_SL with and without sensing layer (SL) according to Eq. 6.4. ϵ and ϵ_SL are calculated according to Eq. 6.5 and read:

$$
\begin{aligned}
\epsilon(x_0) &= G_0\tau d \\
\epsilon_\mathrm{SL}(x_0) &= G_0\tau d\left[1-\frac{l}{d}\cdot\left(\tanh\left(\frac{x_0}{l}\right)+\tanh\left(\frac{d-x_0}{l}\right)\right)\right] \\
&\quad \text{for a constant generation profile,}
\end{aligned}
\tag{B.9a}
$$

$$
\begin{aligned}
\epsilon(x_0) &= G_0\tau g\left[1-\mathrm{e}^{-d/g}\right] \\
\epsilon_\mathrm{SL}(x_0) &= A\left[l\left(\frac{2\mathrm{e}^{-x_0/l}}{\mathrm{e}^{-2d/l}\mathrm{e}^{x_0/l}+\mathrm{e}^{-x_0/l}}-1\right)\cdot\right. \\
&\quad \cdot\left(\mathrm{e}^{-d/g}\mathrm{e}^{-d/l}\mathrm{e}^{x_0/l}+\frac{g}{l}\mathrm{e}^{-x_0/g}\right) \\
&\quad + l\cdot\mathrm{e}^{-d/g}\left(\mathrm{e}^{-d/l}\mathrm{e}^{x_0/l}-1\right)+\frac{g^2}{l}\left(\mathrm{e}^{-d/g}-1\right) \\
&\quad \left.+l\left(1-\mathrm{e}^{x_0/l}\right)+\tanh\left(\frac{x_0}{l}\right)\cdot\left(g\cdot\mathrm{e}^{-x_0/g}+l\cdot\mathrm{e}^{x_0/l}\right)\right] \\
&\quad \text{for an exponential generation profile,}
\end{aligned}
\tag{B.9b}
$$

$$
\begin{aligned}
\epsilon(x_0) &= G_0\tau g\left[1-\mathrm{e}^{-d/g}\right]+U\tau d \\
\epsilon_\mathrm{SL}(x_0) &= \tanh\left(\frac{x_0}{l}\right)\cdot\left[A\left(g\cdot\mathrm{e}^{-x_0/g}+l\cdot\mathrm{e}^{x_0/l}\right)-U\tau l\right] \\
&\quad - A\cdot\left[l\cdot\mathrm{e}^{-d/g}\left(1-\mathrm{e}^{-d/l}\mathrm{e}^{x_0/l}\right)\right. \\
&\quad \left.+\frac{g^2}{l}\left(1-\mathrm{e}^{-d/g}\right)+l\left(\mathrm{e}^{x_0/l}-1\right)\right] \\
&\quad - l\cdot\frac{\mathrm{e}^{-2d/l}\mathrm{e}^{x_0/l}-\mathrm{e}^{-x_0/l}}{\mathrm{e}^{-2d/l}\mathrm{e}^{x_0/l}+\mathrm{e}^{-x_0/l}}\cdot \\
&\quad \cdot\left[A\left(\mathrm{e}^{-d/g}\mathrm{e}^{-d/l}\mathrm{e}^{x_0/l}+\frac{g}{l}\mathrm{e}^{-x_0/g}\right)-U\tau\right]+U\tau d \\
&\quad \text{for an exponential generation profile with background.}
\end{aligned}
\tag{B.9c}
$$

For fitting, the sensing profile $S(x_0)$ of an exponential generation profile with background B is used:

$$\begin{aligned} S(x_0) = 1 - \Bigg[& B + l \cdot \tanh\left(\frac{x_0}{l}\right) \cdot \left(C \left(\mathrm{e}^{x_0/l} + \frac{g}{l} \mathrm{e}^{-x_0/g} \right) - \frac{B}{d} \right) \\ & - C \cdot \Bigg[l \cdot \mathrm{e}^{-d/g} \left(1 - \mathrm{e}^{-d/l} \mathrm{e}^{x_0/l} \right) \\ & + l \left(\mathrm{e}^{x_0/l} - 1 \right) + \frac{g^2}{l} \left(1 - \mathrm{e}^{-d/g} \right) \Bigg] \\ & - l \cdot \frac{\mathrm{e}^{-2d/l} \mathrm{e}^{x_0/l} - \mathrm{e}^{-x_0/l}}{\mathrm{e}^{-2d/l} \mathrm{e}^{x_0/l} + \mathrm{e}^{-x_0/l}} \cdot \\ & \cdot \left[C \left(\mathrm{e}^{-d/g} \mathrm{e}^{-d/l} \mathrm{e}^{x_0/l} + \frac{g}{l} \mathrm{e}^{-x_0/g} \right) \frac{B}{d} \right] \Bigg], \end{aligned} \tag{B.10}$$

$$\text{where} \quad C = \frac{l}{l^2 - g^2} \frac{1 - B}{1 - \mathrm{e}^{-d/g}} \quad \text{and} \quad B = \frac{dU}{k_{\mathrm{Gen}}}.$$

As fit parameters remain the diffusion length l, the width of the generation zone g, and the factor B, which is related to the ratio between the constant background and the exciton density that is created in the exponential generation zone.

C Appendix to Double- and Mixed Emission Layers

C.1 Sample Uniformity

It was indicated in Sec. 6.4 that the performance of the D-EML and M-EML samples varies strongly. This is illustrated in Fig. C.1, where the JV-curves and EQE is shown for D-EML and M-EML devices of the same OLED structure on four different sample runs. Despite the observed variations in both characteristics, distinct properties of D-EML and M-EML can be distinguished:

- The current density at constant voltage is always higher in M-EML than in D-EML.
- The EQE is higher for the D-EML at low current density.
- An initial increase of the EQE with current density is observed for all M-EML samples.
- The efficiency roll-off is weaker in M-EML devices, partially surpassing the EQE of the D-EML at high current densities.

In the main section, the data from run #4 is presented because this run also contains the variation of the matrix ratio of the M-EML ensuring a high comparability between these samples.

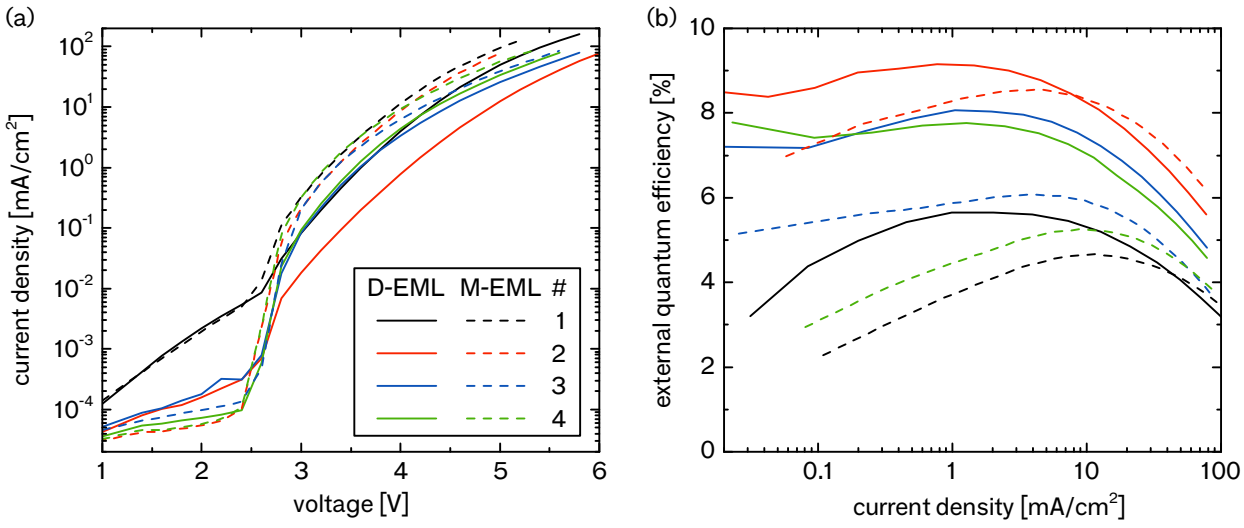

Figure C.1: (a) JV-characteristics and (b) external quantum efficiency vs. current density of D-EML (solid lines) and M-EML samples (dashed lines) from four different sample runs.

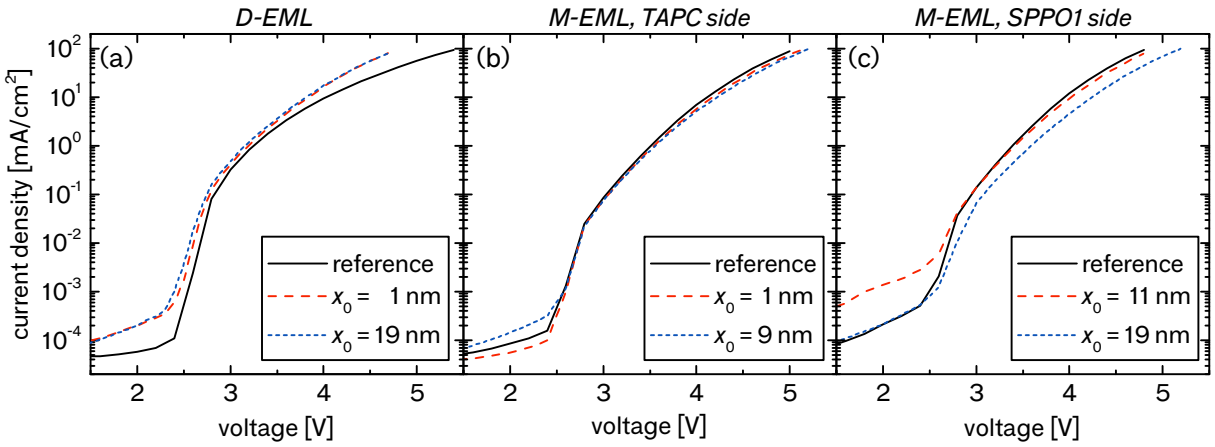

Figure C.2: Current density-voltage behavior of selected D-EML and M-EML samples with and without sensing layer. In (a), the reference device is taken from another sample run.

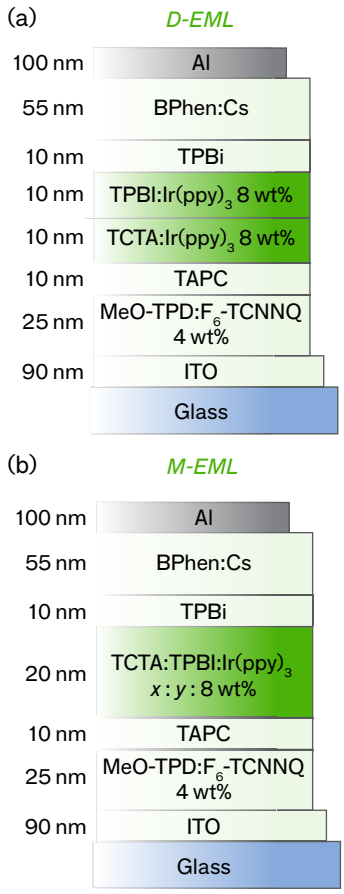

Figure C.3: Structure of the investigated OLEDs: (a) D-EML and (b) M-EML device. For M-EML, the ratio of the two matrix materials $x : y$ is varied.

C.2 *Influence of the Sensor on Current Density*

In order to evaluate the influence of the sensing layer on the performance of D-EML and M-EML sensing intensities (cf. Fig. 6.22), the JV-characteristics of selected samples with and without sensing layer are shown in Fig. C.2. In the D-EML, the current density is similar for all sensor positions. However, as the reference device is taken from another sample run, the current density of the reference exhibits deviations compared to the sensing layer samples, especially at high voltages. Only weak influence of the sensor on the JV-curves is found for the samples containing the sensor at the TAPC side of the M-EML. At the SPPO1-side, however, a decrease of the current density is observed if the sensor is located close to the HBL. Here, the Ir(MDQ)$_2$(acac) molecules seem to trap electrons, which has already been observed previously if Ir(MDQ)$_2$(acac) is located close to SPPO1.[71]

C.3 *Further D-EML and M-EML structures*

Here, the electronic and excitonic properties of D-EML and M-EML devices using the green emitter Ir(ppy)$_3$ embedded in a matrix of the primarily hole transporting TCTA and the primarily electron transporting TPBi are studied. The OLED structures are shown in Fig. C.3.

The JVL-characteristics, EQE, and spectral radiance of the D-EML and the M-EML devices with three different matrix ratios are shown in Fig. C.4. The current density is higher in the M-EML devices compared to the D-EML. Here, higher TPBi contents lead to an increase in current density. The luminance follows the same trend at small voltages. At high voltages, however, the D-EML device shows the highest luminance.

This is also reflected in the EQE, where the D-EML device performs best and reaches an EQE of up to 16 %. In the M-EML devices, the

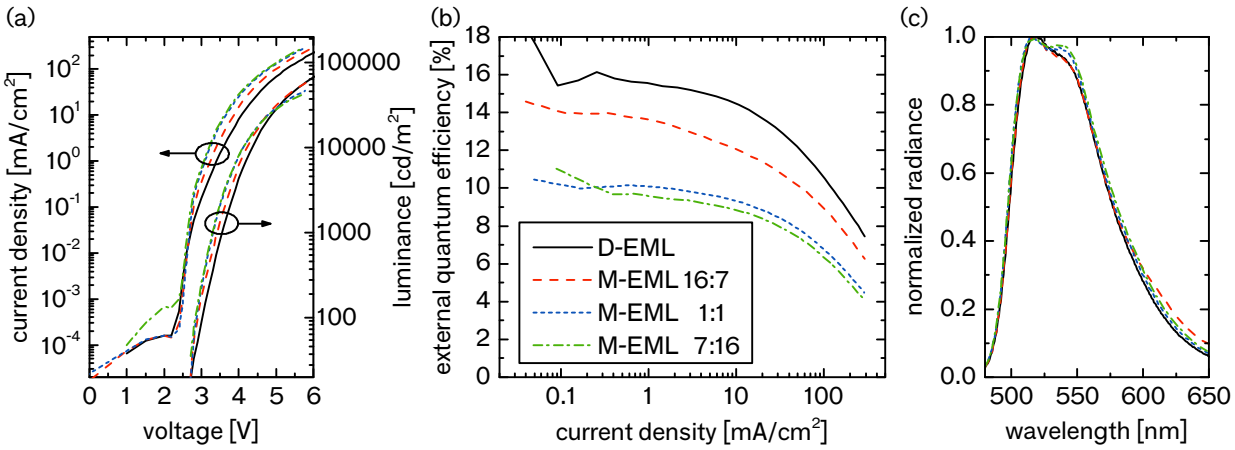

Figure C.4: Performance of OLEDs containing either D-EML or M-EML with varying TCTA:TPBi-ratio $x : y$ (cf. Fig. C.3). (a) Current density (left) and luminance (right) vs. voltage. (b) External quantum efficiency vs. current density. (c) Normalized spectral radiance at 15.4 mA/cm^2.

maximum EQE decreases to 14 % for a TCTA:TPBi-ratio of 16 : 7 and further to around 10 % for matrix ratios of 1 : 1 and 7 : 16. All EQE-current density curves show an initial dip at current densities below 0.3 mA/cm^2, which could be the result of a changed charge carrier balance. Fitting the curves in order to extract J_0 is omitted here, as the initial EQE cannot be properly determined. However, if the EQE decrease at small voltages is disregarded, the critical current density is approximately 200 mA/cm^2 for all four structures suggesting a similar width of the emission zone.

The spectra of the four samples show slight differences: For the M-EMLs with matrix ratios of 1 : 1 and 7 : 16, the centers of mass are slightly red-shifted and the spectra are broadened compared to the other two devices, which would indicate a slightly shifted emission zone. The small shoulder in the red spectral part of the M-EML sample with 16 : 7 is probably related to material contamination or problems with sample production.

Finally, the position and width of the emission zone is studied again using doped blockers. Here, the red emitter Ir(piq)$_3$ is chosen as dopant with a concentration of 1 wt % because it barely influences the current transport in both blockers (a very small increase in current density is observed when doping the TAPC EBL). Figure C.5 shows the normalized spectral radiance of all samples at 15.4 mA/cm^2, together with the PL spectrum of Ir(piq)$_3$. For the D-EML, no red emission from the blockers is observed indicating that the emission zone is well confined at the interface between TCTA and TPBi, and does not reach the blockers. Furthermore, it can be deduced that the emission profile is narrow and that excitons do not reach the blockers. In the M-EML with a matrix ratio of 1 : 1, red emission is mainly detected from the EBL side. This effect is increased in the sample with a matrix ratio of 7 : 16 and results from preferred electron transport in this EML system. This is also in agreement with the observed spectral shift for the two samples in Fig. C.4c. An increase of the TCTA content in the 16 : 7 sample instead leads to a shift of the emission zone towards the HBL. Here, significant red emission from

the HBL side is detected, but also emission from the EBL side. This leads to the conclusion that the generation zone is here positioned closer to the middle of the EML leading to increased EQE compared to the other two M-EML structures.

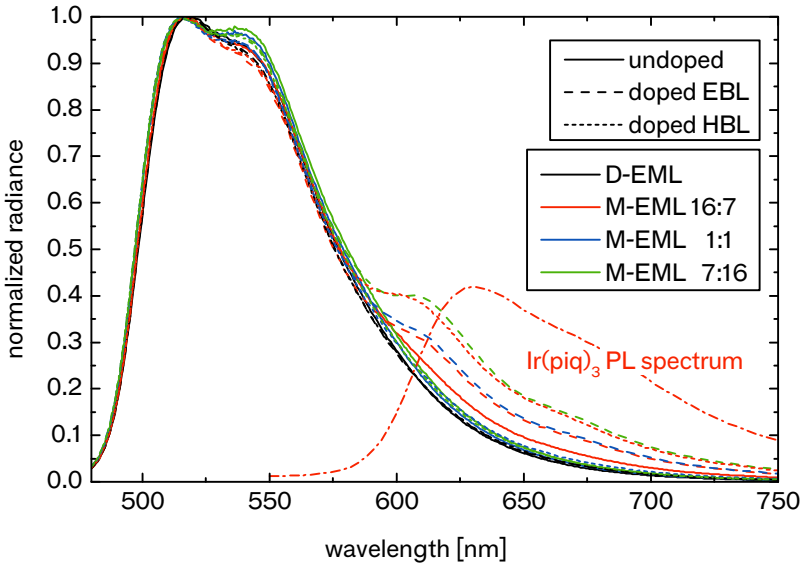

Figure C.5: Normalized spectral radiance of D-EML and M-EML samples with and without doped blockers at a current density of 15.4 mA/cm^2. Dashed/dotted lines show samples where the EBL/HBL is doped with the red emitter Ir(piq)$_3$. The PL spectrum of Ir(piq)$_3$ is given as dash-dotted line.

The observations made on this matrix-emitter system lead to the following conclusions:

- The current density in the M-EML system is enhanced compared to the D-EML.
- The exciton formation region is shifted across the EML by varying the matrix ratio.
- M-EMLs with a ratio of $x \leq y$ primarily transport electrons, which leads to an emission zone close to the EBL.
- The M-EML structure broadens the emission zone compared to the D-EML, but does not lead to an efficiency enhancement.

D Appendix to Molecular Aggregation

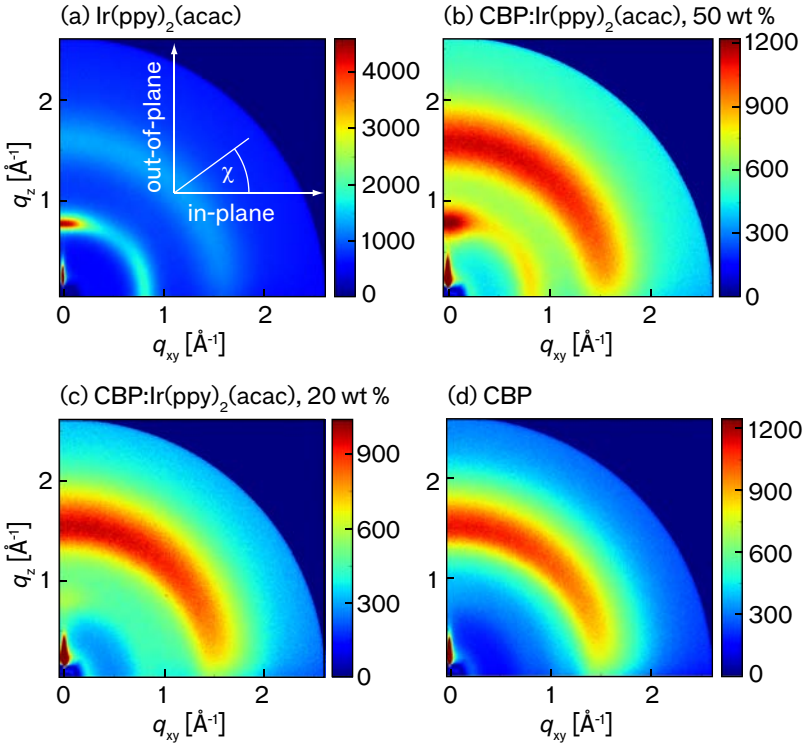

Figure D.1: 2D-GIWAXS measurements on (a) $Ir(ppy)_2(acac)$, (b) CBP:$Ir(ppy)_2(acac)$, 50 wt %, (c) CBP:$Ir(ppy)_2(acac)$, 20 wt %, and (d) CBP.

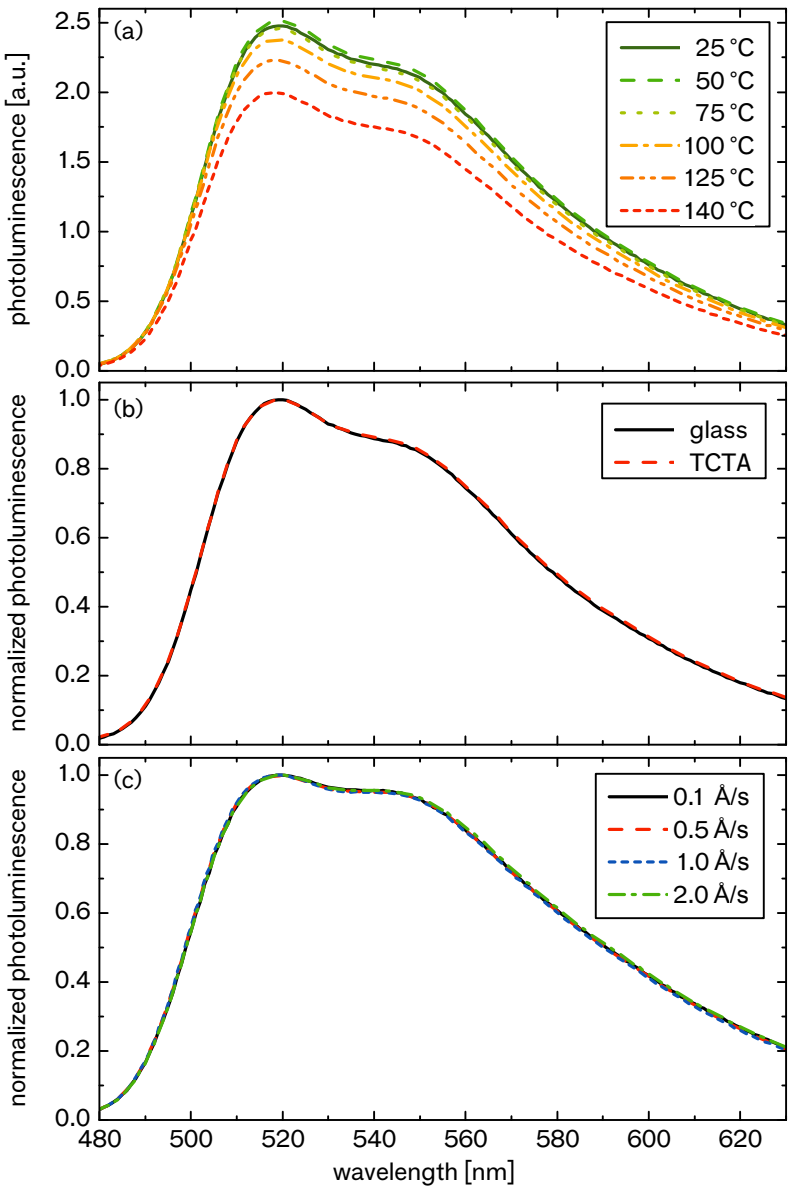

Figure D.2: Influence of processing parameters on the PL spectrum of TCTA:Ir(ppy)$_3$ at 9 mol %: (a) PL intensity varying the substrate temperature, (b) normalized PL intensity for different underlying materials, and (c) normalized PL intensity varying the evaporation rate.

List of Chemical Compounds

Emitter Materials

abbreviation	chemical name
Alq_3	tris(8-hydroxyquinolinato)aluminum
FIr6	iridium(III)bis(4′,6′-difluorophenylpyridinato)tetrakis(1-pyrazolyl)borate
FIrpic	bis[(4,6-difluorophenyl)pyridinato-N,C^2](picolinato)iridium(III)
$Ir(BT)_2(acac)$	bis(2-phenylbenzothiazolato)(acetylacetonate)iridium(III)
$Ir(chpy)_3$	tris(2-(1-cyclohexenyl)pyridine)iridium(III)
$Ir(dhfpy)_2(acac)$	bis(2-(9,9-dihexylfluorenyl)-1-pyridine)(acetylacetonate)iridium(III)
$Ir(MDQ)_2(acac)$	bis(2-methyldibenzo[f,h]quinoxaline)(acetylacetonate)iridium(III)
$Ir(piq)_3$	tris(1-phenylisoquinoline)iridium(III)
$Ir(ppy)_2(acac)$	bis(2-phenylpyridine)(acetylacetonate)iridium(III)
$Ir(ppy)_3$	tris(2-phenylpyridine)iridium(III)
PtOEP	2,3,7,8,12,13,17,18-octaethyl-21H,23H-porphine platinum

Transport Materials

abbreviation	chemical name
4P-NPD	N,N′-di-1-naphthalenyl-N,N′-diphenyl-[1,1′:4′,1″:4″,1‴-quaterphenyl]-4,4‴-diamine
Alq_3	tris(8-hydroxyquinolinato)aluminum
$BAlq_2$	bis-(2-methyl-8-chinolinolato)-(4-phenyl-phenolato)-aluminum(III)
BPhen	4,7-diphenyl-1,10-phenanthroline
CBP	4,4′-bis(carbazol-9-yl)biphenyl
F_6-TCNNQ	2,2′-(perfluoronaphthalene-2,6-diylidene)dimalononitrile
MeO-TPD	N,N,N′,N′-tetrakis(4-methoxyphenyl)-benzidine
MoO_3	molybdenum trioxide
NPB	N,N′-di(naphthalen-1-yl)-N,N′-diphenyl-benzidine
Spiro-TAD	2,2′,7,7′-tetrakis-(N,N-diphenylamino)-9,9′-spirobifluorene
Spiro-TTB	2,2′,7,7′-tetrakis(N,N′-di-p-methylphenylamino)-9,9′-spirobifluorene
SPPO1	2-(diphenylphosphoryl)spirofluorene
TAPC	1,1-bis[(di-4-tolylamino)phenyl]cyclohexane
TCTA	4,4′,4″-tris(N-carbazolyl)-triphenylamine
TPBi	2,2′,2″(1,3,5-benzenetriyl)tris-(1-phenyl-1H-benzimidazole)

List of Abbreviations

AFM	atomic force microscopy
D-EML	double emission layer
DFT	density functional theory
DOS	density of states
EBL	electron blocking layer
EL	electroluminescence
EML	emission layer
EQE	external quantum efficiency
ETL	electron transport layer
FWHM	full width at half maximum
GIWAXS	grazing incidence wide-angle X-ray scattering
GIXRD	grazing incidence X-ray diffraction
HBL	hole blocking layer
HOMO	highest occupied molecular orbital
HTL	hole transport layer
IQE	internal quantum efficiency
ISC	intersystem crossing
LCAO	linear combination of atomic orbitals
LE	luminous efficacy
LED	light-emitting diode
LUMO	lowest unoccupied molecular orbital
M-EML	mixed emission layer
OLED	organic light-emitting diode
pin	p-doped, intrinsic, n-doped
PL	photoluminescence
SCLC	space charge limited current
S-EML	single emission layer
SPA	singlet-polaron annihilation
SSA	singlet-singlet annihilation
STA	singlet-triplet annihilation
TADF	thermally activated delayed fluorescence
TH	triplet harvesting
TPA	triplet-polaron annihilation
TTA	triplet-triplet annihilation
UHV	ultra-high vacuum
UV	ultraviolet
XPS	X-ray photoelectron spectroscopy
XRR	X-ray reflectometry

List of Important Symbols

a	anisotropy factor
B	background intensity
c	speed of light
d	layer thickness
D	diffusion constant
E	energy
$\langle E \rangle$	center of mass
E_0	excitation energy
E_{00}	energy of the fundamental transition
E_{abs}	absorbed energy
EQE	external quantum efficiency
EQE_0	initial EQE
$f_\nu(E)$	Poisson distributed transition
F	Purcell factor
g	generation width
$G(x)$	generation profile
$h, \hbar$	Planck constant
$\hbar\omega$	energetic distance between two spectroscopic lines
I_{e}	radiant intensity
IQE	internal quantum efficiency
J	current density
J_0	critical current density
$J_{90\%}$	current density at which EQE $=90\,\%\cdot\mathrm{EQE}_0$
k	intrinsic decay rate
$k^\star$	effective decay rate
k_{ISC}	intersystem crossing rate
k_{nr}	non-radiative decay rate
k_{r}	radiative decay rate
k_{TP}	triplet-polaron annihilation rate
k_{TT}	triplet-triplet annihilation rate
l	diffusion length
L	luminance
LE	luminous efficacy
$n(x)$	spatial exciton density
n_0	initial exciton density
n_{P}	polaron density
n_{T}	triplet exciton density
q	elementary charge

q_z, q_{xy}	scattering vectors in GIWAXS measurement
R	intermolecular distance
s	Huang-Rhys factor
S	singlet state
$S(x_0)$	sensing profile
t	time
T	triplet state
V	voltage
w	width of the emission zone
x_0	sensing layer position
α	absorption coefficient
Γ	concentration
ϵ	integrated emission profile
ϵ_r	relative permittivity
$\epsilon_{SL}(x_0)$	integrated emission profile with sensing layer
ϵ_0	permittivity of free space
η_{out}	outcoupling efficiency
η_{rad}	intrinsic radiative efficiency
$\eta^\star_{rad}$	effective radiative efficiency
$\theta, 2\theta$	reflection/diffraction angle in XRD
λ	wavelength
μ	mobility
μ_D	dipole moment
ξ	layer roughness
σ_ν	standard deviation of a spectroscopic line ν
τ	intrinsic lifetime
$\tau^\star$	effective lifetime
τ_S	singlet lifetime
τ_T	triplet lifetime
χ	polar angle in GIWAXS measurement
ω	incident angle between ray and sample in XRD

Bibliography

[1] T. A. Edison, *Electric Lamp*, patent no. 223898, USA (1880).

[2] R. V. Steele, *Nature Photonics* 1, 25 (2007).

[3] Y. Narukawa, M. Sano, T. Sakamoto, T. Yamada, and T. Mukai, *Physica Status Solidi A* 205, 1081 (2008).

[4] Press Release, *Cree First to Break 300 Lumens-Per-Watt Barrier*, URL: www.cree.com/News-and-Events/Cree-News/Press-Releases/2014/March/300LPW-LED-barrier, accessed on 2015-04-01.

[5] S. Nakamura and M. R. Krames, *Proceedings of the IEEE* 101, 2211 (2013).

[6] Nobel Media AB 2014, *The Nobel Prize in Physics 2014*, URL: www.nobelprize.org/nobel_prizes/physics/laureates/2014, accessed on 2015-04-01.

[7] C. W. Tang and S. A. VanSlyke, *Applied Physics Letters* 51, 913 (1987).

[8] S. Reineke, F. Lindner, G. Schwartz, N. Seidler, K. Walzer, B. Lüssem, and K. Leo, *Nature* 459, 234 (2009).

[9] G. He, C. Rothe, S. Murano, A. Werner, O. Zeika, and J. Birnstock, *Journal of the Society for Information Display* 17, 159 (2009).

[10] S. Reineke, M. Thomschke, B. Lüssem, and K. Leo, *Reviews of Modern Physics* 85, 1245 (2013).

[11] C. Murawski, K. Leo, and M. C. Gather, *Advanced Materials* 25, 6801 (2013).

[12] M. A. Baldo, C. Adachi, and S. R. Forrest, *Physical Review B* 62, 10967 (2000).

[13] S. Reineke, K. Walzer, and K. Leo, *Physical Review B* 75, 125328 (2007).

[14] M. Schwoerer and H. C. Wolf, *Organic Molecular Solids*. Wiley-VCH Verlag GmbH (2007).

[15] M. Born and R. Oppenheimer, *Annalen der Physik* 389, 457 (1927).

[16] M. Pope and C. E. Swenberg, *Electric Processes in Organic Crystals* (1982).

[17] W. Demtröder, *Molecular Physics – Theoretical Principles and Experimental Methods*. Wiley-VCH Verlag GmbH (2005).

[18] T. Koopmans, *Physica* 1, 104 (1934).

[19] M. Pfeiffer and S. R. Forrest, In: R. Waser (ed.), *Nanoelectronics and Information Technology*, 916–931, Wiley-VCH Verlag GmbH (2003).

[20] G. H. Wannier, *Physical Review* 52, 191 (1937).

[21] J. Frenkel, *Physical Review* 37, 17 (1931).

[22] M. Segal, M. A. Baldo, R. J. Holmes, S. R. Forrest, and Z. G. Soos, *Physical Review B* 68, 75211 (2003).

[23] S. Hofmann, *Exciton Dynamics in White Organic Light-Emitting Diodes comprising Triplet Harvesting*. Ph.D. Thesis, Technische Universität Dresden (2012).

[24] M. Kasha, *Discussions of the Faraday Society* 9, 14 (1950).

[25] J. Kido, H. Hayase, K. Hongawa, K. Nagai, and K. Okuyama, *Applied Physics Letters* 65, 2124 (1994).

[26] Y. Ma, H. Zhang, J. Shen, and C. Che, *Synthetic Metals* 94, 245 (1998).

[27] M. A. Baldo, D. F. O'Brien, Y. You, A. Shoustikov, S. Sibley, M. E. Thompson, and S. R. Forrest, *Nature* 395, 151 (1998).

[28] M. A. Baldo, S. Lamansky, P. E. Burrows, M. E. Thompson, and S. R. Forrest, *Applied Physics Letters* 75, 4 (1999).

[29] D. Kasemann, R. Brückner, H. Fröb, and K. Leo, *Physical Review B* 84, 115208 (2011).

[30] N. Giebink and S. R. Forrest, *Physical Review B* 79, 073302 (2009).

[31] Y. Zhang, M. Whited, M. E. Thompson, and S. R. Forrest, *Chemical Physics Letters* 495, 161 (2010).

[32] M. Lehnhardt, T. Riedl, T. Rabe, and W. Kowalsky, *Organic Electronics* 12, 486 (2011).

[33] K.-C. Tang, K. L. Liu, and I.-C. Chen, *Chemical Physics Letters* 386, 437 (2004).

[34] H. Haken and H. C. Wolf, *Molekülphysik und Quantenchemie*. Springer-Verlag, 5th edition (2006).

[35] A. Köhler and H. Bässler, *Materials Science & Engineering R* 66, 71 (2009).

[36] S. T. Hoffmann, H. Bässler, and A. Köhler, *Journal of Physical Chemistry B* 114, 17 (2010).

[37] R. Meerheim, M. Furno, S. Hofmann, B. Lüssem, and K. Leo, *Applied Physics Letters* 97, 253305 (2010).

[38] T. Förster, *Annalen der Physik* 437, 55 (1948).

[39] Y. Kawamura, J. Brooks, J. J. Brown, H. Sasabe, and C. Adachi, *Physical Review Letters* 96, 17404 (2006).

[40] E. B. Namdas, A. Ruseckas, I. D. W. Samuel, S.-C. Lo, and P. L. Burn, *Applied Physics Letters* 86, 091104 (2005).

[41] W. Staroske, M. Pfeiffer, K. Leo, and M. Hoffmann, *Physical Review Letters* 98, 197402 (2007).

[42] L.-Z. Yu, X.-Y. Jiang, Z.-L. Zhang, L.-R. Lou, and C.-T. Lee, *Journal of Applied Physics* 105, 013105 (2009).

[43] Y. Divayana and X. Sun, *Physical Review Letters* 99, 143003 (2007).

[44] B. W. D'Andrade, M. E. Thompson, and S. R. Forrest, *Advanced Materials* 14, 147 (2002).

[45] D. L. Dexter, *The Journal of Chemical Physics* 21, 836 (1953).

[46] C. Weichsel, S. Reineke, M. Furno, B. Lüssem, and K. Leo, *Journal of Applied Physics* 111, 033102 (2012).

[47] S. Reineke, G. Schwartz, K. Walzer, and K. Leo, *Applied Physics Letters* 91, 123508 (2007).

[48] H. Bässler, *Physica Status Solidi B* 175, 15 (1993).

[49] A. Miller and E. Abrahams, *Physical Review* 120, 745 (1960).

[50] L.-B. Lin, S. A. Jenekhe, and P. M. Borsenberger, *Applied Physics Letters* 69, 3495 (1996).

[51] P. W. M. Blom, M. J. M. de Jong, and S. Breedijk, *Applied Physics Letters* 71, 930 (1997).

[52] W. Brütting, S. Berleb, and A. G. Mückl, *Organic Electronics* 2, 1 (2001).

[53] W. Brütting and C. Adachi (eds.), *Physics of Organic Semiconductors*. Wiley-VCH Verlag GmbH, 2nd edition (2012).

[54] W. Brütting, In W. Brütting (ed.), *Physics of Organic Semiconductors*, 1–11, Wiley-VCH Verlag GmbH (2005).

[55] M. A. Lampert, *Reports on Progress in Physics* 27, 329 (1964).

[56] H. Yamamoto, H. Kasajima, W. Yokoyama, H. Sasabe, and C. Adachi, *Applied Physics Letters* 86, 083502 (2005).

[57] M. Pfeiffer, T. Fritz, J. Blochwitz, A. Nollau, B. Plönnigs, A. Beyer, and K. Leo, *Advances in Solid State Physics* 39, 77 (1999).

[58] K. Walzer, B. Maennig, M. Pfeiffer, and K. Leo, *Chemical Reviews* 107, 1233 (2007).

[59] B. Lüssem, M. Riede, and K. Leo, *Physica Status Solidi A* 210, 9 (2012).

[60] X. Zhou, J. Blochwitz, M. Pfeiffer, A. Nollau, T. Fritz, and K. Leo, *Advanced Functional Materials* 11, 310 (2001).

[61] W. Gao and A. Kahn, *Journal of Applied Physics* 94, 359 (2003).

[62] T. Menke, D. Ray, H. Kleemann, M. P. Hein, K. Leo, and M. Riede, *Organic Electronics* 15, 365 (2014).

[63] T. Menke, *Molecular Doping of Organic Semiconductors – A Conductivity and Seebeck Study*. Ph.D. Thesis, Technische Universität Dresden (2013).

[64] G. Parthasarathy, C. Shen, A. Kahn, and S. R. Forrest, *Journal of Applied Physics* 89, 4986 (2001).

[65] J. Kido and T. Matsumoto, *Applied Physics Letters* 73, 2866 (1998).

[66] M. L. Tietze, L. Burtone, M. Riede, B. Lüssem, and K. Leo, *Physical Review B* 86, 035320 (2012).

[67] S. Hofmann, M. Thomschke, P. Freitag, M. Furno, B. Lüssem, and K. Leo, *Applied Physics Letters* 97, 253308 (2010).

[68] M. Furno, R. Meerheim, S. Hofmann, B. Lüssem, and K. Leo, *Physical Review B* 85, 115205 (2012).

[69] J. Huang, M. Pfeiffer, A. Werner, J. Blochwitz, K. Leo, and S. Liu, *Applied Physics Letters* 80, 139 (2002).

[70] T. Matsushima and C. Adachi, *Applied Physics Letters* 89, 253506 (2006).

[71] C. Weichsel, L. Burtone, S. Reineke, S. I. Hintschich, M. C. Gather, K. Leo, and B. Lüssem, *Physical Review B* 86, 075204 (2012).

[72] C. Yun, G. Xie, C. Murawski, J. Lee, F. Ventsch, K. Leo, and M. C. Gather, *Organic Electronics* 14, 1695 (2013).

[73] P. K. Koech, A. B. Padmaperuma, L. Wang, J. S. Swensen, E. Polikarpov, J. T. Darsell, J. E. Rainbolt, and D. J. Gaspar, *Chemistry of Materials* 22, 3926 (2010).

[74] C. Murawski, C. Fuchs, S. Hofmann, K. Leo, and M. C. Gather, *Applied Physics Letters* 105, 113303 (2014).

[75] Z. B. Wang, M. G. Helander, J. Qiu, D. P. Puzzo, M. T. Greiner, Z. M. Hudson, S. Wang, Z. W. Liu, and Z. H. Lu, *Nature Photonics* 5, 753 (2011).

[76] H. Uoyama, K. Goushi, K. Shizu, H. Nomura, and C. Adachi, *Nature* 492, 234 (2012).

[77] S. O. Jeon, S. E. Jang, H. S. Son, and J. Y. Lee, *Advanced Materials* 23, 1436 (2011).

[78] K.-H. Kim, C.-K. Moon, J.-H. Lee, S.-Y. Kim, and J.-J. Kim, *Advanced Materials* 26, 3844 (2014).

[79] P. E. Burrows, V. Bulović, S. R. Forrest, L. S. Sapochak, D. M. McCarty, and M. E. Thompson, *Applied Physics Letters* 65, 2922 (1994).

[80] D. Y. Kondakov, W. C. Lenhart, and W. F. Nichols, *Journal of Applied Physics* 101 (2007).

[81] M. Hermenau, S. Schubert, H. Klumbies, J. Fahlteich, L. Müller-Meskamp, K. Leo, and M. Riede, *Solar Energy Materials and Solar Cells* 97, 102 (2012).

[82] M. Pfeiffer, S. R. Forrest, K. Leo, and M. E. Thompson, *Advanced Materials* 14, 1633 (2002).

[83] M. Wohlgenannt, K. Tandon, S. Mazumdar, S. Ramasesha, and Z. V. Vardeny, *Nature* 409, 494 (2001).

[84] M. Carvelli, R. Janssen, and R. Coehoorn, *Physical Review B* 83, 075203 (2011).

[85] C. Rothe, S. M. King, and A. P. Monkman, *Physical Review Letters* 97, 076602 (2006).

[86] S. L. M. Van Mensfoort, J. Billen, M. Carvelli, S. I. E. Vulto, R. A. J. Janssen, and R. Coehoorn, *Journal of Applied Physics* 109, 064502 (2011).

[87] A. Endo, M. Ogasawara, A. Takahashi, D. Yokoyama, Y. Kato, and C. Adachi, *Advanced Materials* 21, 4802 (2009).

[88] J. W. Sun, J.-H. Lee, C.-K. Moon, K.-H. Kim, H. Shin, and J.-J. Kim, *Advanced Materials* 26, 5684 (2014).

[89] H. Nakanotani, T. Higuchi, T. Furukawa, K. Masui, K. Morimoto, M. Numata, H. Tanaka, Y. Sagara, T. Yasuda, and C. Adachi, *Nature Communications* 5, 4016 (2014).

[90] K. A. Neyts, *Journal of the Optical Society of America A* 15, 962 (1998).

[91] S. Mladenovski, S. Hofmann, S. Reineke, L. Penninck, T. Verschueren, and K. Neyts, *Journal of Applied Physics* 109, 083114 (2011).

[92] T. D. Schmidt, D. S. Setz, M. Flämmich, J. Frischeisen, D. Michaelis, B. C. Krummacher, N. Danz, and W. Brütting, *Applied Physics Letters* 99, 163302 (2011).

[93] L. Penninck, F. Steinbacher, R. Krause, and K. Neyts, *Organic Electronics* 13, 3079 (2012).

[94] C. Adachi, M. A. Baldo, M. E. Thompson, and S. R. Forrest, *Journal of Applied Physics* 90, 5048 (2001).

[95] S. R. Forrest, D. D. C. Bradley, and M. E. Thompson, *Advanced Materials* 15, 1043 (2003).

[96] K.-H. Kim, S. Lee, C.-K. Moon, S.-Y. Kim, Y.-S. Park, J.-H. Lee, J. W. Lee, J. Huh, Y. You, and J.-J. Kim, *Nature Communications* 5, 4769 (2014).

[97] F. Steiner, S. Bange, J. Vogelsang, and J. M. Lupton, *The Journal of Physical Chemistry Letters* 6, 999 (2015).

[98] P. Liehm, C. Murawski, M. Furno, B. Lüssem, K. Leo, and M. C. Gather, *Applied Physics Letters* 101, 253304 (2012).

[99] A. Graf, P. Liehm, C. Murawski, S. Hofmann, K. Leo, and M. C. Gather, *Journal of Materials Chemistry C* 2, 10298 (2014).

[100] J.-H. Lee, G. Sarada, C.-K. Moon, W. Cho, K.-H. Kim, Y. G. Park, J. Y. Lee, S.-H. Jin, and J.-J. Kim, *Advanced Optical Materials* 3, 211 (2015).

[101] C.-K. Moon, K.-H. Kim, J. W. Lee, and J.-J. Kim, *Chemistry of Materials* DOI: 10.1021/acs.chemmater.5b00469 (2015).

[102] M. Flämmich, J. Frischeisen, D. S. Setz, D. Michaelis, B. C. Krummacher, T. D. Schmidt, W. Brütting, and N. Danz, *Organic Electronics* 12, 1663 (2011).

[103] R. Meerheim, R. Nitsche, and K. Leo, *Applied Physics Letters* 93, 043310 (2008).

[104] S.-J. Su, E. Gonmori, H. Sasabe, and J. Kido, *Advanced Materials* 20, 4189 (2008).

[105] T. Matsushima and C. Adachi, *Applied Physics Letters* 92, 063306 (2008).

[106] K. H. Lee, L. K. Kang, J. Y. Lee, S. Kang, S. O. Jeon, K. S. Yook, J. Y. Lee, and S. S. Yoon, *Advanced Functional Materials* 20, 1345 (2010).

[107] C. A. Parker and C. G. Hatchard, *Proceedings of the Royal Society London A* 269, 574 (1962).

[108] B. Wallikewitz, D. Kabra, S. Gélinas, and R. H. Friend, *Physical Review B* 85, 045209 (2012).

[109] Y. Zhang and S. R. Forrest, *Physical Review Letters* 108, 267404 (2012).

[110] Y. Luo and H. Aziz, *Advanced Functional Materials* 20, 1285 (2010).

[111] C. Adachi, R. C. Kwong, P. Djurovich, V. Adamovich, M. A. Baldo, M. E. Thompson, and S. R. Forrest, *Applied Physics Letters* 79, 2082 (2001).

[112] J. S. Swensen, E. Polikarpov, A. Von Ruden, L. Wang, L. S. Sapochak, and A. B. Padmaperuma, *Advanced Functional Materials* 21, 3250 (2011).

[113] S. Reineke, G. Schwartz, K. Walzer, and K. Leo, *Physica Status Solidi-Rapid Research Letters* 3, 67 (2009).

[114] J. C. Ribierre, A. Ruseckas, K. Knights, S. V. Staton, N. Cumpstey, P. L. Burn, and I. D. W. Samuel, *Physical Review Letters* 100, 017402 (2008).

[115] H. van Eersel, P. A. Bobbert, and R. Coehoorn, *Journal of Applied Physics* 117, 115502 (2015).

[116] Y. Zhang and S. Forrest, *Chemical Physics Letters* 590, 106 (2013).

[117] S. Reineke, G. Schwartz, K. Walzer, M. Falke, and K. Leo, *Applied Physics Letters* 94, 163305 (2009).

[118] R. C. Powell and Z. G. Soos, *Journal of Luminescence* 11, 1 (1975).

[119] J. Kalinowski, J. Mezyk, F. Meinardi, R. Tubino, M. Cocchi, and D. Virgili, *Journal of Applied Physics* 98, 063532 (2005).

[120] E. Engel, K. Leo, and M. Hoffmann, *Chemical Physics* 325, 170 (2006).

[121] M. A. Baldo and S. R. Forrest, *Physical Review B* 62, 10958 (2000).

[122] D. Song, S. Zhao, Y. Luo, and H. Aziz, *Applied Physics Letters* 97, 243304 (2010).

[123] G. Schwartz, T.-H. Ke, C.-C. Wu, K. Walzer, and K. Leo, *Applied Physics Letters* 93, 73304 (2008).

[124] Y. Sun, N. C. Giebink, H. Kanno, B. Ma, M. E. Thompson, and S. R. Forrest, *Nature* 440, 908 (2006).

[125] G. Schwartz, S. Reineke, T. C. Rosenow, K. Walzer, and K. Leo, *Advanced Functional Materials* 19, 1319 (2009).

[126] M. E. Kondakova, J. C. Deaton, T. D. Pawlik, D. J. Giesen, D. Y. Kondakov, R. H. Young, T. L. Royster, D. L. Comfort, and J. D. Shore, *Journal of Applied Physics* 107, 014515 (2010).

[127] T. C. Rosenow, M. Furno, S. Reineke, S. Olthof, B. Lüssem, and K. Leo, *Journal of Applied Physics* 108, 113113 (2010).

[128] S. Hofmann, M. Furno, B. Lüssem, K. Leo, and M. C. Gather, *Physica Status Solidi A* 210, 1467 (2013).

[129] S. Hofmann, M. Hummert, R. Scholz, R. Luschtinetz, C. Murawski, P.-A. Will, S. I. Hintschich, J. Alex, V. Jankus, A. P. Monkman, B. Lüssem, K. Leo, and M. C. Gather, *Chemistry of Materials* 26, 2414 (2014).

[130] J. Kalinowski, W. Stampor, J. Mezyk, M. Cocchi, D. Virgili, V. Fattori, and P. Di Marco, *Physical Review B* 66, 235321 (2002).

[131] H. Bouchriha, G. Delacote, P. Delannoy, and M. Schott, *Le Journal de Physique* 35, 577 (1974).

[132] W. Helfrich, *Physical Review Letters* 16, 401 (1966).

[133] V. Ern, H. Bouchriha, J. Fourny, and G. Delacote, *Solid State Communications* 9, 1201 (1971).

[134] R. B. Comizzoli, *Photochemistry and Photobiology* 15, 399 (1972).

[135] J. Kalinowski, P. Di Marco, M. Cocchi, V. Fattori, N. Camaioni, and J. Duff, *Applied Physics Letters* 68, 2317 (1996).

[136] W. Stampor, J. Kalinowski, P. Di Marco, and V. Fattori, *Applied Physics Letters* 70, 1935 (1997).

[137] J. Szmytkowski, W. Stampor, J. Kalinowski, and Z. H. Kafafi, *Applied Physics Letters* 80, 1465 (2002).

[138] J. Kalinowski, W. Stampor, J. Szmytkowski, D. Virgili, M. Cocchi, V. Fattori, and C. Sabatini, *Physical Review B* 74, 085316 (2006).

[139] M. Deussen, M. Scheidler, and H. Bässler, *Synthetic Metals* 73, 123 (1995).

[140] Z. D. Popovic and H. Aziz, *Journal of Applied Physics* 98, 013510 (2005).

[141] Y. Luo, H. Aziz, Z. D. Popovic, and G. Xu, *Applied Physics Letters* 89, 103505 (2006).

[142] S. Reineke, T. C. Rosenow, B. Lüssem, and K. Leo, *Advanced Materials* 22, 3189 (2010).

[143] N. Chopra, J. Lee, J. G. Xue, and F. So, *IEEE Transactions On Electron Devices* 57, 101 (2010).

[144] A. B. Chwang, R. C. Kwong, and J. J. Brown, *Applied Physics Letters* 80, 725 (2002).

[145] J. C. Scott, S. Karg, and S. A. Carter, *Journal of Applied Physics* 82, 1454 (1997).

[146] B. Ruhstaller, S. A. Carter, S. Barth, H. Riel, W. Riess, and J. C. Scott, *Journal of Applied Physics* 89, 4575 (2001).

[147] D. V. Khramtchenkov, H. Bässler, and V. I. Arkhipov, *Journal of Applied Physics* 79, 9283 (1996).

[148] N. Giebink and S. R. Forrest, *Physical Review B* 77, 235215 (2008).

[149] H. Nakanotani, H. Sasabe, and C. Adachi, *Applied Physics Letters* 86, 213506 (2005).

[150] N. Tessler, N. T. Harrison, D. S. Thomas, and R. H. Friend, *Applied Physics Letters* 73, 732 (1998).

[151] Y. Divayana, B. J. Chen, and X. W. Sun, *Applied Physics Letters* 88, 096101 (2006).

[152] A. A. Zakhidov, S. Reineke, B. Lüssem, and K. Leo, *Organic Electronics* 13, 356 (2012).

[153] K. Hayashi, H. Nakanotani, M. Inoue, K. Yoshida, O. Mikhnenko, T.-Q. Nguyen, and C. Adachi, *Applied Physics Letters* 106, 093301 (2015).

[154] S. L. M. van Mensfoort, M. Carvelli, M. Megens, D. Wehenkel, M. Bartyzel, H. Greiner, R. A. J. Janssen, and R. Coehoorn, *Nature Photonics* 4, 329 (2010).

[155] N. Seidler, S. Reineke, K. Walzer, B. Lüssem, A. Tomkeviciene, J. V. Grazulevicius, and K. Leo, *Applied Physics Letters* 96, 93304 (2010).

[156] X. Ren, J. Li, R. J. Holmes, P. I. Djurovich, S. R. Forrest, and M. E. Thompson, *Chemistry Of Materials* 16, 4743 (2004).

[157] J. Lee, J.-I. Lee, J. Y. Lee, and H. Y. Chu, *Organic Electronics* 10, 1529 (2009).

[158] J. Lee, J.-I. Lee, J. Y. Lee, and H. Y. Chu, *Applied Physics Letters* 95, 253304 (2009).

[159] M.-T. Chu, M.-T. Lee, C. H. Chen, and M.-R. Tseng, *Organic Electronics* 10, 1158 (2009).

[160] R. Coehoorn, H. van Eersel, P. Bobbert, and R. Janssen, *Advanced Functional Materials* 25, 2024 (2014).

[161] S. Wehrmeister, L. Jäger, T. Wehlus, A. F. Rausch, T. C. G. Reusch, T. D. Schmidt, and W. Brütting, *Physical Review Applied* 3, 024008 (2015).

[162] M. Schober, M. Anderson, M. Thomschke, J. Widmer, M. Furno, R. Scholz, B. Lüssem, and K. Leo, *Physical Review B* 84, 165326 (2011).

[163] C. Elschner, *Structural Investigations of Disordered Organic Thin Films*. Ph.D. Thesis, Technische Universität Dresden (2013).

[164] J. Rivnay, S. C. B. Mannsfeld, C. E. Miller, A. Salleo, and M. F. Toney, *Chemical Reviews* 112, 5488 (2012).

[165] S. Reineke, *Controlling Excitons: Concepts for Phosphorescent Organic LEDs at High Brightness*. Ph.D. Thesis, Technische Universität Dresden (2009).

[166] P. Freitag, *White Top-Emitting OLEDs on Metal Substrates*. Ph.D. Thesis, Technische Universität Dresden (2010).

[167] S. Tokito, K. Noda, and Y. Taga, *Journal of Physics D: Applied Physics* 29, 2750 (1996).

[168] T. Matsushima, Y. Kinoshita, and H. Murata, *Applied Physics Letters* 91, 253504 (2007).

[169] L. S. Hung, C. W. Tang, and M. G. Mason, *Applied Physics Letters* 70, 152 (1997).

[170] M. Thelakkat, R. Fink, F. Haubner, and H.-W. Schmidt, *Macromolecular Symposia* 125, 157 (1997).

[171] S. S. Olthof, *Photoelectron Spectroscopy on Doped Organic Semiconductors and Related Interfaces*. Ph.D. Thesis, Technische Universität Dresden (2010).

[172] P. van Gemmern, V. van Elsbergen, S. P. Grabowski, H. Boerner, H.-P. Löbl, H. Becker, H. Kalisch, M. Heuken, and R. H. Jansen, *Journal of Applied Physics* 100, 123707 (2006).

[173] R. Meerheim, K. Walzer, M. Pfeiffer, and K. Leo, *Applied Physics Letters* 89, 061111 (2006).

[174] R. J. Holmes, B. W. D'Andrade, S. R. Forrest, X. F. Ren, J. Li, and M. E. Thompson, *Applied Physics Letters* 83, 3818 (2003).

[175] A. Endo, K. Suzuki, T. Yoshihara, S. Tobita, M. Yahiro, and C. Adachi, *Chemical Physics Letters* 460, 155 (2008).

[176] S. H. Eom, Y. Zheng, N. Chopra, J. Lee, F. So, and J. G. Xue, *Applied Physics Letters* 93, 133309 (2008).

[177] S. H. Eom, Y. Zheng, E. Wrzesniewski, J. Lee, N. Chopra, F. So, and J. G. Xue, *Organic Electronics* 10, 686 (2009).

[178] M. Ikai, S. Tokito, Y. Sakamoto, T. Suzuki, and Y. Taga, *Applied Physics Letters* 79, 156 (2001).

[179] N. Seidler, *Entwicklung einer Architektur für effiziente blaue OLEDs*. Diploma Thesis, Technische Universität Dresden (2009).

[180] Y. Zheng, S. H. Eom, N. Chopra, J. W. Lee, F. So, and J. G. Xue, *Applied Physics Letters* 92, 223301 (2008).

[181] K. Goushi, R. Kwong, J. J. Brown, H. Sasabe, and C. Adachi, *Journal Of Applied Physics* 95, 7798 (2004).

[182] J. H. Jou, C.-P. Wang, M. H. Wu, P.-H. Chiang, H.-L. Lin, H. C. Li, and R.-S. Liu, *Organic Electronics* 8, 29 (2007).

[183] T. C. Wong, J. Kovac, C. S. Lee, L. S. Hung, and S. T. Lee, *Chemical Physics Letters* 334, 61 (2001).

[184] S. O. Jeon, K. S. Yook, C. W. Joo, and J. Y. Lee, *Applied Physics Letters* 94, 13301 (2009).

[185] K. S. Yook, S. O. Jeon, C. W. Joo, and J. Y. Lee, *Organic Electronics* 10, 384 (2009).

[186] C. Adachi, R. Kwong, and S. R. Forrest, *Organic Electronics* 2, 37 (2001).

[187] J.-W. Kang, S.-H. Lee, H.-D. Park, W.-I. Jeong, K.-M. Yoo, Y.-S. Park, and J.-J. Kim, *Applied Physics Letters* 90, 223508 (2007).

[188] C. Murawski, P. Liehm, K. Leo, and M. C. Gather, *Advanced Functional Materials* 24, 1117 (2014).

[189] Q. Huang, S. Reineke, K. Walzer, M. Pfeiffer, and K. Leo, *Applied Physics Letters* 89, 263512 (2006).

[190] W. Ji, L. Zhang, and W. Xie, *Optics letters* 37, 2019 (2012).

[191] D. Song, S. Zhao, and H. Aziz, *Advanced Functional Materials* 21, 2311 (2011).

[192] M. Mesta, M. Carvelli, R. J. de Vries, H. van Eersel, J. J. M. van der Holst, M. Schober, M. Furno, B. Lüssem, K. Leo, P. Loebl, R. Coehoorn, and P. A. Bobbert, *Nature Materials* 12, 652 (2013).

[193] M. Schober, *Charge Transport in Organic Light-Emitting Diodes*. Ph.D. Thesis, Technische Universität Dresden (2012).

[194] D. Zhao, H.-P. Loebl, and V. Van Elsbergen, *Organic Electronics* 14, 3117 (2013).

[195] Y.-S. Park, S. Lee, K.-H. Kim, S.-Y. Kim, J.-H. Lee, and J.-J. Kim, *Advanced Functional Materials* 23, 4914 (2013).

[196] J. Grüner, M. Remmers, and D. Neher, *Advanced Materials* 9, 964 (1997).

[197] T. Granlund, L. A. A. Pettersson, and O. Inganäs, *Journal of Applied Physics* 89, 5897 (2001).

[198] A. Epstein, M. Roberts, N. Tessler, and P. D. Einziger, *Journal of Applied Physics* 115, 223101 (2014).

[199] S. Hofmann, T. Rosenow, M. Gather, B. Lüssem, and K. Leo, *Physical Review B* 85, 245209 (2012).

[200] J. Wünsche, S. Reineke, B. Lüssem, and K. Leo, *Physical Review B* 81, 245201 (2010).

[201] R. R. Lunt, N. C. Giebink, A. A. Belak, J. B. Benziger, and S. R. Forrest, *Journal of Applied Physics* 105, 053711 (2009).

[202] N. C. Erickson and R. J. Holmes, *Advanced Functional Materials* 24, 6074 (2014).

[203] M. Flämmich, M. C. Gather, N. Danz, D. Michaelis, A. H. Bräuer, K. Meerholz, and A. Tünnermann, *Organic Electronics* 11, 1039 (2010).

[204] M. C. Gather, M. Flämmich, N. Danz, D. Michaelis, and K. Meerholz, *Applied Physics Letters* 94, 263301 (2009).

[205] J. Lee, J.-I. Lee, J. Y. Lee, and H. Y. Chu, *Applied Physics Letters* 94, 193305 (2009).

[206] N. C. Erickson and R. J. Holmes, *Journal of Applied Physics* 110, 084515 (2011).

[207] R. Meerheim, S. Scholz, S. S. Olthof, G. Schwartz, S. Reineke, K. Walzer, and K. Leo, *Journal of Applied Physics* 104, 014510 (2008).

[208] R. Meerheim, B. Lüssem, and K. Leo, *Proceedings Of The IEEE* 97, 1606 (2009).

[209] G. He, M. Pfeiffer, K. Leo, M. Hofmann, J. Birnstock, R. Pudzich, and J. Salbeck, *Applied Physics Letters* 85, 3911 (2004).

[210] M.-T. Lee, J.-S. Lin, M.-T. Chu, and M.-R. Tseng, *Applied Physics Letters* 94, 083506 (2009).

[211] J. Lee, J.-I. Lee, and H. Y. Chu, *Synthetic Metals* 159, 1460 (2009).

[212] B. D. Chin, *Journal of Physics D: Applied Physics* 44, 115103 (2011).

[213] S. H. Kim, J. Jang, K. S. Yook, and J. Y. Lee, *Applied Physics Letters* 92, 023513 (2008).

[214] C.-H. Hsiao, Y.-H. Chen, T.-C. Lin, C.-C. Hsiao, and J.-H. Lee, *Applied Physics Letters* 89, 163511 (2006).

[215] S. W. Liu, X. W. Sun, and H. V. Demir, *AIP Advances* 2, 012192 (2012).

[216] N. C. Erickson and R. J. Holmes, *Applied Physics Letters* 97, 083308 (2010).

[217] S. Lee and C. W. Tang, *Journal of Vacuum Science & Technology B* 29, 062401 (2011).

[218] J. Lee, J.-I. Lee, J. Y. Lee, and H. Y. Chu, *Synthetic Metals* 159, 1956 (2009).

[219] Z. M. Hudson, Z. Wang, M. G. Helander, Z.-H. Lu, and S. Wang, *Advanced Materials* 24, 2922 (2012).

[220] X.-K. Liu, C.-J. Zheng, J. Xiao, J. Ye, C.-L. Liu, S.-D. Wang, W.-M. Zhao, and X.-H. Zhang, *Physical Chemistry Chemical Physics* 14, 14255 (2012).

[221] S. Gong, Y. Chen, C. Yang, C. Zhong, J. Qin, and D. Ma, *Advanced Materials* 22, 5370 (2010).

[222] X. Qiao, Y. Tao, Q. Wang, D. Ma, C. Yang, L. Wang, J. Qin, and F. Wang, *Journal of Applied Physics* 108, 034508 (2010).

[223] B. Perucco, N. A. Reinke, D. Rezzonico, M. Moos, and B. Ruhstaller, *Optics express* 18 Suppl 2, A246 (2010).

[224] N. Danz, R. MacCiarnain, D. Michaelis, T. Wehlus, A. F. Rausch, C. A. Wächter, and T. C. G. Reusch, *Proceedings of SPIE* 8829, 882923 (2013).

[225] J. Lam, T. C. Gorjanc, Y. Tao, and M. D'Iorio, *Journal of Vacuum Science & Technology A* 18, 593 (2000).

[226] S.-Y. Kim, D.-S. Leem, and J.-J. Kim, *Optics Express* 18, 16715 (2010).

[227] N. C. Erickson and R. J. Holmes, *Advanced Functional Materials* 23, 5190 (2013).

[228] M. Lebental, H. Choukri, S. Chénais, S. Forget, A. Siove, B. Geffroy, and E. Tutiš, *Physical Review B* 79, 165318 (2009).

[229] Z. B. Wang, M. G. Helander, J. Qiu, D. P. Puzzo, M. T. Greiner, Z. W. Liu, and Z. H. Lu, *Applied Physics Letters* 98, 073310 (2011).

[230] C. Yun, J. Lee, J. Lee, B. Lüssem, F. Ventsch, K. Leo, and M. C. Gather, *Applied Physics Letters* 101, 243303 (2012).

[231] J. Y. Lee, *Synthetic Metals* 157, 1004 (2007).

[232] C.-H. Lin, C.-W. Hsu, J.-L. Liao, Y.-M. Cheng, Y. Chi, T.-Y. Lin, M.-W. Chung, P.-T. Chou, G.-H. Lee, C.-H. Chang, C.-Y. Shih, and C.-L. Ho, *Journal of Materials Chemistry* 22, 10684 (2012).

[233] Q. Wang, C.-L. Ho, Y. Zhao, D. Ma, W.-Y. Wong, and L. Wang, *Organic Electronics* 11, 238 (2010).

[234] Y. C. Zhou, L. L. Ma, J. Zhou, X. M. Ding, and X. Y. Hou, *Physical Review B* 75, 1 (2007).

[235] C. Weichsel, *Weiße voll-phosphoreszente organische Leuchtdioden mit hoher Farbqualität*. Diploma Thesis, Technische Universität Dresden (2010).

[236] S. E. Jang, C. W. Joo, S. O. Jeon, K. S. Yook, and J. Y. Lee, *Organic Electronics* 11, 1059 (2010).

[237] A. R. G. Smith, J. L. Ruggles, H. Cavaye, P. E. Shaw, T. A. Darwish, M. James, I. R. Gentle, and P. L. Burn, *Advanced Functional Materials* 21, 2225 (2011).

[238] Y.-Y. Noh, C.-L. Lee, J.-J. Kim, and K. Yase, *The Journal of Chemical Physics* 118, 2853 (2003).

[239] E. B. Namdas, A. Ruseckas, I. D. W. Samuel, S.-C. Lo, and P. L. Burn, *The Journal of Physical Chemistry B* 108, 1570 (2004).

[240] K. S. Yook, S. O. Jeon, O. Y. Kim, and J. Y. Lee, *Electrochemical And Solid State Letters* 13, J71 (2010).

[241] N. G. Park, G. C. Choi, Y. H. Lee, and Y. S. Kim, *Current Applied Physics* 6, 620 (2006).

[242] L. Chen, Z. Ma, J. Ding, L. Wang, X. Jing, and F. Wang, *Chemical Communications* 47, 9519 (2011).

[243] S.-C. Lo, T. D. Anthopoulos, E. B. Namdas, P. L. Burn, and I. D. W. Samuel, *Advanced Materials* 17, 1945 (2005).

[244] S.-C. Lo, N. A. H. Male, J. P. J. Markham, S. W. Magennis, P. L. Burn, O. V. Salata, and I. D. W. Samuel, *Advanced Materials* 14, 975 (2002).

[245] T. Qin, J. Ding, L. Wang, M. Baumgarten, G. Zhou, and K. Müllen, *Journal of the American Chemical Society* 131, 14329 (2009).

[246] G.-J. Zhou, W.-Y. Wong, B. Yao, Z. Xie, and L. Wang, *Journal of Materials Chemistry* 18, 1799 (2008).

[247] T. Zheng, W. C. H. Choy, C.-L. Ho, and W.-Y. Wong, *Applied Physics Letters* 95, 133304 (2009).

[248] K. S. Yook, S. O. Jeon, C. W. Joo, and J. Y. Lee, *Journal of Industrial and Engineering Chemistry* 15, 420 (2009).

[249] Y. Divayana and X. Sun, *Organic Electronics* 10, 320 (2009).

[250] J. Yu, X. Lei, R. Jiang, and J. Zhao, *Displays* 33, 142 (2012).

[251] D. M. Kang, J.-W. Kang, J. W. Park, S. O. Jung, S.-H. Lee, H.-D. Park, Y.-H. Kim, S. C. Shin, J.-J. Kim, and S.-K. Kwon, *Advanced Materials* 20, 2003 (2008).

[252] A. Graf, *Bestimmung der Orientierung von phosphoreszenten Emittermolekülen in organischen Leuchtdioden*. Bachelor Thesis, Technische Universität Dresden (2013).

[253] Y.-L. Chang, Y. Song, Z. Wang, M. G. Helander, J. Qiu, L. Chai, Z. Liu, G. D. Scholes, and Z. Lu, *Advanced Functional Materials* 23, 705 (2013).

[254] L. Xiao, Z. Chen, B. Qu, J. Luo, S. Kong, Q. Gong, and J. Kido, *Advanced Materials* 23, 926 (2011).

[255] L. Flamigni, A. Barbieri, C. Sabatini, B. Ventura, and F. Barigelletti, *Topics in Current Chemistry* 281, 143 (2007).

[256] R. Scholz, R. Luschtinetz, G. Seifert, T. Jägeler-Hoheisel, C. Körner, K. Leo, and M. Rapacioli, *Journal of Physics: Condensed Matter* 25, 473201 (2013).

[257] R. Loudon, *The Quantum Theory of Light*. Oxford University Press (2000).

[258] R. Scholz and M. Schreiber, *Chemical Physics* 325, 9 (2006).

[259] C. Körner, *Oligothiophene Materials for Organic Solar Cells*. Ph.D. Thesis, Technische Universität Dresden (2012).

[260] L. Li, Q. Tang, H. Li, X. Yang, W. Hu, Y. Song, Z. Shuai, W. Xu, Y. Liu, and D. Zhu, *Advanced Materials* 19, 2613 (2007).

[261] S. C. B. Mannsfeld, M. L. Tang, and Z. Bao, *Advanced Materials* 23, 127 (2011).

[262] H. Kiessig, *Annalen der Physik* 402, 769 (1931).

[263] U. Pietsch, V. Holý, and T. Baumbach, *High-Resolution X-Ray Scattering*. Springer-Verlag New York (2004).

[264] R. J. F. Berger, H. G. Stammler, B. Neumann, and N. W. Mitzel, *European Journal of Inorganic Chemistry* 2010, 1613 (2010).

[265] S. Takayasu, T. Suzuki, and K. Shinozaki, *The Journal of Physical Chemistry B* 117, 9449 (2013).

[266] J. Breu, P. Stössel, S. Schrader, A. Starukhin, W. J. Finkenzeller, and H. Yersin, *Chemistry of Materials* 17, 1745 (2005).

[267] S. Lamansky, P. Djurovich, D. Murphy, F. Abdel-Razzaq, R. Kwong, I. Tsyba, M. Bortz, B. Mui, R. Bau, and M. E. Thompson, *Inorganic Chemistry* 40, 1704 (2001).

[268] Y. H. Lee and Y. S. Kim, *Thin Solid Films* 515, 5079 (2007).

[269] J. Karle and L. Huang, *Journal of Molecular Structure* 647, 9 (2003).

[270] V. Bulović, A. Shoustikov, M. A. Baldo, E. Bose, V. G. Kozlov, M. E. Thompson, and S. R. Forrest, *Chemical Physics Letters* 287, 455 (1998).

[271] V. Bulović, R. Deshpande, M. E. Thompson, and S. R. Forrest, *Chemical Physics Letters* 308, 317 (1999).

[272] D. Xu, Z. Deng, Y. Xu, J. Xiao, and C. Liang, *Displays* 26, 185 (2005).

[273] M. A. Baldo, Z. G. Soos, and S. R. Forrest, *Chemical Physics Letters* 347, 297 (2001).

[274] P.-A. Will, *Zeitlich und spektral aufgelöste Messungen der Energieniveaus organischer Materialien bei tiefen Temperaturen*. Bachelor Thesis, Technische Universität Dresden (2012).

[275] C. Reichardt, *Chemical Reviews* 94, 2319 (1994).

[276] E. Buncel and S. Rajagopal, *Accounts of Chemical Research* 23, 226 (1990).

[277] S. Y. Lee, T. Yasuda, H. Nomura, and C. Adachi, *Applied Physics Letters* 101, 093306 (2012).

[278] J.-H. Jou, Y.-P. Lin, M.-F. Hsu, M.-H. Wu, and P. Lu, *Applied Physics Letters* 92, 193314 (2008).

[279] C. Madigan and V. Bulović, *Physical Review Letters* 91, 247403 (2003).

[280] T.-W. Lee, T. Noh, H.-W. Shin, O. Kwon, J.-J. Park, B.-K. Choi, M.-S. Kim, D. W. Shin, and Y.-R. Kim, *Advanced Functional Materials* 19, 1625 (2009).

[281] Y. Shi, J. Liu, and Y. Yang, *Journal of Applied Physics* 87, 4254 (2000).

[282] P. Peumans, S. Uchida, and S. R. Forrest, *Nature* 425, 158 (2003).

[283] E. Verploegen, R. Mondal, C. J. Bettinger, S. Sok, M. F. Toney, and Z. Bao, *Advanced Functional Materials* 20, 3519 (2010).

[284] S. Pfuetzner, C. Mickel, J. Jankowski, M. Hein, J. Meiss, C. Schuenemann, C. Elschner, A. A. Levin, B. Rellinghaus, K. Leo, and M. Riede, *Organic Electronics* 12, 435 (2011).

[285] J.-R. Gong, L.-J. Wan, S.-B. Lei, C.-L. Bai, X.-H. Zhang, and S.-T. Lee, *The Journal of Physical Chemistry B* 109, 1675 (2005).

[286] C. Mayr and W. Brütting, *Chemistry of Materials* DOI: 10.1021/acs.chemmater.5b00062 (2015).

[287] D. Yokoyama, *Journal of Materials Chemistry* 21, 19187 (2011).

[288] D. Donhauser, M. Pfannmöller, L. Dieterle, K. Schultheiß, R. R. Schröder, W. Kowalsky, and M. Kröger, *Advanced Functional Materials* 23, 2130 (2013).

[289] D. Yokoyama, A. Sakaguchi, M. Suzuki, and C. Adachi, *Organic Electronics* 10, 127 (2009).

[290] C. Schünemann, D. Wynands, K. J. Eichhorn, M. Stamm, K. Leo, and M. Riede, *Journal of Physical Chemistry C* 117, 11600 (2013).

[291] S. W. Liu, C. C. Lee, C. H. Wang, J. H. Lee, C. T. Chen, and J. K. Wang, *Chemical Physics Letters* 474, 207 (2009).

[292] C.-C. Lee, S.-W. Liu, and Y.-T. Chung, *Journal of Physics D: Applied Physics* 43, 075102 (2010).

[293] L. Cheng, L. Liao, W. Lai, X. Sun, N. Wong, C. Lee, and S. Lee, *Chemical Physics Letters* 319, 418 (2000).

[294] M. A. Baldo, M. E. Thompson, and S. R. Forrest, *Pure and Applied Chemistry* 71, 2095 (1999).

[295] Y. Ma, C.-M. Che, H.-Y. Chao, X. Zhou, W.-H. Chan, and J. Shen, *Advanced Materials* 11, 852 (1999).

[296] T. Tsutsui, M.-J. Yang, M. Yahiro, K. Nakamura, T. Watanabe, T. Tsuji, Y. Fukuda, T. Wakimoto, and S. Miyaguchi, *Japanese Journal of Applied Physics* 38, 1502 (1999).

[297] C. Adachi, M. A. Baldo, S. R. Forrest, S. Lamansky, M. E. Thompson, and R. C. Kwong, *Applied Physics Letters* 78, 1622 (2001).

[298] C. Ulbricht, B. Beyer, C. Friebe, A. Winter, and U. S. Schubert, *Advanced Materials* 21, 4418 (2009).

[299] H. Yersin, A. F. Rausch, R. Czerwieniec, T. Hofbeck, and T. Fischer, *Coordination Chemistry Reviews* 255, 2622 (2011).

[300] R. Czerwieniec, J. Yu, and H. Yersin, *Inorganic Chemistry* 50, 8293 (2011).

[301] T. Furukawa, H. Nakanotani, M. Inoue, and C. Adachi, *Scientific Reports* 5, 8429 (2015).

[302] K. Masui, H. Nakanotani, and C. Adachi, *Organic Electronics* 14, 2721 (2013).

[303] D. Patra, I. Gregor, and J. Enderlein, *The Journal of Physical Chemistry A* 108, 6836 (2004).

[304] J. G. Hou, J. Yang, H. Wang, Q. Li, C. Zeng, H. Lin, W. Bing, D. M. Chen, and Q. Zhu, *Physical Review Letters* 83, 3001 (1999).

[305] T. Yokoyama, T. Takahashi, K. Shinozaki, and M. Okamoto, *Physical Review Letters* 98, 206102 (2007).

[306] T. Yokoyama, T. Takahashi, and K. Shinozaki, *Physical Review B* 82, 155414 (2010).

Acknowledgement

During the last years, I have learned a lot—foremost a deeper understanding of physics, creative thinking, collaborating with other researchers, as well as teaching students. I highly enjoyed the working atmosphere, the friendly cooperation, and the social activities in our institute. As this work would have been impossible without the scientific and technical support from many people, I want to express my deepest gratitude:

First, I would like to acknowledge Prof. Dr. Karl Leo, my supervisor, for giving me the opportunity to work on this topic. I am very grateful for his constant guidance and support, and highly enjoyed the scientific freedom he offered me.

I am deeply indebted to Prof. Dr. Malte C. Gather, not only for preparing the second review of this thesis, but also for the countless inspiring discussions we had, his very critical proofreading of my papers, and his strong confidence in my work. I highly appreciate the two years when I worked under his outstanding guidance and supervision.

I want to thank Jun.-Prof. Dr. Sebastian Reineke for his great scientific input, his many ideas, and the motivating atmosphere he creates. I am very happy that I could take over this exciting topic from him, and that our paths crossed again last year.

I am very grateful for the steady support and interest of Dr. Simone Hofmann, for her critical analysis of my work, and for her excellent guidance of our group. I will never forget the time we spent together creating fancy presents for former co-workers, capturing exciting OLED photos, and laser-cutting Christmas cards.

Asst. Prof. Dr. Björn Lüssem deserves my gratitude for guiding me during the first year of my PhD. I highly appreciated his thoughtful leadership and his openness to suggestions.

I want to thank Philipp Liehm and Arko Graf for their cooperation, for measurements and simulations they performed for this work, and for their critical questions. They finally infected me with their excitement for oriented emitters and taught me how to become a better supervisor.

I am grateful to Dr. Chris Elschner for introducing me to X-ray diffraction methods and performing GIWAXS measurements for this thesis. In addition, Dr. Lutz Wilde deserves my thanks for performing XRD measurements.

Furthermore, I am thankful for all my colleagues, especially in the OLED group, and in my offices BEY95 and KOE318, for the stimulating working atmosphere, inspiring discussions, and scientific input. Especially, I thank Cornelius Fuchs for performing various optical simulations, Dr. Reinhard Scholz for calculating emitter dipole moments and providing me fit routines to extract spectral line shapes, and Tobias Mönch for his well-considered questions and many critical discussions we had upon lunch.

For proofreading this manuscript, I thank Prof. Dr. Karl Leo, Jun.-Prof. Dr. Sebastian Reineke, Dr. Simone Hofmann, and Jan Murawski.

A huge "thank you" goes to our Lesker-team, Caroline Walde, Tobias Günther, and Andreas Wendel, for building numerous OLEDs and organic thin-films for this work. Furthermore, I thank Alrun Günther and Markus Fröbel for keeping the UFO evaporation system in top condition, Tina Träger and Annette Petrich for material sublimation, and Sven Kunze and Carsten Wolf for technical support and maintenance of our tools.

I also want to acknowledge our administration team: Johanna Katzschner, Eva Schmidt, Jutta Hunger, Julia Barth, Dr. Annette Polte, Dr. Angelika Wolf, and Dr. Christian Zschalig. Furthermore, I want to thank Kai Schmidt and Peter Leumer for managing our IT.

Besides the exciting scientific environment, our institute also offers excellent leisure activities. For me, the IAPP choir was always one highlight of the week and, besides all members, I want to especially thank our choirmasters Jan Murawski, Ludwig Bormann, and Dr. Ulrich Zerweck-Trogisch for regularly pushing our boundaries further.

Last but not least, I want to thank my family. My husband Jan deserves my deepest gratitude for supporting me all the years—be it in explaining physics to me, teaching me how to write better English, or encouraging me to think outside the box. Your love is so important to me!

I am deeply indebted to my parents for their great interest in my work and their constant support. Especially their help during the last months is invaluable, when they looked after my son so I could finish my work.

My grandfather was always my biggest fan. His curiosity and joy about his granddaughter taking the path he would have liked to follow was my biggest motivation—therefore, this work is dedicated to him.

Erklärung

Diese Arbeit wurde am Institut für Angewandte Photophysik der Fakultät Mathematik und Naturwissenschaften an der Technischen Universität Dresden unter wissenschaftlicher Betreuung von Prof. Dr. Karl Leo angefertigt.

Hiermit versichere ich, dass ich die vorliegende Arbeit ohne unzulässige Hilfe Dritter und ohne Benutzung anderer als der angegebenen Hilfsmittel angefertigt habe; die aus fremden Quellen direkt oder indirekt übernommenen Gedanken sind als solche kenntlich gemacht.

Die Arbeit wurde bisher weder im Inland noch im Ausland in gleicher oder ähnlicher Form einer anderen Prüfungsbehörde vorgelegt.

Ich erkenne die Promotionsordnung der Fakultät Mathematik und Naturwissenschaften der Technischen Universität Dresden vom 23.02.2011 an.

Dresden, 21.04.2015 Caroline Murawski